Collection of Papers

6th Biennial Conference

Particles in Europe, PiE-2018

Lisbon, Portugal

14-17 October 2018

Sponsors:

Sequoia Scientific, Inc. **Instituto Hidrografico, Lisbon, Portugal**

Editors:

Yogesh C Agrawal (Sequoia Scientific, Inc., US)
Ana Santos (Instituto Hidrografico, PT)
Ole Mikkelsen (Sequoia Scientific, Inc., US)

Organizing Committee:

Convenors: Yogesh (Yogi) Agrawal and Wayne Slade (in US);

Co-convenors: Anabela Oliveira, Ana Santos (in Europe)

Sandor Baranya (Hungary), (host at Hungary, co-chair).

Ole Aarup Mikkelsen (Denmark), (Convenor past PiE conferences, co-chair)

Jim Decker (Sequoia Scientific, Inc.), (US), *Exhibits Coordinator*

Alex Nimmo-Smith (United Kingdom)

Katarina Holubova (Slovakia)

Massimo Guerrero

Michael Fettweis (Belgium)

Nils Ruther (Norway)

Piers Larcombe (Australia)

Romaric Verney (France)

Sagan Slowomir (Poland)

Stefan Haun (Germany)

Invited Speakers:

Dr. Cesar Andrade, Portugal

Dr. Claire Chassagne, Netherlands

Dr. Helmut Habersack, Austria.

Dr. Piers Larcombe, Australia

Dr. Luis Quaresma, Portugal

Dr. Paula Freire, Portugal

PREFACE

This volume contains the papers submitted by attendees to the 6th Biennial Particles in Europe Conference. The conference was held at the Instituto Hidrografico, in Lisbon Portugal. Around 60 scientists attended. This PiE Conference conformed to the format of earlier ones. Two days of papers with a day of a field trip on the Tagus estuary in between, and a conference dinner at the beautiful Maritime Museum in Belem. The conferences are sponsored by Sequoia Scientific, Inc. in Bellevue, Washington, USA. This 6th Conference was hosted by Instituto Hidrografico who also kindly provided facilities and their generous hospitality.

Rear-Admiral Carlos Ventura Soares, Director General of the Institut Hidrografico welcomed the attendees.

Contents

[In alpha order by last name of first author]

NOTES

Three Frequency Acoustics for Inverting *Vertical* River Profiles

Yogesh C Agrawal, and Wayne Slade

Sequoia Scientific, Inc. USA

This presentation reviews current methods for interpreting 1-2-3 frequency acoustic backscatter, and examines a method for inverting 3-frequency acoustic signals synthesized from real vertical profiles of particle size distributions measured in a river.

One Frequency System

Given the widespread use of radar, it was obvious that backscatter strength from an acoustic pulse could produce estimates of sediment in water. The early systems were single-frequency systems. To solve the difficulty with having one piece of information (backscatter strength) for two unknowns – grain size and concentration - some auxiliary information was necessary. The assumption of a Rouse profile has been invoked to specify size-dependence along a vertical beam. This approach requires estimates of turbulent friction velocity. An assumption of along-beam homogeneity is a second approach to fill the gap in data. In this case, typically using horizontal beams and assuming horizontal homogeneity of river sediment, the excess in slope of the backscatter profile over that due just to geometric and water attenuation, is attributed to sediment attenuation by fines. With a further assumption of grain size, the attenuation can be converted to concentration of fines. Second, the logarithmic backscatter signal strength profiles conveniently shift up/down with higher/lower concentration of the homogeneous stream. This vertical shift (in principle, constant at all range bins) can be attributed to backscattering signal strength. Again, with assumed grain size, the backscatter strength can be interpreted as concentration of coarse grains. In effect, one must make assumptions of homogeneity along a beam, and obtain somehow the size of attenuating particles and of scattering particles. Hanes (2011) showed that this separation of attenuation due to fines and scattering to coarse grains has validity under restricted conditions. So, the method works, but is less than ideal, requiring too many auxiliary pieces of information. Finally, if both attenuation and backscatter strength are available, why not use the ratio to find grain size? For two reasons: attenuation is often too weak to measure with certainty, and the ratio is not single-valued. Nevertheless, the method has found some acceptance.

Two-Frequency System

In principle, two unknowns can be solved for given two pieces of information. If the backscatter strength from two frequencies is known, their ratio can be uniquely related to grain size. This is so because the scattering strength σ depends on particle density ρ, mass concentration M, grain size *d,* and the size-dependent form function *f* as follows:

$$\sigma = \quad f^2 \, M/\rho d \qquad (1)$$

which adds incoherently (their scattered intensities) in the presence of multiple sizes of grains as:

$$\sigma_1 = \Sigma_\iota \; (f_1^2 \mathrm{M}/\rho d)_i \, ; \qquad (2)$$

The 2-frequency method measures the backscatter at two frequencies and gets two estimates of backscattering cross-section:

$$\sigma_2 = \Sigma_\iota \; (f_2^2 \mathrm{M}/\rho d)_i ; \qquad (3)$$

The ratio of these two scattering cross sections is interpreted as the ratio of scattering from two frequencies for a *single sized* grain: i.e.

$$\sigma_1 / \sigma_2 = [f_1 / f_2]^2 \qquad (4)$$

The left hand is a scalar. The right hand is a function of diameter. In this way, the value of D where the ratio on the right-hand size matches the measured ratio on left, yields the grain size. Once grain size is determined, the mass concentration (a scalar again) is determined from Eq.1. This was the method employed by Agrawal and Hanes (2015). They made estimates of vertical profiles of σ from LISST-measured size distribution, according to Eq. 2. They found that the results came close to laser measured mean size, but only when sand grains were present. In the surface, lacking sand grains, this method produced grossly erroneous estimates of mean size and concentration.

3- Frequency Method:

The first to attempt the use of 3-frequencies were Hay and Sheng (1992). They were successful in working with sands, starting with the assumption of a log-normal *number* density of the sands. Their sediments did not contain fines. Their forward problem was to compute the scattering cross-sections and their ratios for pairs chosen out of the 3 frequencies and find the mean size that fitted those. The measured ratios of scattering at the two pairs of frequencies were compared against the data. The mean size and spread at which the theoretical ratios matched data would be the solution. They noted that a 'solution does not always exist'. To deal with real data, and find solutions, they forced the size spread of 1.2 times mean size. Although we are aware of similar other attempts, we have not seen inversion of acoustic backscatter from vertical profiles of sediments in a real river. This profile contains a wash load at the surface of fine material, and as depth increases, a sand mode appears. With increasing depth, the sand mode grows in magnitude, shifts to larger size, and varies in width of the log-normal distribution. This is the problem we have attempted, synthetically.

Our Approach:

We begin with the same data that were employed for the Agrawal and Hanes (2015) paper. Vertical profiles of full 32-size class particle size distributions (PSDs) from the Cowlitz River in Washington State were used as input. Roughly 4,000 points of PSD were available in the profile.

For each PSD, the scattering *intensity* cross-section was computed for 3 frequencies, following Eq. 2. Each estimate is thus expressible as Eq. 2. Using $\underline{\boldsymbol{\sigma}}$ now for backscatter intensity, in a matrix form:

$$\underline{\boldsymbol{\sigma}} = \underline{\underline{\mathbf{F}}}\;\underline{\mathbf{M}} \qquad (5)$$

where $\underline{\boldsymbol{\sigma}}$ and $\underline{\mathbf{M}}$ are, respectively, 1 x N, and 32 x N arrays. Each element of σ is due to a single PSD, M, and the kernel matrix $\underline{\underline{\mathbf{F}}}$ is a 3x 32 array (scattering for each of 3 frequencies, and 32 sizes).

The problem of solving for PSD from the simulated array amounts to finding a 'best fit' solution to:

$$\underline{\mathbf{M}} = \underline{\underline{\mathbf{F}}}^{-1}\,\underline{\boldsymbol{\sigma}} \qquad (6)$$

We now assume that to recover $\underline{\mathbf{M}}$ we seek its approximate representation $\underline{\mathbf{M}}$ which is expressed as:

$$\underline{\mathscr{M}} = a\,exp[(-n-n_0)^2/\delta n^2] \qquad (7)$$

That is, we seek log-normal distributions of amplitude *a*, centered at size bin number n_0, and of width δn size bins. [The size bins refer to the size-classes of LISST's.] We shall then compute and compare the measurements M with the best fit $\underline{\mathscr{M}}$. The inversion follows the method of steepest descent.

Results

In Fig. 1, on left, I show the profiles of particle size distribution plotted with depth. The profile covers depth from 0 to about 3m, which is most of the Cowlitz River column in Castle Rock, Washington. The data were acquired in March 2011.

It is seen that the near-surface region is mostly fine particles, and that with depth increasing, sand particles begin to appear. In the middle, the acoustic cross sections σ (Eq.2) are shown for the 3 frequencies, 1, 2, and 3 MHz (respectively, blue, green, and red) .

After inversion of Eq. 6, the results are shown on the right panel. A careful look shows first that the first 1.25 meters or so, the reconstructed profiles $\underline{\mathscr{M}}$ are erratic. This is the region of only fine particles (left). Indeed, instead of finding the wash load, sized around 30 microns, there is an erratic tendency to find particles in the large particle range. In this region, the inversion fails.

Going below about 1.25 meters, where the sand grains appear, the measured PSD's and the inversion $\underline{\mathbf{M}}$ reproduce observations well. The pseudo color plots are on the same scale. Even, the amplitudes seem well captured. This is the key result. In effect, when sand mode is present, even with the contamination due to the always present wash load, the fitted log-normal profiles seem to match the LISST-SL data.

Discussion

Why does this result matter? What is the criterion for success?

To our knowledge, inverting vertical profiles of acoustic backscatter remain challenging. The Rayleigh limit for our chosen frequencies are, respectively, 240, 120, and 80 microns (radii). Thus, the wash load is in the Rayleigh limit for all 3 frequencies, whereas the sand load is in the 'Mie' range. The wash load in this case, merely adds a bias to σ from the sand mode scattering. The bias depends on the frequency.

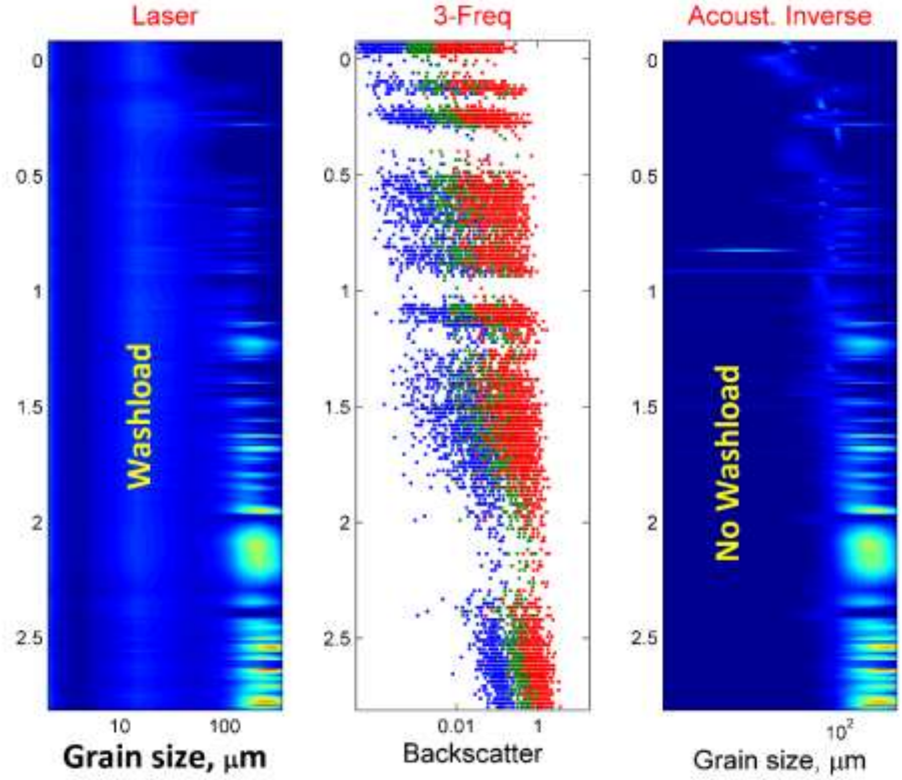

Fig. 1: The laser diffraction measurements of particle size distributions (PSD) profile in the Cowlitz river (left panel); the acoustic cross-sections for each PSD at 1,2 and 3 MHz frequencies synthesized from these data, and the inverted size distributions on the right. [The ordinates for all figures are meters.]

The next question to discuss is what is the criterion for success? It is not sufficient to say that the presence of the wash load does not frustrate the inversion, despite the bias it adds to the cross-sections. This leads to the issue of the ratio of contributions from the sand mode, to the bias from the wash load mode. We shall examine this further in the presentation.

References:

Hay, A. and Sheng, 1992: Vertical Profiles of Suspended Sand Concentration and Size from Multifrequency Acoustic Backscatter; J. Geophys. Res. V 97, pp 16,661-677.

Agrawal, Y. and D. Hanes, 2015: The implications of laser-diffraction measurements of sediment size distributions in a river to the potential use of acoustic backscatter for sediment measurements; Water Res. Res., 51.

Hanes, D. 2011: On the possibility of single-frequency acoustic measurement of sand and clay concentrations in uniform suspensions; Cont. Shelf Res., special issue on Acoustics.

Flocculation of PVC microplastic particles in natural seawater

Thorbjørn Joest Andersen*, Kristoffer Hofer Skinnebach, Mikkel Fruergaard

Department of Geosciences and Natural Ressource Management, University of Copenhagen

***email:** tja@ign.ku.dk

Introduction

Microplastic particles have been identified in all seven oceans and is generally considered to be a potential risk to ecosystems and ultimately human health. The term microplastic is generally used for particles smaller than 5mm. The microplastic enters the sea either in the form of larger debris which is then broken down into smaller particles (secondary microplastic) or in the form primary microplastic which is already smaller than 5mm upon entering the aquatic environment, e.g. beads in cosmetics and body shampoo. The transport and ultimate sink for the particles is dependent on a number of factors including size and density of the particles. Flocculation is also expected to be important since the particles may at least to some extent behave like other fine-grained inorganic particles which tend to be incorporated into aggregates in both fluvial, estuarine and marine environments.

The present study examines the flocculation behavior of one particular kind of plastic: polyvinyl chloride (PVC). This plastic is used in a broad range of materials and settings including piping, automobiles and buildings.

Methods

Microplastic particles were produced by grinding a rod of PVC (density 1.4 g cm^{-3}) on a regular workbench rotating wetstone (Sheppach Tiger 2000s). The particles produced by this grinding were wet-sieved at 20 µm, producing a suspension of microplastic particles smaller than 20 µm. The particles were subsequently introduced in a floc camera/settling chamber system consisting of a "PCam" floc camera measuring below

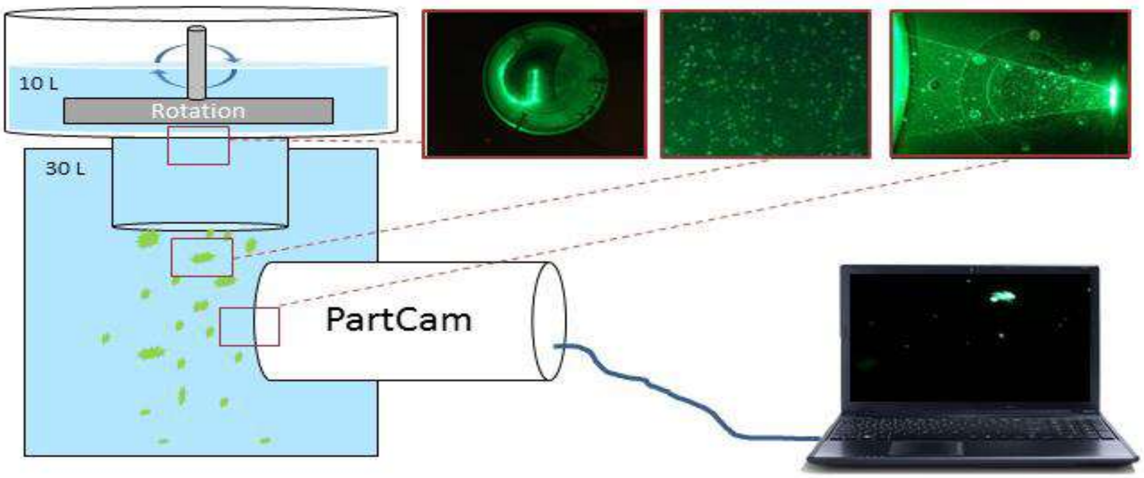

Figur 1: Partcam settling chamber, including incubation chamber, settling chamber and PartCam floc camera (from Andersen et al., in prep)

an incubation chamber with a rotating plate which keeps the particles suspended (fig 1). The system is described in Markussen et al., 2016. The particles were incubated in local seawater collected in the strait "Øresund" situated between Denmark and Sweden. Salinity varied between 8 and 15 PSU and chl a level was low, generally below 2 µg l^{-3}. The suspensions were incubated for two hours after which a sliding door was opened to the settling chamber with the Pcam. Size and settling velocities was measured by the camera and effective densities were subsequently calculated using Stokes law. Examples of flocculated PVC-particles measured in the setup is shown in fig 2.

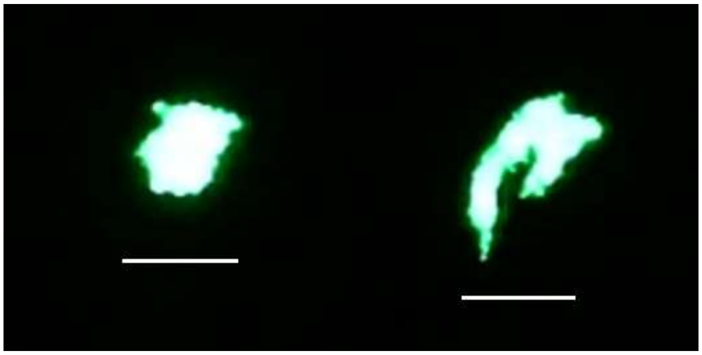

Figur 2: PVC-flocs formed in natural seawater. Scale bar is 500 micron

Results

The experiments showed significant flocculation already during this relatively short incubation period of two hours. Floc sizes up to more than 500 µm were measured whereas the individual, primary particles showed a mean grain size of less than 10 µm. An example of the temporal variation in floc size during the settling phase is shown in fig 3. The floc size is expressed as Equivalent Spherical Diameter (ESD). The decrease in floc size with time is due to the progressive depletion of large and fast settling flocs during the experiment. The large majority of the microplastic particles are flocculated into aggregates larger than 100 µm. The reason for this flocculation is subject to ongoing research but it is believed to be caused at least to some extent by phytoplankton and other organic substances in the seawater. Additional experiments are being carried out in freshwater (results pending at the time of writing).

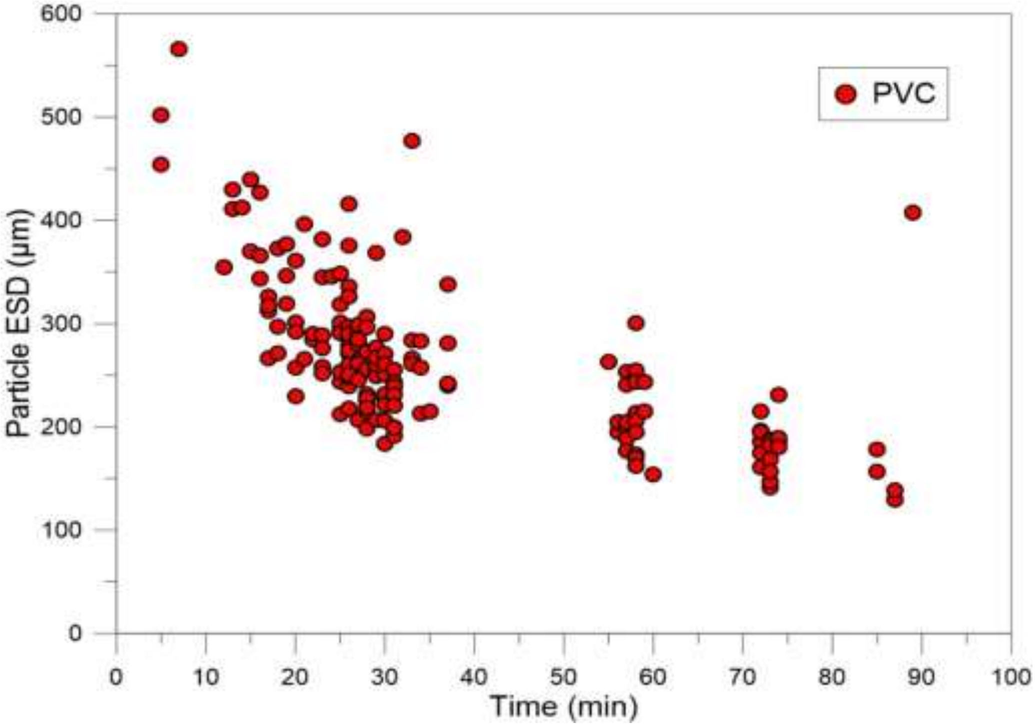

Figur 3: Variation of floc size during the settling phase of the experiments.

The settling velocities were calculated on the basis of video-clips of the settling suspension. An example is shown in fig 4. Settling velocities were generally in the range of 0.2 to 0.5 mm s^{-1} but even higher velocities were measured at the beginning of the settling phase. The black line in fig 4 shows the expected

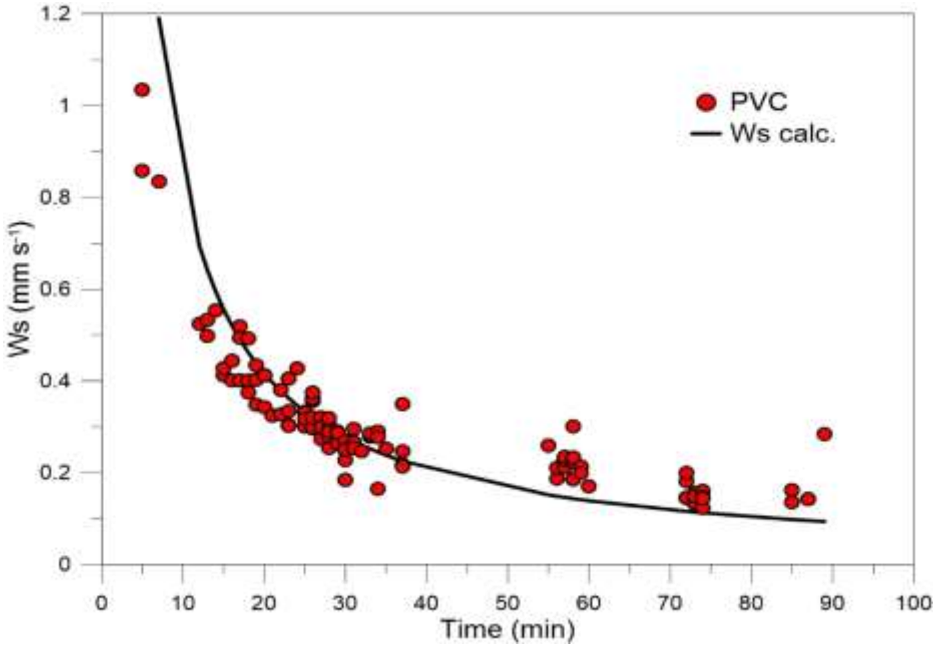

Figur 4: settling velocities of flocculated PVC-particles

velocities through time calculated on the basis of the settling distance between the incubation chamber and the Pcam and the time of observation of the particle. The observations falls relatively close to this line and the tendency to apparent overestimation of settling velocity at the end of the experiment is likely due to ongoing flocculation in the settling chamber, possibly due to differential settling.

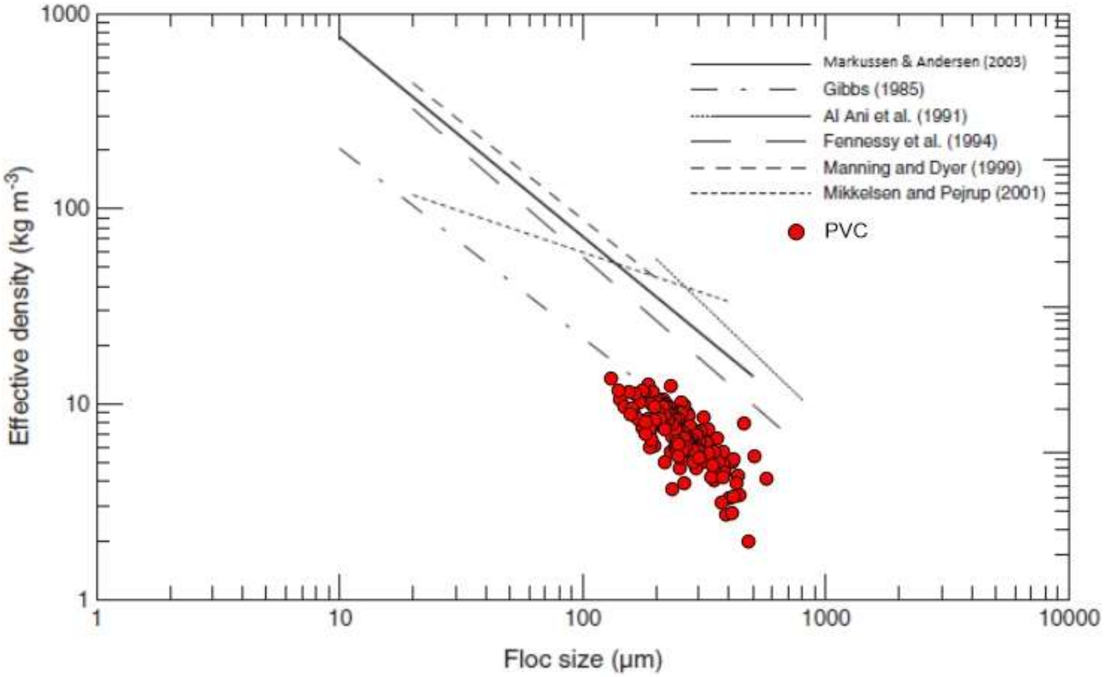

Figur 5: Calculated effective densities of PVC-flocs compared to results from various other studies on natural sediments.

The effective density of the particles have been calculated on the basis of their measured size and settling velocity and the result is plotted in fig 5 together with results from a range of other studies using natural sediments. The present data, on PVC microplastic particles, follows the same trend as natural sediment and shows decreasing effective density with increasing floc size. However, the effective densities are generally lower than that of natural sediment flocs of similar size, reflecting a relatively slow settling of the microplastic flocs compared to natural sediments. This tendency for lower settling velocity is probably at least partly caused by the lower density of the PVC particles (1.4 g cm^{-3} compared to about 2.65 g cm^{-3} for minerogenic particles). We expect that microplastic particles in nature will be incorporated into flocs composed of natural organic and inorganic particles and they may therefore settle at rates similar to that of the remaining flocculated particles. This hypothesis is currently being investigated using basically the same instrumental setup as described here but with various mixtures of microplastic particles, natural sediments and natural seawater.

Reference:

Markussen, T. N., Elberling, B., Winter, C., & Andersen, T. J. (2016). Flocculated meltwater particles control Arctic land-sea fluxes of labile iron. Scientific Reports, 6:24033, DOI: 10.1038/srep24033.

Particle stories: from source to sink

C. Andrade

Instituto Dom Luiz, Departamento de Geologia, Faculdade de Ciências da Universidade de Lisboa

FCUL, Bloco C6 3 piso, Campo Grande, 1749 -016 Lisboa

e-mail: candrade@fc.ul.pt

Abstract

Detritic particles populating the coastal zone and inner shelf are mainly sourced in continents. Once they leave their source areas, both individual and collections of particles do experience changes in a suite of physical and compositional attributes while following different dispersion paths. This talk addresses case-studies showing how particle features, including composition, size, shape and distribution, help us to reconstruct sediment sources as well as to establish and model processes of erosion, transport and deposition.

Evaluation of sediment flux measurements by calibrated ADCP backscatter data in a tide-controlled estuary

Marius Becker[1], Gabriel Herbst[1], Christian Maushake[2], and Christian Winter[1]

[1] Institute of Geosciences, University of Kiel, Germany

[2] BAW - Federal Waterways Engineering and Research Institute, Hamburg, Germany

Acoustic backscatter calibration developed into a frequently applied technique to measure fluxes of suspended sediments in rivers and estuaries. Despite increased knowledge on acoustic properties of suspended particles and on the advantages of multifrequency hydroacoustics, the standard approach still relies on single-frequency profiling devices, such as ADCPs. Calibration data may comprise OBS and LISST data only, and information on floc structure and the properties of primary particles is missing.

In this situation, significant errors might be introduced, in particular in conditions encountered in the turbidity zone of tide-controlled estuaries. High values of SSC require to take sediment absorption into account, but the sediment absorption coefficient must be estimated. Additional errors on flux measurements arise from incomplete vertical and lateral coverage of the cross-section, and the small ratio of the residual transport to the tidal transport, depending on the tidal prism.

We analyzed four sets of 13h cross-sectional ADCP data, collected 2009 at different locations in the range of the turbidity zone of the Weser estuary, North Sea, Germany. Vertical LISST, OBS and CTD casts were obtained very hour. During the calibration, sediment absorption was taken into account. Particle size information was obtained from LISST data and used initially to determine acoustic properties of particles.

Due to the tidal excursion and the displacement of the turbidity zone, acoustic properties of particles changed during the tidal cycle, at all locations. Applying empirical functions, the lowest backscattering cross-section and highest sediment absorption coefficient were found in the center of the turbidity zone. Outside the tidally averaged location of the turbidity zone, changes of acoustic parameters were caused mainly by advection. In the turbidity zone, these properties were also affected by settling and entrainment, inducing vertical differences and systematic errors in concentration. As widely recognized, local errors in concentration propagate and amplify exponentially due to the iterative correction of sediment absorption along the acoustic path. Based on reference concentration obtained from water samples and OBS data, we quantified these errors and their effect on cross-sectional averaged concentration and sediment flux. We found that errors are effectively decreased by applying calibration parameters interpolated in time, and by using the sediment absorption coefficient as a free parameter in a simple optimization procedure. We further discuss practical aspects of residual flux determination in tidal environments and of measuring strategies in relation to site-specific tidal dynamics.

A more recent data set, collected in November 2016, at the same location included water samples, which were analyzed with respect to primary particle size and organic content. Primary particle size was on average 8 µm and almost constant during the tidal cycle, in the range of the turbidity zone. The organic content was comparatively high, up to 18%. Information on floc structure was obtained using the particle camera system PCAM, developed by Gabriel Herbst. Together, these data will allow applying more advanced acoustic models to evaluate, if the sediment absorption correction and, in general, the backscatter calibration can be improved.

Improvement of water quality within Danish blue mussel farms observed using optical methods

Karolina Borzycka*, Sławomir Sagan, Monika Zabłocka

Institute of Oceanology, Polish Academy of Sciences

Powstańców Warszawy 55, 81-712 Sopot, Poland

* borzycka@iopan.gda.pl

One of the primary threats for Baltic ecosystem is eutrophication. High nutrient inputs causes algal and plant growth, increased water turbidity and oxygen depletion at the sea bottom. Suspension-feeders, like blue mussels, filter the sea water, what reduces suspended particle concentrations (Riisgård, 1998). This phenomenon potentially contributes to water quality improvement and mitigate effects of eutrophication.

In the study characteristics of suspended matter and inherent optical properties were analyzed based on empirical data, which were obtained during a campaign in September 2017 on three mussel farms located in Denmark fjords: Horsens and Limfjord.

At each station measurements of suspended matter characteristics, inherent optical properties of seawater, temperature, salinity were pereformed in-situ from surface to the bottom. Particle volume concentration (PVC) were measured in-situ with LISST-100X type B, accompanied with concurrent sampling of inherent optical properties (IOPs), Secchi depth and suspended matter dry mass (SPM) for organic and inorganic fraction.

Despite the different hydrological conditions observed in Limfjord and Horsens Fjord and different absolute values of optical parameters in sampled areas, similar pattern of differences were noticed between inside and outside waters of mussel farmsValues of all measured parameters were lower inside farms than outside. Differences between particles median values inside and outside the farms observed using LISST-100X were up to 33% of Total PVC and 52% of particle number. Moreover higher slope of particles size distribution were observed inside farms, what suggests shift towards smaller sizes of suspended particles. Similar differences of particles quantity have been confirmed by analysis of SPM concentration. The parameter values were similar or up to 34% lower inside the farms, as well as its organic and inorganic fraction (up to respectively 33% and 37%).

Presented study documents changes of optical properties of water within mussel farms as foreseen by eco hydrodynamic models (Nielsen et al., 2016). Improvement of water quality by increasing water transparency is evidenced by particles depletion and domination of its smaller size fraction. This documented feature allows qualitative and quantitative use of optical or remote sensing methods for control of environmental impact of mussel farms.

References

Nielsen, P., Cranford, P., Maar, M., Petersen, J., 2016, *Magnitude, spatial scale and optimization of ecosystem services from a nutrient extraction mussel farm in the eutrophic Skive Fjord, Denmark*. Aquaculture Environment Interactions 8, 311–329. **https://doi.org/10.3354/aei00175**

Riisgård H.U., 1998, *Filter feeding and plankton dynamics in a Danish fjord: a review of the importance of flow, mixing and density-driven circulation,* Journal of Environmental Management, vol. 53, issue 2; 195-207.

Challenges in using Optical Backscatter techniques for sediment monitoring in mixed sediment environments

Klavs Bundgaard[1]; Ulrik Lumborg[2], Lotte Nyborg[2], Bjarne Holm Jakobsen[3]

[1]NIRAS A/S, Sortemosevej 19, 3450 Allerød, Denmark

[2]DHI, Agern Allé 5, DK-2970 Hørsholm, Denmark

[3]Femern A/S, Vester Søgade 10, 1601 København V, Denmark

Introduction

Sediment measurements in shallow coastal lagoons are often associated with challenges relating to determining the actual concentration levels. Sediment concentrations can be determined by a range of methods. All instruments have strengths and weaknesses. Some of these are described in literature like Downing (2006) and Sutherland et al. (2000). Generally, all light scattering devices require calibration and they are sensitive to biofouling. Apart from sediment concentration (TSMC) almost all instruments are sensitive to shifting grain size distributions, sediment grain shapes, sediment reflectivity, suspended organic material and the colour of the sediment and water. Of these grain size distribution is considered the most important factor. The effect has previously been documented by various authors (Battisto et al., 1999; Black and Rosenberg, 1994; Conner and De Visser, 1992; Ludwig and Hanes, 1990; Sutherland et al., 2000). Of these studies only Battisto et al. (1999) used natural mixed sediments. The remaining studies did not include the effect of shifting sediment composition in the water column.

If treated properly, water samples and subsequent filtrations is the only measure that always gives the correct sediment concentration. The down side is that physical presence is needed to take the samples. This can be costly and challenging in rough weather. Therefore, it is attractive to setup systems which are self-recording or online and can operate in shallow lagoons without the need for physical presence during the campaign. This however, leads to a new set of challenges as the applied instruments must be able to measure changing sediment concentrations with varying grain size distributions. One of the most applied instruments is the Optical BackScatter instrument (OBS) (Downing, 2006; Sutherland et al., 2000). The challenge becomes how to make an optimum transfer function between the OBS reading in NTU and the TSMC in mg l^{-1}. The correlation is expected to be linear for fixed sediment properties. But if the sediment properties change over time little is reported on the transfer function to be applied. The present paper studies the correlation between grain size distribution and calibration coefficients for an OBS measuring devices under static sediment conditions only varying concentrations and under dynamic conditions with varying concentrations and grain size distributions.

I many studies the turbidity is obtained from optical instruments. During the recent decades most notably the optical backscatter (OBS). OBS devices do however not measure the sediment concentration directly but rather a calibrated unit like NTU or FTU. The calibrated unit must be transferred to TSMC using manually collected water samples. Turbidity signals obtained from the OBS device are subsequently correlated to the TSMC results from the water samples. From this correlation a transfer function is obtained (Downing, 2006). The transfer function is not uniform as it is dependent on several variables including (but not limited to): Sediment grain size distribution, sediment colour and biological substances. The transfer function therefore changes both in time and in space and therefore needs to be updated regularly.

Results

In the present study NTU values were transferred using different sediment types. The linear correlations that are often used turned out to be poor for high concentrations and could therefore not be used for analytical purposes. For safety reasons water samples could only be taken in relatively fair weather and therefore in an environment where the general turbidity was low especially with respect to the coarser materials. This situation gave a relatively narrow span of concentrations to use for calibrations and they were only representative for calm weather. During storms it was known that the fine sand and silt could resuspend and reach very high concentrations. Therefore, a transfer function based on low concentrations only would be erroneous and probably not representative for the grain size distribution seen under storms. To investigate the effect of this a series of tests were initiated in the laboratory and in the field.

The data used for the study has been gathered partially from an online system placed in the non-tidal lagoon system of Rødsand in southern Denmark and partially based on geotechnical sampling and investigations for coming Fehmarnbelt link between Denmark and Germany.

The static conditions were studied in the laboratory and transfer functions were developed for different sediment types. This lead to an improved understanding of the expected variation that could be found in situ. The assumption was then validated based on a field measurement campaign from the Rødsand lagoon.

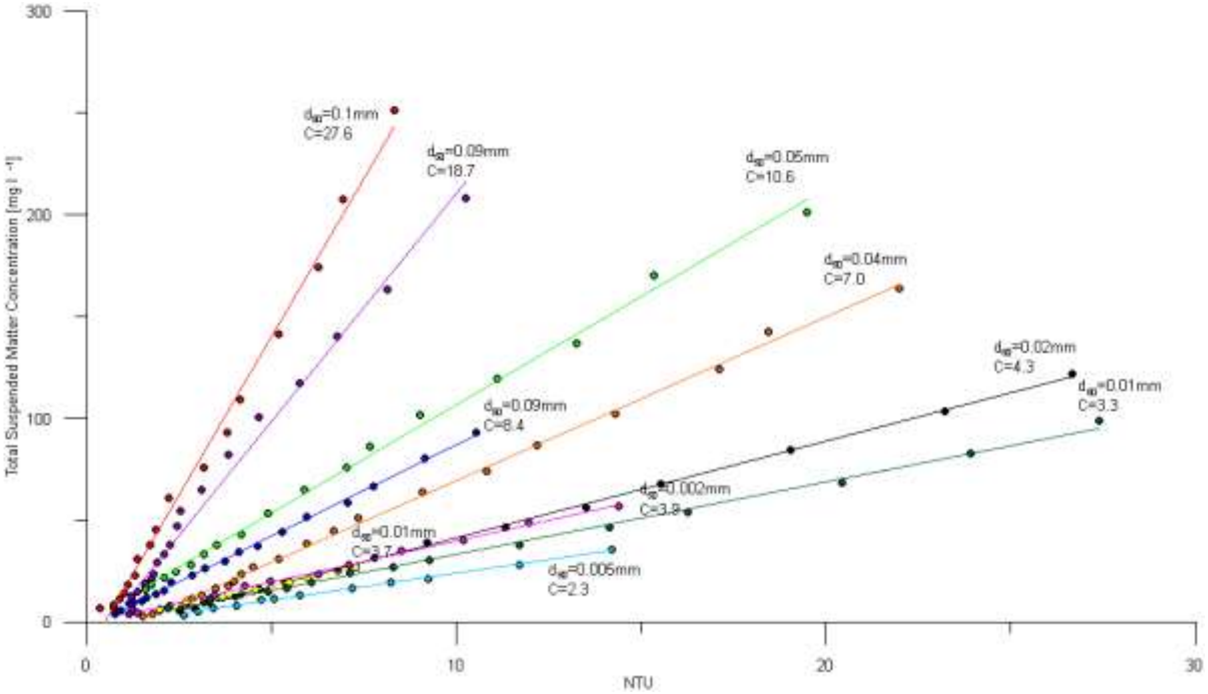

Figure 1Results of applying different grain size distributions to the same OBS device. The slope of the transfer function increase with increasing median grain size. This is important when applying transfer functions in area with varying grain sizes.

In Figure 1 we tested a range of different standard sediments. Each colour and line show the result of one sediment type with the mean grain size indicated. The results clearly show that the correlation factor is

an increasing function of the grain size distribution. If we apply d_{50} as a proxy for the grain size distribution a function for the correlation factor can be worked out. In Figure 2 such a result is provided for the 10 different mean grain sizes. The result is interesting. For any constant grain size distribution, a linear calibration factor can be used. But in this study the calibration factor increases exponentially with mean grain size although the variation is larger with large grain sizes.

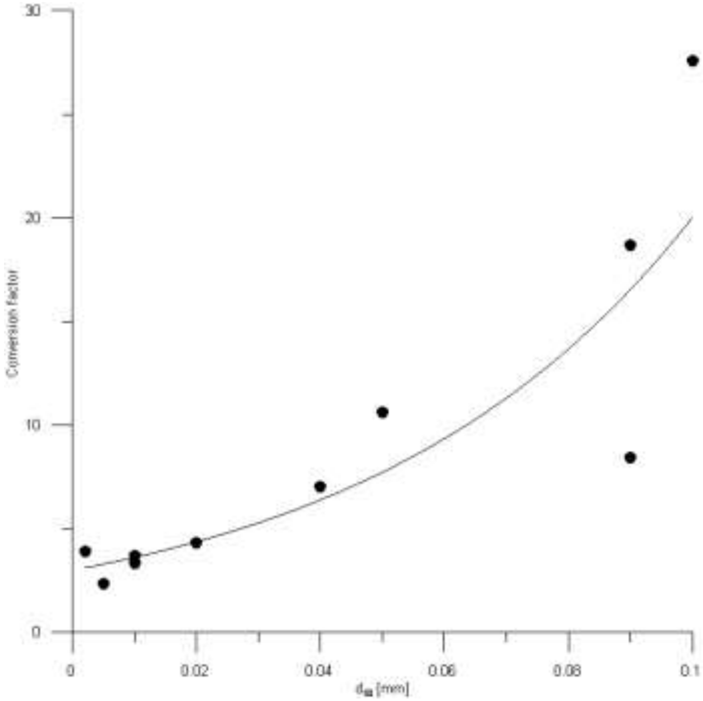

Figure 2The graph shows the interdependency between the correlation factor and the mean grain size. When a range of correlation factors have been obtained with different mean grain sizes it becomes clear that the dependency of grains size is of utmost importance when investigating the output from the sensors.

Sediment in a natural environment

After establishing the fact that the correlation factor is dependent on sediment type field measurements were carried out in a non-tidal lagoon in Denmark. As it was difficult to undertake water sampling in a large range of situations an automatic water sampler was established. The water sampler could be remotely controlled from the office based on turbidity or weather data.

The results of the field tests with the automatic water sampler are evaluated for a position in the southern part of the survey area (NS04a). The measurements were triggered from the office and covered calm periods as well as storm periods. The measured TSMC were plotted against the NTU values from the OBS and the results for station NS04a are given in Figure 3.

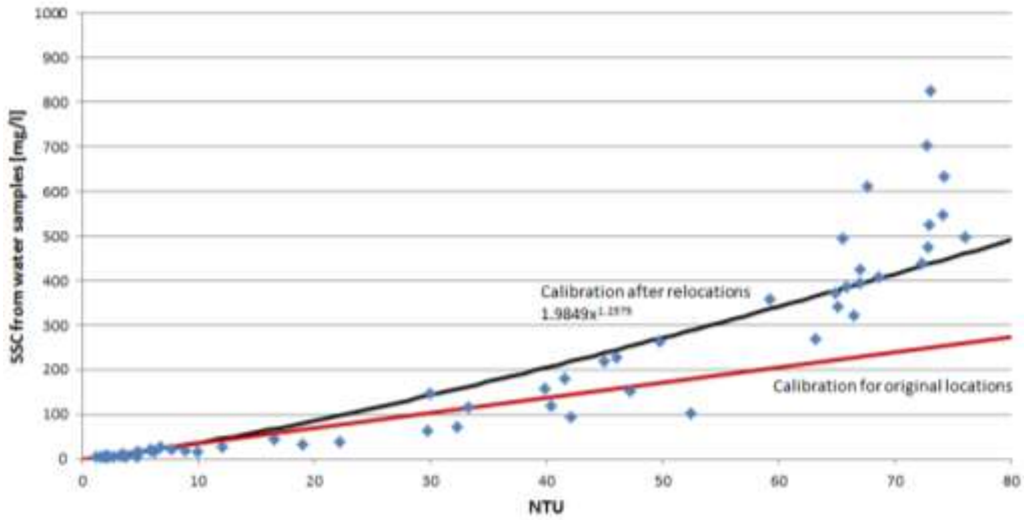

Figure 3Calibration correlation. As expected from the laboratory tests shown in Figure 2 the conversion correlation is exponential which corresponds well with the mixed sediment environment.

Figure 4Grain size variation (blue curve) and wind speed variation (red curve) at position NS04a. At this site, the median grain size is inversely correlated to the wind speed. The wave energy destroys the fragile flocs resulting in a decreasing size during rough periods. The flocs reform quickly as the wind speed decrease.

To show the variability of the grain size distribution during stormy weather the grain size distribution was measured at NS04a. Grain size distribution was measured using laser scattering by a LISST-100x instrument (Figure 4). The grain size measurements show that the grain sizes detected in the suspended sediment vary significantly over time which further supports the need for applying a calibration factor that takes varying grain sizes into account when measuring in a mixed sediment environment. The plot further shows that at this site (and this time period) the grain size can be correlated to the wind speed.

Discussion

If the measured sediment has a uniform structure with respect to grain size distribution the conversion becomes a linear function of concentration only. This is supported by Downing (2006). All sediment types show identical behaviour but different calibration factors (Figure 1). This difference originates only from grain size distribution..

Looking at Figure 1 it is noted that the calibration factor is increasing with increasing median grain size which means that light backscatter is decreasing with increasing grain size. This is consistent with the scattering being a function of the surface area of the sediment (Battisto et al., 1999; Downing, 2006; Ludwig and Hanes, 1990) .

Figure 2 and Figure 3 shows that the conversion factor can be expressed as an exponential function of the median grain size. This means that if one knows the median grain size it is possible to use an exponential transfer function and getter a higher accuracy with respect to the TSMC.

The variation in conversion factors and the shape of the calibration curve is of large importance in a mixed sediment environment where the grain size distribution of the suspended sediment varies. Here the changing conversion factor must be considered as the maximum suspendable grain size will increase with current and wave intensity. Similarly, the floc size can decrease due to increase in turbulence levels (Bundgaard et al., 2011). In such an environment, the optimum conversion will be exponential. Practically, this means that water samples will have to be taken under all occurring conditions to get an optimum calibration otherwise the correlation may be erroneous.

The error will vary from place to place as a function of local sediment and wave conditions but in Rødsand the error can be worked out based on Figure 3. The error will be the difference between applying a standard linear calibration factor based on standard calm weather water samples (the red line in Figure 3) and comparing it with the exponential calibration equation based on water samples covering all conditions (the black line in Figure 3). The result is shown in Figure 5.

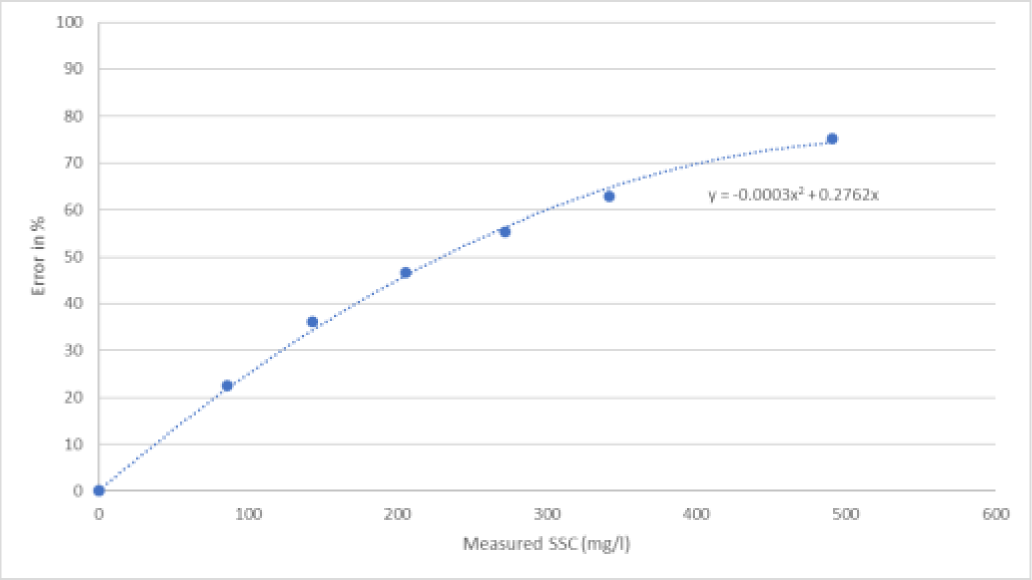

Figure 5 Error in % between using a standard calibration equation a more realistic exponential equation.

The error varies with concentration consistent with the change in grainsize distribution during storms. The error is significant for larger concentrations and should be considered before choosing the approach for calibrations of the OBS measuring device in mixed sediment estuaries.

Conclusions

It was attempted to convert the NTU signal from OBS sensors to total suspended matter concentration using water samples. The analysis showed that the conversion is dependent on grain size distribution. This is consistent with the findings in literature (Battisto et al., 1999; Black and Rosenberg, 1994; Conner and De Visser, 1992; Downing, 2006; Ludwig and Hanes, 1990). Tests with various natural sediments with varying grain size distributions show that the individual conversion factors for each sediment type are linear functions of concentrations whereas the conversion factors themselves are exponential functions of d_{50} for the individual sediments. The precise relation between d_{50} and the conversion factors is most likely a function of local sediment composition and the local wave and current conditions. The conversion factor is therefore site specific and cannot be generalized. Because of this it is concluded that for mixed sediment environments it is not sufficient to extract water samples for conversion during calm weather. During rough weather coarser sediment can be mobilised and floc sizes can change. Therefore, the conversion factor will shift with weather intensity. To determine a reliable local conversion for an OBS in a mixed sediment environment samples are needed under a large range of conditions. An indicative method for assessing grain sizes based on the conversion factors is given. The error is proven to be significant for larger concentrations.

Acknowledgements:

The Authors wish to the Femern A/S to allow use of data to perform the analysis. Palle Østlund Brogaard, Flemming Sams Mathisen, Peter Østrup and Lindsey Aires are thanked for doing the monitoring work even in rough weather. Meven Huiban and Arnoud Doure are thanked for help with the analyses. Ida Brøker is thanked for helpful discussion during preparation of the manuscript.

References

Battisto, G., Friedrichs, C., Miller, H., Resio, D., 1999. Response of OBS to mixed grain size suspensions during Sandyduck ’97, in: Coastal Sediments ’99. pp. 297–312.

Black, K., Rosenberg, M., 1994. Suspended sand measurements in a turbulent environment: field comparison of optical and pump sampling techniques. Coast. Eng. 24, 137–150.

Bundgaard, K., Lumborg, U., Brøker, I., Jensen, A., Andersen, T.J., 2011. Field tests and plume measurements in the Fehmarnbelt, in: CEDA Dredging Days 2011 - Dredging and Beyond.

Conner, C., De Visser, A., 1992. A laboratory investigation of particle size effects on an optical backscatterance sensor. Mar. Geol. 108, 151–159.

Downing, J., 2006. Twenty-five years with OBS sensors: The good, the bad, and the ugly. Cont. Shelf Res. 26, 2299–2318. doi:10.1016/j.csr.2006.07.018

Ludwig, K., Hanes, D.M., 1990. A laboratory evaluation of optical backscatterance suspended solids sensors exposed to sand-mud mixtures. Mar. Geol. 94, 173–179.

Sutherland, T.., Lane, P.., Amos, C.., Downing, J., 2000. The calibration of optical backscatter sensors for suspended sediment of varying darkness levels. Mar. Geol. 162, 587–597. doi:10.1016/S0025-3227(99)00080-8

LISST measurements in the Mediterranean Sea: Relationships between particle optical characteristics and hydrology.

S. Chaikalis[1], D. Velaoras[1], A.P. Karageorgis[1], S. Sofianos[2], A. Gogou[1], V. Cardin[3], D. Hainbucher[4]

[1]Hellenic Centre for Marine Research, Institute of Oceanography, 46.7 km Athens-Sounio Avenue, 19013 Anavyssos, Greece

[2]University of Athens, Ocean Physics and Modeling Group, 15784 Athens, Greece

[3]Dipartimento di Oceanografia, Istituto Nazionale di Oceanografia e Geofisica Sperimentale,Borgo Grotta Gigante 42/c, 34010 Sgonico (Trieste), Italy

[4]Institut für Meereskunde, Universität Hamburg, Bundes str. 53, D-20146 Hamburg, Germany

Abstract

For the first time, LISST-Deep measurements (beam attenuation coefficient, particle volume concentration, and particle size) were obtained across the Mediterranean Sea during the cruise MSM72 (Mediterranean Sea transect). An unexpected increase of particle volume concentration and particle median diameter below ~500 m was observed and was attributed to pressure-derived artefacts. The problem was solved by excluding the six inner rings from the calculations thus limiting the measured particle size spectrum to 1.25-92.6 μm.

A primary interpretation of the results was thereon attempted, searching for any relationship with the known water masses and/or the spatial distribution of temperature and salinity.A straightforward relationship between hydrology and LISST-Deep measured parameters (beam attenuation coefficient (c), particle volume concentration (VC), and median particle diameter (D_{50})) was partially observed. A clear W-E decrease of c and VC was observed, confirming the well-known transition from mesotrophic to oligotrophic conditions, whereas D_{50} followed the inverse distribution pattern. Coupled with biogeochemical parameters obtained during the cruise will provide more insights into particle dynamics of the Mediterranean Sea.

Keywords: Marine Optics, Optical Oceanography, Mediterranean Sea, LISST–Deep

1. Introduction

Particle distribution and abundance, as well as particle size play a paramount role in deep-sea biogeochemistry, with several implications for the marine food web and also remote sensing applications (Karageorgis et al,2012). However, very few particle size data are available to the oceanographic community from deep regional seas, such as the Mediterranean Sea, mainly due to instrumental limitations, since instruments measuring *in-situ* particle size at deep waters are very few. The Institute of Oceanography of the Hellenic Centre for Marine Research (HCMR) operates since 2007 a Laser in Situ Scattering and Transmissometry (LISST–Deep), an autonomous instrument manufactured by Sequoia Scientific Inc., to study particle size distribution patterns and associated optical properties in the deep sea(Agrawal et al,2000). Taking advantage of the trans-Mediterranean cruise (MSM72) organized by Hamburg University, the first data set of LISST-Deep estimated parameters was obtained across the entire Mediterranean Sea.

The aim of the present work is to: a) present the spatial distribution of beam attenuation coefficient (c; m^{-1}), particle volume concentration (VC; $\mu l\ l^{-1}$) and particle median diameter (D_{50}; μm) measured by LISST-Deep; b) examine potential correlations between hydrology and optical properties of seawater; and c) improve LISST-Deep operation modes and data post-processing.

2. Methodology

2.1 Cruise description

LISST-Deep was used on board R/V MARIA S. MERIAN during the cruise MSM72 conducted under the auspices of the University of Hamburg, Germany, together with a standard Sea-Bird 911plus CTD system. The cruise commenced at Heraklion on March 1st 2018 and occupied 136 stations (overall 149 casts) and finished in Cadiz on April 2nd 2018, thus materializing a complete E-W Mediterranean transect plus another one in the Ionian Sea(Fig. 1).

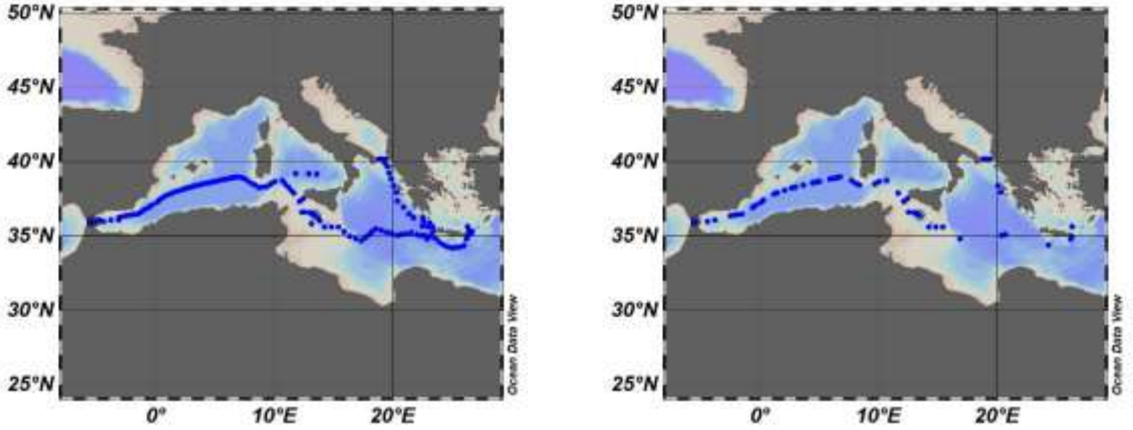

Figure 1: Hydrological stations (left) and LISST-Deep stations (right) occupied during cruise MSM72 in March-April 2018.

2.2 LISST set-up and operation modes

LISST–Deep (s/n 4004) was adjusted horizontally at the bottom of the rosette with a rope, two D-shaped shackle bows, and several tie wraps to stabilize for both horizontal and vertical motions. Power supply during casts was succeeded by connecting directly to the CTD, which provided a stable power supply of 15 V, whereas on deck the instrument was powered with 12 V via the 30 m-long power & communication (RS232) deck cable.

The instrument operated only at stations with water depth <3000 m. Before every cast, the operator followed a standard routine: 1) Connect the instrument to a personal computer running LISST SOP v5; 2) wake-up the instrument; 3) query the instrument and check that date and time were correct; 4) configure the instrument to start/stop data collection by using the external magnetic switch; 5) communicate with the instrument by the terminal window to check current status; 6) execute zero depth command to correct for depth offsets; 7) program the instrument for data collection (fixed sample rate, average of 20 samples at 1 Hz); 8) turn on the CTD deck unit, connect the instrument to the CTD and after that disconnect from the PC (this sequence maintains continuous power supply); 9) turn on the instrument for data collection by removing the external magnet and check that laser is on (a few seconds before the beginning of the cast). After completion of the cast, the instrument was connected again to the PC, and data were offloaded. Because the instrument's operational depth limit (3000 m) and some technical problems, LISST-Deep was used overall at 62 stations (Fig. 1).

2.3 Data processing

Matlab scripts were used for data processing, either provided by Sequoia Inc. or produced in-house. The use of *in-situ* zscat background was preferred over the one obtained in the laboratory (Chaikalis et al, 2016). The procedure is described briefly below:

From each station's binary data, the record showing the minimum sum of light of the 32 log-spaced rings and the record exhibiting the maximum laser power to laser reference ratio were determined.

From those two records we produced a local (from now on "station zscat") *in-situ* background for every station.

From all the stations' zscat we chose the background which had the minimum sum of light at the 32 rings and the maximum laser power to laser reference ratio. This is the final background (from now on "cruise zscat") which was used for the estimation of all derived parameters.

Afterwards, by employing the cruise zscat we estimated the LISST–Deep derived parameters: laser transmission (LT – units: %), beam attenuation coefficient (c, units: m^{-1}), particle volume concentration (VC, units: $\mu l\ l^{-1}$), particle median diameter (D_{50}, units: μm). It was decided to use only the downcast, because the upcast data were biased by turbulence developed from the overlying CTD/rosette system. Data were averaged at 1-m bins.

For the estimation of all derived variables two methods of calculation were applied: a) by using all the information provided by 32 rings; and b) by excluding the six inner rings, possibly affected by pressure (see next section).

2.4 32 rings vs 26 rings

During data processing of the MSM72 cruise, it was noticed that below ~1000 m depth, a constant increase of VC and D_{50} were recorded, which was almost linear with depth (Fig. 2 left). This unexpected increase was initially attributed to a pressure effect, since there was no physical or natural process that could explain such pattern over the entire Mediterranean Sea, and thus calculations were repeated by excluding the six inner rings that capture light scattered from large particles (92.6-250 µm). Fig. 2 (right) shows the same 3 stations but now variables were calculated from 26 rings. It is apparent that the constant increase with depth is eliminated, resulting in smoother profiles. However, c appears not to be affected by pressure as its variability is similar in both cases. These artefacts limit the operation of LISST-Deep in terms of effective particle size spectrum to 1.25-92.6 µm, which however is probably adequate to record particle-size variations of natural particle populations, excluding micro-aggregates.

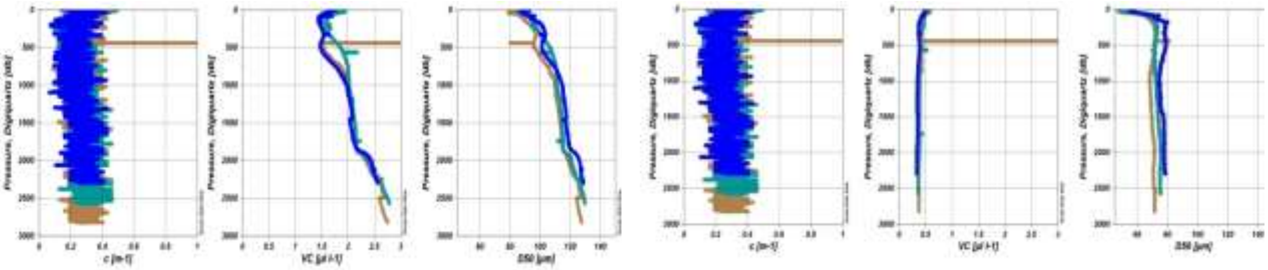

Figure 2: Examples of c, VC, and D_{50} calculated from 32 rings (left) and from 26 rings (right) in deep LISST casts. Blue Stn. 14, Green Stn. 34, Orange Stn. 49.

3. Results and Discussion

3.1. Hydrology and optics in the Mediterranean Sea

The surface/subsurface layer in the Mediterranean Sea (~0-150 m) is dominated by the presence of Atlantic Water (AW) which enters the basin through the Straits of Gibraltar, thereon following an eastward path, finally passing into the eastern Mediterranean through the Strait of Sicily. AW is characterized by its low salinity signal which gradually relaxes towards higher salinity values along its eastward route.

In the eastern Mediterranean, AW is gradually modified into a high salinity surface mass, which during winter convective mixing is transformed into a denser intermediate water mass called Levantine Intermediate Water (LIW). LIW, characterized by its distinct local high salinity signal at intermediate depths (up to ~400 m in the eastern and ~600m in the western Mediterranean), follows an opposite path i.e. from the eastern towards the western Mediterranean through the Strait of Sicily LIW finally exits the basin towards the Atlantic Ocean through Gibraltar. Thus, a two layer, anti-estuarine circulation develops in the Gibraltar Strait, with low salinity AW water intruding at surface and high salinity LIW exiting at intermediate depths. Along its route, LIW becomes gradually less saline and denser.

The deep reservoirs of the east and west Mediterranean sub basins are practically isolated by the shallow (~450 m) Sicily Strait. Deep waters in the eastern Mediterranean are warmer, more saline and denser than those of the western Mediterranean. Moreover, the eastern Mediterranean is a highly oligotrophic basin, much poorer in nutrients compared with the western Mediterranean. (Malanotte_Rizzoli et al., 2014; Cardin et al., 2015).

LISST-Deep measurements

Table 1 and Fig. 3 summarize the mean values of c, VC, and D_{50} in the entire Mediterranean as well as in various sub-regions: Gibraltar, Alboran Sea, Corsica, Sicily Strait, and Ionian Sea. The beam attenuation coefficient throughout the cruise shows an average of 0.53±0.17 m^{-1}. The maximum value observed is 1.77 m^{-1} (near-bottom in the Otranto strait) and the minimum 0.025 m^{-1} (in the intermediate waters east of Crete). As it can be seen from the following Table 1, c values decrease from the western Mediterranean basin to the east. Typically, the average value recorded in the region of Gibraltar (water entry area - AW - in the shallow waters and exit of the Mediterranean water at the mid-waters - MOW -) is 0.79±0.09 m^{-1}, while in the Ionian it is 0.28±0.09 m-^{1}. Thus, in Gibraltar there is an increase of ~0.26 m^{-1} compared to the average of the Mediterranean, while in the Ionian it decreases by ~0.24 m^{-1}.

The particle volume concentrationexhibits an average of 0.89±0.31 μl l^{-1} in the entire Mediterranean Sea. Similarly to c, the maximum value occurs near-bottom in the Otranto strait (3.7 μl l^{-1}), whereas the minimum value appears south of Crete (0.33 μl l^{-1}). The evolution of the VC values in the Mediterranean is similar to the previous one. To the west, the average is significantly higher than the average of the entire Mediterranean; in Gibraltar the average VC is 1.44 μl l^{-1}, whereas in the Ionian it is 0.43 μl l^{-1}.

Finally, the particle median diameter, D_{50}, in the Mediterranean shows an average of 55±8 μm. Its evolution from the west to the east is reversed with respect to the other two parameters mentioned above. In the west, smaller particles are observed than in the eastern basin. Indicatively, in Gibraltar average D_{50}, is estimated at 49 μm, thus ~6μm lower than the overall average. On the other hand, average D_{50} in the Ionian is 69 μm, thus ~14 μm larger than the Mediterranean average. The minimum value of D_{50} is recorded in the Otranto Strait (36 μm), whereas the largest is found south of Crete (79 μm).

Interestingly, c, and VC exhibit little variability along the water column, with the euphotic zone (0-200 m), however, showing slightly higher values of the two parameters, when compared to the deeper waters (200-3000 m), probably due to enhanced primary productivity occurring in the upper water layers. In all sub-regions D_{50} is slightly higher in the deeper part of the water column, suggesting that aggregation is favored below the euphotic zone.All three studied parameters vary progressively from west to east, as shown in the histograms illustrated in Fig. 3.

Table 2 depicts the average values of similar optical parameters, as derived from the literature at various sectorsof the world ocean. Concerning mean c, records were available in the Bohai& Yellow Seas, with values being an order of magnitude higher.Mean VC values are overall higher, although it should be noted that most datawere collected in coastal (Adriatic Sea) or shallow (Aloha Stn.) areas. The average D_{50} values are typically an order of magnitude higher (with the exception of California) than those measured in the Mediterranean Sea.

Previous work in the eastern Mediterranean Sea has been presented by Karageorgis et al. (2012), and particularly for the Ionian, Aegean, and Levantine Seas. In spring, mean VC was 0.29 μl $l^{-1}$and in summer 0.30 μl l^{-1}, whereas D_{50}varied between 86 and 88 μm.Compared to the MSM72 measurements, VC and D_{50}values in the Eastern Mediterranean are fairly similar.

Table 1: Mean Values of c, VC, and D_{50}in the Mediterranean Sea

Depth	Parameters	Cruise	Gibraltar	Alg. Basin	Corsica	Sicily	East Med.
0-3000 m	c [m^{-1}]	0.53±0.17	0.79±0.09	0.62±0.09	0.53±0.07	0.47±0.08	0.28±0.09
	VC [µl l^{-1}]	0.89±0.31	1.44±0.1	1.05±0.14	0.89±0.06	0.81±0.12	0.43±0.14
	D50 [µm]	55±8	48±2	51±2	53±2	54±2	69±7
	n	47100	950	26000	6300	3350	10500
0-200 m	c [m^{-1}]	0.53±0.19	0.82±0.1	0.64±0.12	0.53±0.07	0.48±0.1	0.3±0.09
	VC [µl l^{-1}]	1±0.38	1.51±0.08	1.24±0.24	0.97±0.08	0.9±0.2	0.5±0.12
	D50 [µm]	52±7	48±3	49±3	50±3	52±4	62±8
	n	6900	355	3100	870	800	1700
200-3000 m	c [m^{-1}]	0.53±0.16	0.76±0.07	0.62±0.08	0.54±0.07	0.47±0.07	0.28±0.09
	VC [µl l^{-1}]	0.87±0.3	1.4±0.09	1.03±0.1	0.88±0.04	0.77±0.06	0.41±0.14
	D50 [µm]	56±8	49±1	51±1	53±1	55±1	70±6
	n	40300	585	22900	5430	2530	8800

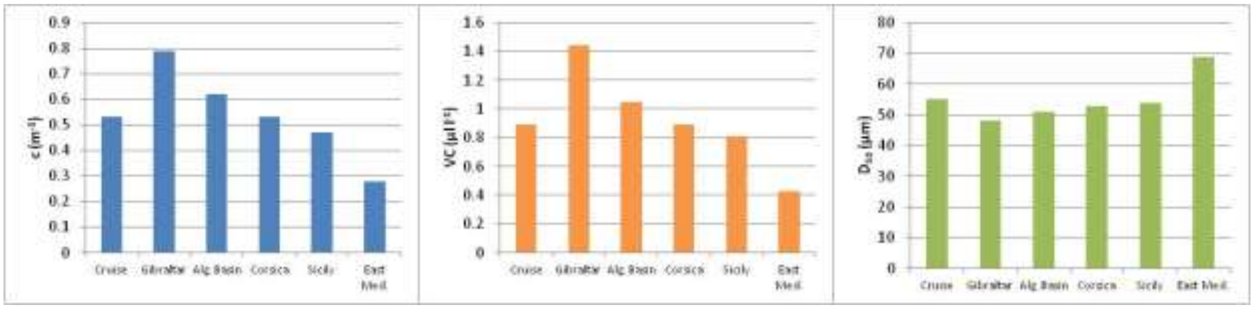

Figure 3: Histograms of beam attenuation coefficient (left: c in m^{-1}), particle volume concentration(middle: VC in µl l^{-1}), and median diameter (right: D_{50} in µm) mean values in different sectors of the Mediterranean Sea.

Table 2: Mean Values of c, VC, and D_{50}in the world ocean

Area	c (m^{-1})	VC ($\mu l\ l^{-1}$)	D_{50} (μm)	Reference
Bohai Sea & Yellow Sea	10 .4		141.5	Qiu et al., 2016
Adriatic Sea				Mikkelsen et al., 2006
(a) Chienti		95	280	
(b) Po		259	291	
(c) Pescara		90	277	
California			15.9	Sławomir et al., 2010
Western Artic				Yamada et al. , 2015
(a) Shelf		5.9		
(b) Slope Basin		2.1		
North Pacific (Aloha Station)				White et al., 2015
(a) 25m		0.065		
(b) 125 m		0.035		
Ionian Sea				Karageorgis et al. , 2012
(a) Spring		0.2	83	
(b) Summer		0.3	81	
Aegean Sea				Karageorgis et al. , 2012
(a) Spring		0.4	92	
(b) Summer		0.4	88	
Levantine Sea				Karageorgis et al. , 2012
(a) Spring		0.3	82	
(b) Summer		0.2	85	

3.2. Relationships between optical properties and water masses

In the following Figure 4 we present a W-E section of temperature (T, in degrees C), practical salinity (S), c (in m^{-1}), VC (in $\mu l\ l^{-1}$), and D_{50}(in μm) obtained from all available data. The Eastern basin appears throughout the water column more saline and warm compared to the Western basin. The sill of Sicily prevents any water mass exchange between the two basins below intermediate layers. The well-defined intermediate salinity maximum signifies the presence of LIW traveling westwards from its origin in the Eastern basin towards the Western basin, while at surface, less saline AW is observed following the opposite path.

Concerning c, we observe that it exhibits higher values throughout the water column in the western Mediterranean, and progressively the c signal decreases at first towards Sicily strait, and then it becomes very weak in the eastern Mediterranean. The highest c values are recorded in the upper ~200 m of the westernmost of the section (>1.0 m^{-1}). Particle volume concentration along the section shows similar characteristics to c with higher values in the western Mediterranean and progressively lower values towards the east. Maxima are also observed within the euphotic zone at the western part of the section (>1.5 $\mu l\ l^{-1}$). Inversely, D_{50} exhibits lower values in the western Mediterranean up to Sicily strait, which increase substantially towards the east (>80 μm).

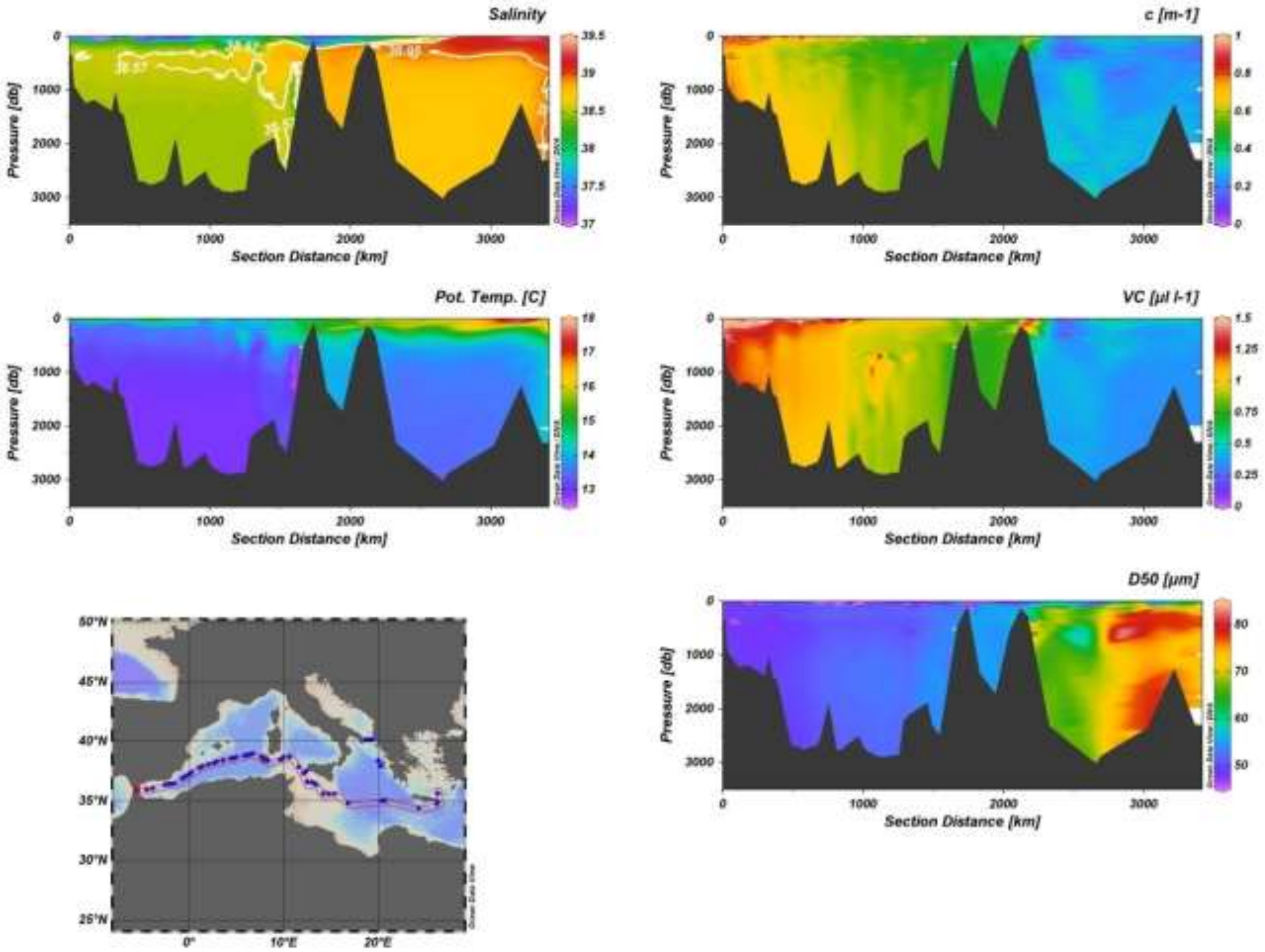

Figure 4: West-East section of temperature, salinity, beam attenuation coefficient, particle volume concentration, and particle median diameter in the Mediterranean Sea. Section location is shown in the lower left panel.

Figure 5 shows the variability of salinity and beam attenuation coefficient. In the Alboran Sea and Algerian basin, a sinusoidal variation of salinity is observed, possibly caused by the presence of anticyclonic eddies (Millot, 1999). A similar variation is also observed in the distribution of the beam attenuation coefficient, suggesting that the inherent optical properties (IOPs) of the water masses, and in particular the spatial variability of the beam attenuation coefficient, are controlled by local mesoscale features' variability and dynamics. It is noted that c is the sum of two fundamental inherent optical properties, scattering and absorption, c = a + b (where c: beam attenuation coefficient, a: absorption, b: scattering, all in m^{-1}). In the future, we could estimate the volume scattering function and investigate whether this parameter has the same variability.

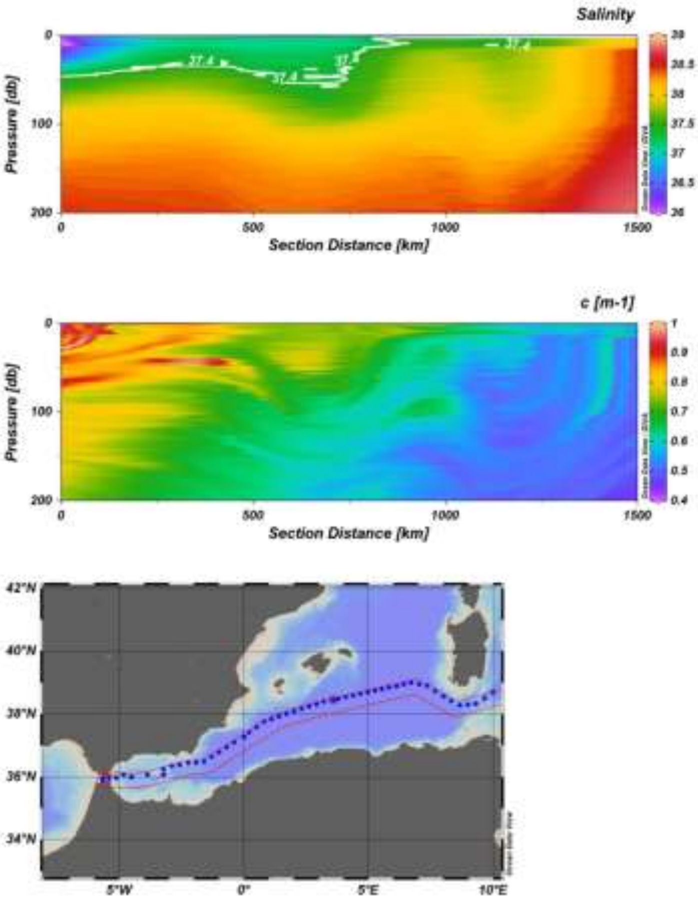

Figure 5: West - East section of salinity and beam attenuation coefficient in the Algerian Basin,Alboran Sea and Gibraltar Strait for the upper 0-200 m depth. Section location is shown in the lower panel.

Apart from the particulate matter optical properties variability in the entire Mediterranean Sea, interesting features were observed in the Otranto Strait. The Strait of Otranto separates the Adriatic and the Ionian Seas. Dense waters formed locally in the Adriatic during winter, exit through the bottom of the Otranto Strait, while LIW enters the basin at intermediate layers. The result is a cyclonic flow pattern, with water entry at the eastern part of the Strait, and exit at the western part (Kovačević et al., 1999).More specifically, maximum values of c and VC are observed near the bottom in the western-central part of the Otranto section (Fig. 6). The water mass occupying this part of the section is identified as Adriatic Deep Water (ADW) with higher density and lower temperature (Fig. 6). Increased c may be associated to: a) more turbid ADW waters than the ambient water masses; and/or b) surface sediment resuspension. Because of the minimum values of D_{50} recorded in the same area, and assuming that resuspension favors smaller particles, the second option is most likely valid. On the other hand, relatively higher D_{50} values observed at the mid-waters in the eastern part of the section, could be attributed to the inflow of the Levantine Intermediate Water (LIW) from the Ionian Sea, which, as it is has been observed (Figure 4) is characterized by higher D_{50} values.

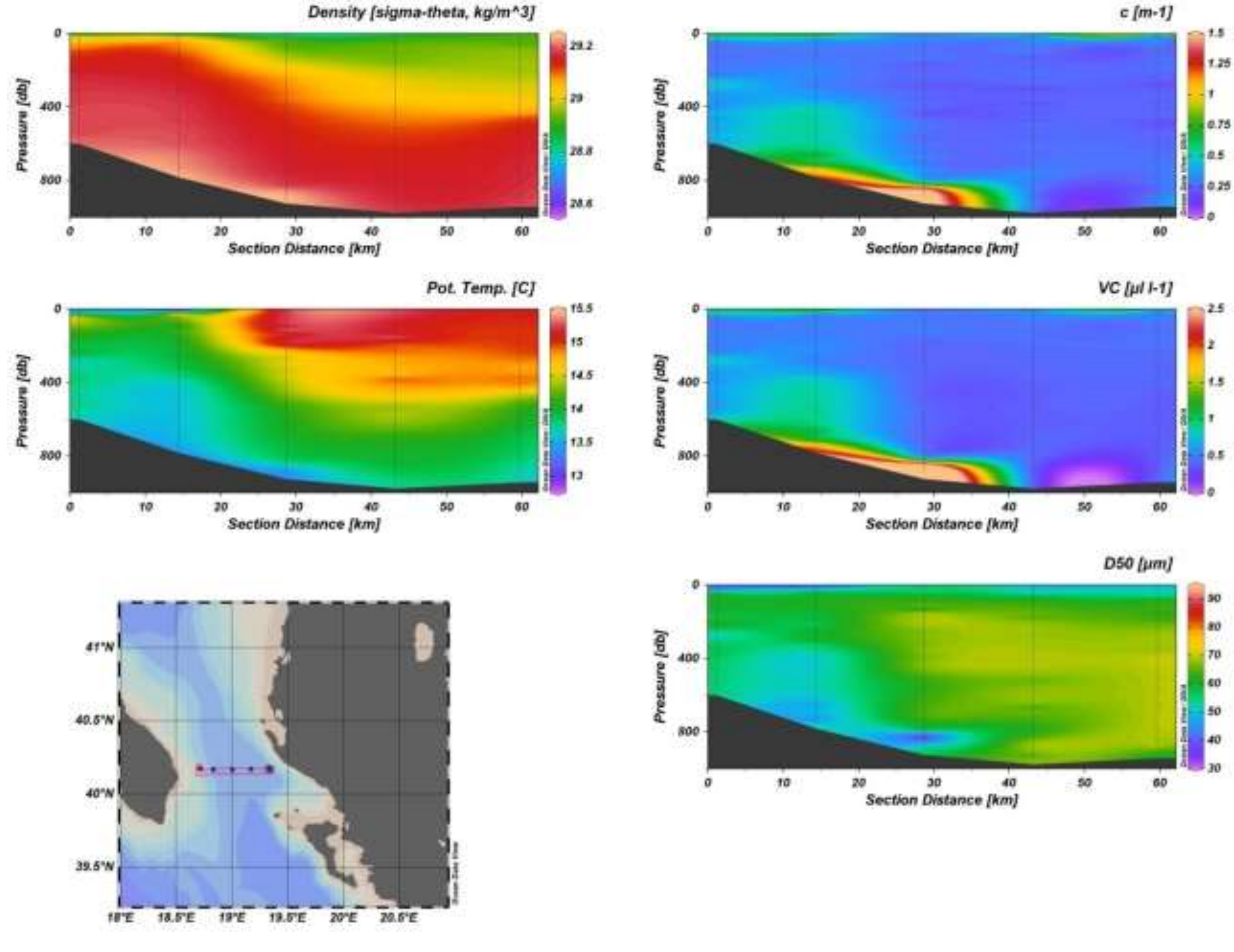

Figure 6: West-East section of temperature, density, beam attenuation coefficient, particle volume concentration, and particle median diameter in the Otranto strait. Section location is shown in the lower left panel.

4. Conclusion

A unique and valuable data set of beam attenuation coefficient, particle volume concentration, and particle median diameterup to 3000-m depth was obtained across the Mediterranean Sea during cruise

MSM72 in March-April 2018.Preliminary analysis showed substantial differences between the western-central and the eastern sector of the basin, highlighting the transition from mesotrophic to oligotrophic conditions, and thus the overall decrease in suspended particles. This pattern is observed both within the euphotic zone as well as the deeper waters. The predominance of larger particles in the eastern Mediterranean compared to the west was also observed, a pattern that might be associated to more favourable conditions for aggregation; a notion that deserves more studyand reanalysis of LISST-Deep data sets in the region. A direct relationship between hydrological parameters and water masses, and LISST-derived particle optical properties was observed in the Alboran Sea, associated with the presence of strong eddies.

References:

Agrawal, Y.C. and Pottsmith, H.C., 2000. Instruments for particle size and settling velocity observations in sediment transport. Marine Geology 168, 89-114.

Cardin, V., Civitarese, G., Hainbucher, D., Bensi, M. and Rubino, A., 2015. Thermohaline properties in the Eastern Mediterranean in the last three decades: is the basin returning to the pre-EMT situation? Ocean Sci. 11(1), 53-66, doi: 10.5194/os-11-53-2015.

Chaikalis, S., Karageorgis, A.P, Sofianos, S. and Drakopoulos, P., 2016.Estimating *zscat* in ultra-oligotrophic seas: implications for LISST-Deep scattering measurements, PiE 2016, Budapest**.**

Karageorgis, A.P., Georgopoulos, D., Kanellopoulos, T.D., Mikkelsen, O.A., Pagou, K., Kontoyiannis, H., Pavlidou, A. and Anagnostou, Ch., 2012. Spatial and seasonal variability of particulate matter optical and size properties in the Eastern Mediterranean Sea. *Journal of Marine Systems*, 105–108, 123–134. doi:10.1016/j.jmarsys.2012.07.

Kovačević, V., Gačić, M. andPoulain, P.-M., 1999. Eulerian current measurements in the Strait of Otranto and in the Southern Adriatic, J. Mar. Sys., 20, 1–4, 255-278, doi: 10.1016/S0924-7963(98)00086-4.

Malanotte-Rizzoli, P., Artale, V., Borzelli-Eusebi, G. L., et al., 2014. Physical forcing and physical/biochemical variability of the Mediterranean Sea: a review of unresolved issues and directions for future research, Ocean Sci., 10, 281-322, doi: 10.5194/os-10-281-2014, 2014.

Mikkelsen,O.A.,Hill, P.S. and Milligan, T.G., 2006. Single-grain, microfloc and macrofloc volume variations observed with a LISST-100 and a digital floc camera. Elsevier Journal of Sea Research 55 (2006) 87– 102, doi:10.1016/j.seares.2005.09.003.

Millot, C., 1999. Circulation in the Western Mediterranean Sea, J. Mar. Sys., 20, 1–4, 423-442, doi: 10.1016/S0924-7963(98)00078-5.

Qiu, Z., Deyong, S., Chuanmin, H., Shengqiang, W., Lufei, Z., Yu, H. and Tian, P., 2016. Variability of Particle Size Distributionsin the Bohai Sea and the Yellow Sea. Remote Sensing, doi: 10.3390/rs8110949.

Sławomir, W.B.,Stramski, D., Stramska, M., Reynolds, R.A., Wright, V.M., Miksic, E.Y., Cichocka, M.andCieplak, A.M., 2010. Optical variability of seawater in relation to particle concentration, composition, and size distribution in the nearshore marine environment at Imperial Beach, California. Journal of Geophysical Research, vol. 115, C08027, doi:10.1029/2009JC005554, 2010.

White Angelicque E., Ricardo M. Letelier, Amanda L. Whitmire, Benedetto Barone, Robert R. Bidigare, Matthew J. Church, and David M. Karl, 2015. Phenology of particle size distributions and primary productivity in the North Pacific subtropical gyre (Station ALOHA). Journal of Geophysical Research, 0.1002/2015JC010897.

Yamada,Y., Fukuda, H., Uchimiya, M., Motegi, C., Nishino, S., Kikuchi, T.and Nagata, T.,2015. Localized accumulation and a shelf-basin gradient of particles in the Chukchi Sea and Canada Basin, western Arctic. Journal of Geophysical Research,10.1002/2015JC010794.

Flocculation of suspended sediment during transport: what is there to learn from combining in-situ and laboratory experiments?

Claire Chassagne[1,*], Andrew Manning[2], Zeinab Safar[1], Zhirui Deng[1,3]

[1] Hydraulic Engineering, Technical University of Delft, 2628 CN Delft, The Netherlands

[2] HR Wallingford Ltd, Coast & Oceans Group, Wallingford, OX10 8BA, United Kingdom

[3] State Key Laboratory of Estuarine and Coastal Research, East China Normal University, Shanghai 200062, People's Republic of China

[*] corresponding author

Sediment transport models are based on the combination of hydrodynamic models coupled with gravitational settling of different sizes of particles (e.g. Soulsby et al., 2013; Mehta et al., 2014). Floc properties are influenced by factors including: turbulent shear, organic matter, mineralogy, suspended sediment concentration and salinity (e.g. Mietta et al., 2009). Sediment particles are introduced to these models by defining two (sometimes three) settling velocities associated with a given initial concentration. These models do not (yet) properly account for the fact that particles can change their structure and size during transport, and hence their settling velocities.

The simplest link between settling velocity in quiescent water and size is given by Stokes Law (Stokes, 1851). One important parameter in the equation is the density of the particle. Most in-situ instruments like the Sequoia Scientific Laser In-Situ Scattering and Transmissometry instrument (LISST) give Particle Size Distributions (PSD's), as it is difficult to consistently estimate accurate settling velocities of different types of flocs in quiescent water in an hydrodynamically active environment, even though some devices are being developed (Smith and Friedrichs, 2015).

PSD's in coastal areas are often found to be bimodal or multimodal, with size peaks in the range [10-20] µm, [50-200] µm and > 200 µm (Lee, 2012). As the particles found in these waters are of multiple nature (mineral sediment, micro-organisms, organic debris and any combination thereof), it is very difficult to attribute a settling velocity to an observed size peak as the density of the particles can vary significantly for a given size (e.g. Manning and Dyer, 2002).

Before setting-up a dynamic Settling Velocity Distribution (SVD) model to be incorporated in large-scale sediment transport models, it is important to get insight in mechanisms leading to the observed PSD's in-situ. Traditionally, the evolution of PSD's with time are interpreted in terms of aggregation and break-up of mineral sediment particles (O'Melia, 1986; Serra, 1998), but present models tend to incorporate the effects of micro-organisms (Maggi, 2013).

In order to study more in detail the contribution of mineral sediment and micro-organisms like algae (diatoms) in the flocs properties, several in-situ (LISST, underwater camera) and laboratory techniques (laser diffraction, LabSFLOC camera) were used in two on-going research projects, one close to the Dutch coast, and another in the Yangtze estuary.

From a survey performed 10 km downstream the mouth of the Rotterdam waterway, done at neap tide during calm weather conditions (no resuspension was expected that day), a bimodal particle size distribution, one peak of the order of 100-200 µm and the other of 200-400 µm, was found from LISST measurements 1.65 m above bed. This size distribution was confirmed by video microscopy using a LabSFLOC-2 (version 2) camera (Manning et al., 2017). This LabSFLOC study was conducted on board the *RV Navivular* on samples collected in the vicinity of the LISST, see Fig.1.

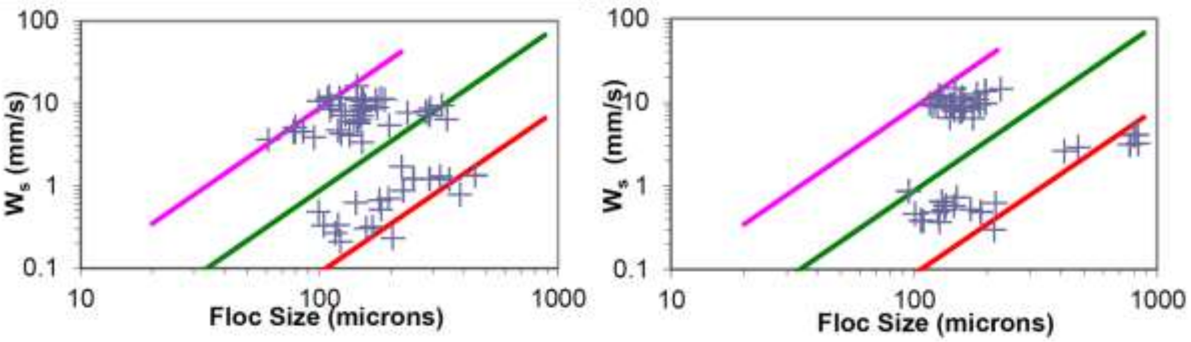

Fig.1 : Settling velocities as function of particle size as measured by the LabsFLOC camera. Samples were collected at 09:50 (left) and 10:40 (right). Relative density lines are 1600 kg/m^3 (magenta), 160 kg/m^3 (green) and 16 kg/m^3 (red)

From Fig.1 one can observe a large spreading (between 0.1 and 10 mm/s) in settling velocity for particles (flocs) of about 150/160 µm in size; this is typically the demarcation region that separate the smaller microflocs, from the larger less dense macroflocs (Manning, 2001). This spreading could be attributed to the composition of the flocs, observed both by LabSFLOC-2 camera and by an underwater camera, see Fig.2.

The large particles with low density are uncoated and uncoiled algae particles (Fig.2a), whereas particles of smaller size and density are algae particles in different states of coiling and coating (Fig.b and c). Other particles (inorganic particles more of less coated with organic debris, or lose organic debris) were also present in the water column (not shown).

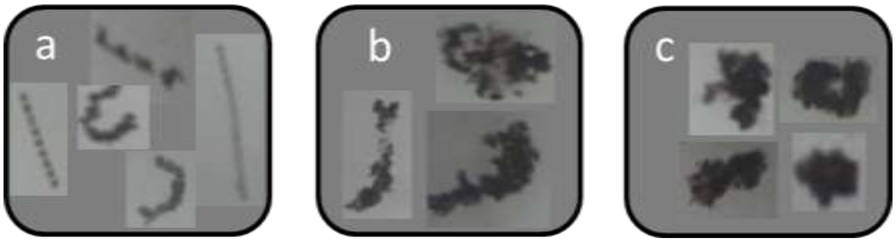

Fig.2 : Snapshots from the underwater camera showing (a) uncoated and uncoiled algae; (b) coated and moderately coiled algae with (in)organic debris; (c) fully coated and coiled algae with (in)organic debris

From the analysis of the aspect ratio of the particles, sampled in-situ and analysed by LabSFLOC-2 camera, it was found that peaks in aspect ratio appeared at changes in cross-shore and along-shore directions (07:00, 10:00 and 17:00 in Fig.3). Only when the cross-shore velocity changed to onshore directed (12:00), this peak in aspect ratio was not observed. More in-situ studies should be carried out to confirm the link between aspect ratio and changes in bottom velocities directions.

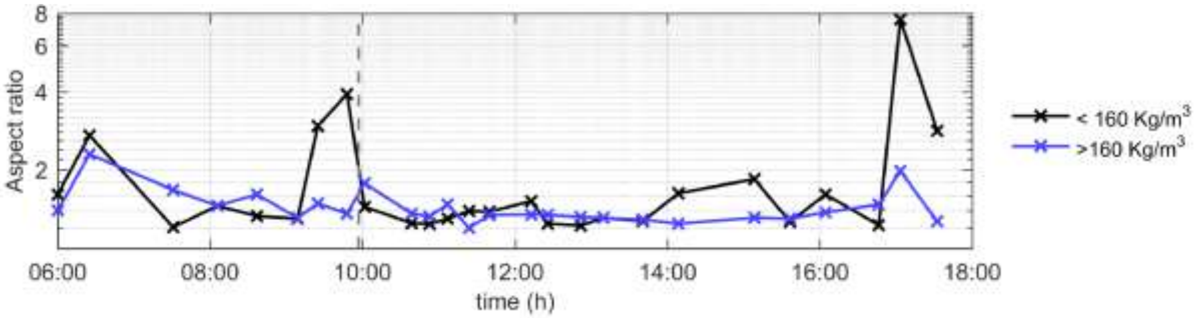

Fig.3 : Aspect ratio of particles as function of sampling time as measured by the LabSFLOC camera for two density classes. The large aspect ratios correspond to the particles with low density in Fig.1.

Laboratory experiments on samples made of mineral sediment and algae mixtures confirmed that mineral sediment could aggregate very easily with algae particles. The PSD of the mixtures were analysed using the same laser diffraction technique as the LISST, by pumping a sample from a suspending jar to the measurement chamber and back, and compared to LabSFLOC recording on the same samples. It was found that (1) the PSD obtained by laser diffraction was different from the one obtained using the LabSFLOC as differential settling was occurring during the LabSFLOC experiment, leading to the creation of very large, elongated flocs. The flocs measured by laser diffraction on the other hand were very isotropic, due to the turbulent mixing experienced by the particles during the diffraction experiment. In-situ, depending on the hydrodynamic conditions, any of these flocs can be observed. (2) Some samples were left to settle at the bottom of the jar and resuspended. The PSD measured by laser diffraction before and after resuspension were barely different, whereas the LabSFLOC sample analysis showed a very different size distribution. The reason for the discrepancies lays in the fact that the laser diffraction software handles suspensions as if the suspended particles are spherical and fit the raw data accordingly. This leads to an underestimation of the largest particle sizes.

In a different study, performed in the South passage of the Yangtze Estuary, the PSD evolution was recorded by LISST along with chlorophyll concentrations, which enables to verify that algae particles are to be found in the whole water column and that there is a strong correlation between Suspended Sediment Concentration (SSC) and Chlorophyll Concentration (CC), see Fig.4. As in the previous study, a bimodal distribution was observed both in time and depth.

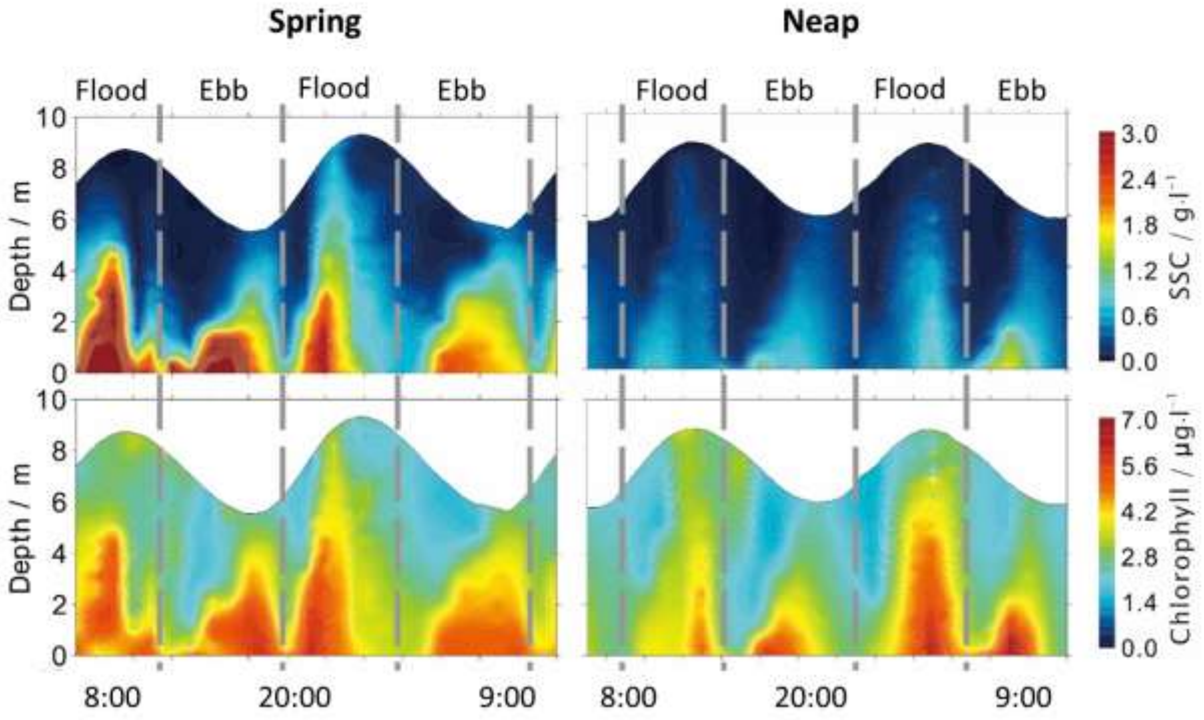

Fig.4 : Suspended Sediment Concentration (SSC) and Chlorophyll Concentration (CC) as function of time. It is clear that SSC and CC are correlated.

Mineral sediment samples (devoid of algae) from the Yangtze were analysed in the laboratory, using the same laser diffraction technique as the LISST, and it was found that (1) mineral sediment particles in the absence of algae do not flocculate and have a D50 of about 20 µm; (2) algae can flocculate with themselves, leading to large flocs of about 250 µm; (3) mixing mineral sediment and algae produce flocs of about 100 µm and (4) depending on the ratio of sediment to algae concentration, large algae flocs (devoid of mineral sediment) cannot form.

The correlation between in-situ and laboratory PSD's is displayed in Fig.5. The small flocs observed in-situ have a mean size that corresponds to the size of mineral sediment particles (brown lines), whereas the largest size peak observed in-situ corresponds to the peak size found in the laboratory for mineral sediment-algae mixtures (light green and dotted blue lines). Very large flocs (dark green line) corresponding to algae flocs were probably also found in-situ, but their low number (as in Fig.2, for the other study) made them undetectable by laser diffraction.

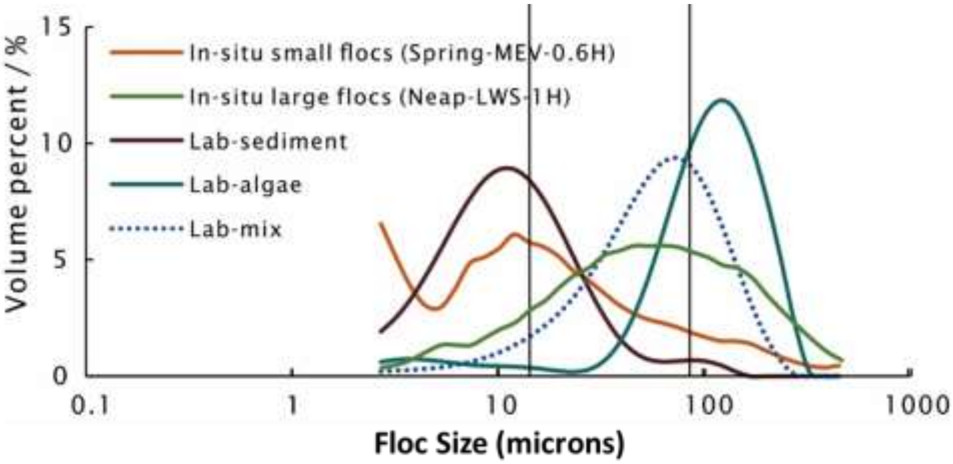

Fig.5 : Comparison between PSD's measured in-situ and in the laboratory; MEV-0.6H refers to Maximum Flood Velocity, in the middle of the water column and LWS-1H refers to Low Water Slack, close to the bed

The presence of elongated particles in coastal waters raises the question whether laser diffraction techniques like the LISST can properly estimate PSD's of non-spherical particles. As we have demonstrated, algae-rich flocs can change their size without losing mass implying that they experience a change in density, due to the coiling of elongated particles under shear. This has consequences in terms in observed particle numbers and turbidity, and requires that PSD/SVD models are adapted, to account for the densification of flocs under shear.

References:

Lee, B. J., Fettweis, M., Toorman, E., & Molz, F. J. (2012). Multimodality of a particle size distribution of cohesive suspended particulate matters in a coastal zone, 117(March).

Maggi, F. (2013). The settling velocity of mineral , biomineral , and biological particles and aggregates in water, *118*(March 2012), 2118–2132. https://doi.org/10.1002/jgrc.20086

Manning, A. J. (2001). A study of the effects of turbulence on the properties of flocculated mud. Ph.D. Thesis. Institute of Marine Studies, University of Plymouth.

Manning, A. J., & Dyer, K. R. (2002). The use of optics for the in situ determination of flocculated mud characteristics. Journal of Optics A: Pure and Applied Optics, 4(4), S71.

Manning, A.J., Whitehouse, R.J.S. and Uncles, R.J. (2017). Chapter 8 – Suspended Particulate Matter: Flocculation Measurements. In: R.J. Uncles and S. Mitchell (Eds), ECSA practical handbooks on survey and analysis methods: Estuarine and Coastal Hydrography and Sedimentology, pp. 211-260, Pub: Cambridge University Press.Mehta, A.J., Manning, A.J. and Khare, Y.P. (2014). A Note on the Krone deposition equation and significance of floc aggregation. Marine Geology, 354, 34-39, doi.org/10.1016/j.margeo.2014.04.002.

Mietta, F., Chassagne, C., Manning, A.J. and Winterwerp, J.C. (2009). Influence of shear rate, organic matter content, pH and salinity on mud flocculation. Ocean Dynamics, 59, 751-763, doi: 10.1007/s10236-009-0231-4.

O'Melia, C., 1986. The influence of coagulation and sedimentation on the fate of particles, associated pollutants, and nutrients in lakes. Chemical Proceeding, 207–224

Serra, T., Casamitjana, X., 1998. Modelling the aggregation and break-up of fractal aggregates in shear flow. Applied Scientific Research 59, 255–268

Smith, S. J., Friedrichs, C.T., 2015. Image processing methods for in situ estimations of cohesive sediment floc size, settling velocity, and density. Limnology and Oceanography Methods, Vol. 13 Issue 5, 250-264

Soulsby, R. L., Manning, A. J., Spearman, J., Whitehouse, R. J. S. (2013). Settling velocity and mass settling flux of flocculated estuarine sediments. Marine Geology 339, 1–12. doi.org/10.1016/j.margeo.2013.04.006.

Stokes, G. G. (1851). On the effect of the internal friction on the motion of pendulums, Transactions of the Cambridge Philosophical Society, 9, 8–106.

Bedload measurements using ultrasound Velocity profilers (UVP) in controlled laboratory conditions

S.Conevski[1, 2] , N. Ruther[1] , M. Guerrero[2], M. Burckbuchler[3]

[1]Department of Civil and Environmental Engineering, Norwegian University of Science and Technology, Trondheim, Norway. **slaven.conevski@ntnu.no**; **nils.ruther@ntnu.no**

[2] Department of Civil, Chemical, Environmental, and Materials Engineering, University of Bologna, Italy. **massimo.guerrero@unibo.it**; **slaven.conevski2@unibo.it**

[3] Ubertone, 14, rue du Brochet, Schiltigheim, France.

marie.burckbuchler@ubertone.fr

Introduction

Accurate estimation of the bedload transport is an engineering challenge since the previous century. Measuring the transport rate, using direct traditional methods (i.e. pressure difference samplers) is notoriously hard and labor intensive procedure. The temporal and spatial variability of the bed load together with the instrument disturbance can induce stochastic and systematic uncertainties. Very often, this data is considered as unreliable and complicates the further elaboration of the sediment transport behavior. On the other hand, statistically valid measurements are extremely important for the evaluation of the sediment transport mases, especially in large navigable or heavily exploited rivers.

One proposed alternative is the use of hydro acoustic instruments, which provide non-intrusive measurements, are easy-to-deploy, and offer detailed data resolution. Recently, many studies [1, 2, 3] elaborated the use of the bottom tracking (BT) feature of the acoustic Doppler current profilers (ADCP), emerging in a promising technique for evaluating the bedload transport. However, ADCP data do not provide the correct bedload velocity and require field-specific calibration in order to derive the bedload transport rate [4]. Recently, a laboratory study has proved that filtering of the apparent bedload velocity efficiently matched the spatial averaged bedload velocity [5]. Blanckaert et al. [6] in another laboratory experiment found out a strong correlation between the near-bed acoustic signal from a custom made acoustic profiler and the image velocity calculated using the optical flow and PTV methods. The latter studies show that the acoustic instruments have the potential to measure the bedload average velocity..

The redistribution of the echo from the sediment bed is quite complex because of variable intensity across the insonified beam width and the bed heterogeneity. Thus, the measured velocity contains many erroneous data and the intensity threshold for the bottom cannot be easily detected, especially during moving bed conditions. Accordingly, this study focuses on identifying and analyzing the acoustic signal from the mobile sediment bed using monostatic ultrasound velocity profilers (UVP) manufactured by Ubertone [7]. Firstly, a simple method for identification of the mobile sediment bed is proposed, then the influence of different frequencies and grazing angles on the backscattered amplitude and the bedload velocity were commented. In order to confirm the bedload velocity high-resolution cameras were used to calculate the surface velocity of the bedload.

Methodology

The Echo from the mobile sediment bed

The UVP use monostatic Doppler probes that emit burst of acoustic pulses at a specified pulse repetition frequency (PRF). This pulse incorporates several periods at a given transducer working frequency. Table 1 presents the deployed frequencies in this campaign of experiments. After emitting the pulse the system switches in receive mode. Each of the incident ultrasound pulses reflects from the riverbed in a different way, depending of the instrument frequency, the particle size distribution (PSD), and the transport conditions. In mobile bed conditions, it can be assumed that the mobile volume of the bed, or the active layer, could be associated with *volume scattering*. In addition, the immobile surface below the active layer could be defined as a *rough surface scattering*. Assuming that the surface of the immobile particles is acoustically impermeable, the sonar equation of the returned signal formula can be modified for the sediment bed intensity (I_r). If the spreading loss and the attenuation in the water column are negligible (i.e. no sediment suspension and short distance to the bed), then the slant range R in the attenuation component could be conveniently considered equal to the active layer thickness (R_{at}). The only reason for volume scattering is the sediment concentration in the active layer (Mat). Similarly, for sound attenuation coefficient α_{at}, the active layer concentration should be considered. The final logarithmic form of the corrected sonar equation is.:

$$Ir = 10 log(I_0 K_p) + 10 log(K_s A_r^2 + K_v^2 M_{at}) + 10 \log(\frac{c\tau}{2}) - 40 R_{at} \alpha_{at} log(e), \qquad (0)$$

where I_r is the received signal intensity (the received echo from the riverbed), I_0 is the transmitted intensity K_p is an instrument constant. The coefficient K_v is the volume scattering coefficient that depends of the frequency and the particle size distribution [8] and K_s accounts for the surface reflection depending on the surface roughness, acoustic frequency and surface to beam inclination. The A_r^2 term is the variance of the surface of the rough bed which accounts for the phase reinforcement, depending on the acoustic and bottom wavelength irregularities [9]. τ is the pulse duration, c is the speed of sound, $b(\theta,\varphi)$ is a beam coefficient that includes the grazing angle θ , the beam half opening angle (φ) and the beam width.

Experimental set up

The experiment was conducted in the hydraulic laboratory at the Norwegian University of Science and Technology (NTNU) in collaboration with Ubertone. In the 60cm wide flume, two hydraulic conditions were performed (Q_1=80 l/s and Q_2=120 l/s) having 40-42 cm water level above the sediment bed. The sediment bed consisted of fine sand with D50= 0.25 mm and D84/D16= 3 mm. The water velocities reached 0.3m/s and 0.5m/s consequently for the two different discharges. The particle Reynolds number (R_{ep}) is 12.17 and the non-dimensional critical shear stress or the critical Shields number (τ_{*cr}) is 0.045. The dimensionless shear stress (τ_*) for the two conditions (0.055 and 0.118) indicated that no sediment suspension will occur [10]. The transducers were mounted 36cm above the sediment bed, three ones perpendicular on the sediment bed and other three tilted for 65 degrees (θ). .

Above the sampling area GoPro Hero6 (3840 x 2160 pixels and 60 frames per second) was installed with planar field of view over the sampling area of the transducers (Fig.1). Five repetitions of each hydraulic condition were performed, in total 10 experiments were conducted.

f	$D_{transducer}$	lamda	φ	Near field	Grazing angle	Slant range	Footprint lenght	1st side lobe length	Cell size	PRF
MHz	m	m	°	m	°	m	m	m	m	
3.0	0.01	0.0005	4.93	0.025	65	0.39	0.07	0.10	0.011	900
1.5	0.02	0.0010	3.45	0.101	65	0.39	0.05	0.06	0.011	900
0.5	0.02	0.0030	13.79	0.019	65	0.39	0.21	0.29	0.004	1400
3.0	0.01	0.0005	4.93	0.025	90	0.35	0.06	0.08	0.004	1400
1.5	0.02	0.0010	3.45	0.101	90	0.35	0.04	0.05	0.004	1000
0.5	0.02	0.0030	13.79	0.019	90	0.35	0.17	0.23	0.004	1000

Table 1. UVP acoustic parameters

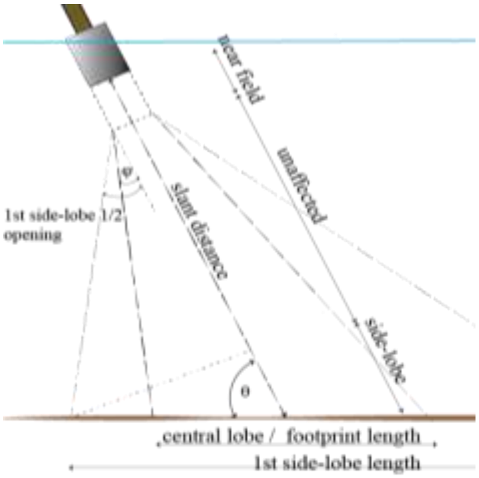

Figure 1. UVP Geometry of the inclined probe

Bedload velocity identification

The scattered signal from the immobile sediment bed is typically the strongest and results with the highest peak in the received echo cloud. In most of the ultrasound studies the bottom is analytically considered as surface scattering and it is the first peak coming after the volume reverberation of the water column above [9]. The sediment used in this experiment has a comparable size with 3MHz wavelength (Tab. 1), but it is smaller than the 1.5MHz and 0.5MHz. It means that the scattering from the particles in saltation or the *volume scattering* will be in the geometric scattering region for the 3MHz (i.e. stronger backscattering strength) and in the Mie or Rayleigh region for the other two frequencies.

As soon as the signal passes the active layer of the bedload a *surface scattering* occurs. It is typically stronger (assume specular reflection) and it depends strongly of the grazing angle. Nevertheless, the are several other parameters that influence the shape of the echo and may cause confusion into the identification of the bottom.

The procedure of bottom identification followed several steps: i.) defining of the near field and first side lobe (Tab.1) distances and discarding all the values before these distances; ii.) Identification of the maximum peak; iii.) Identification of the first high peak (Fig1. larger than the half maximum peak); iv.) Identification of the first low peak (larger than the average water column echo); v.) Extracting the velocity values of the cells that form these peaks. Note that the distance from the sediment bed to the transducers was measured before each measurement. Accordingly the measured bottom distance was compared with the identified bottom using the UVP data. The method was implemented in a MatLab script to run the results automatically.

The echo amplitude values that form first low peak indicate the volume scattering of the active layer, while the first high peak gives the immobile surface scattering. In addition, the more intensive hydraulic conditions (Q_2=*120l/s*) showed higher deviations of the results, but followed the same pattern. Fig.2 also shows that the echo profile of the 0.5MHz frequency contains more spikes and the identification of the bottom is more complicated. This noisy data close to the bottom is associated with the largest side-lobe length influence and the size of the transducer. The velocities were measured only in direction of the flume because the experimental set up allowed considering negligible perpendicular velocities. Obviously, only the inclined probes are to measure the velocities in flow direction, whereas perpendicular ones were used for scattering measurement only.

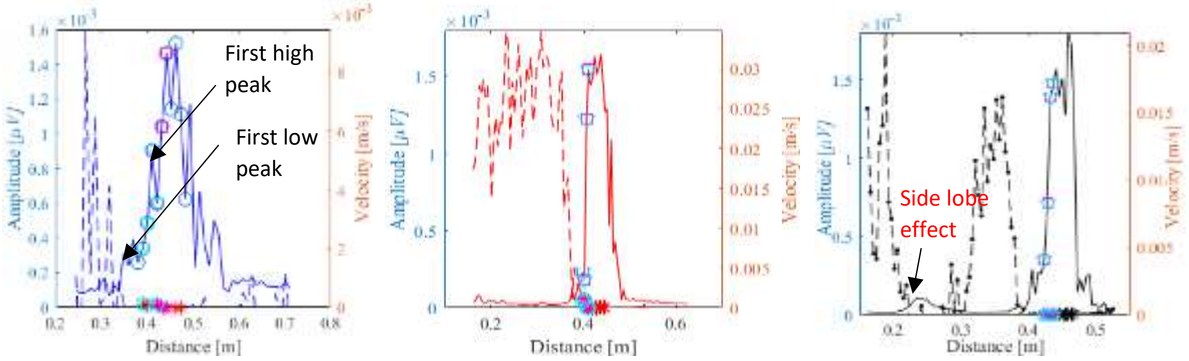

Figure 2. Echo profiles from the inclined transducers (blue-0.5MHz; red-1.5MHz, black-3MHz). The dashed line is the velocity and it is associated with the right y-axis; the solid lines are the echo amplitudes.

Camera velocities

The images were preprocessed in order to equalize the light and de-blur the motion effects. After the preprocessing, image-change detection technique was applied to identify the mobile particles. This technique consists of image subtraction of two consecutive frames and kernel filter to smooth the random noise. The identified mobile particles from two consecutive frames are matched using cross-correlation technique and the velocities of the displaced particles from one to another frame are identified [11, 5].

Results and discussion

Echo amplitudes comparison

The average echo amplitudes of each experiment repetition from the vertical and the tilted transducers are plotted in Fig. 3. The amplitudes include the values from the low first peak to the high first peak, meaning that they contain the information from the static bottom and the mobile particles of the bedload active layer. The vertical probes (Fig.3 empty symbols) scattered the bottom with almost the same intensity for all the frequencies used in both hydraulic conditions, moreover it reflects the fact that the bottom surface roughness depends only on the particles. On the other hand, the amplitudes of the inclined probes (Fig.3 filled symbols) increased when passing from 80 to 120 l/s. The difference between the vertical and inclined amplitudes decreased passing from weak to more intensive transport. This is due to an increase of the volume scattering strength for the more intensive conditions, having the particles transported in the cells above the bottom, forming a thicker active layer. This amplitude increasing change is more evident for the 3 MHz probe, which falls in the transition scattering regime (i.e. Mie regime); in fact, its wavelength is closer to the mean radius of the used sand particles. It is worth noting that the large size of the acoustic footprint and the side lobes of 0.5 MHz probe contributed to wider distributions of the profiled echoes. In this case, the side lobes at the edge of the acoustic footprint contaminated the received echoes from cells close to bottom, which made uncertain its detection and the quantification of corresponding echo amplitude.

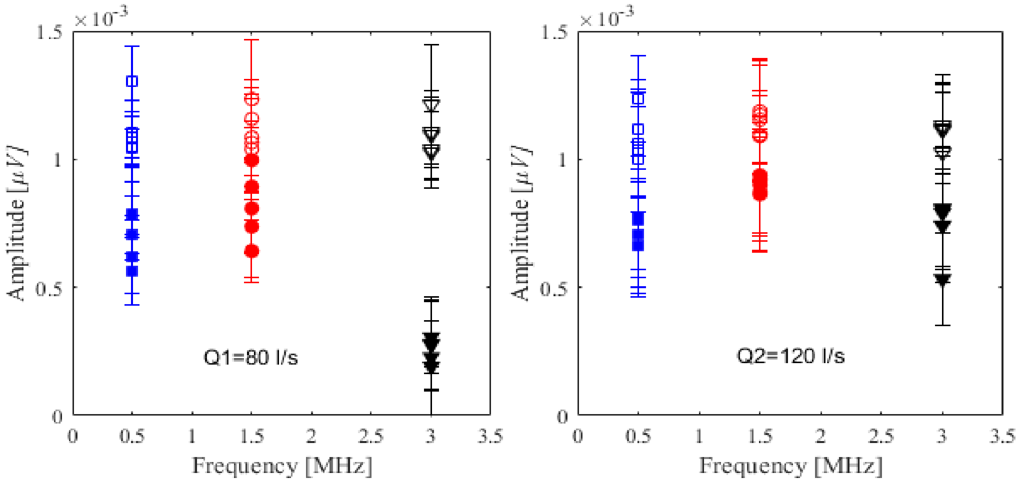

Figure 3. Echo amplitudes variation. The left plot is weak transport condition (Q1=80 l/s), the right plot are the experiments from the more intensive transport conditions (Q2=120l/s). The solid symbols represent the inclined probes, while the empty symbols are the perpendicular probes.

UVP Bedload Velocities

The UVP manufactured by Ubertone uses the Doppler principle for measuring the velocities as any other hydro-acoustic device. The velocities were extracted from the cells that are forming the first low peak (2-3 cells). The data was very noisy showing a standard deviation three times their mean values. Thus, the data was de-spiked using simple local threshold and temporal averages were calculated from each repetition of the experiments. The water velocities were estimated using moving mean averaging of the measured profiles.

Velocities were averaged along the measured profiles from first low to first high echo peaks to represent the bedload velocity. Finally, averages and standard deviations among repeated tests represented the expected bedload velocity and the corresponding variation at each hydraulic condition (Fig. 4). The same figure bears out the transition of the water velocities to the bedload velocities. Each transducer had a bit different distance to the bottom and it varied from one experiment repetition to another that is reflected by the vertical bar. The velocity from 0.5 MHz noticeably underestimates the measured velocities with higher frequencies and the camera during the higher discharge (e.g. blue square, right plot, Fig.4). In fact the 1.5MHz and 3MHz showed very similar averaged values but higher deviations that may be related to turbulence nature of the measured process. The underestimation of 0.5 MHz probe has to be ascribed to side lobe interference, which deteriorates the received signal from the bottom and in the direction of the Doppler angle. This effect eventually enhanced the received scattering from direction closer to vertical (i.e., the more intense and closer target at footprint edge) that entailed velocities close to zero, on average. The low discharge experiments gave the higher difference between the camera and the transducers which appear more similar among them. This is due to the thinner active layer and the prevailing of surface scattering of the immobile bed that entails zero velocity. One should also consider that the very fine particles of sand are having velocity very close to the entraining flow (i.e. the slip velocity is very small) .

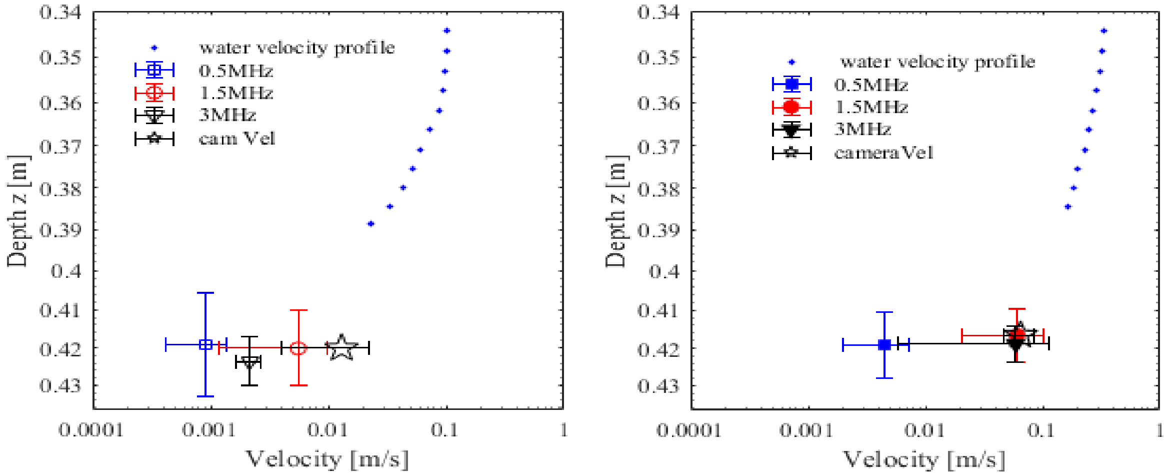

Figure 4. Bedload Velocities. The left plot is weak transport condition (Q1=80 l/s), the right plot are the experiments from the more intensive transport conditions (Q2=120l/s).

Conclusions

The Uber tone UVP probes efficiently measured the bedload average velocities. The analyzed echoes have shown a small decrease of the vertical probes amplitudes while increasing the bedload transport conditions but a noticeable increasing of the inclined probes amplitudes specifically for the frequency (i.e., 3 MHz) more sensitive to the mobile bed particles transported in the active layer. This suggests the possibility of using the difference among echoes from different grazing angles as an index of particles mobility and active layer thickness. The measured velocities were underestimated especially by the lower frequency (i.e., 0.5 MHz) and for the higher discharge experiment, but the 1.5 and 3.0 MHz probes almost fit the values from the camera. This suggests the importance of scaling the footprint to measured environment to limit the side lobe effects. Further analysis of lower resolution (0.4 mm per cell) will be performed and the signal scattered from the active layer will be further elaborated.

References

[1] C. Rennie, R. G. Millar and M. A. ,. Church, "Measurement of bed load velocity using an acoustic Doppler current profile," *Journal of Hydraulic Engineering,* vol. 128(5), p. 473–483, 2002.

[2] D. Gaeuman og R. B. Jacobson, «Acoustic bed velocity and bed load dynamics in a large sand bed river,» *J Geophys Res Earth Surf,* vol. 111(F2), nr. F02005, 2006.

[3] F. G. Latosinski, R. N. zupiany, M. Guerrero, M. L. Amsler og C. Vionnet, «The ADCP's bottom track capability for bedload prediction: Evidence on method reliability from sandy river applications,» *Flow Measurement and Instrumentation,* vol. 54, nr. June 2016, pp. 124-135, 2017.

[4] C. Rennie, D. Vericat, R. Williams, J. Brasington og M. Hicks, «"Calibration of aDcp apparent bedload velocity to bedload transport rate" in Gravel-Bed Rivers,» i *Processes and Disasters*, Tsutsumi, D., and Laronne, J., Wiley., 2017.

[5] S. Conevski, M. Guerrero, N. Ruther og C. Rennie, «ADCP performance of measuring the bedload velocity under changing conditions of particles mobility/bedload transport conditions,» *in submition,* 2018.

[6] Blanckaert K., H. Heyman J. og R. C.D., «Measurments of bedload sediment transport with an Acoustic Doppler Velocity Profiler(ADVP),» *J. Hydraulic Engineering,* October 2017.

[7] Ubertone, «UB-Lab - The versatile ultrasonic profiler,» Ubertone, 2016. [Internett]. Available: http://www.ubertone.com/products-ub-lab.html.

[8] P. Thorne, C. Vincent, H. P. S. Rehman og N. and Pearson, «Measuring suspended sediment concentrations using acoustic backscatter devices,» *Marine Geology,* pp. 7-16, 1991.

[9] R. J. Urick, Principles of Underwater Sound, McGraw-Hill, 1983.

[10] G. Parker, ID SEDIMENT TRANSPORT MORPHODYNAMICS with applications to RIVERS AND TURBIDITY CURRENTS, St. Anthony Falls Laboratory, Mississippi River at 3rd Avenue SE, 2004.

[11] A. Radice, S. Malavasi og F. Bailio, «Solid transport measurements through image processing,» vol. 41, nr. 5, pp. 721-734, 2006.

Real-time suspended sediment measurements at hydropower plant Fieschertal using LISST and Coriolis Flow- and Density Meter (CFDM)

David Felix, Ismail Albayrak, Robert M. Boes

ETH Zurich, Laboratory of Hydraulics, Hydrology and Glaciology (VAW), Switzerland

Abstract

Several instruments for real-time measurements of suspended sediment mass concentration (*SSC*) and particle size distribution (PSD) were investigated at the waterway of the hydropower plant (HPP) Fieschertal in the Swiss Alps. The present contribution focusses on the *SSC* measuring ranges of a Laser In-Situ Scattering and Transmissometry instrument (*LISST-100x* with a 90% path reduction module) and a Coriolis Flow- and Density Meter (CFDM). The LISST allowed measuring *SSC* up to a few g/l of the graded, angular and flaky silt particles. A site-specific equation was derived to estimate this *SSC* limit as a function of the median particle size d_{50}. The CFDM with periodic field calibration was found to be suitable to measure $SSC \geq 1.5$ g/l with an uncertainty of ≤ 20%. Hence, combining a standard LISST instrument (without dilution) and a CFDM is an option to cover a wide range of *SSC*.

1. Introduction

Measurements of *SSC* and PSD are important for a better understanding and management of fine-sediment related processes in rivers and hydraulic schemes. In particular, real-time *SSC* and PSD are required to optimize the operation of HPPs with respect to hydro-abrasive erosion on turbines. For this application, *SSC* from some 10 mg/l up to about 100 g/l are of interest.

In a research project on turbine erosion at the HPP Fieschertal in the canton of Valais, Switzerland, several instruments for real-time *SSC* and PSD measurements were investigated. These include turbidimeters, a single-frequency acoustic system, a standard LISST device without dilution, a CFDM and pressure sensors (Felix 2017). The present contribution focusses on the *SSC* measuring ranges of LISST and CFDM. Firstly, these measurement techniques are introduced, secondly the set-up and methods of the field study are described, thirdly selected results are presented and discussed, and finally recommendations are given.

2. Measuring techniques

2.1 LISST

The LISST instruments' working principle is laser diffraction, as described e.g. by Agrawal & Pottsmith (2000). Such instruments provide real-time volume concentrations of particles in 32 or 36 size classes, from which detailed PSDs and *SSC* are evaluated. In contrast to turbidimeters and single-frequency acoustic systems, LISST offers the advantage that temporal variations of PSDs are considered in the *SSC* output.

A drawback of LISST in the present application is that no measurement results are available if the water is too turbid, i.e. the optical transmission τ is too low. In such situations the raw data (scattered light intensities) are not invertible. Generally $\tau \geq 0.3$ is recommended to avoid degradation of the measurement results due to multiple scattering. The manufacturer (Sequoia 2016) indicates the following upper limit of the *SSC* measuring range SSC_{lim} (mg/l) for spherical, mono-disperse particles with a particle density of ρ_p = 2.65 g/cm^3 (as for quartz):

$$SSC_{\mathrm{lim}} = \frac{c \cdot d}{1.13} \tag{1a}$$

where d = particle diameter (µm), $c = -\ln(\tau) / L$ = beam attenuation coefficient (m^{-1}), and L = optical path length (m) ranging from 0.003 to 0.05 m depending on the instrument model. The SSC_{lim} increases hence with the particle diameter. Because the range of occurring particle sizes is often poorly known prior to a field study, it is difficult to judge if the *SSC* measuring range of a certain LISST model is appropriate for a certain application.

For graded and non-spherical particles, d is replaced by the Sauter Mean Diameter *SMD*. Using *SMD* and considering the effect of particle density ρ_p (g/cm^3), Felix *et al.* (2018) re-wrote Equation (1a) for SSC_{lim} (g/l):

$$SSC_{\mathrm{lim}} = \frac{c \;\; SMD \;\; \rho_{\mathrm{p}}}{1.13 \cdot 10^3 \cdot 2.65} = \frac{-ln(\tau)\; SMD \;\; \rho_{\mathrm{p}}}{2995\, L} \tag{1b}$$

Because *SMD* depends not only on the PSDs but also on the particle shapes, *SMD* is not readily available in field studies at sites with varying mixtures of potentially highly non-spherical particles. In such situations, the median particle diameter d_{50}, i.e. the diameter which is not exceeded by 50 % of the particles' mass, is often used in engineering practice to indicate a characteristic particle size. It should be noted that for non-spherical particles, d_{50} is an apparent diameter, depending on the real particle shapes and the PSD measuring system (typically laser diffraction).

2.2 CFDM

CFDM instruments measure the flow rate, fluid density and temperature in a pipe. The fluid density is determined from the natural frequency of oscillating measuring tubes inside the instrument (Holcomb & Outcalt 1998). To determine the *SSC*, firstly the clear water density ρ_w is calculated as a function of temperature $T(t)$. With the solid density of the particle material ρ_s obtained from pycnometer, *SSC* is then evaluated from the mixture density ρ_m as:

$$SSC(t) = \frac{\rho_{\mathrm{m}}(t) - \rho_{\mathrm{w}}(T(t))}{1 - \frac{\rho_{\mathrm{w}}(T(t))}{\rho_{\mathrm{s}}}} + K(t) \tag{2}$$

$K(t)$ is a minor offset correction, which compensates offsets due to slight depositions and fouling in the measuring tubes. $K(t)$ is periodically updated based on comparison to gravimetrically determined *SSC* (Felix *et al*. 2018). *SSC* can be measured by CFDM with reasonably low uncertainty if the mixture density is significantly higher than the clear water density. Hence, the *SSC* measuring range of CFDM has a lower limit.

3. Set-up, instruments and methods

In the valve chamber at the top of the penstock of HPP Fieschertal, a sampling pipe was connected to the penstock (Fig. 1). About 0.2 l/s were released from the penstock through the pipe and the CFDM into a bucket, at which the LISST was installed. To extend its *SSC* measuring range, the optical path was shortened from 50 to 5 mm by a 90% path reduction module.

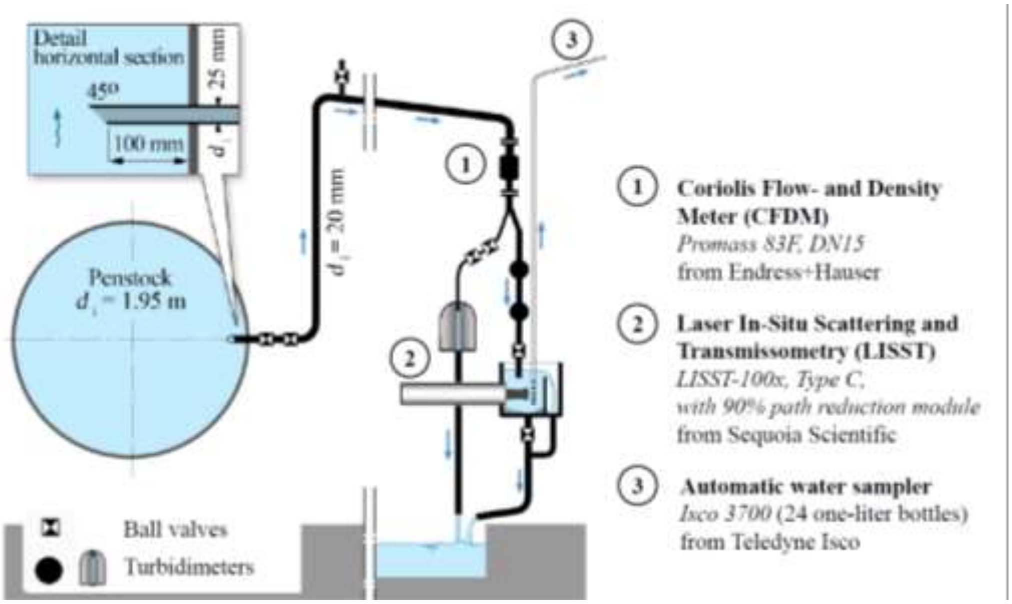

Fig. 1: Vertical section of the penstock and the set-up with the instruments for suspended sediment monitoring in the valve chamber of HPP Fieschertal (modified from Felix *et al.* 2018).

Water samples were pumped from the bucket every few days or more frequently if certain thresholds of ρ_m measured by CFDM were exceeded. From the water samples, *SSC*s were gravimetrically determined in the laboratory (denoted as SSC_G). LISST data were processed using the inversion mode for 'randomly shaped' particles, i.e. irregular particles with no preferred axes (Agrawal *et al*. 2008). The LISST volume concentrations of bins 1 to 3 (approx. 2 to 3 µm) seemed to be unrealistically high and were omitted in the evaluation of the PSDs and *SSC*s (Felix *et al.* 2013). As described by Felix *et al.* (2014), the total volume concentrations from LISST were converted to *SSC* based on the SSC_G. The resulting minute-by-minute *SSC* were denoted as SSC_L. The d_{50} were evaluated from the volume concentrations per size class, assuming that the particle density does not vary with particle size. From the CFDM data, minute-by-minute *SSC* (denoted as SSC_C) were computed using time-averaging and Equation (2).

4. Results and Discussion

4.1 Upper limit of SSC measuring range of LISST (without dilution)

Figure 2a shows the SSC_L as a function of d_{50} measured in the wet seasons of 2013 and 2014 (dots). The black dots represent the results of the measurements at $\tau \geq 0.3$, the grey dots the rest of the data (at lower τ). For selected events with temporarily high *SSC*, SSC_{lim} and the corresponding d_{50} were determined for $\tau \geq 0.3$ (triangular markers) and for unconstrained τ (circular markers), respectively. Linear least square fits for SSC_{lim} are indicated for both cases. These SSC_{lim} refer to site-specific particle properties. Microscope images showed flaky (sheet silicates) and angular particles (mainly quartz and feldspar). According to pycnometer measurements on 12 samples of dried particles, the solid density of the particle material was on average 2.73 g/cm³. With this density, $\tau = 0.3$ and $L = 0.005$ m, Equation (1b) yields

$$SSC_{\text{lim}} = 0.22\ SMD \qquad (3)$$

where *SMD* is in µm and SSC_{lim} in g/l (as in Fig. 2a).

If *SMD* is not available and d_{50} is taken instead in Eq. (3), the SSC_{lim} shown as the dotted line in Figure 2a would result, which is more than four times the actual SSC_{lim} from the measurements with $\tau \geq 0.3$ (solid green line). This deviation is explained by the fact that for graded and highly non-spherical particles, *SMD* is considerably smaller than d_{50}. In the laboratory investigation prior to this field study, Felix et al. (2013) found that for graded, angular feldspar and flaky mica particles *SMD* was only 41 and 14 % of the d_{50}, respectively. A further possible reason for the deviation is that the particle density in HPP Fieschertal might have been lower than 2.73 g/cm^3 due to potential agglomeration of particles in the clay and silt size range (flocs).

4.2 Lower limit of SSC measuring range of CFDM

Figure 2b shows the comparison of the SSC_G (from gravimetric analysis of the bottle samples) and the corresponding SSC_C (from CFDM) in the wet seasons of the years 2013 and 2014. A measuring uncertainty of ±0.3 g/l (95% confidence interval) was estimated for *SSC* from CFDM with periodic field calibration (Felix *et al.* 2018). For $SSC \geq 1.5$ g/l, the relative measuring uncertainty is hence ≤ 20%, which is judged to be acceptable. In the years 2013 and 2014, *SSC* up to 13 g/l were measured. It is expected that the CFDM is able to measure even higher *SSC* as long as the measurement tubes inside the instrument are not clogged.

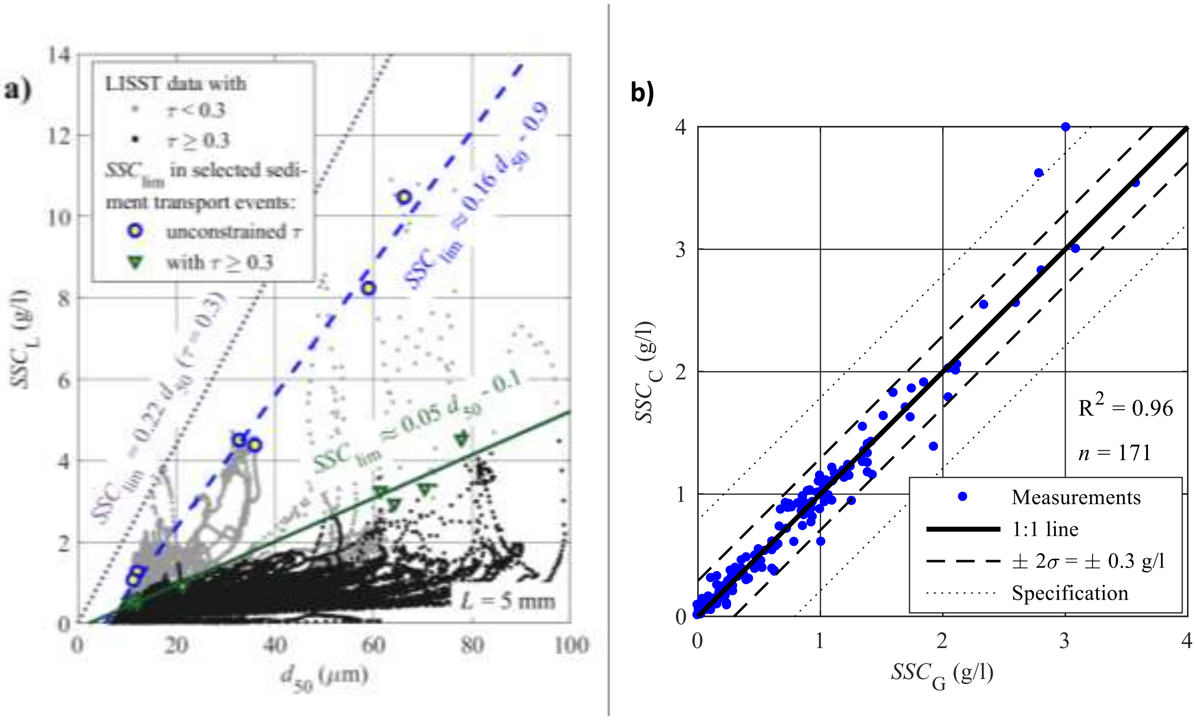

Fig. 2: a) SSC_L and d_{50} obtained from LISST with analysis of upper limits of measuring range SSC_{lim}, b) comparison of SSC_C (from CFDM) and SSC_G (from gravimetric analysis); a) and b) are based on measurements on the waterway of HPP Fieschertal in the years 2013 and 2014 (Felix *et al.* 2018).

5. Conclusions and Outlook

The upper and lower limits of the *SSC* measuring ranges of a LISST instrument without dilution and a CFDM, respectively, were investigated in a field study. To estimate the upper limit of LISST's *SSC* measuring range SSC_{lim}, Equation (1b) is recommended. If *SMD* is not available and d_{50} is used instead in practice, the actual SSC_{lim} may be considerably lower than estimated if the particles are well-graded and/or highly non-spherical. With the angular and flaky graded silt particles typically prevailing at HPP Fieschertal and an optical path length of 5 mm, SSC_{lim} was a few g/l. In contrast, CFDM was found to be suitable to measure $SSC \geq 1.5$ g/l with uncertainty of ≤ 20%. Hence, a combination of a standard LISST instrument and a CFDM allows measuring both low and high *SSC*. If the lack of PSD data at higher *SSC* is not acceptable, the use of a LISST instrument with an automatic dilution mechanism (*LISST-Infinite*) is an option. Gravimetric analyses of bottle samples are still highly recommended as a reference for any indirect *SSC* measuring technique.

The study at HPP Fieschertal is continued to improve the knowledge on practically applicable measuring systems for sediment monitoring on rivers and in HPPs.

Acknowledgements

The authors gratefully acknowledge the support by Swisselectric Research, the Swiss Federal Office of Energy and Gommerkraftwerke AG (the operator of the study HPP), measuring equipment manufacturers (Endress+Hauser, Rittmeyer, Sigrist Process Photometer) and other project partners, as well as the good collaboration with Hochschule Luzern. The present research is embedded in the Swiss Competence Center for Energy Research, Supply of Energy (SCCER-SoE) – an initiative supported by the Swiss Confederation through Innosuisse.

References

Agrawal Y.C., Pottsmith H.C. (2000). Instruments for particle size and settling velocity observations in sediment transport. *Marine Geology, 168*, 89–114.

Agrawal Y. C., Whitmire A., Mikkelsen O. A., Pottsmith H. C. (2008). Light scattering by random shaped particles and consequences on measuring suspended sediments by laser diffraction, *J. Geophysical Research*, 113, C04023.

Felix D. (2017). Experimental investigation on suspended sediment, hydro-abrasive erosion and efficiency reductions of coated Pelton turbines. ***Diss.* 24145**, ETH Zurich, Switzerland.

Felix D., Albayrak I., Boes R. M. (2013). Laboratory investigation on measuring suspended sediment by portable laser diffractometer (LISST) focusing on particle shape. *Geo-marine Letters* 33(6): 485-498.

Felix D., Albayrak I., Boes R.M. (2014). Site-specific Conversion of Laser Diffractometer (LISST) Data to Suspended Sediment Mass Concentration (SSC). *Proc.* PiE, Esbjerg, Denmark.

Felix D., Albayrak I., Boes R.M. (2018). In-situ investigation on real-time suspended sediment measurement techniques: Turbidimetry, acoustic attenuation, laser diffraction (LISST) and vibrating tube densimetry. *Int. J. of Sediment Research* 33: 3–17.

Holcomb C.D., Outcalt S.L. (1998). A theoretically-based calibration and evaluation procedure for vibrating-tube densimeters. *Fluid Phase Equilibria*, 150-151, 815–827.

Sequoia (2016). Concentration Limits – Advanced. Article updated 05.12.2014. https://www.sequoiasci.com/article/lisst-concentration-limits/

Variations in SPM characteristics and its consequences for long-term in situ measurements using optical and acoustical sensors

Michael Fettweis

Royal Belgian Institute of Natural Sciences

OD Natural Environment, Gulledelle 100, 1200 Brussels, Belgium

Knowledge on the dynamics of Suspended Particute Matter (SPM) is relevant for most oceanographic disciplines. SPM is a mixture of clay to sand sized particles in suspension that consists of varying amounts of minerals from physico-chemical (e.g. clay minerals, quartz, feldspar) and biogenic origin (e.g. calcite, aragonite, opal), living (bacteria, phyto- and zooplankton) and non-living organic matter (fecal and pseudo-fecal pellets, detritus and its decomposed products from microbial activity such as mucus, exopolymers), and particles from human origin (microplastics). The SPM characteristics (concentration, size and composition) are varying through the mutual interactions between physical forcings (tides, meteorology, climate), biological cycles (algae blooms), chemical processes (carbon cycle) and human activities (nutrient and pollutant release, dredging and dumping activities, offshore constructions).

In situ water samples have been collected since 2000 in the turbide Belgian coastal area to determine the biogeochemical characteristics (mineral, organic matter, chlorophyll and phaeophytine, exoploymers). Long-term time series of SPM concentration from acoustical and optical backscatter sensors and particle size from laser diffraction are available since 2004. Figure 1a shows that Chlorophyl-a concentration (Chl-a) is high between March and September (with the prominent algae bloom in spring and a secondary peak in summer) and low during winter. For the particulate organic carbon (POC) content in the SPM, the values are almost similar during whole the year, except during the spring bloom when the POC content also increases. The POC represents the refractory fraction of the organic matter (OM), while the Chl-a can be seen as a proxy for the labile fraction of the OM that is associated with the seasonal formation and decay of fresh organic matter by e.g. algae bloom, bacterial activity. The freshness of the organic matter is further detectable in the chl-a versus phaeophytine-a content of the SPM, the latter being associated with decaying chlorophyll (Figure 1b).

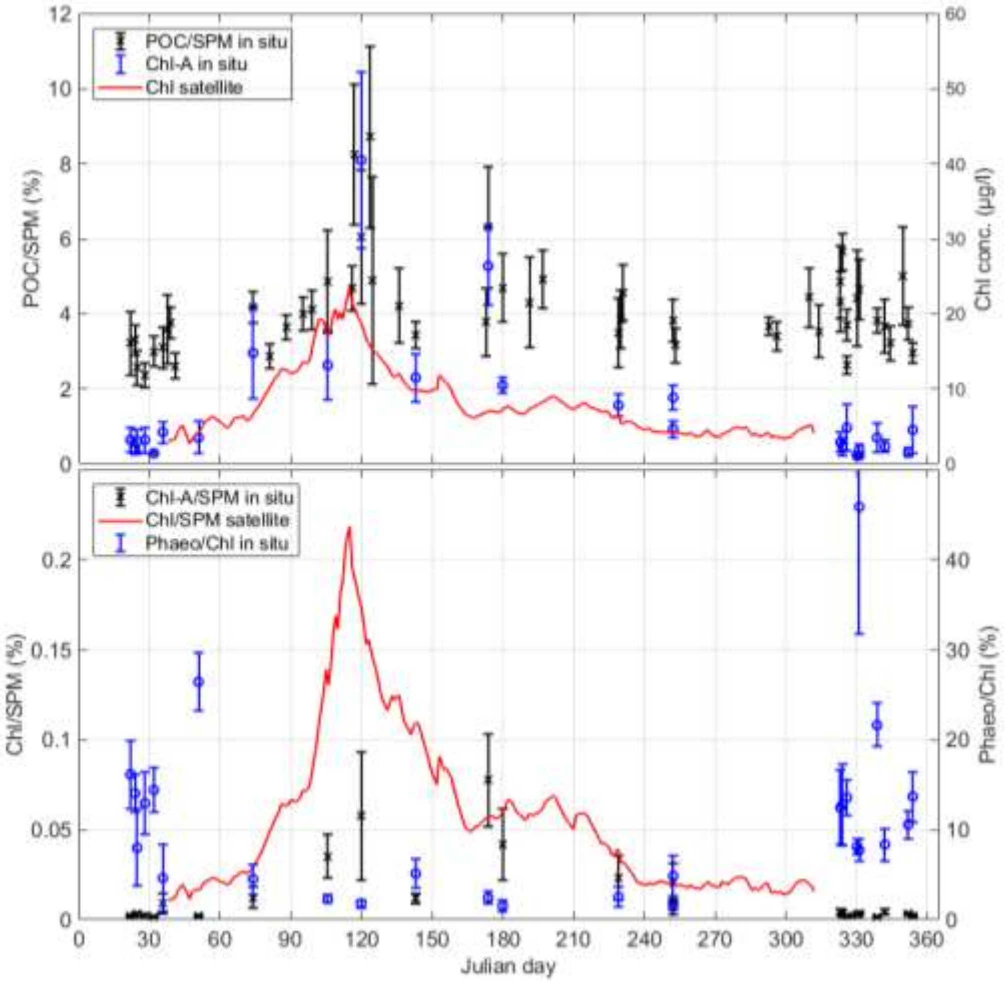

Figure 1 : Seasonal variation of the OM (above) and the Chlorophyl-A and Phaeophytine-A content of the SPM (below) derived from water samples over the period 2000 to 2018 in the Belgian nearshore area (at about 3 m above the bed). Each dot and errorbar represents the mean and standard deviation of 13 samples taken during a tidal cycle. The solid line are the surface Chl and SPM concentration from MERIS satellite over the period 2002-2012.

Further to seasonal changes the SPM characteristics exhibit substantial gradients with distance from the coast. The SPM concentration is generally higher in the nearshore areas, than in more offshore deeper areas of the continental shelf, while the composition of the SPM becomes more organic, see Figure 2. Although SPM in the high turbidity and the offshore zone had similar mineralogical composition, they encountered different fates in association with biomass (Fettweis and Lee, 2017). While in the high turbidity zone the SPM consist of mineral-enriched, dense, and settleable biomineral aggregates, the SPM in the offshore zone is composed of biomass-enriched, less dense and less settleable flocs, see Figure 3.

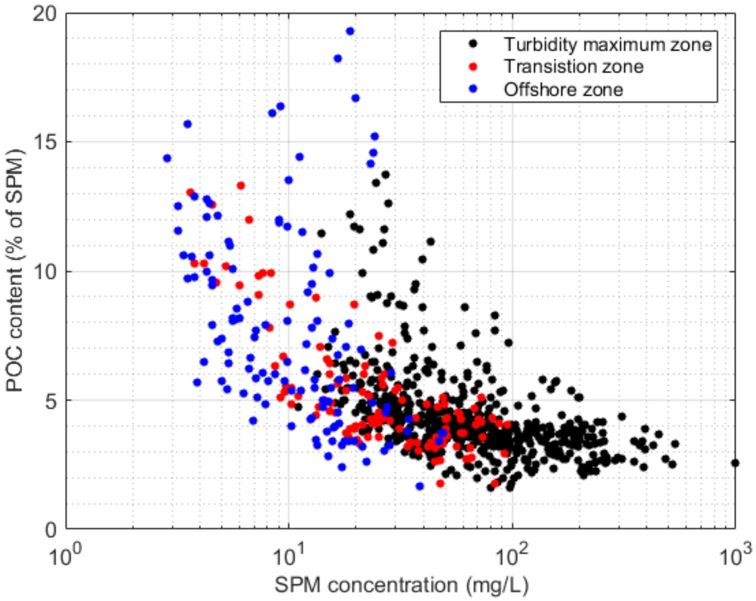

Figure 2 : POC content (% of SPM) as a function of SPM concentration in the high turbid nearshore and the low turbid offshore areas of the Belgian continental shelf.

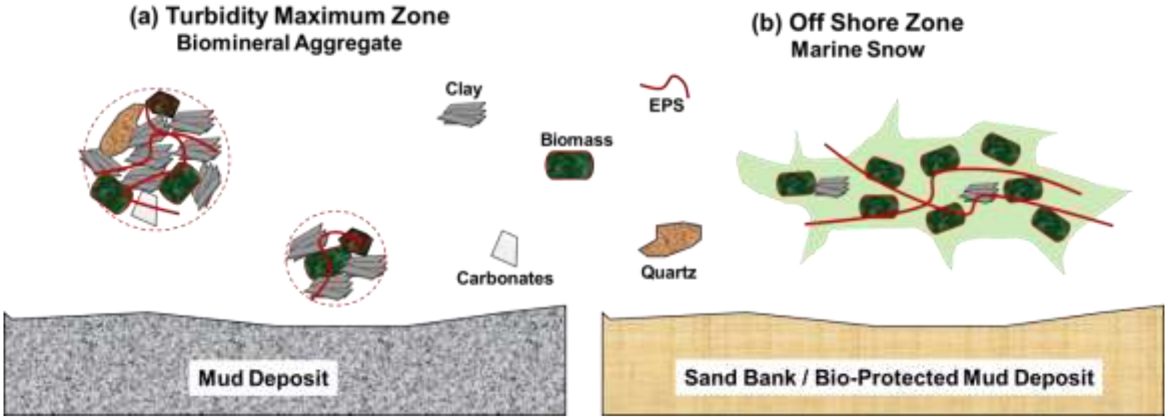

Figure 3 : Schematic diagrams of (a) biomineral aggregates in the turbidity maximum zone and (b) in the offshore zone. EPS: extracellular polymeric substances.

The influence of biological cycles on SPM dynamics are multiple and mutual. A prominent example is the seasonality in floc size and thus settling velocity of the SPM that impacts the surface and near-bed SPM concentration in winter and summer and thus the water clarity, the formation of fluid mud layers, the smothering of benthic ecosystems, and the fate of carbon and SPM on a regional scale (Fettweis et al., 2014). Changes in the concentration and the composition of the SPM influences the optical and acoustical properties of the particles in suspension and if not calibrated for these conditions also the sensor derived SPM concentration. This has as consequence that the calibration of these sensors used in long-term and continuous measurements has to be adapted in order to reduce the uncertainty associated with the sensor-derived SPM concentration. Controling uncertainties will become an important issue when observation comprises systems of sensors spanning large spatial and temporal scales in order to detect trends in the data, to separate anthropogenic impact from natural variations or to evaluate numerical models over a broad ensemble of different conditions using validated field data.

References

Fettweis M, Lee BJ. 2017. Spatial and seasonal variation of biomineral suspended particulate matter properties in high-turbid nearshore and low-turbid offshore zones. *Water*, 9, 694. doi:10.3390/w9090694

Fettweis M, Baeye M, Van der Zande D, Van den Eynde D, Lee BJ. 2014. Seasonality of floc strength in the southern North Sea. *Journal of Geophysical Research* 119, 1911-1926. doi:10.1002/2013JC009750

The Tagus estuary

Paula Freire

National Civil Engineering Laboratory

Av. do Brasil 101, 1700-066 Lisbon, Portugal

pfreire@lnec.pt

The estuary of the Tagus river is one of the largest estuaries in Europe covering an area of about 320 km^2. It is located in the Portuguese west coast, in the metropolitan area of Lisbon, and due to its social and economic context and environmental characteristics it is the Portuguese most relevant estuary. The estuary comprises along its margins 11 municipalities with about 1.6 million inhabitants (Tavares *et al.*, 2015). It hosts the Port of Lisbon, the national leader in the movement of vessels (in number and in GT), and the Tagus Estuary Natural Reserve considered one of the most important sanctuaries for birds in Europe.

The estuary has a peculiar morphology characterised by a wide inner bay with extensive tidal flats (about 43% of the total estuarine area) that connects to the ocean by a narrow and deep fault-controlled channel. The Tagus estuary is a mesotidal system with tidal amplitudes of 1.5 m (neap tide) and 3.2 m (spring tide) at Lisbon that are amplified within the estuary due to resonance (Fortunato *et al.* 1999). In average conditions, the upstream limit of the salt-water intrusion is about 50 km from the estuary mouth and the dynamic influence of the tide reaches 80 km upstream. The average discharge that reaches the estuary is about 370 m^3 s^{-1} (Neves, 2010), largely controlled by several large dams built in the Tagus River and its tributaries. The estuary narrow inlet channel restricts the upstream propagation of ocean waves, while the elongate shape of the inner bay in the prevailing wind direction favours local generation of waves (Freire and Andrade 1999).

The estuarine bottom sediments are mainly from fluvial and local origin (Freire *et al*., 2007). Fine-grained riverine sediments are mainly distributed along the tidal flats and salt marshes. Sands from local sources are found along the deeper channels and on beaches. The presence of marine sediments is limited to the estuary mouth and inlet channel. Sedimentation rates of the Tagus estuarine marshes varies between 0.4 and 2.2 cm $year^{-1}$ and are higher in the upstream areas (Silva *et al.*, 2013). A sediment retention within the estuary of 0.6×10^6 ton $year^{-1}$ is estimated (Portela, 2004). The maintenance dredging in the main estuary access channel (sands and gravel) was about 2×10^6 m^3 between 1998 and 2007; the estimated annual value in the inner domain is about 0.9×10^6 m^3, mainly of fine sediments (Portela, 2011).

The estuarine fringe is densely occupied including some of the most important infrastructures, equipment and strategic services on national level. Occupation contrasts between margins can be found: in the northern side urban (34% of the total margin area) and industrial/port facilities (24%) are dominant, while agriculture (35%) and isolated towns occupy the most area of southern margin (Rilo *et al.*, 2012). The estuary geomorphology, the hydrodynamic characteristics and the territory occupation promote high risk of the margins to floods as confirmed by the impact of past occurrences. A regional geodatabase of historical flood occurrences in the Tagus estuary indicates that the probability of occurrence of one or more flood events in one year is about 26% (Rilo *et al.*, 2015).

The most recent flood event with the highest impact along both Tagus estuarine margins occurred on February 27, 2010, associated with the Xynthia storm, which had tragic effects in the western coast of France (Freire *et al.*, 2016). The event promoted considerable damages in the waterfront of five municipalities in the Lisbon Metropolitan Area, in different territorial contexts as urbanised and productive agricultural areas.

In estuaries, the management of flood risk needs an integrated view considering the multiplicity of hazard-forcing factors and the territorial and social complexity. An innovative approach to support flood risk management in estuaries is presented at a local scale. The approach includes a decision-making supporting framework constructed for the high risk areas, considering the emergency planning and response to floods, based on a real-time forecast and an early-warning system (Fortunato *et al.*, 2017).

References

Fortunato AB, Oliveira A, Baptista AM, 1999. On the effect of tidal flats on the hydrodynamics of the Tagus estuary. Oceanol Acta 22(1): 31-44

Fortunato AB., Oliveira A, Rogeiro J., Costa R., Gomes JL, Li K, Jesus G, Freire P, Rilo A, Mendes A, Rodrigues M, Azevedo A. Operational forecast framework applied to extreme sea levels 1 at regional and 2 local scales. Journal of Operational Oceanography, Volume 10, 2017 - Issue 1: 1-15

Freire P and Andrade C, 1999. Wind-induced sand transport in Tagus estuarine beaches. First results. Aquatic Ecology, 33(3), 225–233

Freire P, Taborda R, Silva AM, 2007. Sedimentary Characterization of Tagus Estuarine Beaches (Portugal). A contribution to the sediment budget assessment. Journal of Soils and Sediments, 7 (5), 296-302

Freire P, Tavares A, Sá L, Oliveira A, Fortunato AB, Santos PP, Rilo A, Gomes, JL, Rogeiro, J, Pablo R, Pinto PJ, 2016. A local scale approach to estuarine flood risk management. Nat. Hazards. Natural Hazards, 84(3), 359 1705-1739

Neves FS, 2010. Dynamics and hydrology of the Tagus estuary: results from in situ observations. 210p, PhD thesis, Universidade de Lisboa, Portugal. Unpublished. Available on-line at http://repositorio.ul.pt/handle/10451/2003

Portela LI, 2004. An approximate sediment budget for the Tagus estuary. In: 3rd International SedNet Conference: The future of sediment management in Europe, 3 pp. European Sediment Research Network

Portela LI, 2011. Dragagens nos portos comerciais de Portugal Continental: dados preliminares. In: 7as Jornadas Portuguesas de Engenharia Costeira e Portuária, Porto, 6 e 7 de Outubro de 2011, 9 pp

Rilo A, Freire P, Ceia R, Mendes RN, Catalão J, Taborda R, 2012. Human effects on estuarine shoreline decadal evolution. Geophysical Research Abstracts, Vol. 14, EGU2012-10863, 2012, EGU General Assembly 2012

Rilo AR, Freire P, Santos PP, Tavares AO, Sa´ L, 2015. Historical flood events in the Tagus estuary: contribution to risk assessment and management tools. In: Pedofillini et al (eds) Safety and reliability of complex engineered systems, natural hazards. CRC Press, Taylor and Francis Group, London, pp 4281–4286

Silva TA, Freitas MC, Andrade C, Taborda R, Freire P, Schmidt S, Antunes C, 2013. Geomorphological response of the salt-marshes in the Tagus estuary to sea level rise. In: Conley,

D.C., Masselink, G., Russell, P.E. and O'Hare, T.J. (eds.), Proceedings 12th International Coastal Symposium (Plymouth, England), Journal of Coastal Research, Special Issue No. 65, pp. 582-587, ISSN 0749-0208

Tavares AO, Santos PP, Freire P, Fortunato AB, Rilo A, Sá L, 2015. Flooding hazard in the Tagus estuarine area: The challenge of scale in vulnerability assessments. Environ Sci Policy 51:238–255

Novel approach to measure the rate of sediment resuspension at the ocean and to estimate the contribution of fish activity to this process

Merav Gilboa[1], Timor Katz[2], Uri Shavit[3], Shachar Grosbard[3], Adi Torfstien[4] and Gitai Yahel[1]

[1]The School of Marine Sciences, Ruppin Academic Center, Michmoret, Israel

[2]Israel Oceanographic & Limnological Research, Tel Shikmona, Haifa, Israel

[3]Civil and Environmental Engineering, Technion, Haifa, Israel

Electrical Engineering, Technion, Haifa, Israel

Department for Marine Technologies, University of Haifa, Haifa, Israel

Institute of Earth Sciences, the Hebrew University of Jerusalem, Jerusalem, Israel

Sediment resuspension, defined as the dislodgement and redistribution of previously settled particles back into the overlying water, disturbs the bottom sediment and can potentially control key sedimentary processes such as remineralization rates, silica dissolution, denitrification and the quality and burial rate of organic matter and hence carbon sequestration (Inthorn et al. 2006), (Yahel et al. 2008b, Katz et al. 2009). Sediment resuspension plays a major role in sediment transport which affects sediment erosion and accumulation (Teague et al. 2006), the distribution and winnowing of fine particles, and the formation of benthic and midwater nepheloid layers (Yahel et al. 2002, Katz et al. 2012). High amount of suspended solids alter water transparency (Breukelaar 1994) and light permeability (Onuf 1994). Resuspension also affects the chemistry of the sediment, the pore-water and the overlying water, and hence the pelagic ecosystem above (Ingall & Cappellen 1990, Vidal 1994, Loeff & Boudreau 1997, Katz et al. 2009). Such effects includes adsorption processes and control of nutrient dynamics (Fanning et al. 1982, Breukelaar 1994, Yahel et al. 2008b). Sediment resuspension also affect the state, function, and distribution of microorganisms in the benthic nepheloid layer (Bai & Lung 2005) and the suspended grains may have a deleterious effects on suspension feeders (Snelgrove & Butman 1994, Tompkins-Macdonald & Leys 2008).

Sediment resuspension has been described and studied in shallow lakes, the breaker zone and estuaries (Bloesch 1995, Stahlberg et al. 2006, Chung et al. 2009) where it is largely controlled by physical mechanisms (Harris 2014). Although physical resuspension mechanisms have been described deeper along the continental shelves (Harris 2014), their direct effects are diminishing with depth. Storm events and waves that leads to high velocity currents near the seafloor are the predominant resuspension processes up to 60 m (Ingall & Cappellen 1990). Physical processes taking part in deeper waters include near-bottom currents and internal waves driven by tidal forces. Geologic events such as landslides and earthquakes as well as anthropogenic activity such as trawling and dredging also resuspend large amounts of sediments.

The role of fish induced resuspension is widely acknowledged in the limnological literature, where fish removal serves as standard tool for controlling turbidity levels of shallow lakes and streams. In contrasts, biological resuspension has gained much less attention from oceanographers and marine biogeochemists. The marine literature that discuss sediment disturbance by biological factors (Takeuchi & Tamaki 2014), converge mostly on rates of mixing within the sediments (Guinasso & Schink 1975). However, the activity of large mobile organisms such as ground fish looking for shelter or food in bottom sediments, can potentially trigger significant resuspension processes(Snelgrove 1994, Yahel et al. 2002, 2008a, Flecker & Taylor 2009, Robert & Juniper 2012). Unlike physical resuspension that concurrently affects large swaths of the seafloor and act mostly on the sediment water interface, fish induce resuspension is characterized by sporadic, short-term, and localized events that some time penetrates deep (centimeters) into the sediment. The high temporal and spatial variation of this process pose a challenge for measurements but, as suggested below, could potentially be harnessed to differentiate biologically induced resuspension from other factors responsible for resuspension.

Despite its potential to control large-scale biogeochemical cycles and affect both sedimentary and pelagic processes, quantitative information regarding sediment resuspension in the deeper parts of the ocean is meager, largely due to the lack of established methodology to quantify these processes. In an effort to close this gap, we have devised and tested an inexpensive and reliable method to measure overall resuspension rate (g m^{-2} day^{-1}) in deep water (>50-5000 m) and to estimate the contribution of fish activity to this process.

System overview

To quantify sediment resuspension and estimate the potential contribution of biological induced resuspension to this process we have developed a combined setup (Figure 1) consisting of sediment traps, Optical Backscatter Sensors (OBS) and a tilt current meter. A pair of sediment traps is deployed near the seabed and a second pair is moored above the benthic nepheloid layer (BNL) so the difference between the sedimentation rate in these two locations provides a direct measurement of the resuspension rate(Bloesch 1994). An OBS sensor is attached next to each trap pair to measure overall turbidity levels and the occurrence of "turbidity spikes" in the time series (a proxy for sporadic fish induced resuspension events, see below). To prevents contamination during deployment, the bottom traps are capped and equipped with a time release opening mechanism (see videos of the **sediment cloud raised during the landing of a system** and **a demo of the opening mechanism**). Near-bottom currents are continually recorded with a tilt meter (TCM-1, Lowell inst.) to estimate the potential for physical resuspension. Taken together, this set of instruments measured the rate of sediment resuspension at the study site and estimate the potential contribution of biological activity to this process.

To validate the utility of the proposed methodology, we have deployed a lander system for 12 times at depths ranging from 600 to 75 m in the sheltered desert enclosed Gulf of Aqaba where terrestrial sediment inputs and wave effects are minimal. In these deployments the lander was also equipped with a custom-made video camera (Astral Sub-Sea) that documented near-bottom biological activity and its correlation to the observed backscatter spikes. In some deployments we also used an in-situ particles size analyzer (LISST 200X, Sequoia) that recorded particle concentration at 1 Hz over a range of sizes from 1-500 µm 0.3 meter above bottom. An accurate characterization of the near-bottom flow field was achieved using an Acoustic Doppler Velocimeter and a 2 MHz profiler (Vector, and Aquadopp, respectively, Nortek-AS).

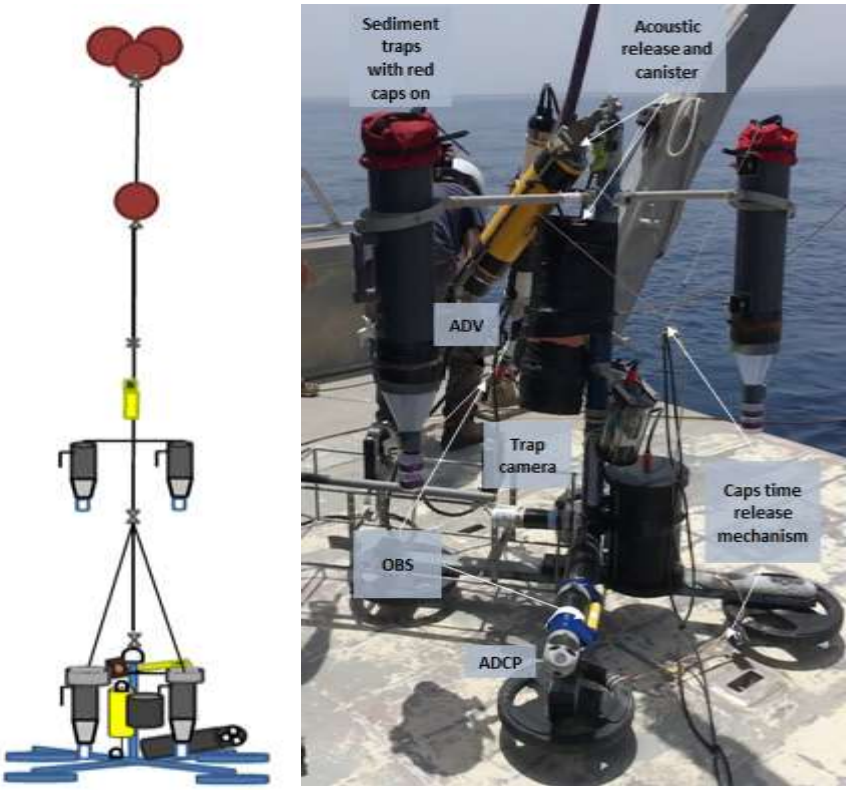

Figure 1. The lander system with a pair of capped sediment traps at the bottom controlled by a time release mechanism, a second pair of traps 10 m above bottom, OBS sensors, an Acoustic Doppler Current Profiler and Acoustic Doppler Velocimeter as well as a custom-made trap camera. a. A schematic representation of the moored setup. b. A picture of the lower part of the moored setup ready to deployment.

Event detection

Due to the sporadic nature of fish induced resuspension, these events are typified as 'spikes' in a noisy turbidity signal (Yahel et al. 2002, 2008) embedded within a fluctuating background turbidity. Background turbidity levels are partly fueled by spiking events in the vicinity, and partly by lateral advection and vertical sedimentation. To quantify the number of OBS (or acoustic backscatter) “spikes” in the time series we calculated a smoothed local central tendency of the time series and a backward moving prediction interval for each data point. We considered events with a turbidity signal above this threshold as resuspension events and their frequency and magnitude was recorded. Parameterization of the spike detection algorithm was based on the analysis of a synthetic data set generated by a numerical model of sediment resuspension jets (Shavit et al. 2018). The algorithm performance was then validated by analyzing resuspension events recorded by the underwater camera. In this analysis, we assume that strong resuspension events observed by the camera when its field of view was upstream from the system, was also recorded by the near-bottom instruments (Figure 2).

Overall sediment resuspension flux measured at 0.7 m above the bottom (calculated as the difference between the flux at the bottom to that 10 m above) ranged from 200 to 1500 mg m^{-2} day^{-1} while the background sedimentation flux (10 m above bottom) was 50-1400 mg m^{-2} day^{-1}. The suspended sediment concentration at 0.3 m above the bottom was on average six folds higher and at least twice more variable than the concentration measured ten meters above (mean±95% confidence interval, 3.04±0.02 mg L^{-1} and 0.54±0.01 mg L^{-1}, respectively). Near-bottom currents were low (8.2±0.06 cm s^{-1}) and normally below the threshold for sediment mobility. Using our algorithm, we calculated a range of 100 – 300 OBS ‘spiking’ events per day, 80% of these were short, lasting less than 5 s. A similar rate to that reported from visual observations in the shallow coral reefs of the Gulf of Aqaba by Yahel et al. (2002). The low current velocity, the lack of correlation between near bottom current speed and suspended sediment concentration and the high frequency of resuspension events near the bottom but not ten meter above, suggest that except rare occasions, most of the local resuspension flux in the deeper parts of the gulf of Aqaba if mediated by fish activity rather than by physical forces.

The simple and inexpensive time-release based opening mechanism we developed allow the unattended deployment of sediment tarps >1 meter above the bottom without the risk of contamination during deployment. Pairing near-bottom traps with traps deployed above the benthic nepheloid layer provides effective and efficient mean to measure overall sediment resuspension flux at any depth in the ocean.

Coupling the system with high frequency OBS data loggers and a current meter provides an estimate of the amount of biologically induced resuspension. To actually measure the biologically induced sediment resuspension flux we will need to implement the algorithm proposed by Shavit et al. 2018 (this meeting) into the benthic lander system, based on insights gained from controlled laboratory and filed visualizations of the resuspension clouds as described by Grosbard et al. 2018 and Vainiger et al. 2018. (this meeting).

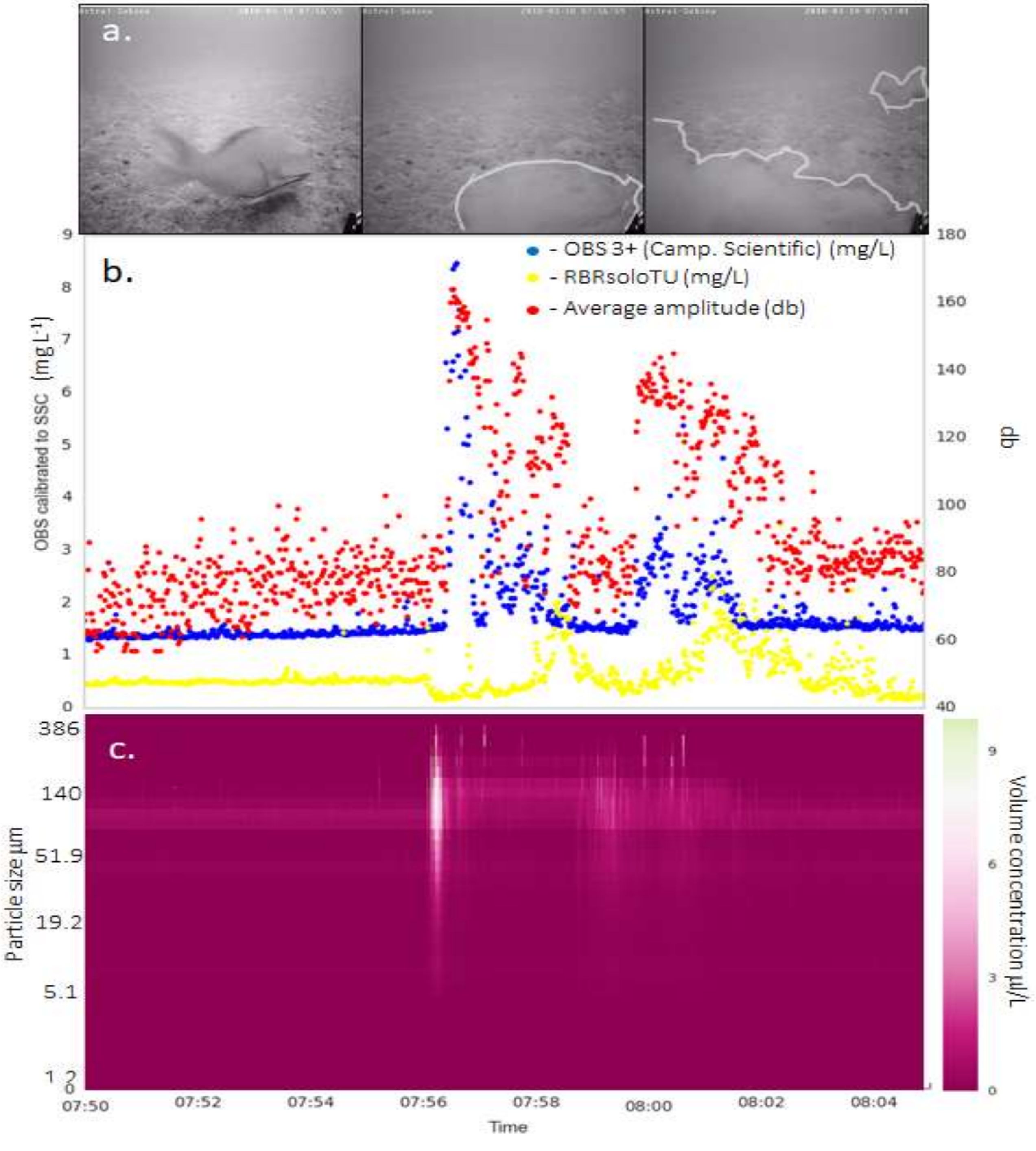

Figure 2. A data segment depicting a fish induced resuspension event at 75 m at the Gulf of Aqaba. (A) A sequence of frame grabs from the underwater trap video camera. The resuspending fish (*Scaridae sp.*) is seen in the first frame, the ensuing sediment cloud is outlined in white in the next two frames. (B) Optical Backscatter signal from two separate OBSs calibrated with local sediment to suspended sediment concentration and an acoustic backscatter signal from an Acoustic Doppler Velocimeter (Vector, Nortek). The sensing volume of the OBS3+ (blue) and the Vector (red) were positioned together whereas the RBR SoloTu OBS (yellow) was located some 50 cm aside. (C) A heatmap of the same time series with volumetric

concentration (µL L^{-1}) of 36 particle size classes obtained with a LiSST 200X (Sequoia) plotted according to the color scale to the right.

Acknowledgments

This research was funded by the Israeli Ministry of Science, Technology and Space 3-12478. We would like to thank the marine tech. department at the Inter University Institute of marine sciences in Eilat as well as the Michmoret Sailing club for their support.

References

Bai S, Lung WS (2005) Modeling sediment impact on the transport of fecal bacteria. Water Res 39:5232–5240

Bloesch J (1994) A review of methods used to measure sediment resuspension. Hydrobiologia 284:13–18

Bloesch J (1995) Mechanisms, measurement and importance of sediment resuspension in lakes. Mar Freshw Res 46:295–304

Breukelaar A (1994) Effects of benthivorous bream (Abramis brama) and carp (Cyprinus carpio) on sediment resuspension and concentrations of nutrients and chlorophyll a. Freshw …:113–121

Chung EG, Bombardelli F a., Schladow SG (2009) Sediment resuspension in a shallow lake. Water Resour Res 45:n/a-n/a

Fanning KA, Carder KL, Betzer PR (1982) Sediment resuspension by coastal waters: a potential mechanism for nutrient re-cycling on the ocean’s margins. Deep Sea Res Part A, Oceanogr Res Pap 29:953–965

Flecker AS, Taylor BW (2009) Tropical Fishes as Biological Bulldozers : Density Effects on Resource Heterogeneity and Species Diversity Published by : Ecological Society of America tropical fish as biological bulldozers : density effects on resource heterogeneity and species divers. Ecology 85:2267–2278

Grossbard S, Gilboa M., Katz T, Yahel G., Shavit U, Developing a laboratory simulator for the study of resuspension events. PiE 2018.

Guinasso NL, Schink DR (1975) Quantitative estimates of biological mixing rates in abyssal sediments. J Geophys Res 80:3032–3043

Harris PT (2014) Shelf and deep-sea sedimentary environments and physical benthic disturbance regimes: A review and synthesis. Mar Geol 353:169–184

Ingall ED, Cappellen P Van (1990) Relation between sedimentation rate and burial of organic phosphorus and organic carbon in marine sediments. Geochim Cosmochim Acta 54:373–386

Inthorn M, Wagner T, Scheeder G, Zabel M (2006) Lateral transport controls distribution, quality, and burial of organic matter along continental slopes in high-productivity areas. Geology 34:205 LP-208

Katz T, Yahel G, Reidenbach M, Tunnicliffe V (2009) Sediment resuspension by groundfish facilitates the transport and redistribution of sediments in deep coastal basins. uvic.ca:1–44

Katz T, Yahel G, Reidenbach M, Tunnicliffe V, Herut B, Crusius J, Whitney F, Snelgrove PVR, Lazar B (2012) Resuspension by fish facilitates the transport and redistribution of coastal sediments. Limnol Oceanogr 57:945–958

Loeff MR van der, Boudreau B (1997) The effect of resuspension on chemical exchanges at the sediment-water interface in the deep sea—A modelling and natural radiotracer approach. J Mar Syst 7963

Onuf CP (1994) Seagrasses, Dredging and Light in Laguna Madre, Texas, U.S.A. Estuar Coast Shelf Sci 39:75–91

Robert K, Juniper S (2012) Surface-sediment bioturbation quantified with cameras on the NEPTUNE Canada cabled observatory. Mar Ecol Prog Ser 453:137–149

Shavit U, Halamish A, Grossbard S, Asher S, Gilboa M, Katz T, Yahel G, Testing a biological resuspension footprint model using Lagrangian simulations. PiE 2018.

Snelgrove PVR& CAB (1994) Animal-sediment relationships rrevisited: cause versus effect. Oceanogr Mar Biol an Annu Rev 32:111–177

Snelgrove PVR, Butman C (1994) Animal-sediment relationships revisited: cause versus effect. Oceanogr Mar Biol an Annu Rev:111–177

Stahlberg C, Bastviken D, Svensson BH, Rahm L (2006) Mineralisation of organic matter in coastal sediments at different frequency and duration of resuspension. Estuar Coast Shelf Sci 70:317–325

Takeuchi S, Tamaki A (2014) Assessment of benthic disturbance associated with stingray foraging for ghost shrimp by aerial survey over an intertidal sandflat. Cont Shelf Res 84:139–157

Teague WJ, Jarosz E, Keen TR, Wang DW, Hulbert MS (2006) Bottom scour observed under Hurricane Ivan. Geophys Res Lett 33

Tompkins-Macdonald GJ, Leys SP (2008) Glass sponges arrest pumping in response to sediment: Implications for the physiology of the hexactinellid conduction system. Mar Biol 154:973–984

Vainiger A, Schechner YY, Treibitz T, Avni A , Timor DS, Underwater Wide-Field Tomography of Sediment Resuspension. PiE 2018.

Vidal M (1994) Phosphate dynamics tied to sediment disturbances in Alfacs Bay (NW Mediterranean). Mar Ecol Prog Ser 110:211–221

Yahel R, Yahel G, Genin A (2002) Daily cycles of suspended sand at coral reefs: A biological control. Limnol Oceanogr 47:1071–1083

Yahel G, Yahel R, Katz T, Lazar B, Herut B, Tunnicliffe V (2008a) Fish activity: a major mechanism for sediment resuspension and organic matter remineralization in coastal marine sediments. Mar Ecol Prog Ser 372:195–209

Yahel G, Yahel R, Katz T, Lazar B, Herut B, Tunnicliffe V (2008b) Fish activity: a major mechanism for sediment resuspension and organic matter remineralization in coastal marine sediments. Mar Ecol Prog Ser 372:195–209

Developing a laboratory simulator for the study of resuspension events

Shahar Grossbard[1], Merav Gilboa[2], Timor Katz[3], Gitai Yahel[2] and Uri Shavit[1]

[1]Civil and Environmental Engineering, Technion, Haifa, Israel

[2]The School of Marine Sciences, Ruppin Academic Center, Michmoret, Israel

[3]Israel Oceanographic & Limnological Research, Tel Shikmona, 31080 Haifa, Israel

Introduction

Experimentalists who study transport of heavy particles acknowledge that well-controlled experiments are technically challenging. Examples of such studies include the whereabouts of particles that are released from a point source, the sedimentation of particles that enter from above and the dispersion of particle plumes that are generated by sediment resuspension. Simple tasks such as maintaining perfectly mixed suspensions in the supply reservoir and the need to avoid an accumulation of particles along the supply tubes, often turn out to be major obstacles.

The current study focuses on aquatic fauna, such as fish, that perturb the bottom sediments while searching for food (Yahel et al. 2002) and shelter (Yahel et al. 2008), a phenomenon called "biological resuspension". As a result, a cloud of particles is lifted from the bottom and fills the water column to a certain height. This cloud is then transported by the local current, mixed by dispersion and sinks back to the bottom by gravity. Recent evidences indicate that the amount of sediments that is released to the water column is significant and often dominants regions of weak currents and negligible waves. And yet, the number of studies that address biological resuspension and provide quantitative measures is limited (Yahel et al. 2018).

Here we present a new resuspension generator designed for laboratory flume experiments, that with some modifications can be used for in-situ underwater studies. The resuspension generator was used by us, a group of marine biologists and engineers, in order to characterize the detailed physical properties of resuspension events that are caused by biological activity (Yahel et al. 2018). The generator was used to describe the velocity and concentration of the particle clouds and compare measurement techniques as potential tools for biological resuspension monitoring (Gilboa et al., 2018, Vainiger et al., 2018).

The resuspension generator

The resuspension generator was designed to test the influence of experimental variables such as injection speed, particle size, release concentration and the duration of the event. As opposed to the injection of dissolved tracers (such as dyes), the injection of heavy particles requires special attention. The difficulty to maintain perfect mixing in the supply reservoir and their accumulation along the supply tubes result in a serious ambiguity with respect to the actual concentration that is released to the test section. In addition, many laboratory setups suffer from flow interference caused by the source tube or the resuspension device when deployed in the water. The new resuspension generator allows individual control of each of the experimental variables and solves the technical pitfalls of many traditional systems.

Instead of using an external reservoir and pumping the particles through tubes into the test section, the resuspension generator was embedded in the flume floor. The flume bottom is covered, along its full length, by 2 cm thick Plexiglas boards. We removed a short section (22 cm long) of one of these boards and replaced it with the resuspension generator. By maintaining the exact external dimensions of the removed board (22 cm long, 40 cm width and 2 cm thickness), the new resuspension generator avoids the potential of disturbance to the flow as it lacks a particle-releasing tube. Instead, the new generator utilizes a one-way valve, located flat at the flume bottom. A round cavity, 10 cm in diameter and 1.3 cm deep, was engraved in the middle of the board to serve as the particle suspension reservoir (having a volume of 101.5 cm^3). After filling the reservoir with the particle suspension, the cavity was sealed from above by a round 0.4 cm thick polycarbonate cover (14.4 cm in diameter) using a 5 mm O-ring rubber seal and 12 screws (Fig. 1). In the cover's center, a 9.5 mm cross-silt one-way valve (model CR 095.001 SD, MiniValve®) was fixed using a specially designed PVC holder that allows an easy replacement of the valve. The properties of the resuspension plume can be modified by choosing the one-way valve from a large variety of available valves (MiniValve®). A continuous mixing inside the cavity was achieved by rotating a thin magnet stirrer (3 mm diameter and 30 mm long, made by Cowie®) by a magnet motor that was located underneath the bottom of the flume. The one-way valve is closed as long as the cavity's inner pressure does not exceed the outside pressure by a critical value. Resuspension events were generated by pumping small amounts of clear water into the cavity and increasing the inner pressure in order to open the one-way valve. The clear water was introduced through a 0.65 cm horizontal hole that was drilled through the board, below the flume bottom, connecting the cavity to a dual syringe pump (GenieTouch®, Kent Scientific Inc.). To begin a set of resuspension experiments, a mass of 10 gr of particles was initially mixed with clear water to a final volume of 100 cm^3 and poured into the cavity before it was sealed. The stirring magnet was placed inside the cavity which was then sealed with the cover before turning on the stirring motor. Two 60 ml syringes were installed on the syringe pump which was connected to a controlling computer and used to operate the syringe pump while controlling the injection speed and duration.

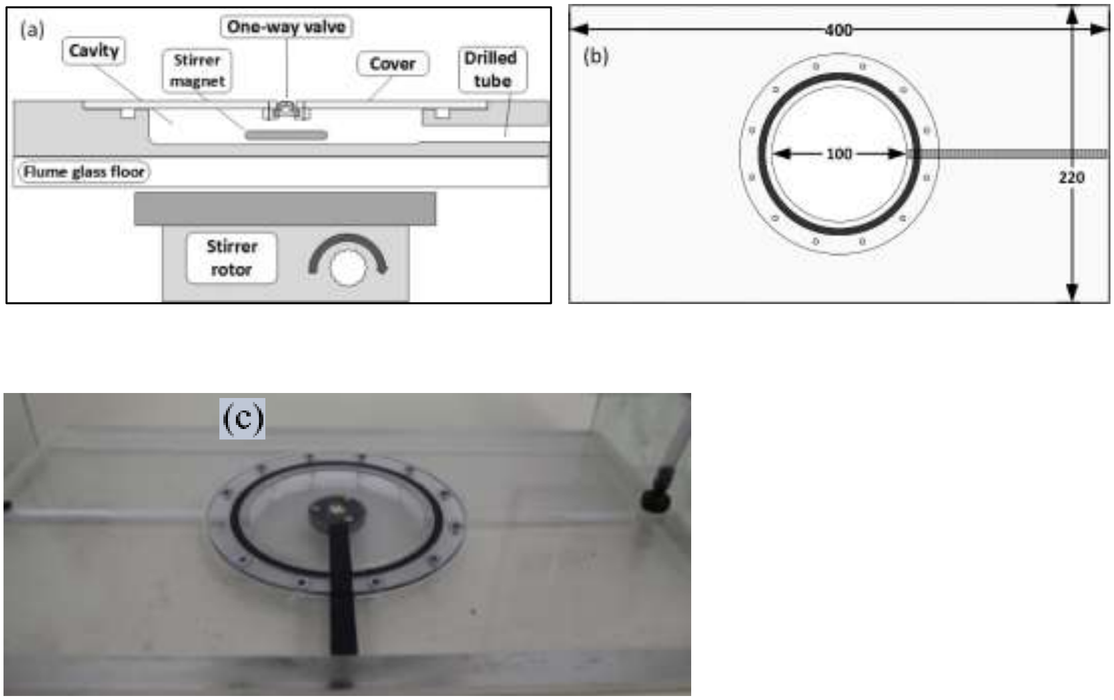

Fig. 1 The resuspension generator. (a) a vertical cross section; (b) a top view; (c) a photo of the cover, the valve and the drilled horizontal hole. The flume central line is marked by a black thick line.

Experimental setup and conditions

Experiments were carried out in a glass-wall flume, 13.4 m long, 0.4 m wide and 0.5 m deep, paved with 2 cm thick Plexiglas boards (Fig. 2). Flow rate and water height were adjusted using a discharge controller and a tailgate. Since water was circulated, seeding and suspended particles were constantly removed using a custom-made filtering bag of 1 µm pore size, placed inside the outlet container. The experimental conditions included four mean velocities of the flume water ($u_m = 4.4$, 7.8, 14.5 and 20.6 cm s^{-1}), four particle sizes (d_{50} = 34.2, 62.0, 110.4 and 183.8 µm, with a density of 2 g cm^{-3}), five injection discharges ($q_{sp} = 6$, 10, 20, 30 and 45 ml min^{-1}) and three event durations ($T = 5$ seconds, 30 seconds and continuous). Each combination of these conditions was repeated 2-3 times. The characteristics of the flow were obtained without releasing suspended particles, at the beginning and end of each work day. The resuspension events were recorded using a special illumination and a camera. Velocities were measured using particle image velocimetry (PIV) and a laboratory acoustic Doppler velocimeter (Vectrino I, Nortek). Concentration was measured using a diffraction based technique (LISST 200X, Sequoia Scientific), calibration based imaging (using the PIV setup) and by the intensity of the Vectrino backscatter signal. The resuspension camera, the PIV system and the Vectrino were synchronized and the LISST was matched such that all data sets could be plotted on a shared time axis.

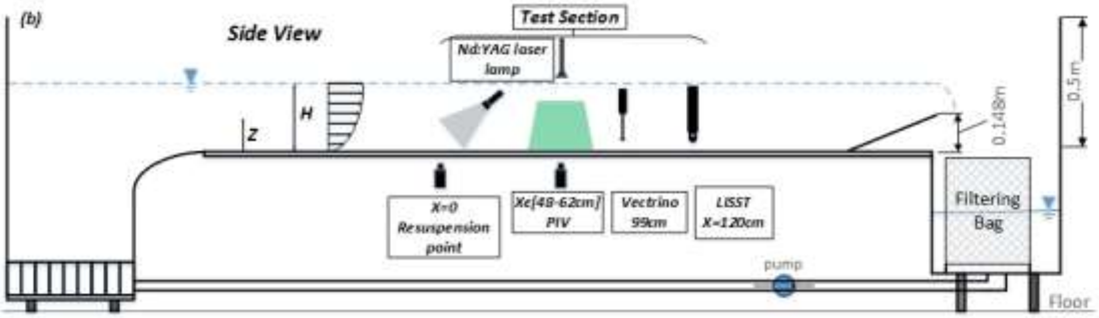

Fig. 2 A side view of the flume setup and instrumentation (not to scale).

Results and discussion

4.1 Characterization of the flow and resuspension events

Snapshots of resuspension events generated by a range of injection discharges (q_{sp}) are demonstrated in Fig. 3. As shown, an increase in q_{sp} increases the plume height and decreases the deflection angle. The opposite occurs when the flume water velocity (u_m) increases while diluting the plume and decreasing its visibility.

The background flow was measured by the PIV at 5 Hz, using d_{50} = 13 µm seeding particles. Fig. 4 shows vertical profiles of mean velocity, $\langle \bar{u} \rangle_x$, and Reynolds stresses, $\langle \overline{u'w'} \rangle_x$. An extrapolation of the Reynolds stresses to $z = 0$ was used to calculate the shear velocity, u^*, which was then used to plot the normalized velocities in Fig. 4c. It shows that all four flow rates collapse onto a single profile, indicating that the flow follows a classical boundary layer logarithmic velocity profile.

Fig. 3 Snapshots of resuspension events for a flume mean velocity $u_m = 7.8\ cm\ s^{-1}$, particle size d_{50} = 34.2 µm and injection flow rates of q_{sp} = (a) 6 ml min^{-1}; (b) 20 ml min^{-1}; and (c) 45 ml min^{-1}.

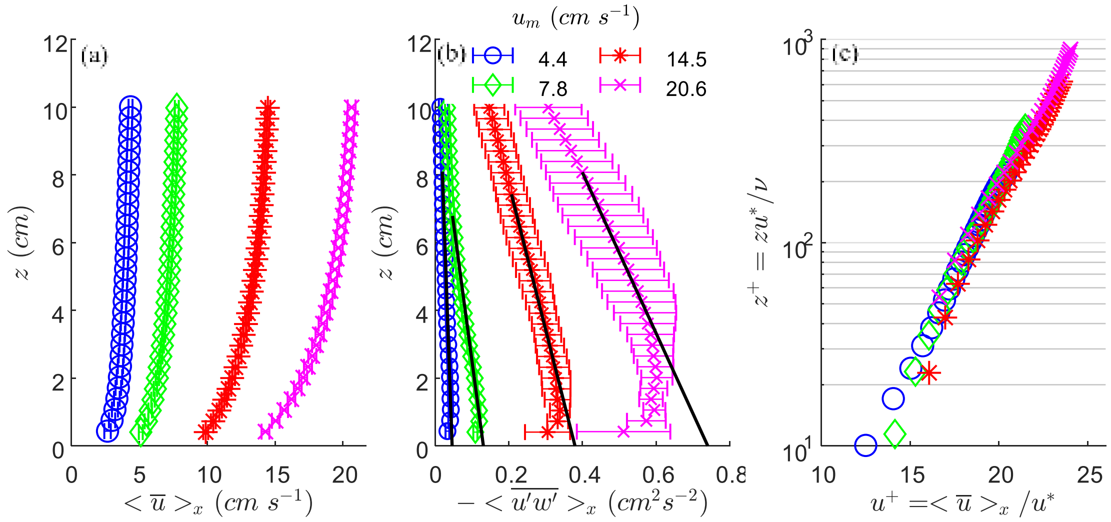

Fig. 4 The flow field: (a) Mean velocity $\langle \bar{u} \rangle_x$; (b) Reynolds stresses, $\langle u'w' \rangle_x$, and interpolation lines showing the choice of u^*; (c) Normalized velocity versus normalized height, $u^+ = u^+(z^+)$.

As a preparation for the resuspension experiments, particle size distributions of the four groups of particles were measured by laser diffraction (Mastersizer 2000, Malvern Instruments). These distributions are compared in Fig. 5 with the distributions obtained during resuspension experiments inside the flume by the LISST 200X instrument, that was positioned 120 cm downstream from the injection point. The results, plotted for two flow rates, show an excellent agreement as well as the effect of dilution by the flow rate in the flume (Fig. 5b).

The results shown in Figs. 3, 4 and 5 represent measurements that serve as a baseline for the resuspension experiments. They provide a description of the experimental ambient conditions and point on our ability to control the flow and vary the properties of the resuspension events when using the new resuspension generator.

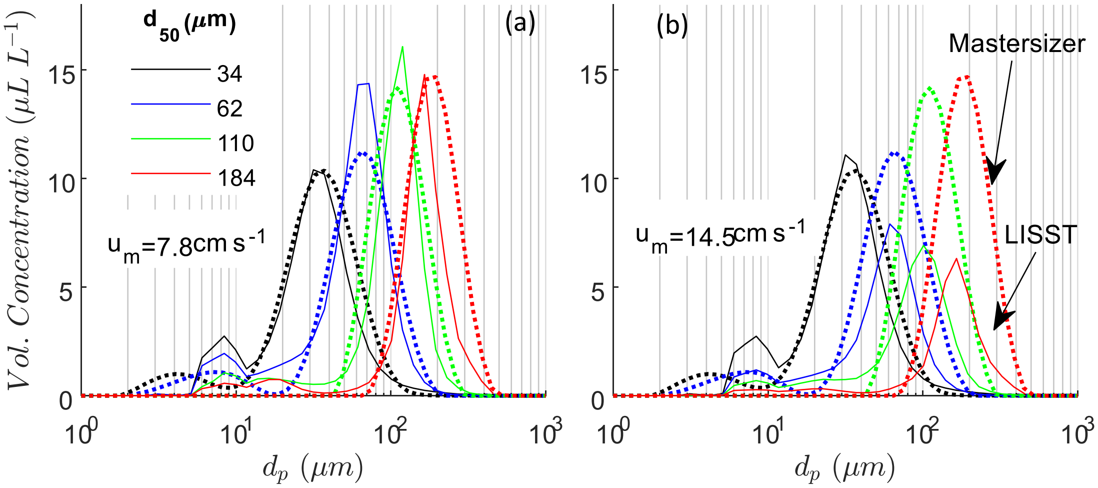

Fig. 5 Particle size distributions obtain by a Mastersizer 2000 outside the flume and by a LISST 200X during the resuspension experiments inside the flume. The results were obtained for two water velocities, (a) $u_m = 7.8$ and (b) $14.5\ cm\ s^{-1}$. Other conditions: $q_{sp} = 45\ ml\ min^{-1}$, $T = 30s$ and d_{50} = 34.2 µm.

4.2 *Concentration measurements*

Concentration profiles measured by the PIV imaging system are shown in Fig. 6. The instantaneous measurements were averaged in time and along x and are shown as a function of height. The results demonstrate the ability of the generator to change the concentration field in a controlled manner. Fig. 6a shows that as long as q_{sp} is low, the concentration profiles follow the expected exponential curve, however, as q_{sp} increases, the injected particles result in higher concentration at increasing heights.

The results of Fig. 6a were obtained for the smallest particle size and the distance between the resuspension generator and the center of the PIV images ($55\ cm$) was too short for these particles to sink. However, when increasing the particle size from $34\ \mu m$ (Fig. 6a) to $110\ \mu m$ (Fig. 6b), the particles sank

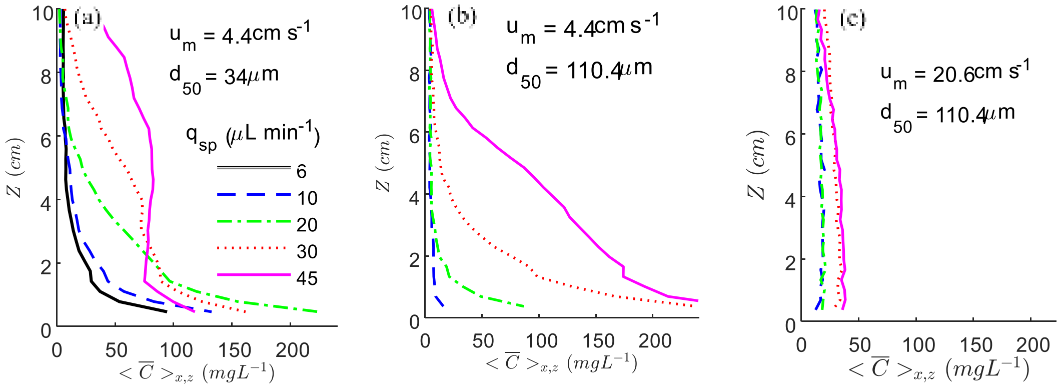

Fig. 6 The influence of injection discharge, ambient velocity and particle size on concentration profiles obtained during the $T = 30s$ experiments. The profiles represent a spatial averaging along the flow direction, x, and a temporal averaging during 20 seconds.

faster and the concentration profiles had changed accordingly, showing zero and almost zero concentration for the two smaller particles and a modification in the shape of the profiles in the others. Increasing the ambient velocity dilute the plumes and mix them with the flume water due to high turbulence. As shown in Fig. 6c, despite the much shorter time of particle arrival, the concentration is small and the vertical profiles are nearly uniform.

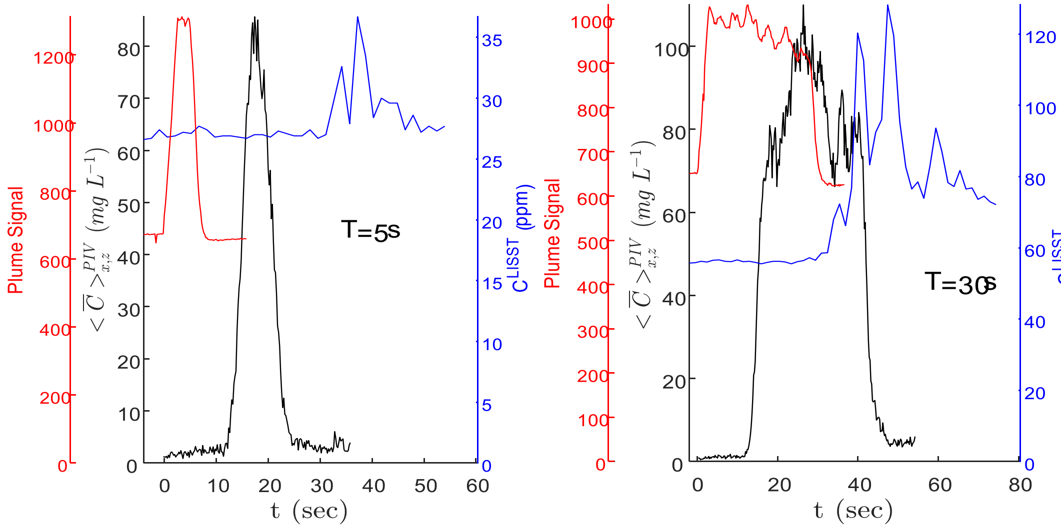

Fig. 7 Time history of the plume signal for $T = 5\ s$ (a) and $T = 30s$ (b). Three signals are shown: Red - for the plume signal at its generation location ($x = 0$); Black – for the concentration measured by the PIV system at $x = 55\ cm$; Green – for the concentration measured by the LISST at $x = 120\ cm$. Other conditions are: $q_{sp} = 45\ ml\ min^{-1}$, u_m = 4.4 cm s^{-1} and d$_{50}$ = 34.2 µm.

In addition to an analysis in space, the PIV imaging system can be used to describe the time dependent signal. Fig. 7 shows the temporal evolution of the plumes at the resuspension point ($x = 0$), the space average concentrion measured by the PIV system at $x = 55\ cm$ and the concentration measured by the

LISST at $x = 120\ cm$. The plume evolution was obtained by computing the average grayscale values taken by the monitoring camera that was positioned near the resuspension generator. The trace of plume generation is highly apparent at $x = 55\ cm$ but more fluctuating at $x = 120\ cm$.

Finally, an interesting observation is the velocity time evolution, before, during and after the plume is passing through the PIV laser light sheet. Fig. 8 shows simultaneous measurements of concentration (black) and the vertical component of the velocity (green). Superimposed on these two curves is an example of the vertical velocity, measured when no particles were released by the resuspension generator (blue). The sudden drop of the velocity vertical component is apparent only when the heavy particles are passing by.

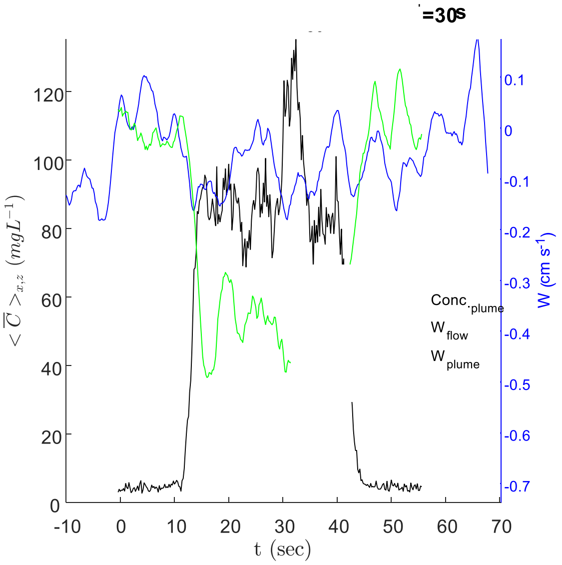

Fig. 8 Concentration (black) and velocity vertical component w (green and blue) as a function of time. The green curve was measured when a plume of heavy particles ($d_{50} = 184\ \mu m$) crossed the measurement location. The blue curve also shows a time history of w, however, it was measured at a different time when no particles were released by the resuspension generator. $T = 30s$, $q_{sp} = 45\ ml\ min^{-1}$ and $u_m =$ 4.4 cm s^{-1}.

Acknowledgment: We wish to acknowledge the generous financial support received from the Israeli Ministry of Science, Technology and Space (Grant 3-12478).

References

Gilboa M, Katz T, Shavit U, Grosbard S, Torfstien A and Yahel G (2018) Novel approach to measure the rate of sediment resuspension at the ocean and to estimate the contribution of fish activity to this process. PiE2018, Lisbon, October 2018.

Shavit U, Halamish A, Grossbard S, Asher S, Gilboa M, Katz T and Yahel G (2018) Testing a biological resuspension footprint model using Lagrangian simulations. PiE2018, Lisbon, October 2018

Vainiger A, Schechner YY, Treibitz T, Avni A and Timor DS (2018) Underwater wide-field tomography of sediment resuspension. PiE2018, Lisbon, October 2018.

Yahel R, Yahel G, Genin A (2002) Daily cycles of suspended sand at coral reefs: A biological control. Limnol Oceanogr 47:1071–1083

Yahel G, Yahel R, Katz T, Lazar B, Herut B, Tunnicliffe V (2008) Fish activity: a major mechanism for sediment resuspension and organic matter remineralization in coastal marine sediments. Mar Ecol Prog Ser 372:195–209

Yahel G, Gilboa M, Grossbard S, Vainiger A, Treibitz T, Schechner Y, Shavit U and Katz T (2018) Biological activity: an overlooked, mechanism for sediment resuspension, transport, and modification in the ocean. PiE2018, Lisbon, October 2018.

Suspended sediment transport in a submarine canyon: What are we looking at?

S. Haalboom[1], H.C. de Stigter[1], G.C.A. Duineveld[1], G.-J. Reichart[1,2], F. Mienis[1]

[1]Royal Netherlands Institute for Sea Research (NIOZ), department of Ocean Systems and Utrecht University, Landsdiep 4, 1797 SZ ‘t Horntje, The Netherlands

[2]Utrecht University, Faculty of Geosciences, 3584 CD Utrecht, The Netherlands

Abstract

Optical and acoustic backscatter sensors are commonly used for detection and quantification of biotic and abiotic particulate matter in terrestrial and marine aquatic environments. For example they are used to characterise nepheloid layers, which may act as important pathways for transport of (organic) matter. Optical and acoustic backscatter sensors record the intensity of light or sound reflected from, refracted by or passing through a suspension of particles. The detected signal not only depends on the concentration of particles, but on many other parameters including the grain size distribution and composition, making a quantitative interpretation of signals cumbersome, as this requires multi-variate calibrations. To investigate the differences between measurements made by optical and acoustic sensors, we have simultaneously deployed various types of commonly used sensors in the Whittard Canyon (Bay of Biscay, NE Atlantic Ocean) during RV Pelagia cruise 64PE421 in May 2017. Data are subsequently compared to quantitative results on measured concentrations and size distributions of suspended particulate matter (SPM) from water samples, which were collected in parallel with the sensor deployments. Results showed significant differences between the records of the optical backscatter sensors and the acoustic backscatter sensors in their responses to changing SPM concentrations. Such differences have important implications on the estimation of the mass fluxes of SPM, which are vital for understanding particle transport processes in the bottom boundary layer, among others in submarine canyons. Future intercalibration of these sensors is needed for more robust mass fluxes if the effects of the physical properties on the measurements can are quantified.

Introduction

Optical and acoustic backscatter sensors are used for detection and quantification of suspended particulate matter (SPM) in terrestrial and marine aquatic environments. These field-deployable sensors are used in scientific, engineering and environmental-monitoring applications, contributing to our understanding of for instance sediment transport processes. This includes measurements of turbidity, which are needed to quantify sediment fluxes at continental margins (Guillen et al., 2000), in submarine canyons (Puig et al., 2014, Wilson et al., 2015), contaminant transport (Latimer et al., 1999) and anthropogenic disturbances e.g. deep-sea mining (van den Eynde et al., 2014, Glover and Smith, 2003) .

Optical and acoustic backscatter sensors are based on the recording the intensity of light or sound reflected from, refracted by or passing through a suspension of particles in water (or other medium). The detected signal is not only dependent on concentrations of particles, but also on particle size and flocculation (Bunt et al., 1999, Hatcher et al., 2001, Fetweiss et al., 2007, Slade et al., 2011, Voichick and Topping, 2010, Baker and Lavelle, 1984, Perkey et al., 2010), shape and surface roughness (Gibbs, 1978, Bunt et al., 1999, Schaafsma and Hay, 1997), composition (Maa et al., 1992, Moate and Thorne, 2012), colour of the material (Hatcher et al., 2000), bubbles (Bunt et al., 1999, Puleo et al., 2006, Meral, 2008), and chemical and biological fouling (Bunt et al., 1999), which makes quantitative analysis of natural particle suspensions often cumbersome (Downing, 2006).

In this study records of optical and acoustic backscatter were analysed, obtained by different types of commonly used sensors (JFE Advantech Infinity and WETLabs ECO FLNTU optical backscatter sensors, WETLabs C-Star transmissometer and RDI Workhorse ADCP acoustic backscatter), which were deployed simultaneously in the Whittard Canyon (northern Bay of Biscay, NE Atlantic Ocean). The sensor data are compared to quantitative results on concentrations and size distributions of SPM in water samples collected in parallel with the sensor deployments. The Whittard Canyon was visited in May 2017 during RV Pelagia cruise 64PE421 as part of the larger BYPASS? project. This project aims to identify whether submarine canyons form pathways or sinks for organic carbon. It is hypothesized that most of the organic matter is transported through the canyon via nepheloid layers. To understand the effect of the physical properties on the different type of measurements it is vital to quantify the amount and type of material that is transported. Submarine canyons like the Whittard Canyon are very suited for such sensor inter-comparisons because of the ubiquitous presence of nepheloid layers over a wide range of concentrations (Gardner, 1989, Durrieu de Madron, 1994, Puig et al., 2014, Wilson et al., 2015). The presence of biologically productive surface water during spring overlying the northern Bay of Biscay margin, allows comparison of sensor output for surface water containing primarily live plankton and bottom water containing primarily abiotic sediment. The differences of simultaneous observations with different sensors and their implications on the estimates of suspended particulate matter concentrations will be discussed.

Setting

The Whittard Canyon (Fig.1) is a dendritic submarine canyon complex, incising the Celtic continental margin (Amaro et al., 2016). The four main, NNW-SSE to NNE-SSW oriented branches of the canyons' system extend from the continental shelf at approximately 200 m water depth to the abyss at depths exceeding 3500 m, where the branches converge into the so-called Whittard Channel (Wilson et al., 2015) .

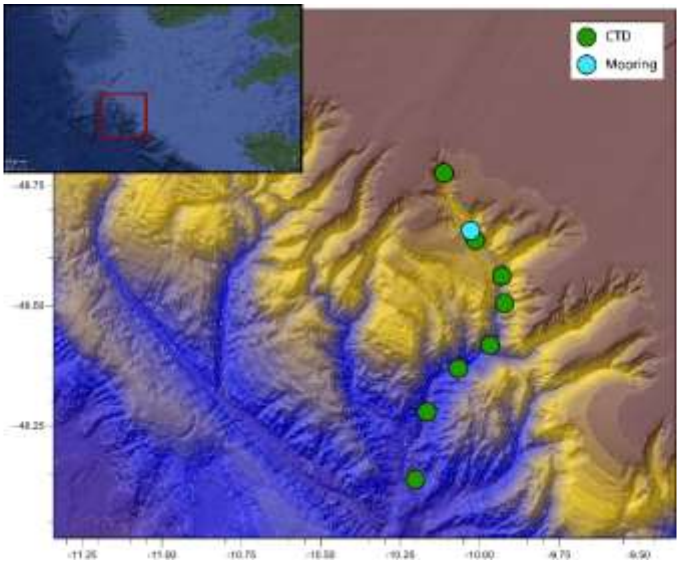

Figure 6: Location of the Whittard Canyon and sampling locations

Methods

Hydrographic observations were carried out using a SBE CTD system with a Rosette frame with 24 11L Niskin bottles. Turbidity was measured using a WETLabs ECO FLNTU and JFE Advantech Infinity ATUD-USB optical backscatter sensor (OBS) operating at 700 and 880 nm, respectively. Beam transmission was measured using a 25 cm pathlength WETLabs C-Star transmissometer operating at 650 nm.

From the Niskin bottles 5L of water were filtered over 47 mm 0.4 um polycarbonate filters, which were weighed before and after sampling to determine the SPM concentration in order to calibrate the sensors.

A mooring of 320 m was deployed for 9 days at ~1400 m water depth equipped with a downward-looking RDI Workhorse Long Ranger ADCP operating at 75 kHz, with vertical intervals binned over 5 m. At 5 and 310 m above the seabed JFE Advantech OBS's were mounted on the mooring wire. The sampling frequency was set to one minute for all sensors.

Quantification of measured turbidity

Turbidity values were converted to absolute SPM concentrations, using the relation between the measured turbidity and the measured SPM concentrations (weight in mg/L). Both the OBS and the transmissometer showed a linear relationship between the measured turbidity and SPM concentration (Fig. 2). Two regression lines were made, one for surface- and one for deep water, since suspended

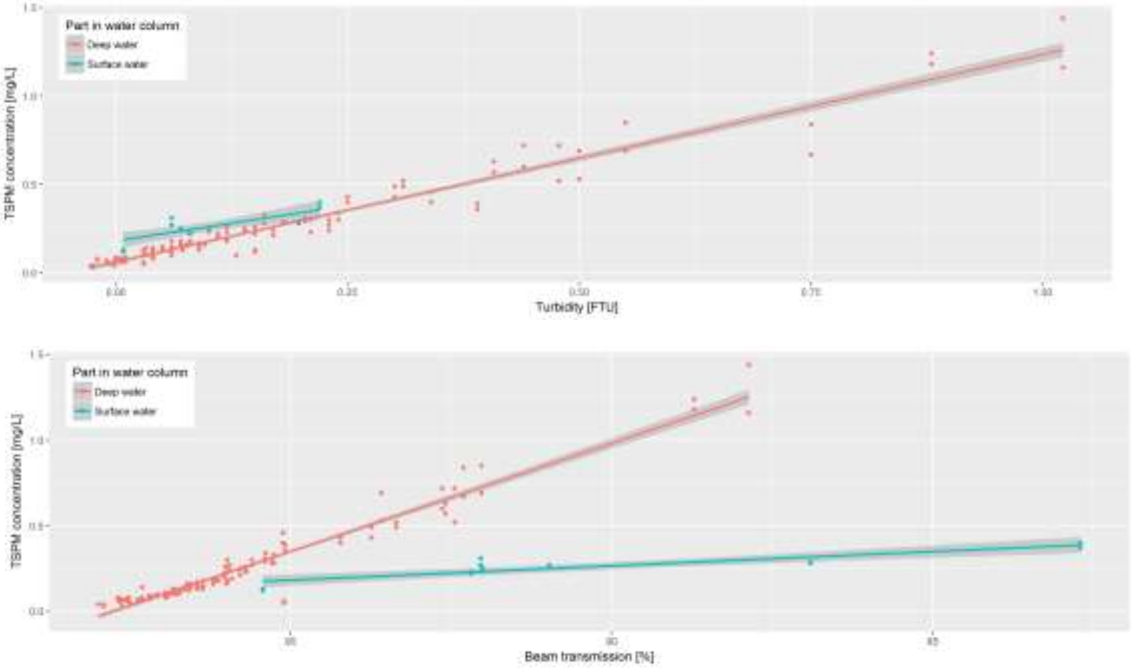

Figure 7: Relation between turbidity and SPM concentrations. A) JFE Advantech OBS; B) C-Star transmissometer

The stronger response of beam transmission in surface waters may be attributed to stronger absorption of light with a wavelength of 650 nm by chlorophyll-bearing phytoplankton which is abundantly present in the surface waters during spring. The near-bottom samples were characterised by a mixture of predominantly biogenic carbonate and silica particles and lithogenic material as observed by SEM images of the filtered particles (Fig. 3). The lower response of OBS in surface water is attributed to the coarser average particle size and absorption of light by phytoplankton.

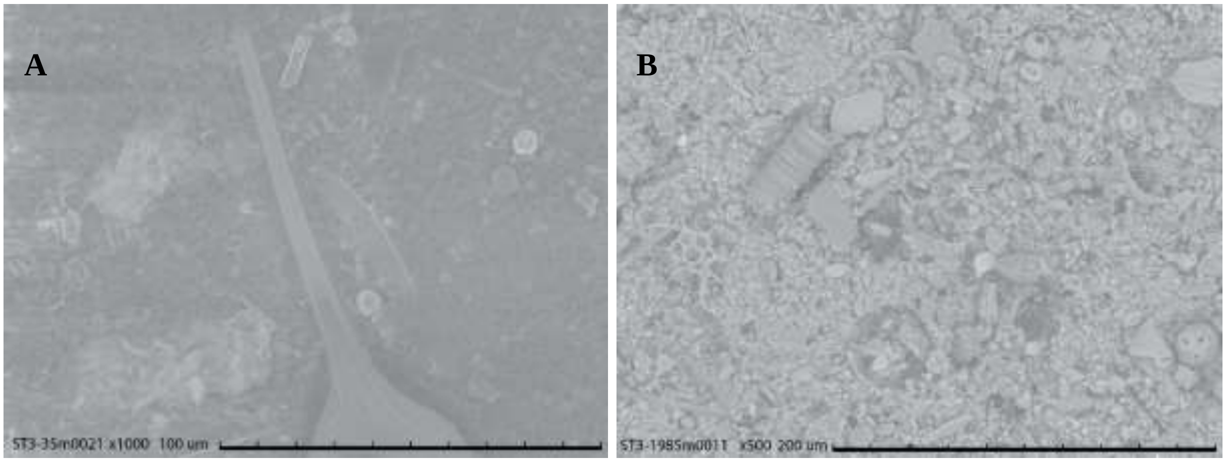

Figure 8: SEM images of filtered particles. A) Surface sample; B) Near-bottom sample

Near-bottom sediment dynamics

During the 9-day deployment of the mooring a clear tidal signal was found throughout the water column, though more prominent closer to the seabed, where the main flow direction was 335-155° (upstream-downstream along the canyon axis). An increase in turbidity was observed during flow reversal. During the upstream and downstream flow generally two peaks in maximum current speed were found. The ADCP mainly responded to the initial current speed increase (upstream flow), whereas the OBS mainly responded to the second current speed increase (downstream flow).

Differences between the records of the ADCP and the OBS can be explained by different resuspension processes dependent on current speed and direction. The long range ADCP is more sensitive for larger particles, which are brought into suspension during the higher current speed of the upstream flow. During the downstream flow, when the current speed is lower, the coarser particles start to settle while the finer grained particles stay in suspension, resulting in a stronger response of the OBS.

Outlook

It has been shown that the records of optical and acoustic backscatter differ. First results implicate that this can be related to the differences in sensor response on type of material (biotic or abiotic) and the grain size of the SPM. To quantify which further can be analysed chemically (e.g. organic matter flux through a canyon system like the Whittard Canyon), use of multiple types of sensors is favourable since it would result in more reliable estimates of mass fluxes.

Acknowledgements

Fieldwork was carried out during RV Pelagia cruise 64PE421, for which ship time was provided by Royal NIOZ. Sabine Haalboom and Henko de Stigter received funding from the Blue Nodules project, EU H2020, EC grant agreement no. 688785. Furu Mienis received funding from the Bypass project, NWO-VIDI grant 016.161.366.

References:

Amaro, T., Huvenne, V.A.I., Allcock, A.L., Aslam, T., Davies, J.S., Danovaro, R., De Stigter, H.C., Duineveld, G.C.A., Gambi, C., Gooday, A.J., Gunton, L.M., Hall, R., Howell, K.L., Ingels, J., Kiriakoulakis, K., Kershaw, C.E., Lavaleye, M.S.S., Robert, K., Stewart, H., Van Rooij, D., White, M. and Wilson, A.M., 2016. The Whittard Canyon - A case study of submarine canyon processes. Progress in Oceanography, 146: 38-57.

Baker, E.T. and Lavelle, J.W., 1984. The effect of particle size on the light attenuation coefficient of natural suspensions. Journal of Geophysical Research, 89(C5).

Bunt, J.A.C., Larcombe, P. and Jago, C.F., 1999. Quantifying the response of optical backscatter devices and transmissometers to variations in suspended particulate matter. Continental Shelf Research, 19(9): 1199-1220.

Downing, J., 2006. Twenty-five years with OBS sensors: The good, the bad, and the ugly. Continental Shelf Research, 26(17-18): 2299-2318.

Gibbs, R.J., 1978. Light-Scattering from Particles of Different Shapes. Journal of Geophysical Research-Oceans and Atmospheres, 83(Nc1): 501-502.

Guillen, J., Palanques, A., Puig, P., De Madron, X.D. and Nyffeler, F., 2000. Field calibration of optical sensors for measuring suspended sediment concentration in the western Mediterranean. Scientia Marina, 64(4): 427-435.

Hatcher, A., Hill, P. and Grant, J., 2001. Optical backscatter of marine flocs. Journal of Sea Research, 46(1): 1-12.

Hatcher, A., Hill, P., Grant, J. and Macpherson, P., 2000. Spectral optical backscatter of sand in suspension: effects of particle size, composition and colour. Marine Geology, 168(1-4): 115-128.

Latimer, J.S., Davis, W.R. and Keith, D.J., 1999. Mobilization of PAHs and PCBs from in-place contaminated marine sediments. Estuarine Coastal and Shelf Science, 49: 577–595.

Maa, J.P.Y., Xu, J.P. and Victor, M., 1992. Notes on the Performance of an Optical Backscatter Sensor for Cohesive Sediments. Marine Geology, 104(1-4): 215-218.

Meral, R., 2008. Laboratory Evaluation of Acoustic Backscatter and LISST Methods for Measurements of Suspended Sediments. Sensors (Basel), 8(2): 979-993.

Moate, B.D. and Thorne, P.D., 2012. Interpreting acoustic backscatter from suspended sediments of different and mixed mineralogical composition. Continental Shelf Research, 46: 67-82.

Perkey, D., Pratt, T. and Ganesh, N., 2010. Comparison of SSC measurements with acoustic backscatter data: West Bay sediment diversion, Mississippi river, 2nd Joint Federal Interagency Conference, Las Vegas.

Puig, P., Palanques, A. and Martin, J., 2014. Contemporary sediment-transport processes in submarine canyons. Ann Rev Mar Sci, 6: 53-77.

Puleo, J.A., Johnson, R.V., Butt, T., Kooney, T.N. and Holland, K.T., 2006. The effect of air bubbles on optical backscatter sensors. Marine Geology, 230(1-2): 87-97.

Schaafsma, A.S. and Hay, A.E., 1997. Attenuation in suspensions of irregularly shaped sediment particles: A two-parameter equivalent spherical scatterer model. The Journal of the Acoustical Society of America, 102(3): 1485-1502.

Wilson, A.M., Raine, R., Mohn, C. and White, M., 2015. Nepheloid layer distribution in the Whittard Canyon, NE Atlantic Margin. Marine Geology, 367: 130-142.

Particle Size Dependence of Heavy Metal Concentrations in the Lower Meramec River, Missouri, USA, Originating From Legacy Lead Mining

Daniel M. Hanes

Saint Louis University (dhanes@slu.edu)

Lead (Pb) mining began in the mid-18th century within the “Old Lead Belt” of southern

Missouri, USA. This region was the largest producer of lead worldwide from approximately 1869 to 1972. Both unused ore and waste products were discharged directly into the Big River watershed. Particles containing heavy metals varied significantly in size, corresponding to the geologic equivalent sizes ranging from clay to cobble. Flood events have transported and mixed these materials through the watershed and over 100 km downstream into the lower Meramec River, a tributary of the Mississippi River which flows near the city of St. Louis, MO.

Elevated Pb levels (> 100 ppm) are documented for fine-sediment drape deposits near the banks of the lower Meramec River after recent overbank deposition following storm events. The concentration of Pb is examined as a function of the particle size using wet-sieving, laser diffraction, and X-ray fluorescence. Discussion regarding both techniques and results will be presented.

Experimental study of critical angle peak shift in bubble volume scattering function for different sizes

V G Hariharasudhan, Bhogeswara Rao A, Palanisamy Shunmugam*

Ocean optics and imaging laboratory, Department of Ocean Engineering,

Indian Institute of Technology Madras, Chennai-600036, India

*Corresponding author:

Email: pshanmugam@iitm.ac.in; hariinstru88@gmail.com; Phone: 91-44-22574818

Abstract:

The volume scattering function (VSF) of the bubble population was measured for a given water column under laboratory conditions. The critical angle peak of phase function (obtained from the VSF) enables bubble population distinct from that of a particulate matter. In case of realistic bubble size ranges (usually from 1 to 300 µm in ocean waters), the critical angle peak was observed around 80º and could possibly shift to near-forward angles for increasing bubble size. This study along with hydrodynamic concepts provides a good understanding in estimating bubble backscattering coefficient. Using an extensive simulation data, it was observed that oceanic bubble clouds would have a significant influence on the remote sensing reflectance in near-surface waters and could potentially introduce biases in the derived ocean colour products. It is important that the present study will have direct implications for the radiative transfer calculations, ecosystem modelling, and remote sensing studies.

Keywords: Oceanic bubbles, Optical modelling, Phase function, Backscattering, Remote sensing

Introduction

The oceanic bubble population plays a significant role in the air-sea interface optical processes. The breaking of waves produces bubble clouds in the sea surface layer. The size and concentration of bubbles and their depth of penetration depend on the surface wind intensity, wave breaking conditions, density, and contents of the seawater. The bubbles in the near surface waters are generated due to the breaking of waves. Breaking waves and formation of bubble clouds have a significant impact on light penetration in the water column. The scattering of light in the near-surface ocean layer is predominantly influenced by the bubble clouds. The scattering of bubbles can be estimated as a function of the refractive index and bubble size distribution. The refractive index of bubbles is generally less than that of seawater, but their size distribution has a much wide range. This makes bubbles an efficient scattering component especially in the backward angles (backscattering). The present study aims to estimate the scattering effect of bubble population experimentally by measuring the bubble volume scattering function and hence the backscattering coefficient.

Experimental and field results

The physical condition of the water column in which the experiment was conducted as described in Table. 1. The bubble volume scattering function was measured using a LISST VSF sensor (Slade et al., 2013) for bubble radius ranging from 100 µm to 700 µm and the experimental setup is shown in Fig. 1a. Bubble volume scattering function was different from that of the particle volume scattering function with a peak at the critical angle. Figure 1b shows the bubble volume scattering function for bubbles in sizes ranging from 100 μm to 300 μm. For bubble radius ranging from 100 μm to 300 μm, the critical angle peak is around 80°. In this study, bubble radius of 300 μm was considered to distinguish between larger and smaller bubbles because in open ocean water the bubble size ranges between 0.5 to 300 μm (Reynolds et al., 2010). In case of bubble radius (300 μm to 700 μm), the critical angle peak shifts to forward angles between 40°~ 60° as shown in Fig. 1c. The volume scattering function of two bubbles of different size measured simultaneously is shown in Fig. 1d. It is evident that the critical angle peak extends from 25°~ 75°.

Based on observation from these results that, the phenomenon of diffraction and refraction describes forward scattering (Sutherland et al. 2000) and critical angle peak (Lee et al., 2002) respectively. Also, the critical angle peak is not constant and shifts toward a near or far forward angle depending on the size of the bubble. This is further confirmed by field measurement. For simultaneous measurement of underwater optical parameters, photometric (volume scattering function (LISST- VSF) along with backscattering, particulate backscattering) and radiometric instruments were assembled as shown in Fig. 2a. The bubble volume scattering function along the water column depth for two stations were shown in Fig. 2 (b & c). In this study, the bubble volume scattering function from surface to a depth of 50m is presented. The mean radius of the bubble population is larger in surface when compared at a particular depth. It is observed in this result as the critical angle peak shifts from near to far forward angle. Also the antiquated bubble population beyond 40 m is visible in this result.

In conclusion, the bubble feature in the intermediate angle is prominent and is bubble size dependent. This study is important in analysing and developing models for the remote sensing and numerical modelling studies.

Table1. Water parameters of experimental setup

Temperature	28°C
Turbidity	0.53 *NTU*
Chlorophyll	0.34 (*μg/l*)

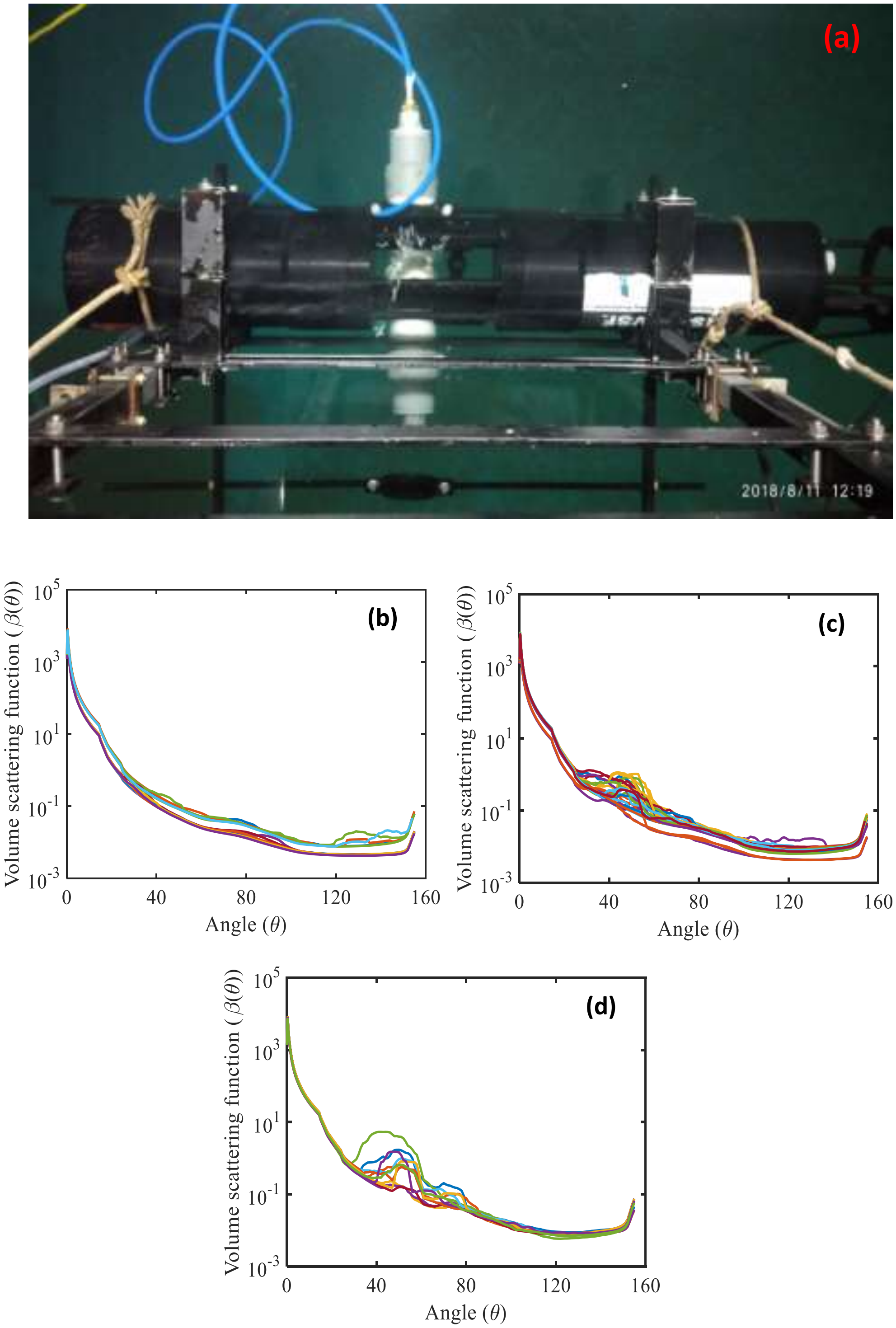

Fig. 1. (a) Experimental setup to measure bubble volume scattering function, (b) Measured volume scattering function for bubble ranging from 100 *μm* to 300 *μm*, (c) Measured volume scattering function for bubble ranging from 350 *μm* to 700 *μm*, (d) Measured volume scattering function for two different bubble size

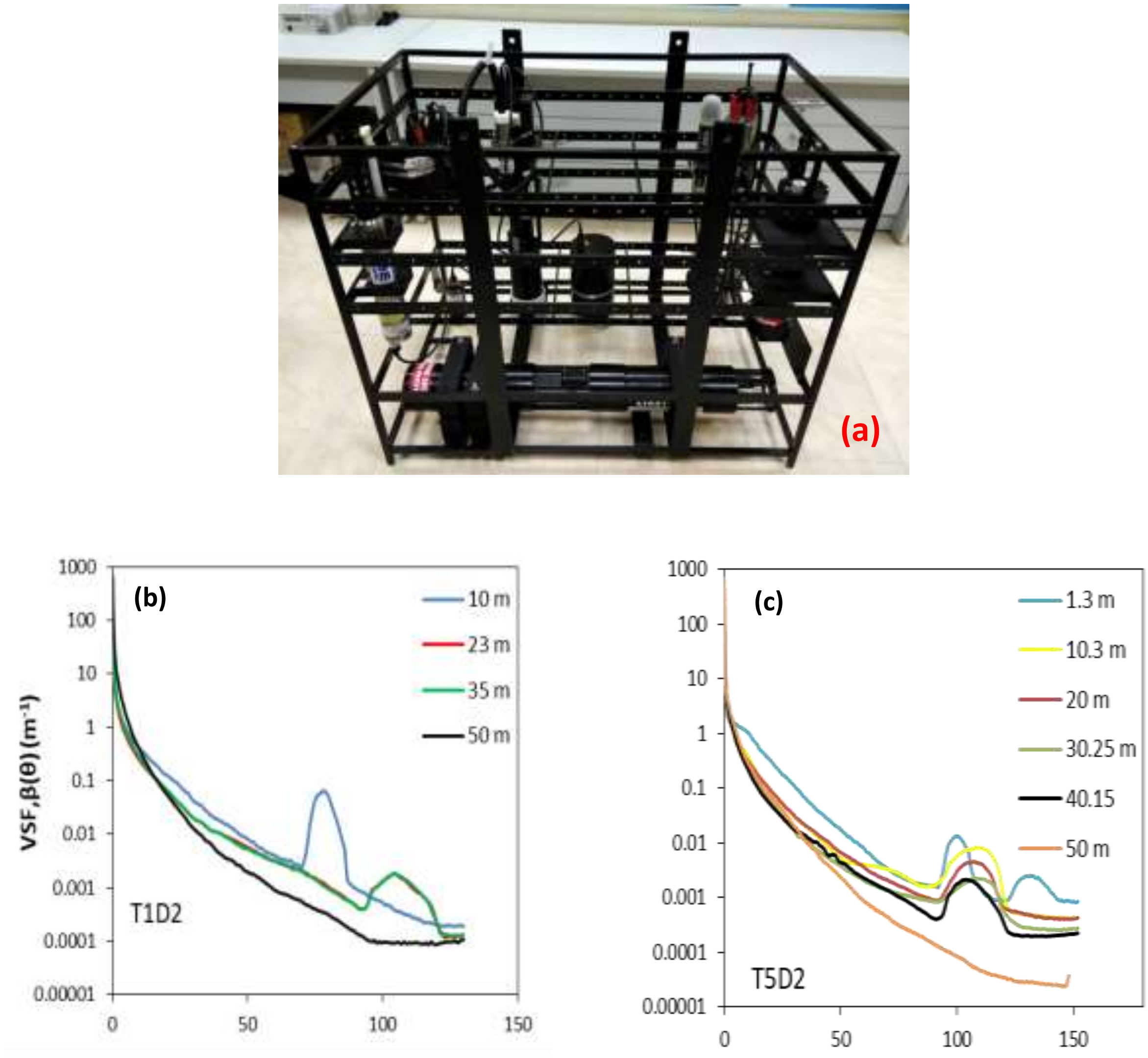

Fig. 2. (a) Field instruments to measure inherent and apparent optical property, (b) Measured bubble volume scattering function with critical angle peak shift along the depth in ocean waters, (c) [below, next page] Measured bubble volume scattering function in oceanic waters along the depth.

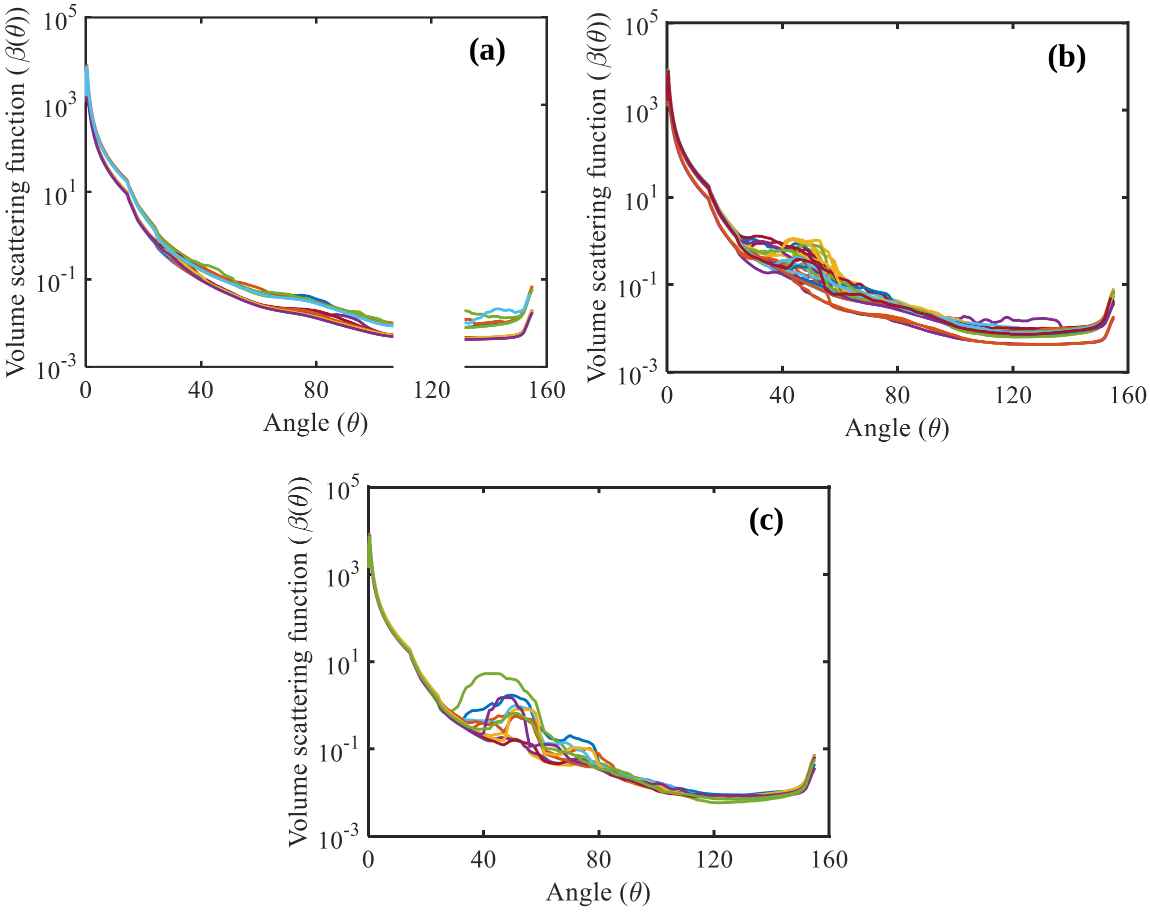

References

Slade, W. H.; Agrawal, Y. C.; Mikkelsen, O. A (**2013)**. Comparison of measured and theoretical scattering and polarization properties of narrow size range irregular sediment particles. *Oceans* **,** 23–27.

Lee M, Johnson B, Lewis XZ and M (2002) The volume scattering function of natural bubble populations. Limnol Oceanogr 47:1273–1282. doi: 10.4319/lo.2002.47.5.1273

Mulhearn P J (1981) Distribution of microbubbles in coastal waters. J Geophys Res 86:6429–6434. doi: 10.1029/JC086iC07p06429

Quirantes A, Bernard S (2004) Light scattering by marine algae: two-layer spherical and nonspherical models. J Quant Spectrosc Radiat Transf 89:311–321. doi: 10.1016/j.jqsrt.2004.05.031

Reynolds R A, Stramski D, Wright VM, Woźniak SB (2010) Measurements and characterization of particle size distributions in coastal waters. J Geophys Res 115:1–19. doi: 10.1029/2009JC005930

Sutherland, T. F.; Lane, P. M.; Amos, C. L.; Downing, J. (2000) The calibration of optical backscatter sensors for suspended sediment of varying darkness levels. *Marine Geology*, *162*, 587–597, doi:10.1016/S0025-3227(99)00080-8.

Zhang X, Lewis M, Johnson B (1998) Influence of bubbles on scattering of light in the ocean. Appl Opt 37:6525–6536. doi: 10.1364/AO.37.006.

A new Self-flushing rock trap concept for Pump-storage plants

Ola Haugen Havrevoll, Silje Kreken Almeland, and Kaspar Vereide

Department of Civil and Environmental Engineering

Norwegian University of Science and Technology

Abstract

A novel concept for self-flushing rock traps for pumped storage plants is introduced in this paper. The main idea is to utilize the reversible flow in pumped storage plants and design the rock trap to function optimally in the flow direction towards the turbine, and to flush itself in the flow direction away from the turbine. With this approach, the rock trap will never fill up, and it will never be necessary to empty the rock trap manually or spill water as necessary with traditional flushing. In this paper, the idea is presented and demonstrated with CFD simulations. In addition a general introduction of rock traps in pressurized conduits is given.

Introduction

Rock traps are necessary for hydropower plants where rocks, sand or silt potentially is transported in the power plant waterways. Rock traps are also referred to as sand traps, desilting basins, desanders and various other names. This paper concerns rock traps placed inside the pressurized tunnel as is the typical solution in Norway for several reasons.

Norwegian power plants are for a large part high head plants. Most commonly, the head- and tailrace tunnels have been constructed with minimal concrete lining and permanent support [1]. Also, the muck from the blasting has been used as foundation for a driveway during construction. The invert is in many cases left untouched, with no or only rough cleaning before commissioning. Rough cleaning of the invert, as opposed to full cleaning, smooths the invert, resulting in lower friction headloss [2]. The downside of leaving muck in the invert after start of power production is that the water will erode the sediments and transport them further downstream until it reaches the turbines, where erosion of the runner wheel and other parts ensures [3-6]. Erosion of turbines negatively influences the efficiency and lifetime of the turbines. Maintenance and replacement of turbines is costly. To prevent materials from reaching the turbines, rock traps are routinely constructed at the downstream end of the headrace tunnel, before the transition to the pressure shaft.

Hydraulic Design of rock traps

As the sediments enter the rock trap, they should separate from the flow and settle while the water flows through. In Norway, two types of rock traps have mainly been built, see Figure 1. In an open rock trap, the enlarged cross section causes lower velocity that increases the limit of the sediment size the water is able to transport. Thus, the sediments settle in piles in the middle of the trap. As the pile increases in size, the available cross section decreases, and the water may once more be accelerated. Turbulence may be introduced, and the maximum capacity of the rock trap is reached long before the chamber is actually full of sediments.

The rib type has another way of functioning. As the water enters the rock trap, it will flow past the ribs, mostly undisturbed. The sediments that are transported as bed load will fall down between the ribs and settle there. The principle is to separate the flow from the settling basins, so no turbulence will work on the already settled sediments. Thus, the basin is allowed to fill completely under the ribs. The settling basin may be separated into cells with stop logs. In this way, the flow of the water beneath the ribs is even more limited [5, 7, 8].

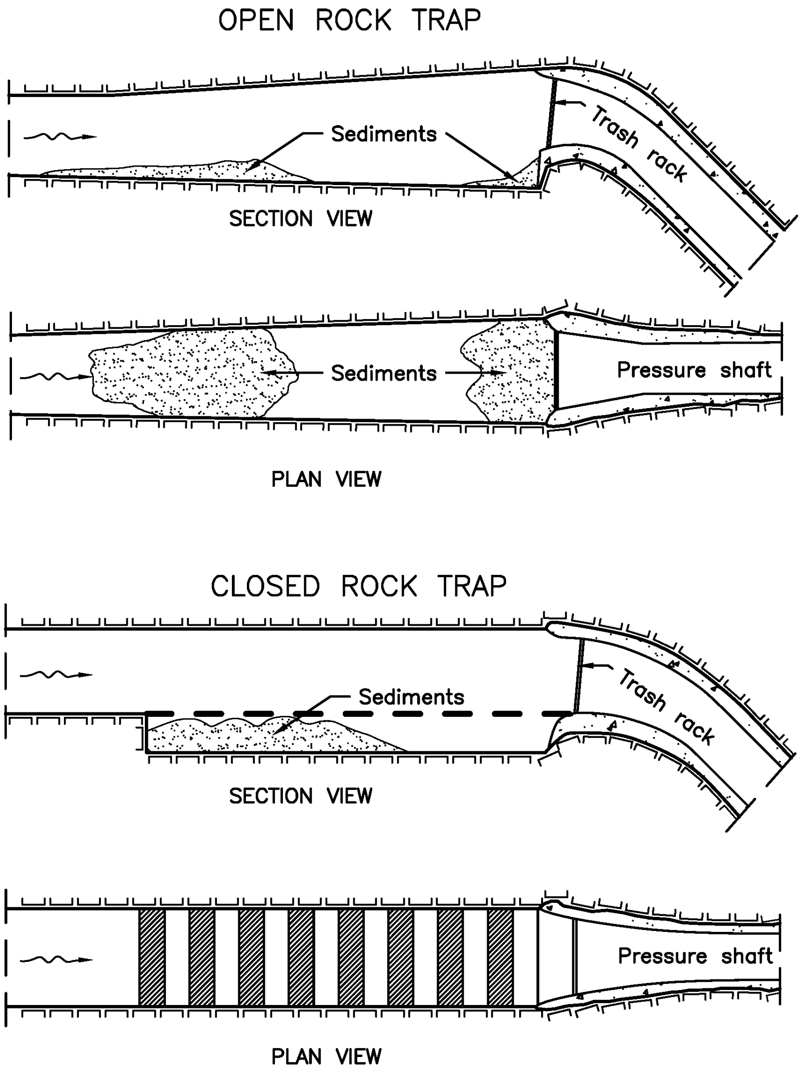

Figur 6 Norwegian rock trap types

CASE-STUDY: Duge pumped storage plant

Duge pumped storage plant was commissioned in 1973. It has two reversible Francis turbines with an installed effect of 100 MW each. The discharge is approximately 100 m^3/s in generator mode and 80 m^3/s in pumping mode. Upstream and downstream of the plant are a large reservoirs, Svartevatn and Gravann-Valevatn, with 1400 mill. m^3 and 1100 mill. m^3 storage capacity respectively. The pumping mode is mainly used during the snow-melting season of the spring, where Duge power plant is pumping water from the lower reservoir, lake Gravatn-Valevatn up to Svartevatn. The rest of the year, Duge mainly operates in turbine mode, except for shorter periods with significant price peaks.

Duge pumped storage plant has a short headrace and a long tailrace tunnel of 12 km. Owing to the large reservoir and short headrace tunnel, no sediment problems are found from the headrace side. In the tailrace tunnel, it is possible for sediments from the invert to be transported to the turbines when the power plant is in pump mode. Also, the conditions at the outlet of the tailrace tunnel makes it possible for sediments to enter the tunnel, especially at low water levels in lake Gravatn/Valevatn. The recent years, the operator of the power plant has seen a rise in wear on the machines, something which might be caused by erosion from sediments transported from the tailrace tunnel and downstream reservoir.

During the design phase of the power plant, it was planned to construct a rock trap in the outlet tunnel. It seems, however, that this work never was carried out during the construction in 1970's, and inspections with a submerged, remotely operated vehicle (R.O.V.), has not shown any indications of a rock trap in the tunnel. The tunnel has not been drained and inspected in dry condition since commission, since the tunnel invert lies below the water level of lake Gravatn/Valevatn resulting in very costly dewatering.

Recent changes in the operation of the power plant has resulted in sediments clogging the filters of the revision valve on the main valves. This problem resulted in the need to dewater the headrace tunnel and repair the revision valve. Sand has also been found in the turbine seals and the power company expects there are some minor wear on the turbine that might reduce efficiency. To prevent further damages and costs, Sira-Kvina power company has renewed the plans to construct a rock trap in the tailrace tunnel, not far from the turbines.

Because the dewatering of the tailrace tunnel is unusually costly for this power plant, it will be difficult to empty the rock trap at regular intervals, as required in a normal rock trap. A key requirement for the rock trap is therefore that manual cleaning will be unnecessary.

One possibility is to construct a rock trap that is large enough to contain all the remaining sediments that can be transported in the tunnel, a so-called "one-time use" rock trap. It is unknown how thick the remaining sediment layer in the tailrace tunnel is. It may be around 10–20 cm. In that case, the remaining sediment volume in the tunnel totals to 10 000 –20 000 m³. A rock trap with a capacity of 10 000 m³, depth 3 m and width 8 m, will have to be over 400 m long, which is unacceptable. The rock trap has to be much shorter to be feasible for construction.

The new concept: A Self-cleaning rock trap

Since Duge is a pumped storage power plant, the water flows both ways over the year. It is only in pumping mode that the flow will be able to transport sediments to the turbines. In generator mode, the water will flow from the turbines and the rock trap to the outlet. If the water can be used to flush the rock trap and transport the sediments out of the tunnel, the rock trap will never fill completely, and the sediments will not reach the turbines. Duge pumped storage plant is mainly used in turbine mode, meaning that the net amount of water transport in towards the downstream reservoir.

A self-cleaning rock trap will have to be able to trap the rocks in pumping mode, and flush the rock trap in generator mode. Ribs will be placed along the invert will separate the flow and lead sediments into the settling chamber. In the upstream end of the rock trap, an inclined impermeable plate will be placed as illustrated in figure 2.

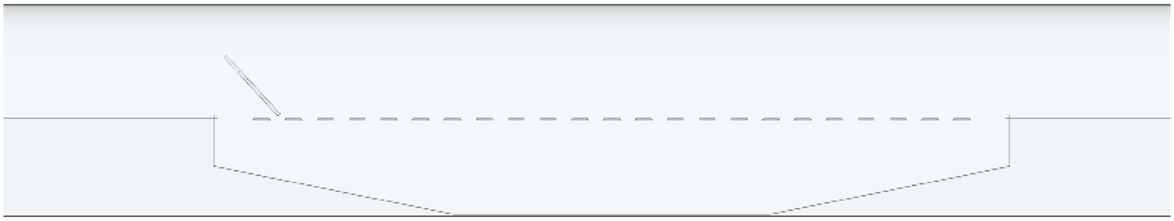

Figur 7 Self-cleaning rock trap, longitudinal section

In generator mode, the inclined plate will lead water down under the ribs, to create turbulence that flushes the sediments up and out of the rock trap. The flow will then lead the sediments further downstream.

Efficiency of Simulated rock traps

Brox[8] suggests that the turbulent kinetic energy (TKE) that is computed with CFD modelling can be used as a measure of the efficiency of rock traps. He sets up two equations for beginning of transport. These two criteria will be used here, but more research is recommended to confirm suitable criteria for efficiency of simulated rock traps.

$$\frac{TKE}{gD} > 0.05 \tag{1}$$

$$\frac{TKE}{gD} > 0.78 \tag{2}$$

Equation 1 shows the limit for beginning of bedload transport, and equation 2 shows the limit for beginning of suspended transport.

CFD simulations

The rock trap was modelled and simulated in OpenFOAM. Four different cases were simulated, with discharges increased with 10 %:

Tunnel with symmetrical rock trap without ribs or inclined plate (Q = 92.4 m^3/s).

Tunnel with symmetrical rock trap with horizontal ribs, without inclined plate (Q = 110 m^3/s).

Tunnel with rock trap with ribs and inclined plate, reverse flow (pump mode, Q = 92.4 m^3/s)

Tunnel with rock trap with ribs and inclined plate, normal flow (generator mode, Q = 110 m^3/s)

STL-files with the rock trap designs were used for the mesh generators within OpenFOAM, blockMesh and snappyHexMesh. A stationary solver was used for the simulations. The mesh was created in three dimensions and the simulations were run using the simpleFOAM solver in OpenFOAM. This is the OpenFOAM implementation of the SIMPLE routine [9], and it contains both the standard SIMPLE version and its consistent formulation, SIMPLEC. In this study, the consistent version SIMPLEC was utilized. The turbulence was modelled by RANS and the standard *k*-ε model [10]. The near-wall behaviour was computed by wall functions.

Results

The interesting point in the analysis is to quantify the differences in rock trap efficiency between different rock trap designs. The dimensions used for analysis are streamwise velocity and total kinetic energy. As the velocity and kinetic energy increase, the conditions for sediment settling is reduced, and the rock trap efficiency is reduced correspondingly. In the further discussions, the terms *upstream* and *downstream* always are used as if in turbine mode, with water flowing from the turbine to the outlet. In pumping mode, the water therefore flows through the rock trap from downstream to upstream.

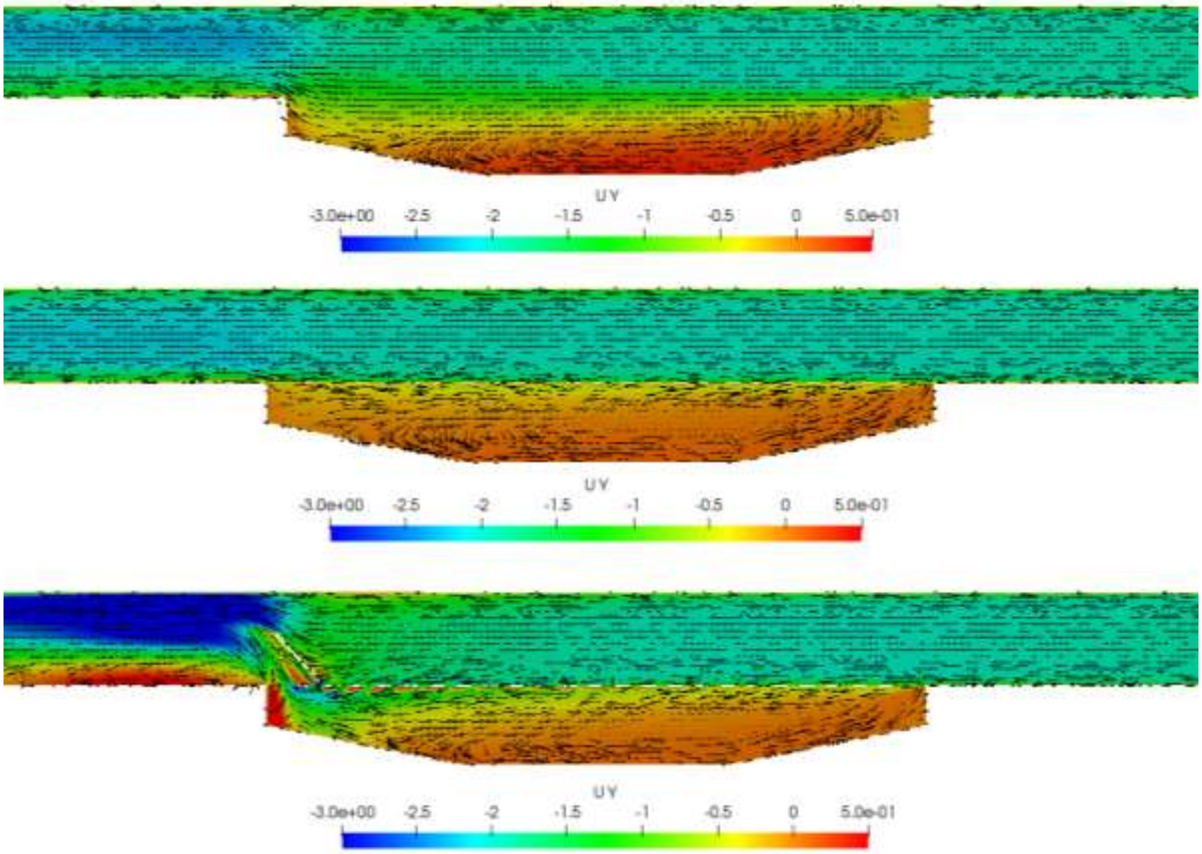

Figur 8 Streamwise velocity for case 1-3

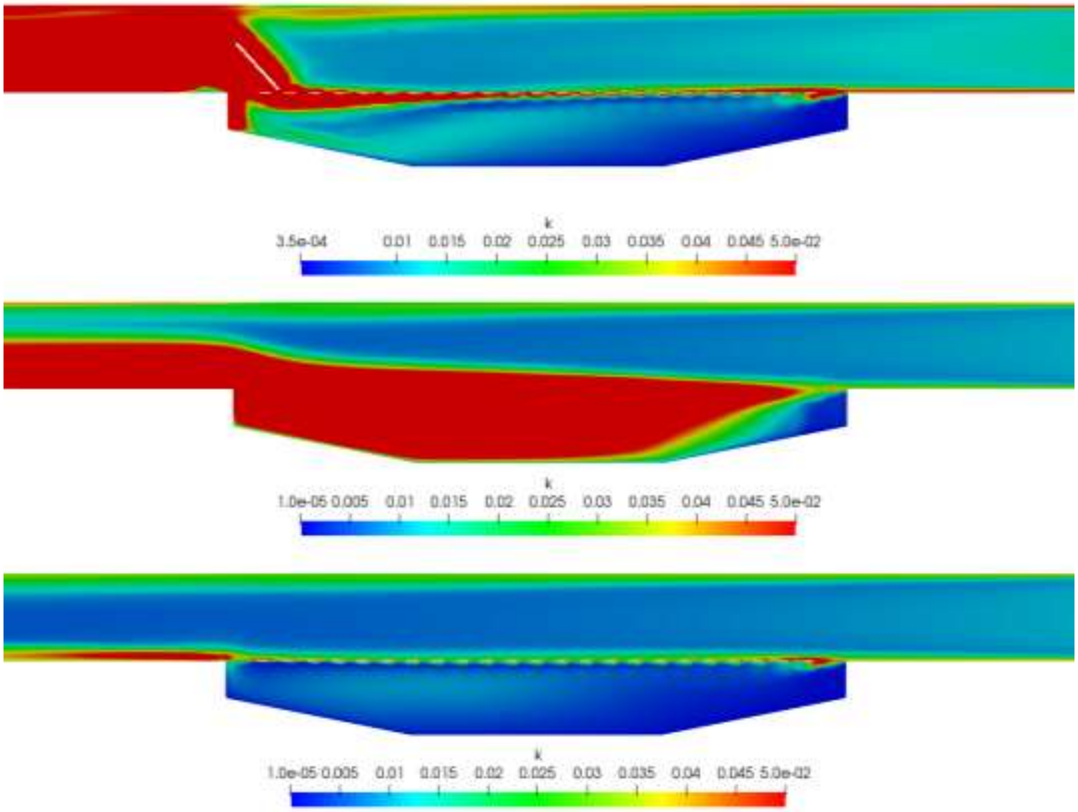

Figur 9 Kinetic energy for case 1-3

Both Figure 3 and Figure 4 show results from pump mode. Therefore, the flow is going from right to left in the figures. Figure 3 shows the streamwise velocity for the cases 1, 2 and 3. The velocity field looks similar for the open rock trap and the rock trap with ribs. The velocity is relatively steady at the upper part of the rock trap, and a recirculation zone emerges in the settling chamber. Even if the flow situation seems similar, it is evident that the flow velocity is higher for case 1 that for case 2. The kinetic energy (Figure 4), and thus the turbulence, is noticeable higher for the case with no ribs (Figure 4a) than for the case with horizontal ribs over the settling chamber. From Figure 4 it is evident that case 2 will be the preferable configuration in terms of rock trap efficiency.

Results from case 3 shows that the turbulence upstream of the inclined plate is quite high. The turbulence inflicts head loss, which should be kept at a minimum. Nevertheless, compared to case 1, case 3 is not that bad. The advantage of the configuration of case 3 is the self-cleaning feature it exhibits in production mode. The headloss of the inclined plate is 0.65 m, which is 0.3 % of the total head in Duge pumped storage plant. With an annual production of 248 GWh, this head loss is equal to 0.75 GWh per year, equivalent to 3.7 hours of power production at the plant.

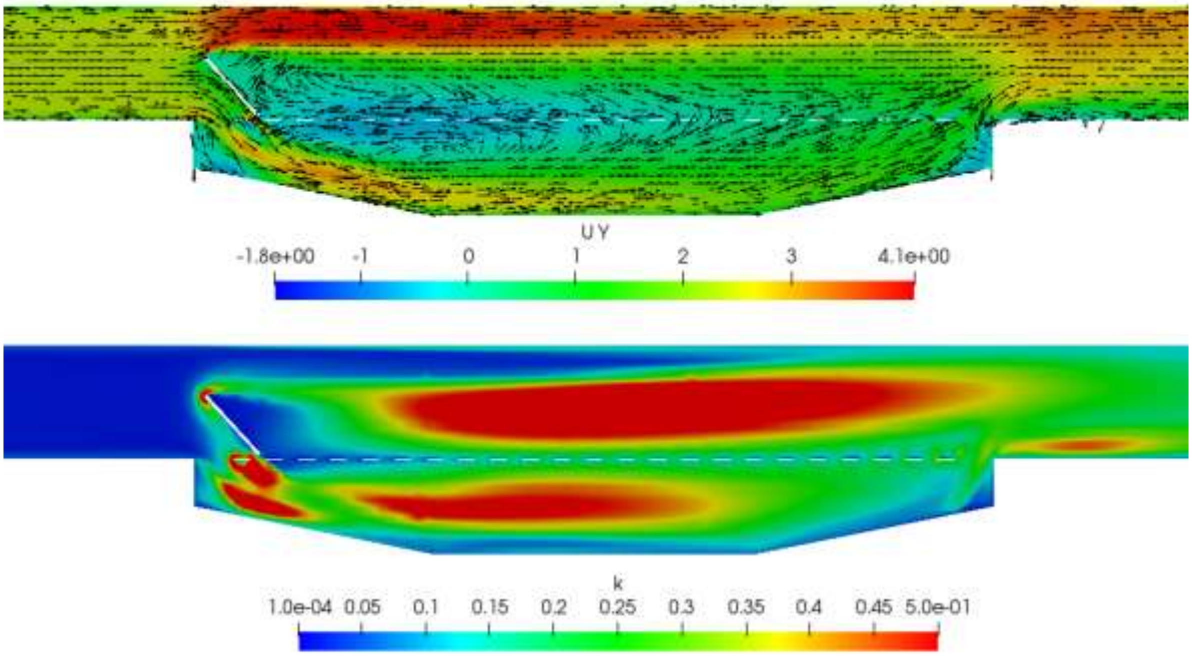

Figur 10 Velocity and kinetic energy for case 5

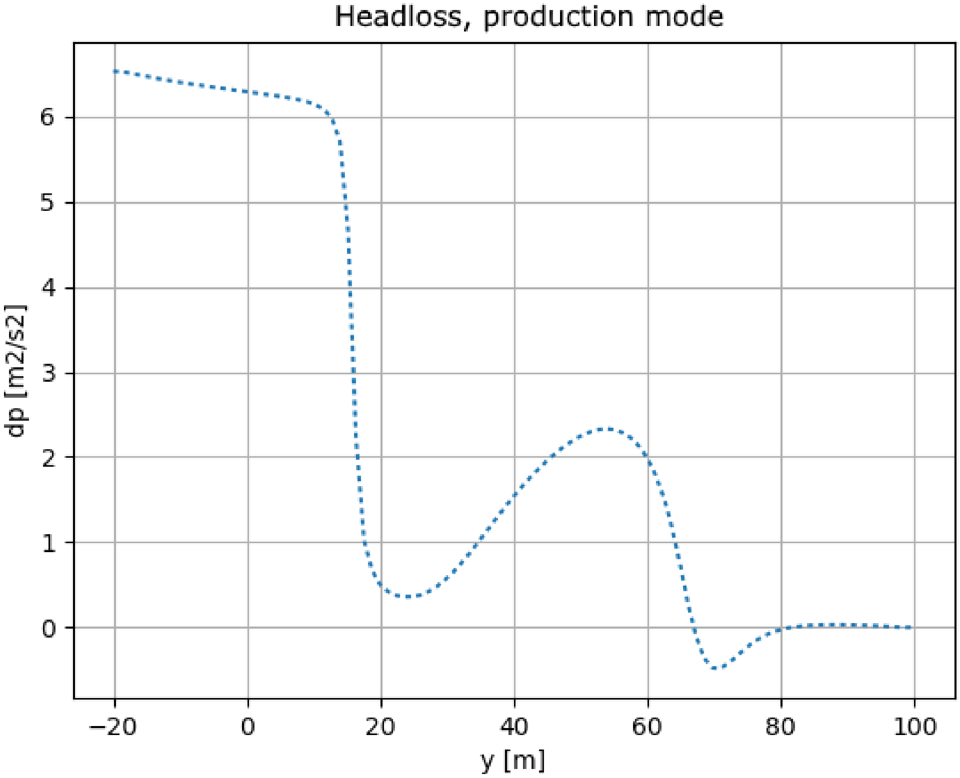

Figur 11 Headloss in production mode

Figure 5 shows the result from simulation of the rock trap with ribs and inclined plate, in production mode, i.e. with flow the opposite direction of case 3. The flow is split, and a significant part of the flow enters the settling chamber, although the major flow is sent along the roof of the tunnel. The turbulence both above and below the ribs is greatly increased, which makes it possible for the flow to move sediments and clean the rock trap as intended.

Conclusions

A new self-flushing rock trap solution has been presented and compared with traditional rock trap design typical in Norway. The main goal of the simulations is to test the self-cleaning abilities of a rock trap where an inclined plate will lead flow into the settling chamber and flush it when water is flowing one way, while functioning as a normal rock trap with flow the opposite direction. The results are promising and show that such a function indeed is obtainable. The headloss is tolerable, and amounts to a very small part of the total production. The idea needs more refining and most likely physical model studies before the construction is advisable. This work also shows that horizontal ribs greatly improves the rock trap efficiency by preventing turbulence in the settling chamber.

References

1. Broch, E. and A. Palmström, *The design of unlined hydropower tunnels and shafts: 100 years of Norwegian experience.* The International Journal on Hydropower & Dams, 2017. **24**(3): p. 72-79.

2. Rønn, P.E. and M. Skog. *Economic design of hydropower tunnels*. in *Hydropower'97: Proceedings of the 3rd International Conference on Hydropower: Trondheim/Norway/30 June-2 July, 1997*. 1997. Trondheim, Norway: A.A. Balkema.

3. Felix, D., *Experimental investigation on suspended sediment, hydro-abrasive erosion and efficiency reductions of coated Pelton turbines*, in *Versuchanstalt für Wasserbau, Hydrologie und Glaziologie*. 2017, ETH Zürich: Zürich, Switzerland.

4. Eltvik, M., *Sediment erosion in Francis turbines*, in *Institutt for energi-og prosessteknikk*. 2013, NTNU.

5. Komitéen for undersøkelse av sandslitasje på turbiner, *Sandslitasje på vannkraftturbiner - hovedrapport*, S. Pettersen, Editor. 1984.

6. Padhy, M.K. and R.P. Saini, *Study of silt erosion on performance of a Pelton turbine.* Energy, 2011. **36**(1): p. 141-147.

7. Mattimoe, J.J., E.R. Tinney, and W.W. Wolcott, *Rock trap experience in unlined tunnels.* American Society of Civil Engineers Proceedings, Journal of the Power Division, 1964. **90**(3): p. 16.

8. Brox, D., *Design and Functional Requirements for Rock Traps for Hydropower Pressure Tunnels.* International Journal on Hydropower and Dams, 2016. **23**(1).

9. Patankar, S.V. and D.B. Spalding, *A calculation procedure for heat, mass and momentum transfer in three-dimensional parabolic flows.* International Journal of Heat and Mass Transfer, 1972. **15**(10): p. 1787-1806.

10. Launder, B.E. and D.B. Spalding, *The numerical computation of turbulent flows.* Computer Methods in Applied Mechanics and Engineering, 1974. **3**(2): p. 269-289.

LISST-VSF calibration from a series of lab experiments

Lianbo Hu[1,2], Xiaodong Zhang[1], Yuancheng Xiong[1] and Yogi Agrawal[3]

[1] Department of Earth Science System & Policy, University of North Dakota, ND, 58203, USA

[2] Ocean Remote Sensing Institute, Ocean University of China, Qingdao, 266003, China

[3] Sequoia Scientific, Inc., WA, 98005, USA

1. Introduction

The volume scattering function (VSF) and the absorption coefficient are two fundamental inherent optical properties of particles. The VSF, $\beta(\theta,\lambda)$ is defined as the radiant intensity, $I(\theta,\lambda)$, scattered at a scattering angle θ per unit spectral irradiance, $E(\lambda)$ and per unit volume of water, Δv [1].

$$\beta(\theta,\lambda) = \lim_{\Delta v \to 0} \frac{I(\theta,\lambda)}{E(\lambda)\Delta v} \qquad (1)$$

While the absorption coefficients of seawater have been extensively measured in the field, thanks to the commercially available absorption-attenuation meters [2], the *in situ* VSF measurement were scarce mainly due to engineering difficulties and hence a lack of commercial instruments [3]. The pioneering work of VSF measurements started more than a half century ago [4-6]. The Petzold's measurements were widely adopted by ocean optics and ocean color communities in radiative transfer simulation and algorithm development. With the significant advance in the field of modern optical technology, a few prototype VSF instruments were built measuring VSF over a broad angular range [3, 7-10]. However, these custom-built prototype instruments are generally inaccessible for wider research communities for routine observations.

LISST-VSF built by Sequoia Scientific Inc. is the first commercial instrument capable of measuring a wide angular range of the VSF (i.e., P11) from 0.08 to 150 degree as well as the P12 and P22 scattering elements in the Muller matrix [11]. A LISST-VSF consists of two components, a laser diffraction unit (LISST) and an eyeball optics. The LISST measures VSF at small angles (<15°) using ring detectors and are absolutely calibrated [12]. The eyeball component measures VSF at large angles (>15°) with two photomultiplier tubes (PMT) but are not calibrated. The relative calibration is performed in data processing by scaling eyeball measured-VSF at 15° to the LISST ring detector measured-VSF at the same angle. This relative calibration works in most cases but will fail in relatively clear waters due to weak forward scattering by small particles. Also, this requires a background, representing pure water or pure seawater, to be determined beforehand. Because of difficulty in preparing pure water or pure seawater, the background is typically prepared by passing water through a 0.2 µm filter. This, however, would preclude any possibility of studying particles of sizes < 0.2 µm, which could play a significant role in backscattering [13, 14]. On the other hand, LISST-VSF ring detector measurement can be used to retrieve particle size distribution (PSD) like LISST-100, while only uncalibrated particle volume distribution (PVD) are provided by the manufacture as the instrument is not initially set up for PSD observation. In this study, we report a series of lab experiments using standard beads of different sizes and concentrations to develop an absolute VSF calibration for the LISST-VSF eyeball measurements (>15°) and PVD/PSD calibration for the LISST-VSF ring detectors measurements (<15°).

2. Data and methodology

2.1 VSF calibration of LISST-VSF eyeball measurement

Polystyrene microsphere DUKE STANDARDS™ beads of various sizes ordered from Thermo Scientific Inc. were used for calibrating VSF of the LISST-VSF eyeball measurement. As these artificial monodispersed particles are more or less spherical with known size and refractive index, their scattering coefficient can be well predicted by Mie theory. The specification of beads used in the calibration are summarized in Table 1.

Table 1. The specification of beads used in the calibration.

Mean diameter (µm)	Uncertainty in mean diameter (µm)	Standard deviation (µm)	Concentration (#/ml)
0.152	0.005	0.005	5.18E12
0.203	0.005	0.0053	2.21E12
0.508	0.008	0.0085	1.39E11
5.0	0.3	0.6	1.46E8
11.1	0.5	0.6	1.33E7

The concentration of each stock solution of beads (N_0; ml^{-1}) was calculated:

$$N_0 = \frac{6\rho_w}{\pi u_d^3(\rho_w + \frac{\rho_b}{C_b} - \rho_b)} \quad (2)$$

where, $u_d$is mean diameter of particle in centimeter; C_b is particle concentration by mass; ρ is density in gram per milliliter and the subscript *w* and *b* indicate water and beads, respectively. The bead solutions were diluted with Milli-Q® water and agitated by hand or ultra-sonicated, and the concentration was calculated using Eq. (1). For each beads solution, the LISST-VSF collected data 20 times. In each collection, the PMT gain was automatically adjusted internally by changing the PMT control voltage until the signal was within the optimal range. The LISST-VSF has a total of 10 gain levels (i.e. 10 PMT control voltages), each doubling the previous gain value. The calibration coefficient $\kappa(\theta)$ was derived as:

$$\kappa(\theta) = \frac{\beta_{Mie}(\theta)}{P_{11}/2^n} \quad (3)$$

where, $\beta_{Mie}(\theta)$ is Mie calculated volume scattering coefficients, P_{11} is LISST-VSF recorded raw data in counts and *n* is the PMT gain level between 0 and 9. A Model II linear regression method was used to derive $\kappa(\theta)$ from variable beads size and concentration measurements. Since the eyeball optics has only one detector, the calibration coefficient should be the same for all scattering angles. Here, only calibration coefficient at 15 scattering angle $\kappa(\theta = 15^o)$ was calculated and applied to all other scattering angles.

2.1 PVD/PSD calibration of LISST-VSF ring detectors measurement

PVD/PSD volume conversion coefficients (VCC) were determined for two polarization states, vertical and horizontal. Since the forward scattering is not very sensitive to the polarizations states, the PVD/PSD derived from the forward LISST unit should be similar. The VCCs were calculated as follows:

$$VCC = \sum_{i=1}^{i=32} uPVD_i \frac{6(V_w+V_b)}{\pi({u_D}^3+3\sigma_D^3)N_0V_b} \tag{4}$$

where, uPVD is uncalibrated particle volume distribution derived from the Matlab code provided by the manufacture; the subscript *i* is the *i*th particle size bin class; $u_D$and σ_D are beads mean diameter and standard deviation; *V* is solution volume and the subscripts *b* and are for beads and water, respectively; N_0 is the number of particles in beads stock solution derived from Eq.2. With VCC, PVD (ml/m^3) and PSD (m^{-3} µm^{-1}) can be determined as follows:

$$PVD_i = \frac{uPVD_i}{VCC}$$

$$PSD_i = \frac{uPVD_i}{VCC}\frac{6}{\pi D_i^3 w_i} * 10^{12} \tag{5}$$

where, D_i and w_i is the midpoint diameter and width of *i*th size bin class, respectively.

3. Results and discussion

A total of 5 bead sizes, each with three concentration, were used to derive the VSF calibration coefficient $\kappa(\theta = 15^o)$. Fig.1 compares the gain value -corrected P11 at 15 degree measured by LISST-VSF and the VSF calculated by Mie theory. The horizontal error bars indicate the standard deviation of corrected P11 counts in the 20 measurements, while the vertical error bars indicate the standard deviation of VSF calculated by Mie theory that takes the uncertainties of median diameter of beads into account. The VSF calculated by Mie theory is linearly correlated with corrected P11 counts with R^2>0.99. The Model II linear regression is used to fit the VSF and P11 counts and the slope will be the calibration coefficient $\kappa(\theta = 15^o)$=8.8231×10^{-5}.

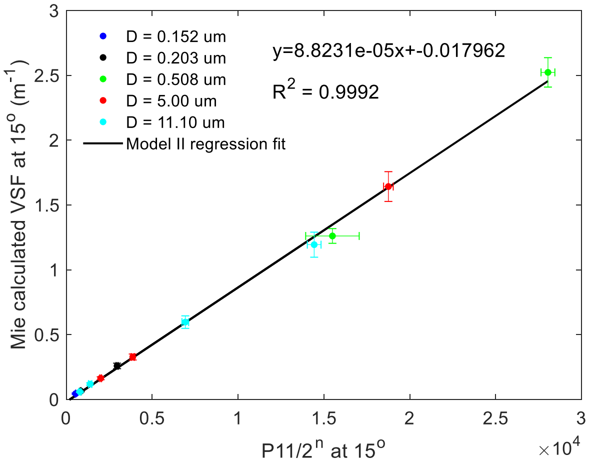

Fig.1. Scatter plot between P11 counts measured by LISST-VSF corrected by PMT gains and VSF calculated by Mie theory at 15 scattering degree.

Applying the calibration coefficient to other scattering angles, the VSF measured by the LISST-VSF eyeball can be absolutely calibrated. Fig.2 compares the calibrated VSFs between 15^o and 150^o (blue dots) in this study, the VSFs estimated using the default calibration provided by the manufacture (black dots) and the VSFs calculated from Mie theory (red line). The VSF in forward small angle (<15°) measured by LISST-VSF ring detectors are also overlaid in Fig.2 to interpret the results. Clearly, VSF at small forward angles (<15°) measured by the LISST-VSF ring detectors are significantly overestimated mainly due to the weak forward scattering of small particles. Because of the inaccurate measurement of ring detector around 15°, the default calibration provided by the manufacturer produces either no VSFs (Fig.2a-d, Fig.2h) or largely overestimated VSFs (Fig.2g). This default calibration only works when the LISST-VSF ring detectors measure good quality data around 15° in the relative high scattering samples (Fig.2e-f). The VSF derived from this study agrees well with Mie calculation in all conditions even at very low scattering regimes when the scattering of the samples is comparable to pure water.

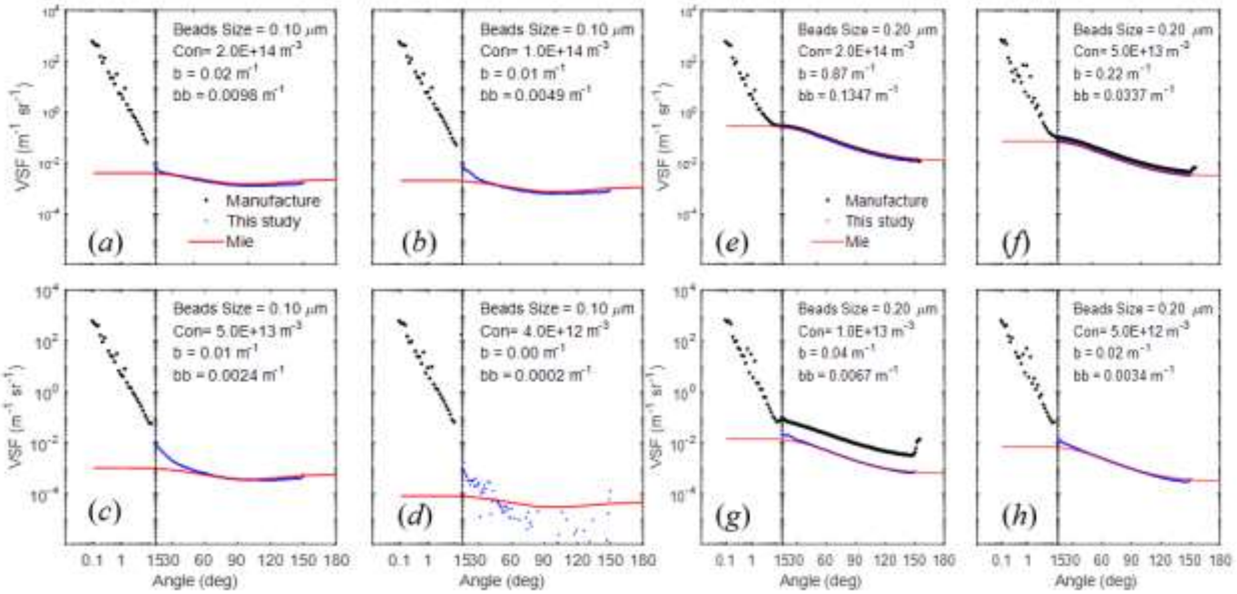

Fig.2 Comparison of VSF between calculated by default calibration provided by manufacture (black dots), this study (blue dots) and Mie theory (red line) for different bead sizes and concentrations. (left: u_D=0.1um, right: u_D=0.2um).

The VCC were derived from bead of diameter 11.10 um at two concentrations of 5.73×10^5 and 8.13×10^5 ml^{-1}. Applying the coefficients to uncalibrated volume distribution, the absolute PVD and PSD can be determined for any beads solution. Fig.3 gives an example of calibrated PVD and PSD for a bead solution (u_D=20.1um, Con=2.0×10^3 m^{-3}). Assuming the bead size is normally distributed, the bead PSD and PVD are also calculated and plotted in Fig.3 (blue line) for comparison. Both PVD and PSD derived using two VCC coefficients are almost identical suggesting the reliable performance of the instrument. The derived PVDs agree well with theoretically calculated volume distribution and the integrated particle volumes are close to the truth with the relative percentage difference of 11.2%.

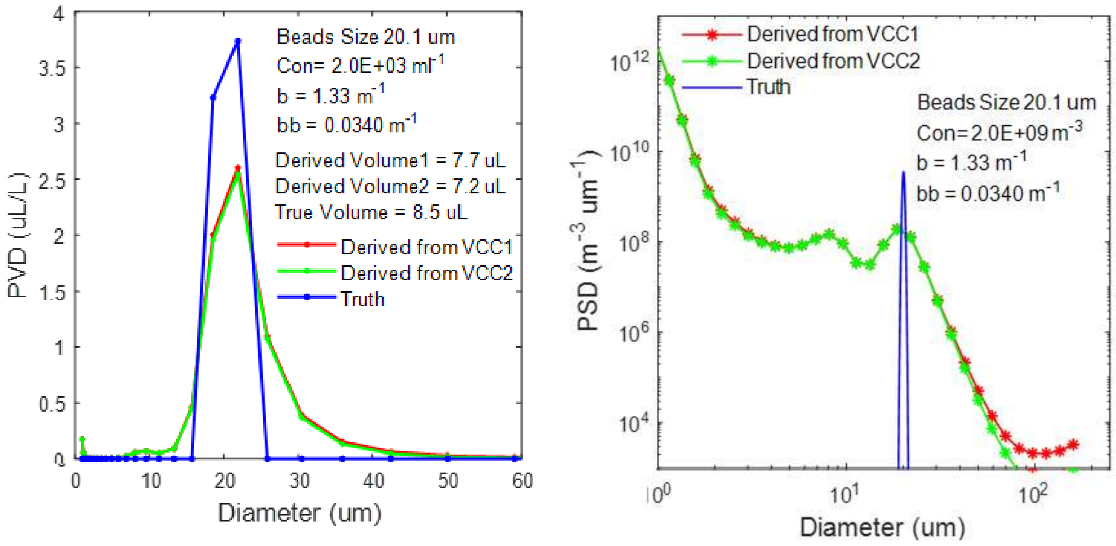

Fig.3 Particle volume distribution (left) and size distribution (right) derived from two LISST-VSF ring detector measurements in vertical and horizontal polarization.

4. Conclusion

From a series of lab experiments using standard beads, we calibrated the LISST-VSF eyeball component to eliminate the dependency on the ring detector measurement. The calibrated VSF agreed well with Mie calculation even under small particles and low concentration scenarios, which will significantly improve the LISST-VSF performance in the clear oceanic waters. Meanwhile, the particle volume and size distribution calibration factors are also determined.

5. Reference

1. C. Mobley, *Light and Water: Radiative Transfer in Natural Waters* (Academic Press., 1994).

2. J. R. V. Zaneveld, J. C. Kitchen, A. Bricaud, and C. C. Moore, "Analysis of in-situ spectral absorption meter data," in *San Diego '92*, (SPIE, 1992), 14.

3. M. E. Lee and M. R. Lewis, "A New Method for the Measurement of the Optical Volume Scattering Function in the Upper Ocean," Journal of Atmospheric and Oceanic Technology **20**, 563-571 (2003).

4. T. J. Petzold, "Volume scattering functions for selected ocean waters," Report (Scripps Institution of Oceanography), 72-78 (1972).

5. G. Kullenberg, "Scattering of light by Sargasso Sea water," Deep Sea Research and Oceanographic Abstracts **15**, 423-432 (1968).

6. J. E. Tyler and W. H. Richardson, "Nephelometer for the Measurement of Volume Scattering Function in Situ*†," Journal of the Optical Society of America **48**, 354-357 (1958).

7. M. Chami, A. Thirouard, and T. Harmel, "POLVSM (Polarized Volume Scattering Meter) instrument: an innovative device to measure the directional and polarized scattering properties of hydrosols," Optics Express **22**, 26403-26428 (2014).

8. H. Tan, R. Doerffer, T. Oishi, and A. Tanaka, "A new approach to measure the volume scattering function," Optics Express **21**, 18697-18711 (2013).

9. J. K. Lotsberg, E. Marken, J. J. Stamnes, S. R. Erga, K. Aursland, and C. Olseng, "Laboratory measurements of light scattering from marine particles," Limnology and Oceanography: Methods **5**, 34-40 (2007).

10. M. Twardowski, X. Zhang, S. Vagle, J. Sullivan, S. Freeman, H. Czerski , Y. You, L. Bi , and G. Kattawar, "The optical volume scattering function in a surf zone inverted to derive sediment and bubble particle subpopulations," Journal of Geophysical Research: Oceans **117**(2012).

11. W. H. Slade, Y. C. Agrawal, and O. A. Mikkelsen, "Comparison of measured and theoretical scattering and polarization properties of narrow size range irregular sediment particles," in *2013 OCEANS - San Diego*, 2013), 1-6.

12. Y. C. Agrawal and O. A. Mikkelsen, "Empirical forward scattering phase functions from 0.08 to 16 deg. for randomly shaped terrigenous 1–21 µm sediment grains," Optics Express **17**, 8805-8814 (2009).

13. X. Zhang and D. J. Gray, "Backscattering by very small particles in coastal waters," Journal of Geophysical Research: Oceans **120**, 6914-6926 (2015).

14. X. Zhang, D. J. Gray, Y. Huot, Y. You, and L. Bi, "Comparison of optically derived particle size distributions: scattering over the full angular range versus diffraction at near forward angles," Applied Optics **51**, 5085-5099 (2012).

The effect of aggregation/disaggregation on Suspended Particulate Matter transport in a sea strait

Suzanna Jackson, Dave Bowers, Michael Harris

School of Ocean Sciences, Bangor University, UK

Predicting net suspended sediment fluxes in coastal areas is important in terms of environmental health, coastal defence, transport and marine industries. Our current understanding of suspended sediment transport does not address the transport of different sized suspended particles. It is known that suspended particulate matter changes in size according to local hydrodynamic properties, namely current speed via aggregation/disaggregation. This research aims to measure the SPM transport in a sea strait and determine whether aggregation/disaggregation is important to varying sizes of suspended particles.

The net suspended sediment flux in the Menai Strait was calculated over a tidal cycle on a spring tide in November 2015. Profiles using Laser in situ Scattering Transmissometry (LISST-100X) and a hull-mounted Acoustic Doppler Current Profiler (ADCP) were conducted over a 12 hour period across the strait to measure suspended sediment concentration, particle size distributions and current speeds.

A south-westerly average residual flow of 0.15 ms^{-1} has previously been observed on a spring tide in the Menai Strait. The observed net sediment flux of 143 tonnes per tidal cycle was found to be transported in the same direction as the residual flow, which could be the source of sediment maintaining the sand bar (Caernarfon Bar) at the South-West end of the strait. Conversely, a smaller net flux of fine-grained particles (~30µm) were transported in the opposite direction to the residual flow over the tidal cycle sampled.

Modelling the main physical parameters driving the transport of suspended sediments in a tidal strait shows particles are continually being torn apart and then re-forming into aggregates as they travel back and forth along the strait. Particles entering an area of high turbulence on the flood tide emerged on the far side as a group of dis-aggregated smaller particles. These then reform into an aggregate in the region of lower turbulence but then the new floc is carried back into the area of high turbulence by the ebb tide, where it breaks up again and the process is repeated.

This is relevant to the formation and maintenance of isolated turbidity maxima (ITM) in shelf seas. These features are localised regions of turbid water found in areas of particularly strong tidal currents. The turbidity is maintained without any apparent source of fine material. Without a source, the material in suspension will diffuse away down the concentration gradient and so it is difficult to see how these features can be sustained. In the Menai Strait, the tide itself acting upon the gradient of particle size, creates a flux of small particles towards the region of intense turbulence and a corresponding flux of larger particles in the opposite direction. This mechanism would also work in isolated turbidity maxima. Therefore, there is no need to postulate an arbitrary diffusion mechanism to carry the large particles into the ITM.

Dynamics of suspended sediment fluxes and their composition over the shallow shelf of Israel in the Mediterranean Sea

Timor Katz[1], and Onn Crouvi[2]

[1]Israel Oceanographic and Limnological Research, [2]Geological Survey of Israel

Suspended sediment concentrations, composition and fluxes in coastal waters correlate to sediment transport, physical properties in the water column, geochemical cycles and various biological processes. The Israeli shelf of the Mediterranean Sea has been extensively studied since the 1960s. However, very little was known about the dynamics, constituents and drivers of sediment fluxes in this area. The aim of this study was to help bridge some of this knowledge gap. The inner shelf along the Israeli coast of the Mediterranean Sea is an exposed, high-energy environment (particularly during winter, see Katz and Mushkin, 2013). It is a part of the Nile littoral cell (Fig 1), wherein sediment from the Nile delta (mostly sand) is transported to the east and north, ultimately reaching Haifa Bay (Carmel et al., 1984; Inman and Jenkins, 1984). This ~650 km long stretch is one of the longest littoral cells in the world (Zviely et al., 2007). The long shore transport of sand gradually diminishes as the coastline inclination changes from east to north reducing the wave radiation stress (Carmel et al., 1984). Further losses occur as sediments are diverted offshore (Nir, 1984) and onshore (Tsoar, 2000). Conversely, sediments enter the coastal water via local rivers (mostly small and ephemeral, see Sandler and Herut, 2000), erosion of the coastal escarpment (Mushkin et al., 2016), windblown dust (Ganor and Mamane, 1982), biological productivity (Avnaim-Katav et al., 2015), and anthropogenic waste. All of these expectedly play a part in the sediment fluxes over the shelf. In this study, we investigated both the annual dynamics of mass fluxes and their composition and sources, with respect to environmental variables including currents, waves, rainfall and temperature. For this end we deployed sediment traps at the inner shelf, two km offshore the Hadera power station (Orot Rabin, see Fig 1), 10 m above a 25 m deep seafloor. The traps where placed next to an acoustic Doppler current profiler (ADCP) that continuously measured waves, current profiles and temperatures. The traps were replaced monthly over a one-year period (Sept 2015-Sept 2016) and the sediments were analyzed for total mass fluxes, particle size distribution and a set of chemical analyses including concentrations of light and heavy elements and stable isotopes ($\delta^{13}C$ and $\delta^{18}O$). The measured sediment fluxes greatly varied between sampling periods, with a minimum value of 1.8 g m^{-2} d^{-1} in autumn and a maximum value of 83 g m^{-2} d^{-1} in mid-winter (Fig 2). This variation was mostly effected by wave-induced resuspension of sediment. A strong correlation (R^2=0.97) was found between integrated wave heights that exceeded 1.5 m and the measured sediment fluxes (Fig 3). Based on the sea state conditions and sediment trap data we conclude that the direction of sand transport at the study area was strictly northwards and that almost all of the annual sand transport occurred during several high-energy events in the winter. Mass fluxes contained mostly clastic (lithogenic) material with fine (<63 µm) to sand size ratio > 1 in all but one deployment period, during midwinter (Fig 2). Nonetheless, fine particles were practically absent in the underlying, 25 m deep seafloor, suggesting that they are very effectively winnowed off beyond the sand strip. Measurements of $\delta^{13}C$ and of $\delta^{18}O$ in the carbonates demonstrated that the sediment fluxes contained a combination of marine and terrestrial carbonates. We expect that the main source of the latter is eroded Eolianite stone (Kurkar) from the coastal escarpment. Some Eolianite rocks, which are lithified sand dunes, cemented by precipitated, carbonaceous matrix disintegrate during winter storms and are backwashed into the sea (Katz and Mushkin, 2013) where they can be re-suspended thereafter. Occasional floods during winter, in otherwise ephemeral rivers, are also likely to contribute to the terrestrial component of the flux. Pure marine carbonates were only observed in the traps during late summer.

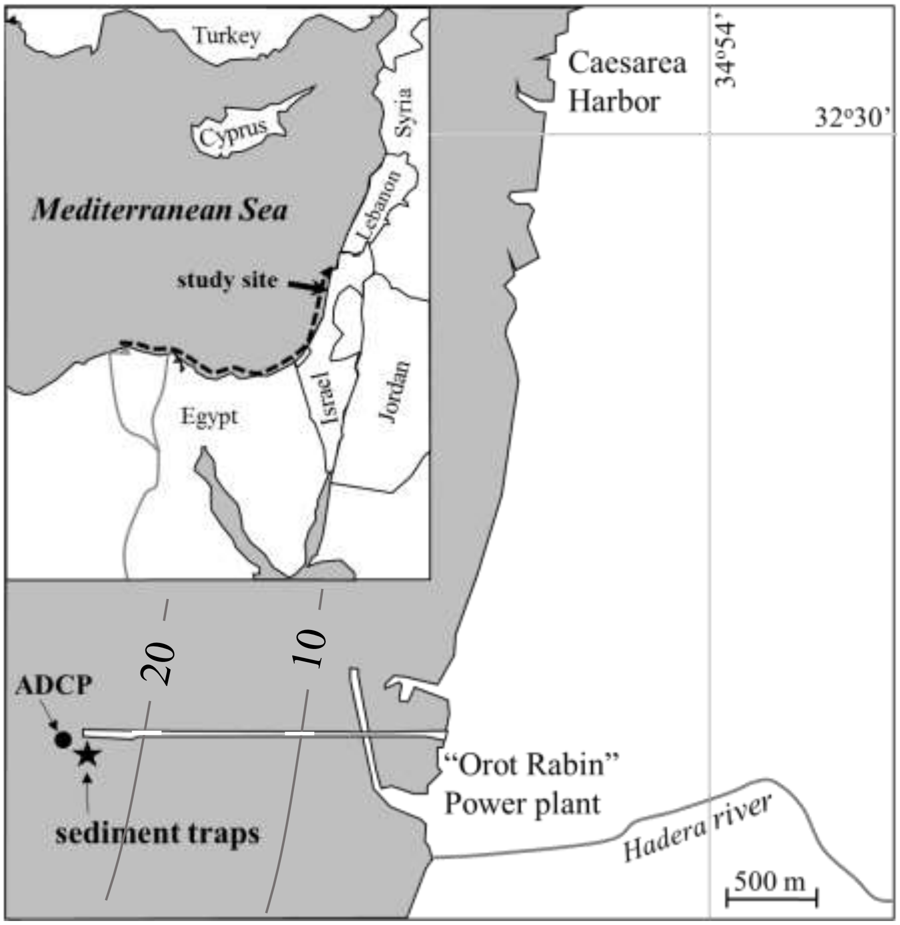

Figure 1: Map showing the study area and location of the moored sediment traps (black star) and the acoustic Doppler current profiler (ADCP; black circle) by the coal, offloading pier of the "Orot Rabin" power plant (Hadera). Inset map shows the location of the study area in the Levantine basin of the Mediterranean Sea. The dashed line represents the long shore transport (LST) of sand along the Nilotic littoral cell (based on Inman and Jenkins, 1984) that spans between the Nile Delta and Haifa Bay.

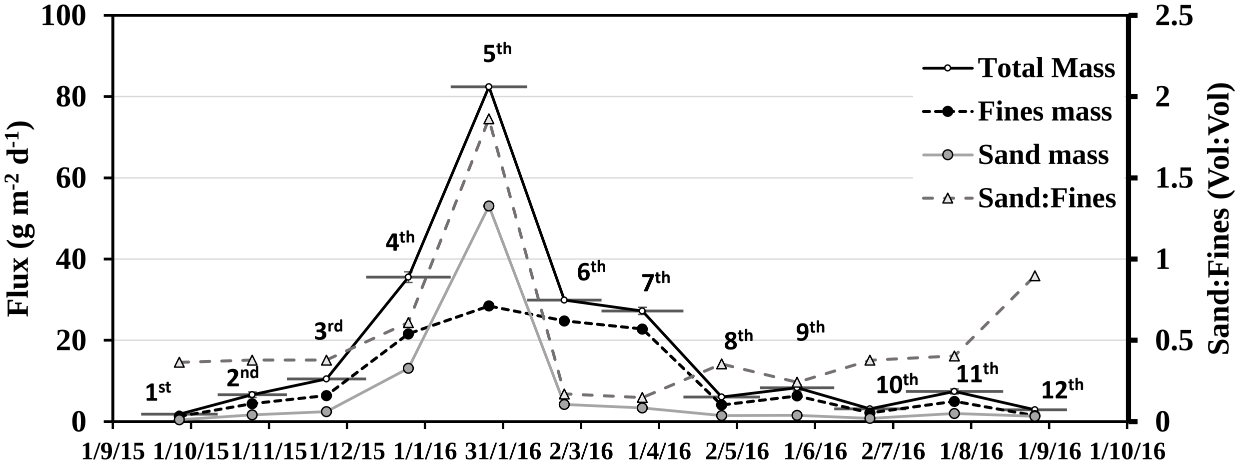

Figure 2: Means of total mass fluxes and fluxes of inorganic sand (63µm > GS < 2000 µm) and fine particles (silt and clay, GS < 63 µm) and their ratio in each sampling period. The deployment periods (numbered, as in Table 1) are delimited by horizontal bars. Vertical error bars (barely seen) in the total mass flux mark the standard deviation (SD) of the mean based on two traps that were deployed in each period.

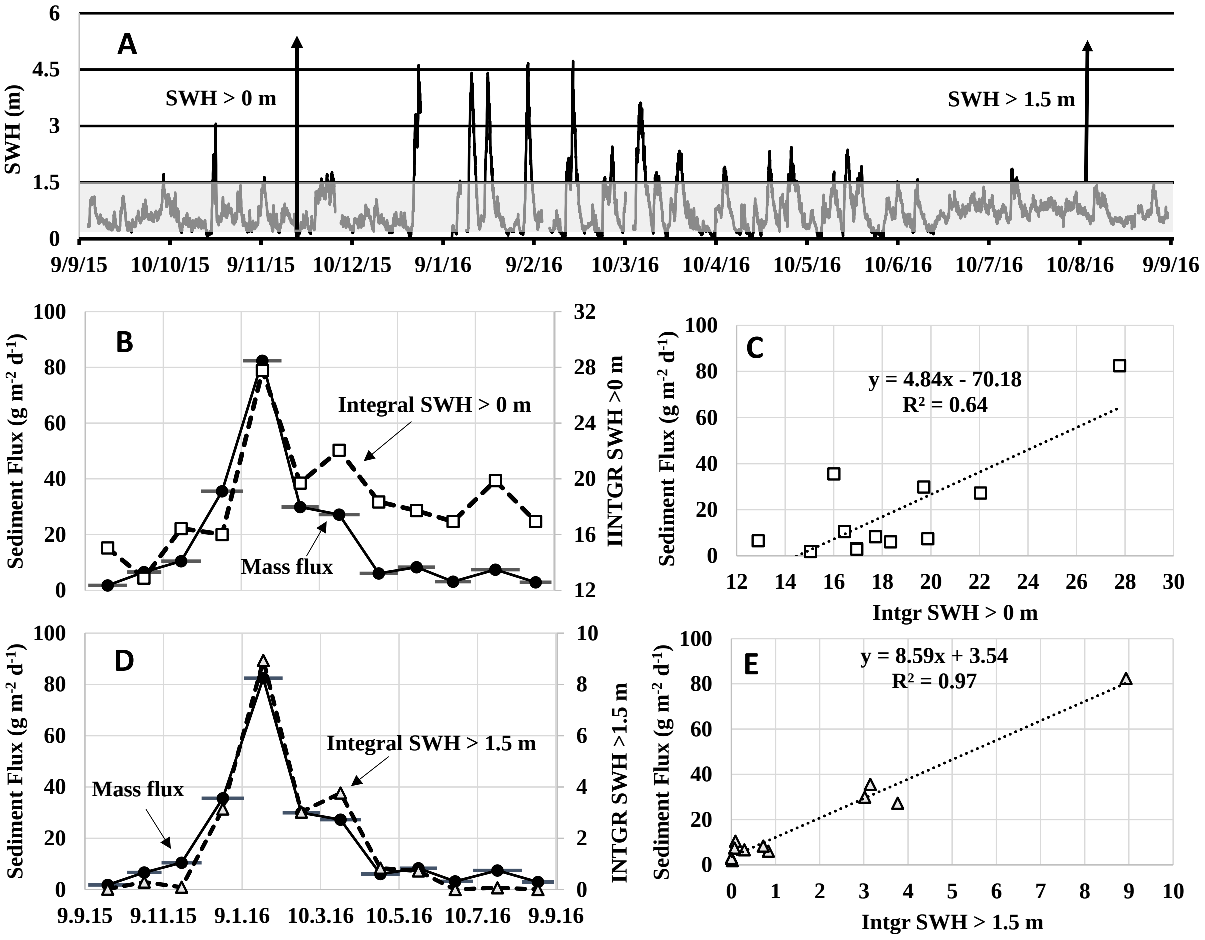

Figure 3: A) a time series of significant wave heights (SWH) at the study site. B) Plots of mean mass fluxes and of normalized time integration of all SWH (SWH > 0m in (A) in each of the sampling periods over time. C) Plot of the mean mass fluxes in the different sampling periods versus the integrated SWH > 0 m, the dotted regression line is shown with its linear equation and R^2. D) Plots of mean mass fluxes and normalized time integration of only SWH > 1.5 m (see A) in each of the sampling periods over time. E) Mean mass fluxes in the different sampling periods versus the integrated SWH > 1.5 m, the dotted regression line is shown with its linear equation and R^2. Horizontal bars in panels B and D, delimit the traps deployment periods.

References

Avnaim-Katav, S., Hyams-Kaphzan, O., Milker, Y., Almogi-Labin, A., 2015. Bathymetric zonation of modern shelf benthic foraminifera in the Levantine Basin, eastern Mediterranean Sea. J. Sea Res. 99, 97–106.

Carmel, Z., Inman, D.L., Golik, A., 1984. Transport of Nile sand along the southeastern Mediterranean coast, in: Edge, B.L. (Ed.), Coastal Engineering. New York, NY: American Society of Civil Engineers, pp. 1282–1290.

Ganor, E., Mamane, Y., 1982. Transport of Saharan dust across the eastern Mediterranean. Atmos. Environ. 16, 581–587.

Inman, D., Jenkins, S., 1984. The Nile littoral cell and man's impact on the coastal zone of the southeastern mediterranean. Coast. Eng. Proc. 1, 1600–1617.

Katz, O., Mushkin, A., 2013. Characteristics of sea-cliff erosion induced by a strong winter storm in the eastern Mediterranean. Quat. Res. (United States) 80, 20–32.

Mushkin, A., Katz, O., Crouvi, O., Alter, S.R., Shemesh, R., 2016. Sediment contribution from Israel's coastal cliffs into the Nile's littoral cell and its significance to cliff-retreat mitigation efforts. Eng. Geol. 215, 91–94.

Nir, Y., 1984. Recent sediments of the Israel Mediterranean Continental Shelf and Slope. Ph.D thesis, University of Gothenburg, Sweden Department of Marine Geology, 1984.

Sandler, A., Herut, B., 2000. Composition of clays along the continental shelf off Israel: Contribution of the Nile versus local sources. Mar. Geol. 167, 339–354.

Tsoar, H., 2000. Geomorphology and paleogeography of sand dunes that have formed the kurkar ridges in the coastal plain of Israel. Isr. J. Earth Sci. 49, 189–196.

Zviely, D., Kit, E., Klein, M., 2007. Longshore sand transport estimates along the Mediterraneancoast of Israel in the Holocene. Mar. Geol. 238, 61–73.

Sediment monitoring in hydropower stations of Indian Himalayas: Issues, practices and future outlook

Arun Kumar

Professor, Alternate Hydro Energy Centre, Indian Institute of Technology Roorkee, Roorkee – 247667

akumafah@iitr.ac.in

ABSTRACT

Himalayas being the young mountain has substantial soil erosion and the sediment concentration is high in rivers. One of the main challenges for hydropower development and operation in the Himalayan region is the sediment laden water in the rivers. It impacts the longevity of hydropower stations during the high flow period consisting of snow melt and rainy season by reducing the storage of reservoirs and hydro-abrasive erosion of turbines, valves, gates, penstocks and other hydraulic components. The remedial and preventive measures for the issues require accurate measurement of suspended sediment properties, which is not a general practice at present in Indian hydropower plans. This article presents various methodologies/instruments available for online measurement with respective cost, availability, advantages and limitations. The increased demand of electricity from renewable sources requires sustainable development of hydropower which in turn necessitates the online measurement of suspended sediment concentration and particle size distribution, especially in Indian Himalayan region. The author shall also present about the laboratory setup made at Indian Institute of Technology Roorkee to study and mitigate the hydro-abrasive issues in Himalayan region, a laboratory with state of the art instrumentation is established at AHEC, IIT Roorkee with support from the Ministry of New and Renewable Energy, Govt. of India and Dam rehabilitation and improvement project (DRIP), Central Water Commission.

How the offshore industry uses particle measurements – examples, gaps and opportunities

Piers Larcombe[1], Sylvain Ouillon[2]

[1]RPS MetOcean Perth & University of Western Australia)

[2]IRD, UMR LEGOS, OMP (University of Toulouse, France)

Scope

This paper addresses work conducted by those parts of the offshore industry that are involved in finding, assessing and exploiting oil and gas in geological formations beneath the seabed, or that conduct similar operations, such as for offshore windfarms, wave farms or tidal farms. Many traditional hydrocarbon-based industries are diversifying into such renewables. Our focus is continental shelf and deeper environments rather than at the coast, mostly physical science and particles generally smaller than 2 mm (although we may comment on coastal and biological aspects) and on field measurements rather than laboratory or modelling simulations. The work is intended to provide ideas for measurement opportunities rather than be profound and exhaustive.

Why measure particles?

The reasons why particle measurements are made vary through the various phases of the development process. At the early stages of exploration, there is relatively little use of measurements of particles in the ocean, but this expands greatly when the focus turns to understanding the environment to assess engineering hazards and options. A key need for industry is to understand the environment sufficiently well to design efficiently for the multi-decadal project lifetime. Here, relevant measurements might vary from regional studies of relative seabed mobility using seabed samples, to the high-frequency sampling of near-bed water to assess the effects of the passage of internal waves or turbidity currents.

Environmental requirements demanded by regulation can be poorly tuned to the environments and systems concerned, and in some jurisdictions, regulatory requirements are not necessarily scientifically defensible. In general, the practical application of regulations has great difficulty dealing with multi-decadal timespans. In Australia, for example, i) the use of turbidity remains a fundamental non-negotiable requirement, in ignorance of the limitations of the technique, and ii) there is no account taken of the natural multi-decadal dynamics of the sea bed and associated habitats (e.g. Larcombe & Morrison-Saunders, 2017). Those companies who value highly their corporate environmental credentials will invest in measurement work exceeding regulatory requirements.

Examples of particle measurements

A wide range of techniques is available to measure particle characteristics in water, (often seasonal) biogenic particles and perhaps especially sediments related to seabed mobility, and downward particle fluxes (Ouillon, 2018). These techniques have various inherent sensitivities and dependencies, and therefore varying practical applicability, depending on purpose, environments, particles types and other factors. Techniques and resulting parameters include (in no particular order, and with some duplication:

Optical backscatter (nephelometer) → Turbidity

Laser diffraction → Volume concentration & Particle Size Distribution

Acoustic sensors (point readings, profilers), Impact probes, Radioactive absorption, Conductivity → Volume concentration, etc.

Optical techniques – e.g. video capture & counting, Holograms (machine learning) → Particle counting, shape & nature

Settling rates → Settling velocity distribution

Laser diffraction or holograms (volume concentration) and sampling (weight concentration) → Density (absolute & relative)

Sequential sediment traps (automatic sampling) → Downward sediment fluxes and their properties.

Within the water column, water-quality data (TSS, grain PSD, grain hardness etc.) are collected against which to measure actual impacts of operations, or, for example, to understand the seasonal variations in the quality of ocean water taken in and used for cooling or on-board industrial processes by the increasing number and scale of floating facilities. In many cases, there are trade-offs in project design, including that between accuracy and spatial coverage.

We describe some case studies of measurements for the offshore industry, highlighting the purpose, some aspects of the data and interpretations, and the conclusions drawn.

Scientific and technical gaps

Various scientific gaps exist, some of which are significant issues for the offshore sector. These gaps include knowledge of:

Active off-shelf particulate transport (oceanography & sedimentary history, sediment transport rates);

Oceanographic and sediment transport regimes at depths >500 m down to >4 km, required to support the oil and gas sector moving to deep water work; and

The role of internal waves and along-slope currents in initiating turbidity currents on the upper slope.

In many cases, there remains critical associated issues regarding the magnitude, frequency & timing of past sediment transport events.

Some of these gaps are historical in nature, but also are related to the relative lack of available deep-water instrumentation, including workable biofouling control. It is also to be noted that the complexities of identifying particles remains an issue - it is likely that machine-learning techniques are at least part of the answer here, in order to put meat on the bones of time-series data.

Future opportunities for the use of particle measurements

Increasingly, the industry is targeting the exploitation of hydrocarbon reserves that requires work in physical environments that are close to the present boundaries of working. There is also a huge amount of decommissioning activity projected for the next two decades or so. Some future opportunities for measurements can thus be summarised by 3 Ds – difficult, deep and decommissioning.

Difficult

As industry experience develops, work is increasingly located in difficult environments, where currents may be faster (e.g. tidal farms) and/or less predictable, internal waves stronger or more frequent, visibility less and seabed mobility greater. The effects of extreme wave conditions or Tropical Cyclones (typhoons, hurricanes) can be severe. Some examples will be described where measurements have been crucial to understand particles and their dynamics and to design work accordingly.

Deep

Many major developments in the offshore industry for the next 20 years or more will involve pipeline and seabed structure being located in depths measured in 1000s of m. This is reflected in a range of ongoing projects off East Africa, in the Indonesian Archipelago, and elsewhere. Here, there are considerable measurement opportunities, both using standalone moored instruments, and for use of instrument packages that can be plugged into the increasing number of ROVs which operate in these depths. There is great value to be had by taking measurements of opportunity to help design the necessary dedicated measurement programs. Aspects of these environments associated with measurements of particles include:

The transport of sediment across and along the continental shelf from tropical and sub-tropical river systems, including those affected by major active deltas; and

Downslope transport of existing shelf or slope sediments (including canyons), by the occurrence of turbidity currents and or associated with internal waves.

The number of deep-sea mining operations is growing, and these will require proper assessment of their effects on water quality and sedimentation. Further, geographically, the sediment dynamics of many relevant continental margins remain relatively poorly known, including, but not limited to, W & E Africa, South America & Myanmar.

Decommissioning

Taking the N Sea as an example, after ~40 years of production, there are over 600 offshore oil and gas installations (OSPAR, 2015) including topsides, steel platforms, concrete gravity-based sub-structures, subsea and floating equipment, plus more than 10,000 km of pipelines, ~ 5,000 wells and their drill cuttings (DECC, 2014). Many installations are nearing the end of their design life, and most will have to be removed completely and disposed of on land, with total costs estimated at £40-70 billion by 2040 (Genesis and DECC, 2015; Ahiaga-Dagbui et al. 2017). The nature and scale of the work provides opportunities to use particle measurements to support subsea operations related to, for example, assessing the physical state of facilities, including assessing their weight, and supporting their physical removal. Issues include subsea visibility and the assessment of dispersal of tailings from operations (using existing sediments and subsequent sampling of seabed sediments). Although the history of working in such environments is a relatively long one and methods of operation are often well-established, efficiencies can be gained from knowledge of sediment transport.

As a final and parenthetic aside, there is a gathering archaeological focus across the globe on the past and present dynamics of the marine environment, relating especially to the past migration of humans across now drowned landscapes, at times of lower sea level. Assessment of the possible negative impacts upon marine archaeology is becoming incorporated into development regulations (e.g. Ward et al., 2014; Sturt et al., in press), and will in time be an extra and interesting, if minor, source of demand for measurements.

References

Ahiaga-Dagbui D, Love P, Whyte A & Boateng P, (2017) Costing & Technological Challenges of Offshore Oil & Gas Decommissioning in the UK North Sea. ASCE Journal of Construction Engineering & Management, 143 (4) 05017008-1, DOI: 10.1061/(ASCE)CO.1943-7862.0001317

DECC (2014). UK Energy in Brief. Department of Energy and Climate Change.

Genesis and DECC (2015) The real costs of decommissioning. **http://decomnorthsea.com/news/the-real-costs-ofdecommissioning**. Decom North Sea.

Larcombe, P. & Morrison-Saunders, A. (2017) Managing marine environments and decision-making requires better application of the physical sedimentary sciences. Australasian Journal of Environmental Management, 24 (2): 200-221.

OSPAR (2015). Inventory of Offshore Installations. In: OSPAR Commission (ed.) Publication 656. London, **http://www.ospar.org**.

Ouillon, S. (2018). Why and How Do We Study Sediment Transport? Focus on Coastal Zones and Ongoing Methods. Water, 10, 390. doi:10.3390/w10040390

Sturt et al (in press) The next frontiers in research on submerged prehistoric sites and landscapes on the continental shelf. Proceedings of the Geological Association.

Ward, I., Larcombe, P., Firth, A., Manders, M. (2014) Practical approaches to management of the marine prehistoric environment. Netherlands Journal of Geosciences, 93, 71-82.

Evaluating Particle Packaging and Transport at an Active Area of Salmon Aquaculture over a Mixed Grain Size Seabed

Brent A. Law*, Timothy Milligan, Vanessa Zions, Peter Cranford, Lindsay Brager, Raymond Bannister, and Nigel Keeley

Bedford Institute of Oceanography

Fisheries and Oceans Canada

Dartmouth, N.S., Canada, B2Y 4A2

*Brent.Law@dfo-mpo.gc.ca

As part of the Ecosystem Response to Aquaculture (ERA) project at the Ratteran and Ornoya salmon aquaculture farm sites in Froya, Norway, instrument pods were deployed in August 2015 and again in May 2016. The instrument pods (Fig 1 A and B) included:

A digital video camera inside a stainless steel pressure housing with attached settling column measured settling particles from approximately 200 µm to mm size scale and sat just above the seabed. In addition the instrument pod contained a Nortek high resolution Aquadopp current meter which measured near bed currents and waves, an RBR wave gauge, and RBR turbidity sensor.

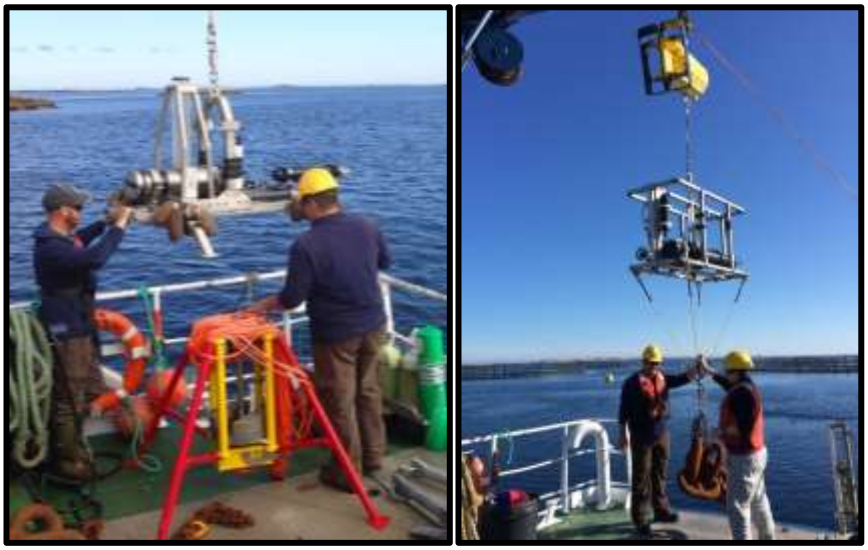

Fig.1(A) Settling Pod w/ Aquadopp B) Floc Camera / LISST Pod

A second instrument pod was co-located and moored 1 m off the seabed and contained a Machine Vision Floc Camera (MVFC) and Sequoia LISST 100x which measured particle size in-situ from 1.25 µm to mm size. In addition the pod contained an RBR CTD measuring salinity, temperature and pressure along with dissolved oxygen and turbidity. An eco-BB instrument from Wetlabs measured Coloured Dissolved Organic Matter (CDOM), Chlorophyll concentration and backscattering in the red.

The data will be discussed in terms of the particle size, packaging and transport of possible aquaculture derived waste material from the farm sites. These data will help explore linkages between organic matter transport, its deposition and possible effects in the near field and far field associated with aquaculture operations and understanding salmon aquaculture sustainability in the marine environment.

Evidence of Muddy Aggregates as Resilient Pellets in Suspension Throughout the Water Column Using Traps and a Particle Image Camera System (PICS) in a Tidal Estuary.

Grace M. Massey[1], Kelsey A. Fall[1,2], Carl T. Friedrichs[1] , Danielle R.N. Tarpley[1] and S. Jarrell Smith[2]

[1]Virginia Institute of Marine Science

College of William & Mary, Gloucester Point, VA 23062, USA

[2]U.S. Army Engineer Research and Development Center

Coastal and Hydraulics Laboratory, Vicksburg, MS 39180, USA

Whereas flocculation is an important process in the deposition of fine sediments in deltaic and estuarine environments, biogenic pelletization may also play an important roll in the packaging of these sediments to prevent their availability in contributing to the water clarity issues. On the order of a thousand 5µm equivalent spherical diameter clay flocculi primary particles can be packaged in a single elliptical-in-shape pellet, 100µm long and 30µm wide. This is a size consistent of those observed in our study area in the Clay Bank area of the York River estuary, a tributary of the Chesapeake Bay, Virginia, USA. If resuspended, this one pellet will have nearly 25 times less surface area and thus have that much less impact on water clarity, compared to its constituent particles. Biogenic pelletization can be significant where there are large numbers of organisms that suspension feed. It can be even more significant when the pellets are resistant to degradation and breakup under normal tidal stress. For example, one study of *Callianassa major*, a ghost shrimp, estimates it produces 2,480 medium sand size resilient pellets per day, which collect and are transported in the troughs of sand ripples (Pryor, 1975). In the study, Pryor estimates in an area of the Mississippi Sound, where the density of *Callianassa* burrows approach 500/m^2, they can remove and pelletize nearly 618 metric tons of suspended solids per square kilometer each year. “Enough to cover each square metre of the back island shoreface with 141 mm of fecal pellets each year” (Pryor, 1975).

Resilient pellets have been found to comprise up to 40% of the bottom sediments in the Clay Bank region of the York River estuary (Kraatz, 2013; Rodríguez-Calderón and Kuehl, 2013). Based on video collected by Robert Diaz’s WormCam, we believe these resilient pellets are produced by polychaetes. The burrows and fecal pellets, though smaller, are very similar to those described of the polychaete *Nereis diversicolor* in the Kundalika Estuary on the west coast of India (Kulkarni and Panchang, 2015). A nearly continuous series of sediment trap deployments on benthic tripods, with inlet holes located at 0.4 mab (meters above the bed), from September 2012 through March 2015 show a loosely seasonal trend in the pellet concentration (dotted line in Figure 1) of the homogenized sediment collected in each trap. X-rays of the traps show that the sediment collected, however, is anything but homogenous. They show thin laminations of coarser material throughout the trap, which we hypothesize are tidally resuspended pellets, sand and coarse debris (for example see x-ray of tripod trap in Figure 3).

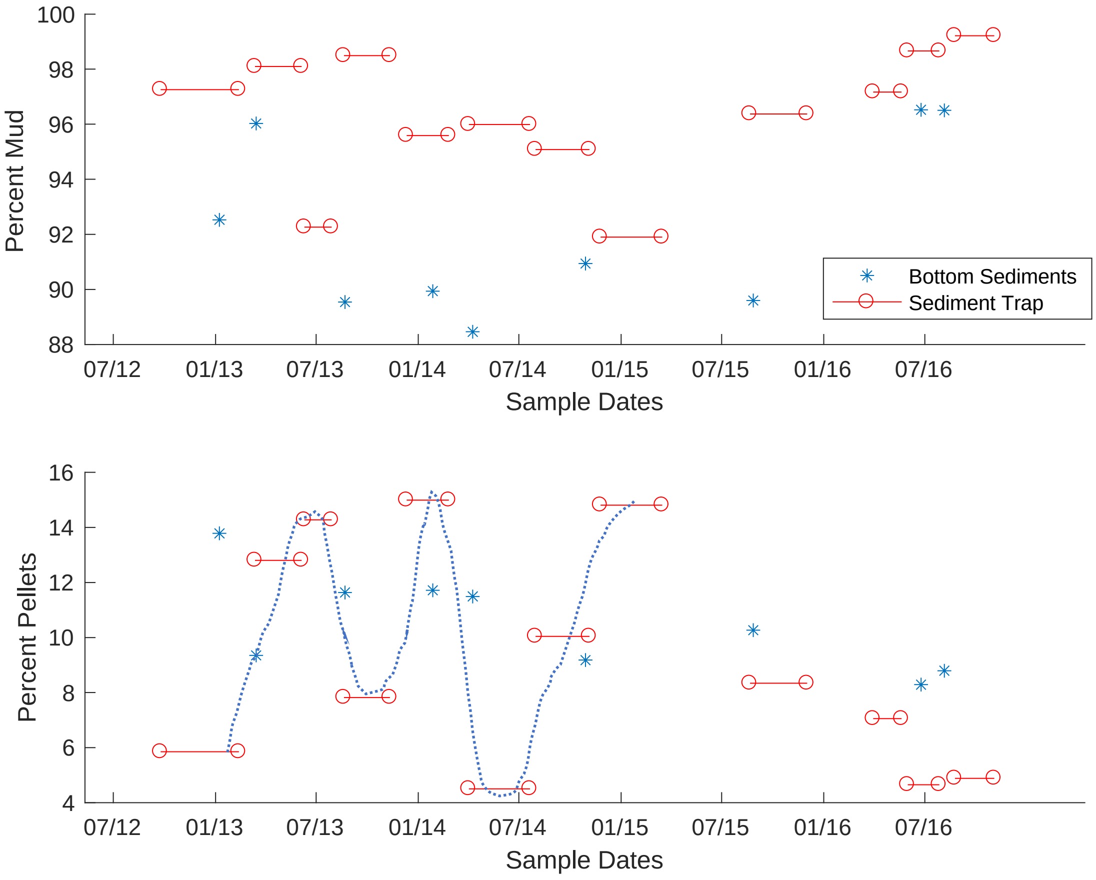

Figure 1. A) Red bars are the homogenized percentage mud of particles captured by sediment traps with inlet holes at 0.4 mab deployed between the time frame indicated by the red circles on benthic tripods in the Clay Bank region of the York River Estuary, Virginia, USA. Blue stars are the average percent mud of the top two centimeters from bottom sediment cores. B) Red bars are the percentage of mud packages as resilient pellets captured between the time frame indicated by the red circles. Blue stars are the average of the top two centimeters of percent mud packaged as resilient pellets from bottom sediment cores.

Two additional sediment traps were deployed on the ADV tower in conjunction with the deployment of the benthic tripod from August 24, 2016 through November 3, 2016 (Figure 2). The top trap's 1 cm diameter inlet holes were within 2 meters of the surface at ~ 5.2 mab, and the bottom trap's inlet holes were at a mid-water depth of ~3.2 mab. Upon retrieval, the mid and top traps were not full, the sediment surfaces in the traps were 4.5 cm and 11 cm below the 1cm diameter inlet holes, respectively, and the X-rays showed signs of bioturbation (Figure 3, top row). Care will need to be taken in limiting the length of future deployments to prevent opportunistic colonization of the traps by organisms such as the crabs, fish and worms found in the two traps. The X-ray of the tripod trap shows the fine scale laminations seen in other traps collected within 0.4 mab.

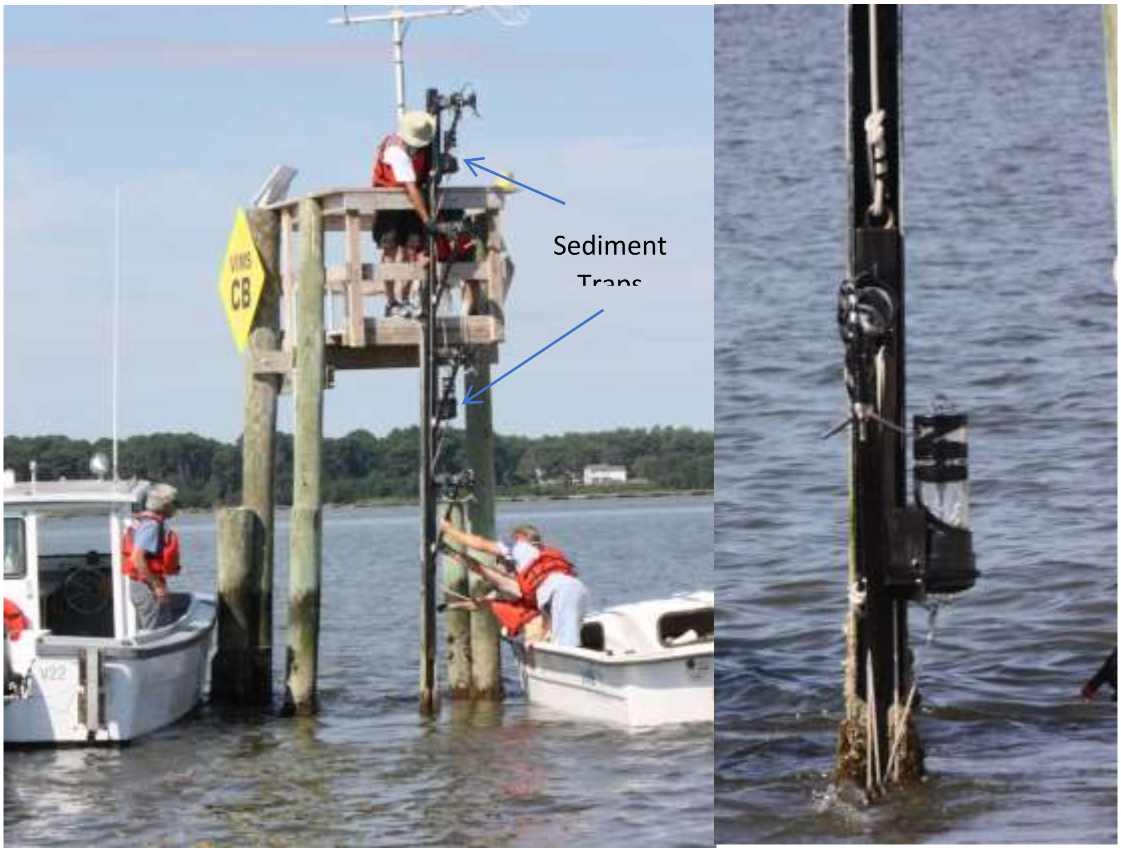

Figure 2. Deployment of water column sediment traps as part of the Acoustic Doppler Velocimeter (ADV) tower on the VIMS CB platform in the Clay Bank area of the York River estuary, Virginia, USA

Each trap contained over 99% mud, with a clay/silt ratio of 44.19/55.21 (0.80), 42.33/56.74 (0.74) and 40.25/58.96 (0.68) for the top, mid and tripod traps, respectively. The percentage of mud packaged as pellets in each of the traps was 2.00, 4.05 and 4.89 for the top, mid and tripod traps, respectively. Pellets were separated using a 90µm and a 63µm sieve from the sediment collected in each of the three traps. Pellet shape and color were visually similar (Figure 3, rows 2 and 3 respectively). There appears to be more debris in the mid-depth and tripod traps than in the surface trap, and there are some very large pellets visible in the mid-depth trap.

While 2 percent of the mud in suspension packaged as resilient pellets within 2 meters of the surface is relatively small in comparison to the near-surface unpelletized fraction, it does show that these pellets are being resuspended and transported throughout the water column. This is

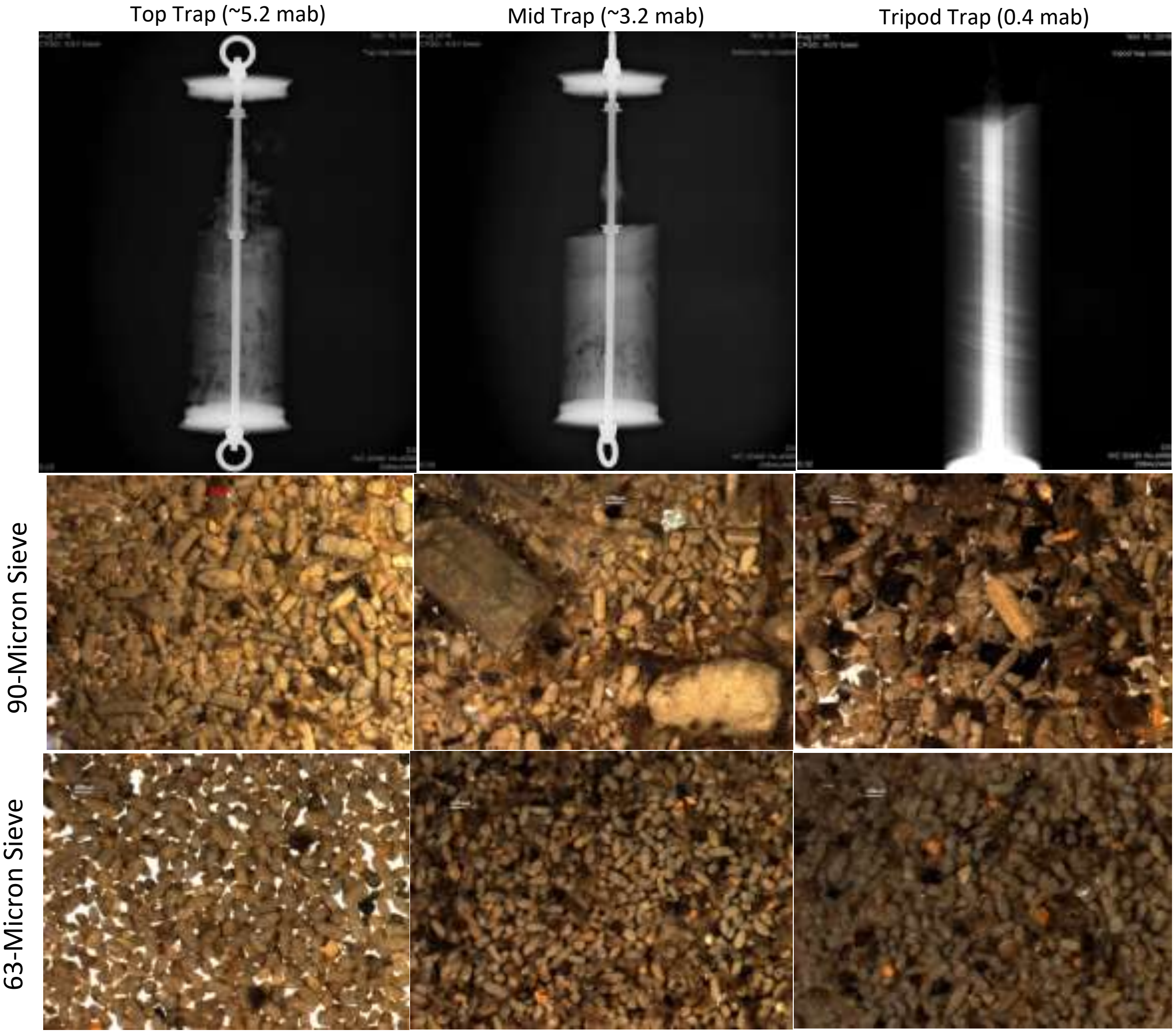

Figure 3. Sediment traps deployed August – November, 2016.

consistent with the findings of Haven and Morales-Alamo (1968) during a study in the James River, an adjacent tributary of the York River to the Chesapeake Bay. They identified a combined average of 26.6% of particles, captured from water pumped from 1m below the surface through 125μm and 44μm sieves, as fecal pellets. They suggested that sorting during transportation and deposition could result in accumulation in areas of the estuary where fine sediment would not otherwise settle out. Two 4-6 hr profile cruises, one around max flood and the other around max ebb, were conducted early in the deployment of the sediment traps to in to investigate the transport and deposition of pellets in this area. The instruments mounted on the profiler included a Particle Imaging Camera System (PICS), a LISST 100X, a YSI EXO sonde, and a pump for water samples. Future work will include identifying pellets in Particle Imaging Camera System (PICS) video sequences using axis ratios, pixel intensity and density to differentiate them from similar diameter flocculated particles.

References:

Haven, D., Morales-Alamo, R., 1968, Occurrence and transport of fecal pellets in suspension in a tidal estuary: Sedimentary Geology, v. 2, p.141-151.

Haven, D., Morales-Alamo, R., 1970, Filtration of particles from suspension by the American oyster Crassostrea virginica: Biol. Bull., v. 139, p. 248-264.

Kraatz, L.M., 2013. Evolution of the seabed of the York River Estuary, Virginia, following dissipation of a turbidity maximum: consolidation, pelletization and spring-neap disturbance. Chapter 3 in: Acoustic and sedimentological investigations of seabed conditions and related bio-physio-geological parameters in a tidally energetic, fine-grained environment: York River Estuary, Virginia. Ph.D. Dissertation, pp. 59-114. http://www.vims.edu/~cfried/cv/2013/Kraatz_2013_PhD.pdf

Kulkarni KG, Panchang R (2015) New Insights into Polychaete Traces and Fecal Pellets: Another Complex Ichnotaxon? PLoS ONE 10(10): e0139933. doi:10.1371/journal.pone.0139933

Pryor WA. Biogenic sedimentation and alteration of argillaceous sediments in shallow marine environments. Geol. Soc. America Bull. 1975;86:1244–54.

Rodríguez-Calderón, C. and Kuehl, S.A., 2013. Spatial and temporal patterns in erosion and deposition in the York River, Chesapeake Bay, VA. Estuarine, Coastal and Shelf Science, 117: 148-158. http://dx.doi.org/10.1016/j.ecss.2012.11.004

Suspended Sediment Profiles in Rivers With LISST-SL2 Laser Diffraction Instrument

O. A. Mikkelsen[1,2] and Yogi Agrawal[2]

1) MacArtney A/S, Gl. Guldagervej 48, 6710 Esbjerg V, Denmark

2) Sequoia Scientific, Inc., Bellevue, WA, USA

1. ABSTRACT

Measurements of sediment transport in rivers have for long been done laboriously with water samples drawn infrequently, requiring subseqent time-consuming analysis. A new laser diffraction instrument LISST-SL2 has been developed to make these same measurements in real-time, with sediment concentration, grain size distribution, water velocity, and temperature all stored as a function of depth. This capability permits efficient data collection for monitoring agencies, while at the same time, opening new avenues for scientific research. In this paper, we offer a preview of data collected from two rivers on two continents: the Cowlitz river in Washington, US, and the Yangtze river at Wuhan city, China. We discuss similarities, statistics of the data, vertical structure of river columns, time-scales of sediment fluctuation, and derivable flow quantities.

Keywords – River sediments, size distribution, real-time.

2. INTRODUCTION

Sediment transport in rivers has important societal consequences; as such it is a subject of significant scientific research. River meander, sand formations, erosion around bridge pilings, and discharges into estuaries and deltas are all related subjects. The effort in measuring suspended and bedload discharge has a long history (see Orton and Kineke, 2001 for a review; also Kazimierz et al. 2010). Routine monitoring by governments have evolved rigorous procedures and standardized instruments and methods. The present work confirms some old ideas, and advances others.

The simplest study areas on rivers are straight sections which are devoid of secondary motions associated with river meanders, describable, to first order, as a classic flow in a turbulent channel (Schlichting,1968). In these flows, a 'law of the wall' region may exist near the riverbed, where the velocity profile scales as logarithm of the distance from the bed. Such a region exists so long as the channel bed roughness is not a significant portion of the channel depth. Above this logarithmic velocity region, a 'law of the wake' applies where scaling is with channel depth. In these flows, sediment is carried both as suspended load and as bedload. The suspended load carried by rivers can typically be partitioned into a 'wash load' of fine material that is too fine to settle and a resuspended load if the river velocity is sufficient to force resuspension. A vertical gradient in suspended sediment concentration (SSC) exists in the water column. The gradient is established under the competing actions of turbulent diffusion gravitational settling. Since settling velocity depends on grain size and mass density, size principally determines the gradient when flocculation is small. The vertical profile was formalized by Rouse (1937). Thus, river channels are expected to exhibit velocity and SSC profiles with scaling laws similar to classic turbulent channels. The SSC profiles are expected to be a composite of component profiles of different size sediments (modified by sediment-induced density stratification when it exists). It is this last item – gradients of different sized grains – that have remained poorly studied, and remain a source of error and disorder in past data because of instrumental limitations to observe size distributions and accurate sediment concentrations. We review these briefly.

Orton and Kineke (2001) measured velocities and sediments in the Hudson River estuary and compared model results with measurements. They used a single calibration of an OBS, which by implication assumes a constant size distribution throughout the water column. With no data on size distribution variability in the water column, they assumed a single settling velocity for their model, 0.22cm/s, which applies to 50 µm sand grains. They reported that the theory-data match was best when a power law relationship was employed between settling velocity and concentration. Even so, data and their models disagreed by orders of magnitude at just short distances above the riverbed. In the end, the use of turbidity type sensors appears to have been unsuitable in this vertically changing PSD environment. It appears to be responsible, at least in part, for the poor match between data and their sophisticated models.

Still other studies have employed physical samples, e.g. Richey et al.(1986). They employed bag samplers and partitioned a vertically integrated sample into fine and coarse sediment with the break at 63 µm. These data are more likely to be accurate, but for sampling errors. Unfortunately, this limits the number of available data points, and vertical structure of PSD was not revealed. The use of bottle samplers is widespread, and it is a de facto standard operating procedure of government agencies. A physical sample promotes confidence in the results. However, as Gitto et al.(2017), using a LISST-SL instrument show, single bottle samples do not represent mean values of SSC. Acoustic backscatter as a surrogate has been an area of promise for a few decades (Guerrero, 2017), but inversion of even the multi-frequency data in a varying situation such as a river column has not been done routinely to date. The laser diffraction method (LD) described in this paper remains the only reliable way to observe river column sediments, although it is a point measurement and requires physical profiling. For completeness, we describe the principle.

The LD method is an international standard, ISO-13320:2009. The LISST-SL is a submersible LD instrument, developed in a Cooperative Research and Development Agreement (CRADA) between Sequoia Scientific, Inc. of Bellevue, Washington and the United States Geological Survey1 (USGS). This instrument measures PSD, SSC, velocity, temperature, optical transmission, and depth, all at 1Hz. Czube et al.(2015) published an instrument evaluation. The data presented in this paper are from 2 rivers, one in Washington State,US and another in Yangtze river at Wuhan, China.

INSTRUMENTATION

The measurements were made with the LISST-SL instrument, and more recently with its successor the LISST-SL2. The instrument is a complete package that includes sensors for flow velocity, depth, water temperature, iso-kinetic intake control, laser diffraction optics, and sensors for engineering parameters. Power is provided via a 2-conductor wire (USGS standard B-reel), and data is transmitted from the instrument to a surface Topside Box (TB) which contains battery and data relay electronics. The TB delivers data to a laptop computer where data are processed for immediate display and storage. The data from

---

1 The CRADA does not imply an endorsement of the instrument by USGS.

LISST-SL2 are processed every second and all parameters (PSD, depth, temp., velocity) are displayed. Upon saving a datafile, a menu option on LISST-SL2 software computes and displays averaged quantities over selected depths and depth ranges. Details are at https://www.sequoiasci.com/product/lisst-sl/ . The instrument can be used from bridges following USGS procedures as used for samplers, or a boat, Fig. 1.

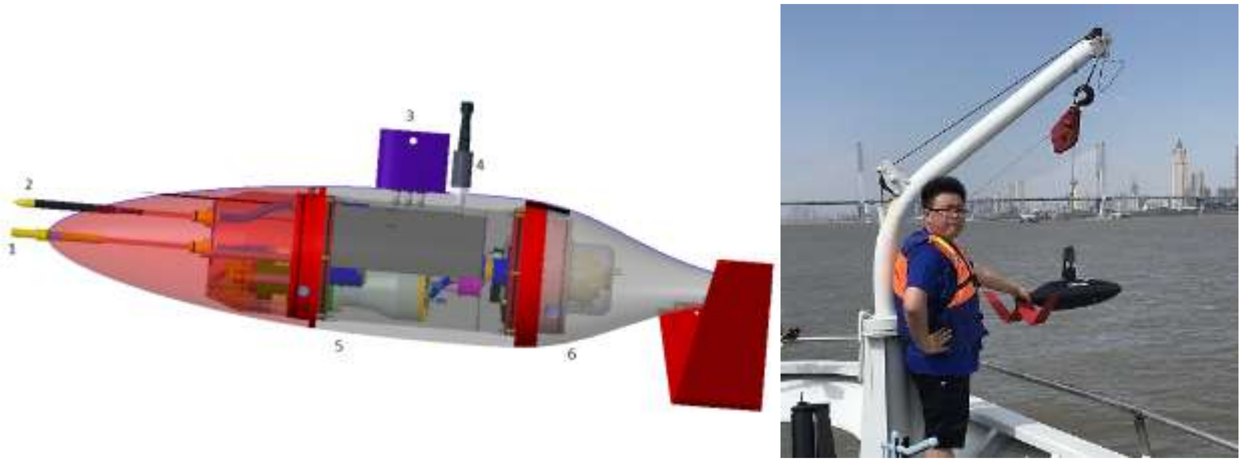

Figure - 1: LISST-SL2 with shown transparent colors, and as used from a boat in Wuhan, China.

3. DATA

Cowlitz River, Washington, USA: Data acquired during a field test of the original LISST-SL by USGS personnel were plotted as vertical profiles. The LISST-SL and -SL2 record optical transmission across a

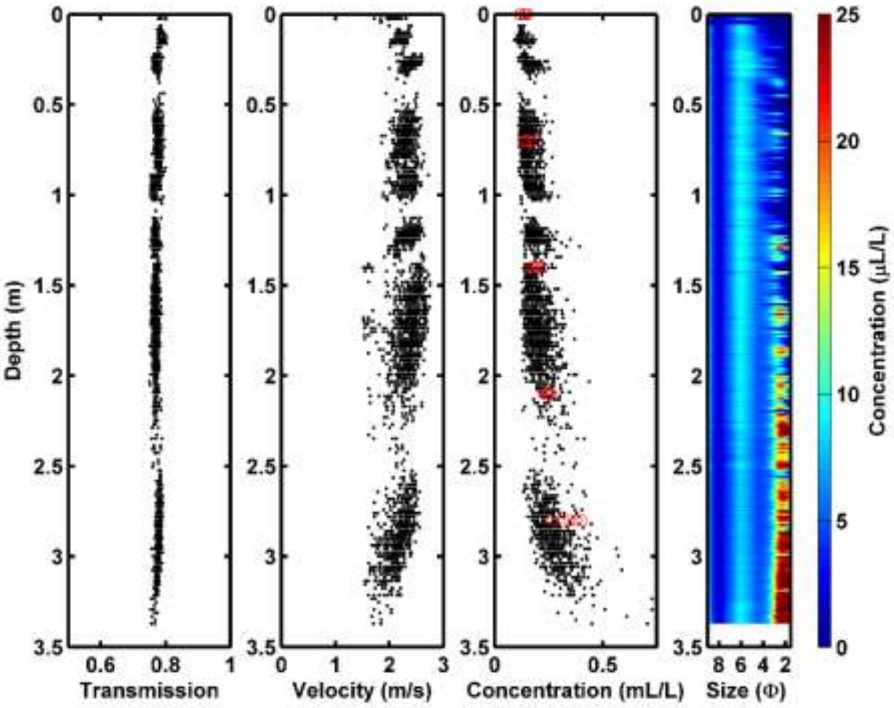

Figure - 2. Vertical profiles of transmission, velocity, SSC, and particle size distribution from Cowlitz River, Washington, USA. Data were obtained on 15 March 2011 by USGS personnel. Red circles in concentration profiles (3rd panel) are physical samples obtained by USGS personnel.

3mm path, which is a single-parameter measure that acts as indicator of turbidity. Transmission, velocity, SSC and PSD are shown below plotted as functions of depth.

These data show the difficulty of SSC measurement with turbidity sensors. Whereas the turbidity appears nearly constant through the water column, the concentration shows an increase with depth. Similarly, the particle size distribution shows a sand mode that is absent at the surface but grows to become prominent with depth. The SSC profile shows a distinct minimum at each depth, except the lowest. This corresponds to the vertically constant wash load at a ⍰ value of 6 throughout the water column, as clearly seen in the PSD data. This structure fits the classical channel flow. The apparently constant turbidity misses this profile view due to the poor responsivity of turbidity to increasing grain size. These detailed data contain lot more information that we shall discuss later.

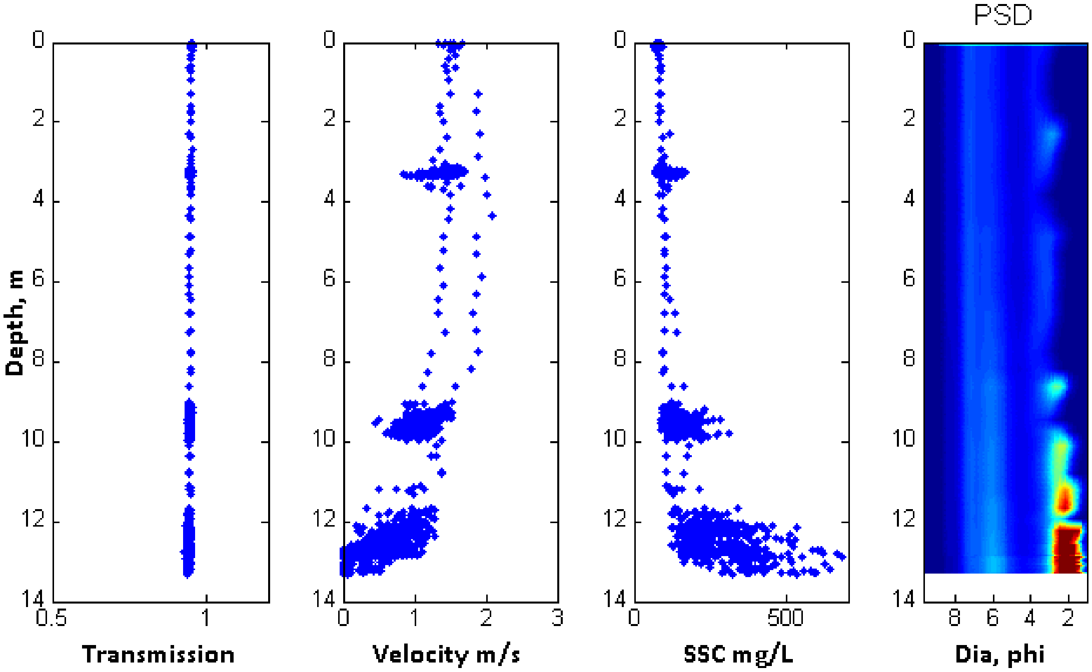

Figure - 3: A single profile at the eastern station in Yangtze river shows 1,272 samples collected over 20 minutes. LISST-SL2 was held at 3.5, 10 and 12.5m depth. Sparse data are obtained during change of instrument depth.

Yangtze River, Hebei Province, China: The more advanced LISST-SL2 was used in the Yangtze river at 3 stations across the river channel, on 27 June, 2018. Data were collected by local river personnel, principally at a few discrete depths selected as 60% of nominal depth and deepest. Figure 3 shows the results, qualitatively similar to Figure 2.

4. DISCUSSION

In both rivers, the turbidity-like optical transmission is vertically uniform, left panels, Figs. 2 and 3. Thus turbidity measurements misrepresent the true structure, as revealed in the concentration profiles, panels 3, Figs.2 and 3 . This is a well-known behavior of turbidity sensors, whose response (V/concentration) varies as 1/*d, d* being grain diameter of sediment. Consequently, the larger grains of suspended sand do not significantly affect turbidity. Regarding the velocity data, we note only that they are relatively constant until the reduction near-bottom.

Returning to measurements of sediment concentrations and particle size distributions, we briefly discuss the statistics of concentrations, time-scales of fluctuations of different size fractions, vertical variation of particle size distribution averaged over small depths (compared to river depth), the vertical gradients of different size classes in the context of Rouse profiles, and the direct estimate of turbulent flux.

Concentration statistics: A close look at the concentration profiles of Figs.2-3 (3rd panels) reveals that for any depth, there exists a sharp minimum, to which an apparently random scatter of concentrations is observed. The size distributions in the 4th panel on each figure explain this behavior – the minimum is defined by the vertically uniform wash-load, on which fluctuating suspended load is superposed. An examination of the histograms of data of Fig.2 clearly displays the

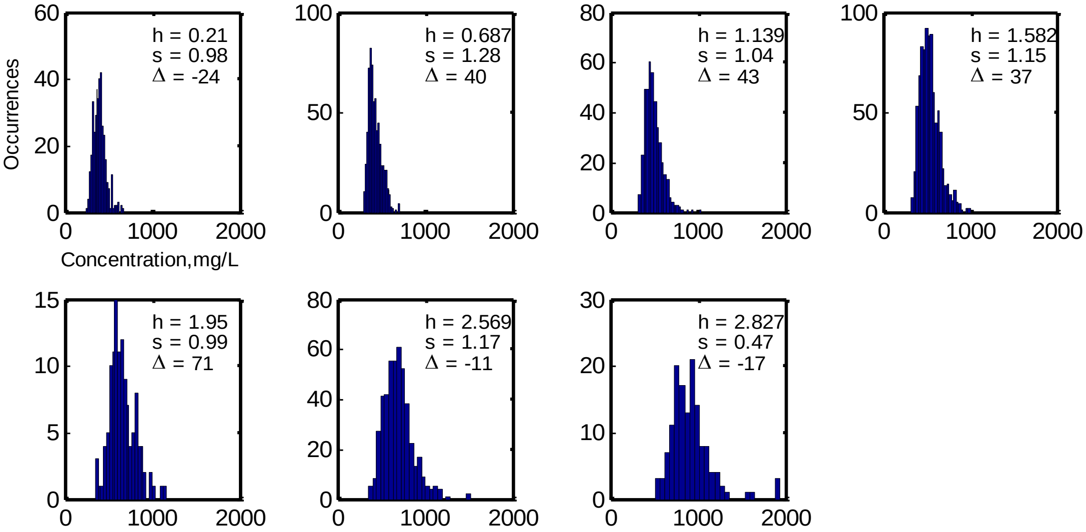

the need for 16 bottle samples to obtain a stable mean.

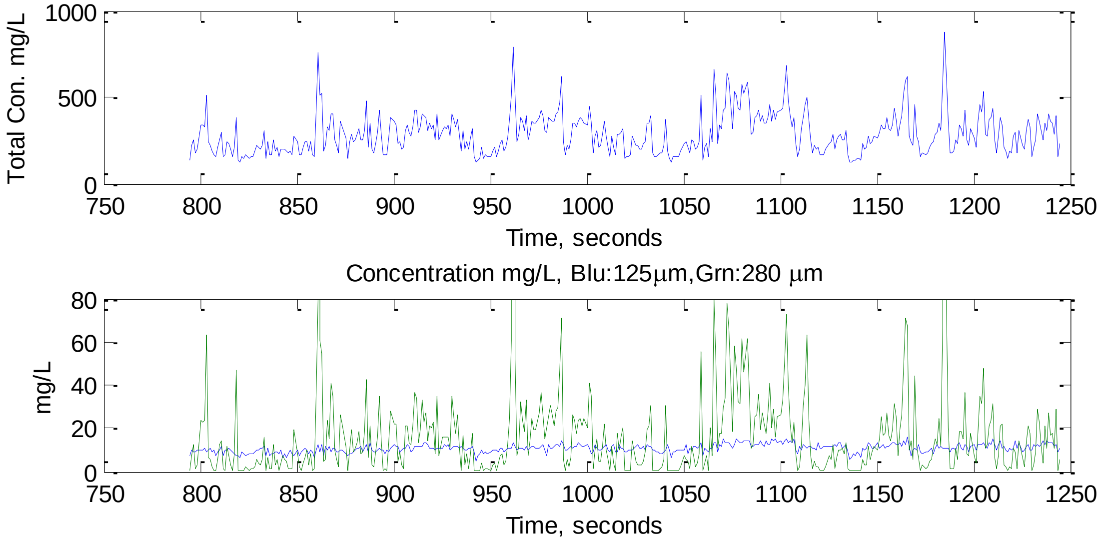

Figure -5: Time scales of fluctuations (top), and of two size classes – 125 and 280µm; Yangtze river data.

Integral Time Scales: A look at the time series of total concentration reveals long period fluctuations, showin in Fig. 5 (top). When the time-series of distinct sizes is plotted, the differing time scales for sands that are quite close in size, 125 and 280µm are distinct. This clearly points to resuspension of fine sand and coarse sand in uncorrelated events. One can qualitatively infer that concentration fluctuations near this riverbed had time scales of order 50 seconds, so that, again it follows that to obtain good averages, several minutes of the time series are necessary.

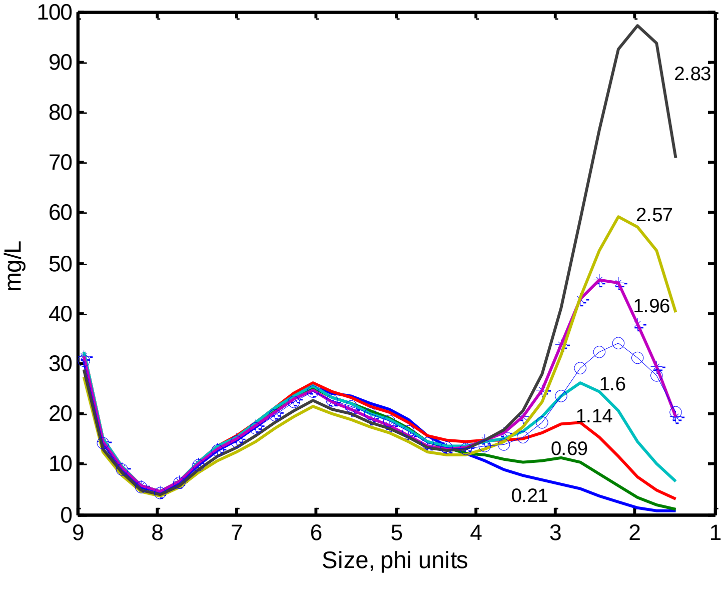

Figure - 6: Mean PSD at depths marked on each curve, Cowlitz river data.

Particle Size Distribution: Due to the rich depth profile of the Cowlitz river data, we choose to display the vertical variation of PSD in it. Fig. 6 shows the PSD at depths marked on each curve, and the half-depth profile is identified with circles.

In the final figure we show the vertical profile of concentraton of various size grains (left) and the vertical profile of flux of sediments, separated into washload and suspended load at size 63μm. The flux is computed as the product of means, velocity and concentration. The decomposition into mean and turbulent, correlated flux <U'C'> is omitted for the present.

The vertical profiles of concentration of various grain sizes reflect the Rouse-like increase in gradient with increasing grain size. We have used these profiles of various size grains, along with the Rouse formulation to estimates the bottom friction velocity. To estimate u_*, we equate the slope of logarithmic profiles to -$w_{f,n}/k u_*$, where $w_{f,n}$ is the fall velocity of size *n* and *k* is von Karman's constant. These estimates are reproduced in Table 1, they fall in a narrow range. These estimates can be compared with direct estimates, but we leave that to a later report. There appears to be a consistent increase in estimated value u_* with increasing grain size. We do not have an explanation for this increase. Also, since the location of the riverbed or bed profile is not known exactly, there are unknown errors in these estimates.

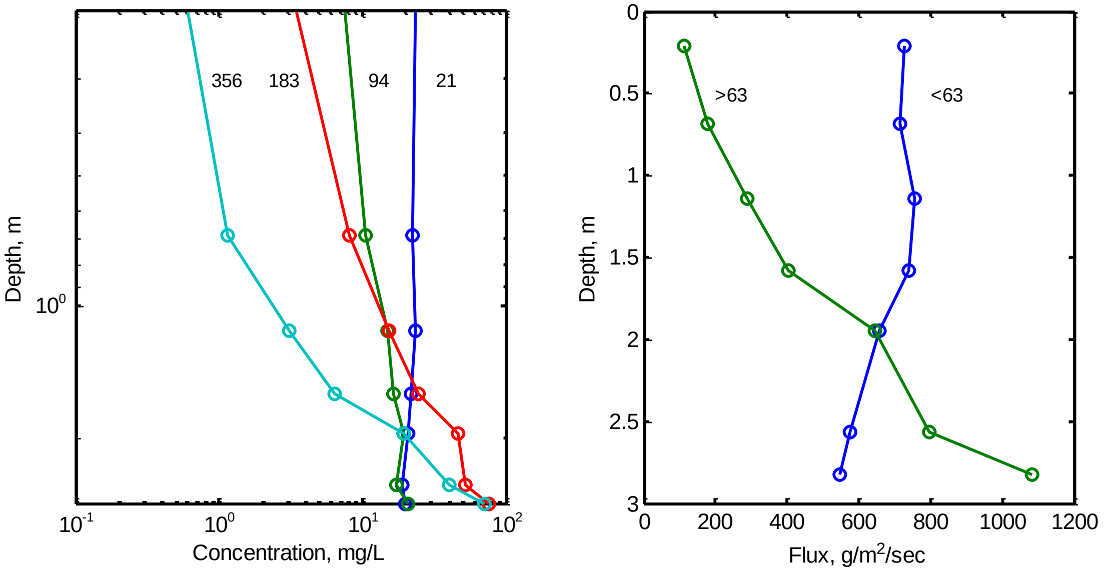

Figure - 7: Vertical profiles of concentration of a few selected size grains (left), and flux of washload and suspended load. Note. the ordinate on left is logarithmic/

Table I: u_* estimates from profiles of different sized grains.

Size *microns*	171	202	238	281	332	391	462
Dia. μm	131	155	183	216	255	302	352
u_* cm/sec	5.2	5.2	5.3	5.6	6.1	6.9	8.3

5. SUMMARY

New instruments provide river column data on sediments and velocity in conformity with iso-kinetic principles. Classical forms of sediment distributions are seen to occur in two rivers. The data permit examination of established theories and conventions on sampling river sediments.

ACKNOWLEDGEMENTS

The Cowlitz river data in this report were collected by USGS personnel as a part of instrument evaluation. The Yangtze river data were obtained on a test cruise with the Yangtze River Authority. We are thankful to both for permitting use of their data.

BIBLIOGRAPHY

Agrawal, Y.C., Amanda Whitmire, Ole A. Mikkelsen and H.C. Pottsmith, 2008: *Light Scattering by Random Shaped Particles and Consequences on Measuring Suspended Sediments by Laser Diffraction*; J. Geophys. Res.

The Biedenharn Group, (2010): *Toutle/Cowlitz River Sediment Budget*, un-numbered Report prepared for the US Army Corps of Engineers, Portland District, OR, USA

Czuba. J.A. et al.(2015) *Comparison of fluvial suspended sediment concentrations and particle size distributions measured with in-stream laser diffraction and in physical samples,* Water Resources Res.

Gitto, A.B., Venditti, J.G., Kistaschuk, R. And M. Church (2017): *Representative point-integrated suspended sedimen sampling in rivers,* Water Resources Res. V 53 1-16pp.

Guerrero,M., Ruther, N. Hau, S. And S. Baranya (2017): *A combined use of acoutcis and optical devices to investigate suspended sedimen in rivers,* Advances in Water Resources, v 102, 1-12pp.

Kazimierz, B. A.J. Horowitz, P.N. Owens, M. Stone and D.E. Walling,(2010) (eds.) IAHS Publication 337, *ISBN 978-1-907161-10-0, 376pp*

Languione, P., A. Crave and A. Jigore, 2007: *Velocity and suspended sediment concentratin profiles in rivers: in situ measurements and flux modeling*, River Basin Management IV, 335., WIT Transactions on Ecology and the Environment, v 104, pp335-343.

Orton, P.M. and G.C. Kineke, 2001: *Comparing calculated and observed vertical suspended-sediment distributions from a Hudson river estuary turbidity maximum*, Estuarine, Coastal and Shelf Science, v 52, pp 401-410

Schlichting, H. (1968): Boundary Layer Theory, McGraw Hill, New York.

Advection by ocean currents modifies phytoplankton size structure

Joan S. Font-Muñoz[1*], Antoni Jordi[1], Idan Tuval[1], Jorge Arrieta[1], Sílvia Anglès[1], Gotzon Basterretxea[1]

[1] Institut Mediterrani d'Estudis Avançats, IMEDEA (UIB-CSIC), Esporles, Mallorca, Spain

*jfont@imedea.uib-csic.es

ABSTRACT

Phytoplankton size structure has a profound effect on the ecology of aquatic environments and, cumulatively, may impact biogeochemical cycling at the global scale. Here we present results of a coastal study where spatial variations in phytoplankton size-structure are analyzed. We use a new methodology that combines simultaneous measures obtained with a laser in situ scattering and transmissometry instrument (LISST) and fluorescence profiles to assess the size-structure of phytoplankton *in situ*. Our results show spatial variations in the dominant size of phytoplankton associated with coastal circulation patterns at relatively large scales (1–10 km). We compare the measured variations with the simulated preferential concentration patterns obtained with a numerical model to assess the role of advection by ocean currents. This physical preferential concentration mechanism has important ecological impacts from the phytoplankton level to the whole ecosystem.

INTRODUCTION

Phytoplankton consists of heterogeneous and phylogenetically diverse microscopic organisms with a cell size ranging from 0.02 to 200 µm [1]. Traditionally, microphytoplankton cell sizes have been measured using light microscopy. However, this methodology is very limited for obtaining an accurate description of the large diversity existing in phytoplankton cell sizes or for assessing rapid variations in time. This is particularly true in coastal ecosystems where phytoplankton dynamics are highly variable and affected by several factors, both natural and anthropogenic [2].

Here we analyze the interplay between biological and physical processes at shaping phytoplankton size structure at relatively large scales (1–10 km). The study was carried out in the inner part of the Palma Bay (Mallorca Island, Mediterranean Sea). We use combined data of fluorescence and laser in situ scattering and transmissometry (LISST) to depict the size-spectrum of microphytoplankton. A new data analysis method is used to extract the phytoplankton signal from the suspended particle size distribution provided by the LISST [3]. This new method is based on the canonical correlation analysis (CCA) [4]. The results of the field data are compared with a preferential concentration particle model to assess the effect of coastal hydrodynamics on phytoplankton size structure.

MATERIAL AND METHODS

Field profiles of particle size distribution and fluorescence were measured in the inner part of Palma Bay. A grid of 37 stations was sampled twice, on June 16-17th and on September 25-26th 2009. At each station a LISST-100X (Sequoia) and a Seabird-25 CTD equipped with a Cyclops-7 fluorometer (Turner Designs) attached to a single frame were lowered to the seafloor at low speed (~0.3 m s^{-1}). The phytoplankton size structure and abundance was separated from the particle size distribution using a CCA along with the chlorophyll concentration [3]. Ocean horizontal currents were recorded underway with a 1200 kHz RDI Workhorse Sentinel acoustic Doppler current profiler (ADCP) during each survey [5].

To assess the influence of hydrodynamics in the size distribution of microphtoplankton we used a preferential concentration model that takes into account the physical interaction between passive particles and the measured near-surface (horizontal) ocean currents. We considered phytoplankton cells as passive particles because we were interested in the effect of advection.

RESULTS AND DISCUSSION

Prior to field sampling, we tested the performance of the CCA method for separating phytoplankton from other non-fluorescence particles with a series of synthetic laboratory samples generated by mixing cultured phytoplankton cells and natural sediments with grain sizes within the size range of phytoplankton. The method yield reliable estimation of the algal fraction allowing the discrimination of phytoplankton size distribution when algal cells constituted more than 25% of total suspended particulate matter. Uncertainties arose at very turbid waters and when samples were composed by two phytoplankton species with very different contribution to chlorophyll in terms of cell size. Nevertheless, high turbidity waters are very exceptional at the sampling site, therefore the CCA methodology is expected to provide good results throughout our surveys.

During the surveys, the highest abundances of phytoplankton were distributed in two size ranges: 11.91 ± 3.24 µm and 30.23 ± 5.58 µm for the June survey, and 12.28 ± 3.65 µm and 30.88 ± 6.29 µm for the September one. Figure 1 shows the spatial distribution of phytoplankton in these two size ranges and the ocean currents at 5 m depth for the two surveys. In the June survey, both phytoplankton size ranges were mainly distributed near the coast in the western side. The alongshore flow direction in this area suggests phytoplankton advection from Palma Harbor to the east. In addition, currents developed an anticyclonic gyre structure as a consequence of the strong wind event three days before the survey. Interestingly, the large phytoplankton size range was almost absent inside the gyre in contrast to the small size range. In the September survey, both phytoplankton size ranges displayed a very distinct distribution. Small size

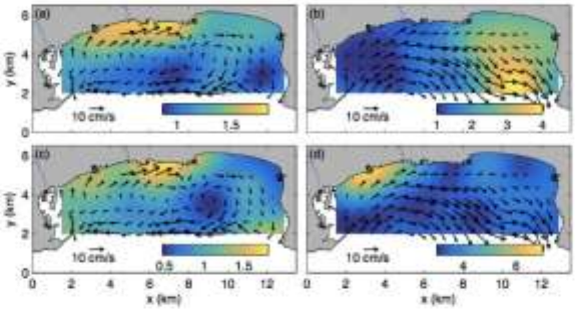

Fig. 1. Near-surface distributions of (a, b) currents (vectors, cm s^{-1}) and smaller phytoplankton size range (colors, 105 cells m-3) and (c, d) currents (vectors, cm s^{-1}) and larger phytoplankton size range (colors, 10^4 cells m^{-3}) for the (a, c) June and (b, d) September surveys.

ranges were widely distributed in the eastern side while large size ranges were localized near the coast close to the Palma Harbor.

Figure 2 compares the measured preferential concentration areas with the model results. During the June survey, measured small cells were preferentially found inside the anticyclonic gyre and near the coastal areas of the eastern side and in front of Gros Torrent. Model results were consistent with the measurements on the location of small cells inside the gyre. Since the model only simulates advection of passive phytoplankton cells, the potential influence of biological processes is not considered. Nevertheless, the agreement in the center of the domain was very high ($r = 0.83$, $p < 0.001$). In the September survey, small cells were preferentially found in the southeastern part of the domain. The model displayed a similar preferential concentration area, although the maximum probability was slightly displaced to the north. The correlation between observed and simulated fields was also very high ($r = 0.81$, $p < 0.001$).

Our results show significant differences in the size structure and spatial distribution of phytoplankton cells associated with the circulation patterns. The preferential concentration model confirms that these differences in phytoplankton are largely explained by the physical advection of phytoplankton cells by the ocean currents, especially in areas away from coastal nutrient inputs.

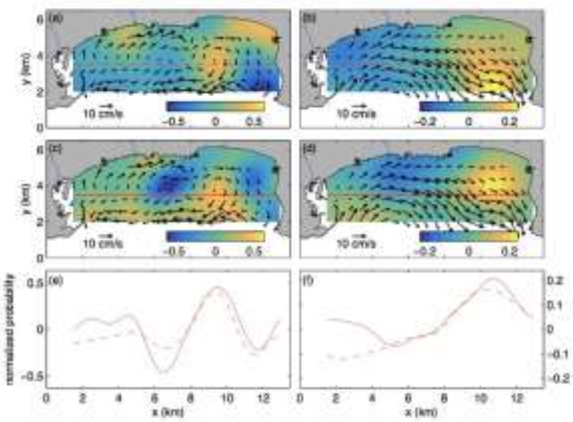

Fig. 2. Near-surface distributions of currents (vectors, cm s^{-1}) and preferential concentration areas (colors, dimensionless) for (a, b) measurements and (c, d) model results during the (a, c) June and (b, d) September surveys. (e, f) Comparison of the measured (dashed red line) and model (red line) preferential concentration along the red line in (a, b, c d) during the (e) June and (f) September surveys.

REFERENCES

1 - Sieburth, J. M., Smetacek, V. & Lenz, J. 1978 Pelagic ecosystem structure: Heterotrophic compartments of the plankton and their relationship to plankton size fractions. *Limnol. Oceanogr*. 23, 1256–1263.

2 - Babin, M. 2003 Variations in the light absorption coefficients of phytoplankton, nonalgal particles, and dissolved organic matter in coastal waters around Europe. *J. Geophys. Res.* 108.

3 - Font-Muñoz, J. S., Jordi, A., Angles, S. & Basterretxea, G. 2015 Estimation of phytoplankton size structure in coastal waters using simultaneous laser diffraction and fluorescence measurements. *J. Plankton Res.* 37, 740–751.

4 - Hotelling, H. 1936 Relations between two sets of variates. Biometrika 28, 321–377.

5- Jordi, A., Basterretxea, G. & Wang, D. P. 2011 Local versus remote wind effects on the coastal circulation of a microtidal bay in the Mediterranean Sea. *J. Mar. Syst*. 88, 312–322.

Remote sensing of sediment settling velocity in estuarine and coastal waters

Hussain J. Nasiha, Palanisamy Shanmugam

Ocean Optics and Imaging Laboratory, Department of Ocean Engineering, Indian Institute of Technology Madras, Chennai, India

*Corresponding author: Email : nasiha.1642@gmail.com

Abstract

The settling velocity is an essential parameter used for quantification of the transport of sediments and investigation of sediment dynamics in coastal, estuarine and harbor waters. In the present study, we developed and demonstrate a robust method to estimate sediment settling velocity (w_s) using Landsat-8 OIL images from coastal water around India. The key input parameters include drag coefficient (C_d), Reynolds number (Re), grain size (D_{50}), specific gravity (Δ_{SG}) and grain shape (CSF) which are derived from remote sensing reflectance data using empirical methods. The particulate inherent optical properties such as backscattering (b_{bp}), beam attenuation (c_p), suspended sediment concentration and turbidity are the intermediate optical parameters derived from remote sensing data. Preliminary results from the Landsat 8 OLI data in Gulf of Cambay in the eastern Arabian Sea showed that settling velocity ($\times 10^{-4}$ cm s^{-1}) varied from 1.5 – 2.0 for clear oceanic waters (low sediment contents), 2.2 – 2.5 for phytoplankton-dominated waters (higher water content), 2.7 – 4.0 for coastal waters (suspended detritus and sediments), and 7.5 – 10.0 for river plumes and sediment-laden coastal waters (high sediment load). These preliminary results were consistent with those obtained in the previous field and laboratory studies.

Introduction

Sediment settling velocity is an important parameter for the quantification of sediment load and transport for various engineering and environmental applications. When a solid particle is released in a less dense flowing fluid medium, it will initially accelerate due to its mass and gravity force (F_g). Resistance to deformation of the fluid, transferred to the particle by the surface drag on it and pressure differences across the particle, generates forces that act to resist the particle motion (Dietrich, 1982). The resistance forces are drag force (F_d) generated by fluid flow and buoyancy force (F_b) generated by pressure difference on the submerged particle. Deposition or entrainment of sedimentary particles is determined by the enforcement of downward force of gravity (F_g) and the restraining force of drag (F_d) plus the buoyancy force (F_b). When the particle's downward gravitational force exactly equalizes these two resistant forces, the particle acceleration is terminated and it attains a constant velocity (Stokes, 1850) termed as settling velocity. Settling velocity of particles varies widely by the origin and nature of sediments together with the flow conditions in natural waters (Stokes, 1850; Dallavalle 1948; Van Leussen, 1994; Guo 2002). Currently, the Stokes' law applied is not adequate to estimate sediment velocity in a wide range of flow conditions. Recently, Nasiha and Shanmugam (2018) gave a solution on the estimation of the influencing parameters of settling velocity from the optical measurements. In their work, good correlations between the grain properties (size, shape and composition) and backscattering and attenuation coefficients were found. These inherent optical properties can be easily derived from remote sensing reflectance data (Loisel et al., 2006; Vadakke-Chanat et al., 2017). This study attempts to derive the model parameters and estimate sediment settling velocity using high spatial resolution remote sensing data.

Preliminary Results

Sediment settling velocity was estimated from satellite remote sensing data using a robust method proposed by Nasiha and Shanmugam (2018). A number of the key input parameters needed for this method are namely particle median diameter (D_{50}), shape factor (*CSF*) and sediment specific gravity (Δ). These parameters were derived from the remote-sensing reflectance using empirical relationships established in this work (Table 2). The sediment settling velocity was then estimated from,

$$w_s = \left[\frac{-42\times10^{-6}}{D_{50}} + \left(\frac{0.176\times10^{-8}}{D_{50}^2} + \frac{290.93D_{50}\Delta}{10.1148^{CSF}} - 44.57D_{50}\Delta ln(CSF) + 8.543D_{50}\Delta\right)^{\frac{1}{2}}\right] \times \left[(11.135\times10.1148^{-CSF}) - \left(1.706ln(CSF)\right) + 0.327\right]^{-1} \quad (1)$$

Comprehensive understanding of the physical and hydrodynamic properties of sediment settling process was essential when deriving the relationships between the input model parameters and in-situ collected remote-sensing reflectance. The applicability of this method was increased by using data from a wide variety of waters in the coastal, estuarine and oceanic regions. (cont.)

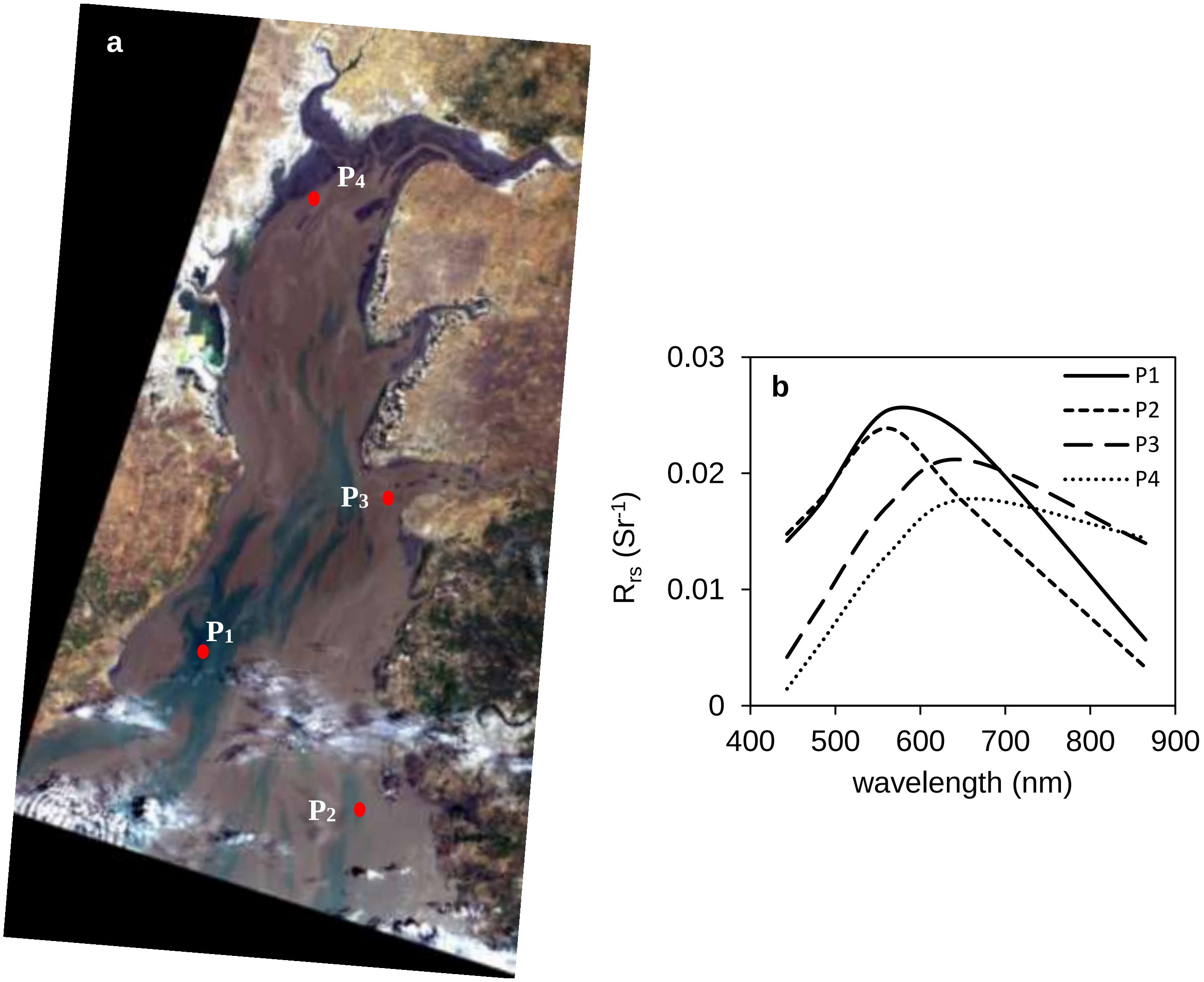

Fig. 1. (a) True Colour Composite (R-655 nm, G-561 nm, B-482 nm) of total radiance (L_t) image acquired by Landsat 8 over Gulf of Cambay on 03 May 2016**;** (b) R_{rs} spectra of random points (P_1, P_2, P_3 and P_4 respectively with increasing sediment concentration).

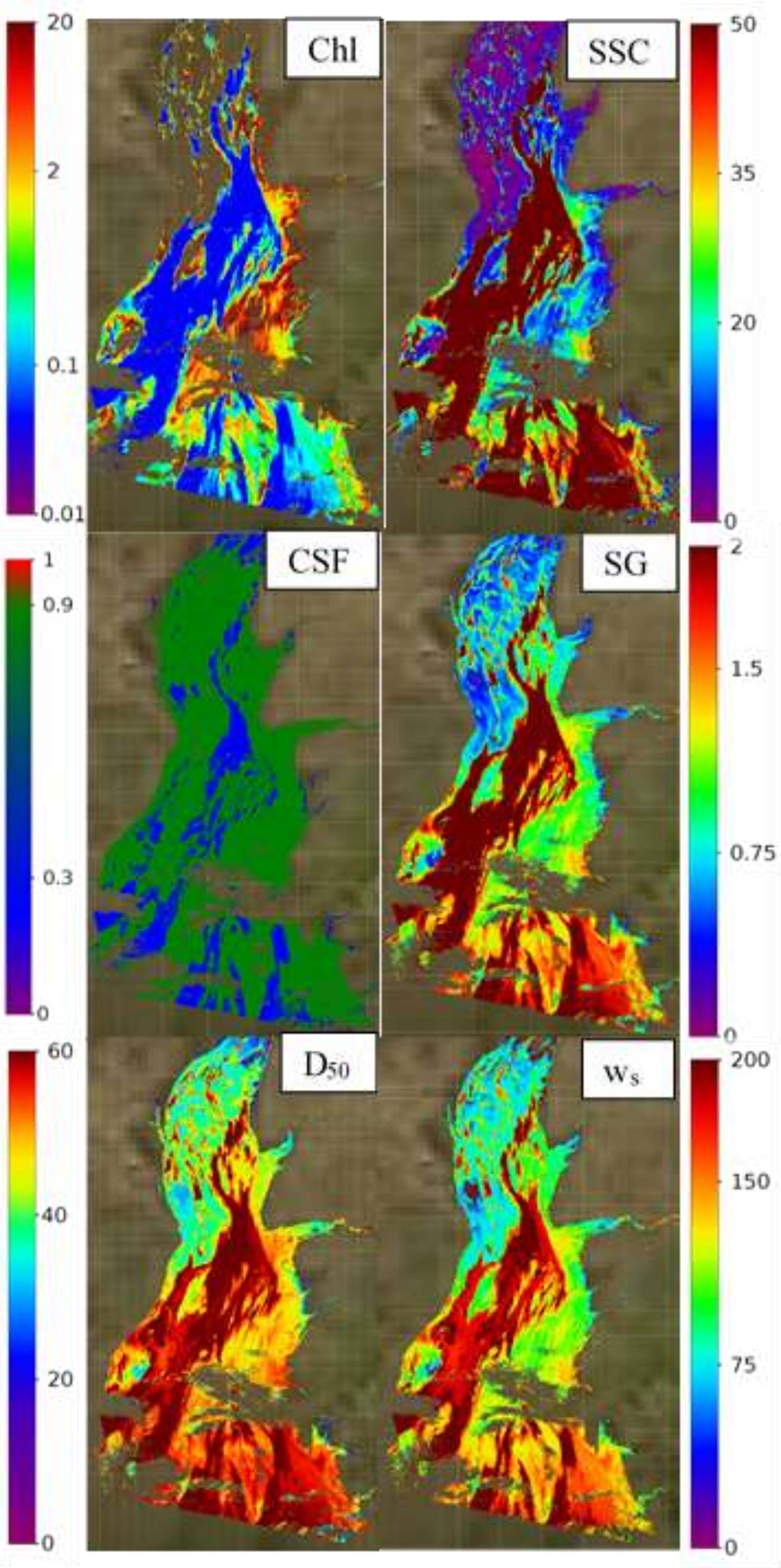

Fig. 2. Maps of the ABI-chlorophyll (*Chl-a*), suspended sediment concentration (*SSC*), Specific gravity (*SG*), Corey shape factor (*CSF*), particulate median diameter (D_{50}), and sediment settling velocity (w_s) derived from the Landsat 8 imagery over Gulf of Cambay on 03 May 2016 using the present remote sensing method.

A biophysical food pump: mechanisms promoting prey availability to top predators at a tropical seamount

Alex Nimmo Smith, Phil Hosegood and Jill Schwarz,

University of Plymouth, School of Biological and Marine Sciences, Plymouth, United Kingdom

Tropical seamounts are recognised as hotspots for top-level marine predators (e.g. sharks, tuna, seabirds), but the physical mechanisms that promote prey availability (macro-zooplankton, small fish) to these are not well understood. Taylor-columns located over seamount summits have been postulated as trapping prey, primarily immotile phytoplankton, but require a steady and stable background mean current flowing past the seamount. In contrast, we show how regular, periodic injections of food to the summit waters of a shallow seamount are driven by the combined actions of the tides, the background internal wave field, and diurnal migration patterns of zooplankton. The observations are derived from a mooring deployed for a two-week period in February 2016 over the summit of a shallow (~70m) seamount in the Chagos Archipelago, British Indian Ocean Territory – recognised as a shark and seabird hotspot of global significance. The mooring comprised of ADCPs and thermistors to measure at high spatiotemporal resolution the currents, acoustic backscatter and temperature structure throughout the water column, as well as near-bed (8m HAB) instruments to image suspended particles (LISST-HOLO) and record nitrate concentrations.

The data reveal periodic injections of cold, nutrient rich water onto the seamount summit, driven by the semi-diurnal tides and higher frequency internal waves breaking over the summit flanks. Appearing as turbulent, sharp- fronted bores with dynamic characteristics consistent with breaking internal waves, these injections resuspend and transport detrital material in patches, including dense accumulations of zooplankton trapped at the seabed at dawn as they attempted to descend to the Deep Scattering Layer (trophic focussing). These combined mechanisms enhance prey availability at lower trophic levels and, we propose, sustains through bottom-up forcing the dense shark population observed to be omnipresent around the seamount summit.

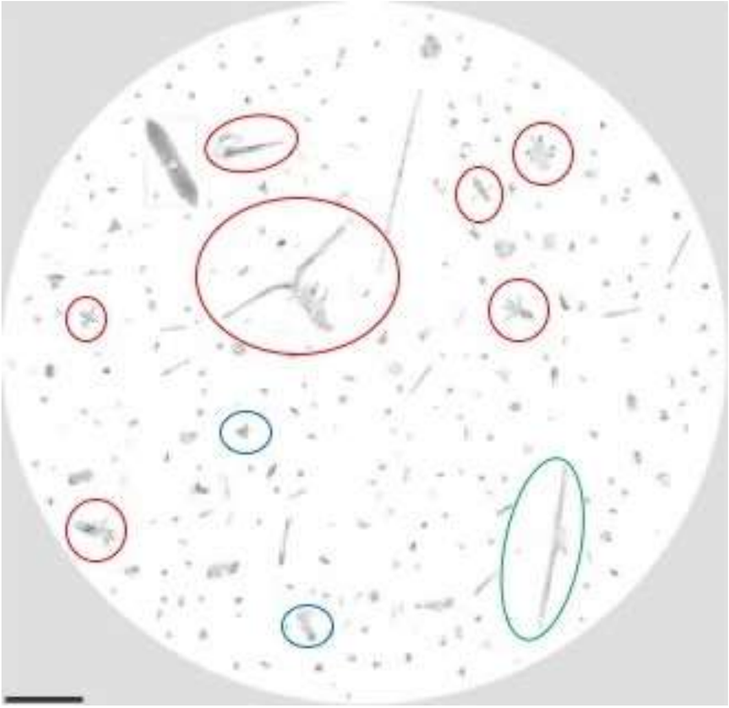

Figure 9 - Sample montage of suspended particles and plankton imaged by the LISST-HOLO, collated from a period when colder water is injected over the seamount summit, resuspending material and transporting plankton. The white circle indicates the total sample-volume from which the individual particles have been extracted for display (~400ml). The scale bar is 500microns. Examples of flocs, diatoms (phytoplankton) and zooplankton have been circled in blue, green and red respectively.

LISST200X - Instrumental response to suspended volcanic particles with low concentration values (Madeira Island - Portugal)

Oliveira[1] and A. I. Santos[1,2]

[1]Instituto Hidrográfico, R. das Trinas, nº 49 – 1249-093 Lisboa, Portugal,
anabela.oliveira@hidrografico.pt

[2]IDL/Faculdade de Ciências da Universidade de Lisboa, Campo Grande, 1749-016 Lisboa, Portugal

INTRODUCTION

Madeira Island is located in the subtropical region of the Atlantic Ocean, presenting a mild weather pattern, both in summer and winter with mean temperature of 18,7ºC (Funchal). Generally, winds originate from the N-NE quadrant and are stronger during late spring and early summer (Caldeira & Sangrà, 2012). Madeira Island is characterized by a high energy wave regime, with waves coming from W-NW direction, with mean heights between 2.5 and 5.0m (Rusu *et al.,* 2008; Rusu & Soares, 2012).

Studies related with the Madeira shelf sediment dynamics are almost nonexistent or very limited in time and space. Recently published studies concerning the southern area show the presence of a coastal current, parallel to the bathymetry contrasting from the oceanic current. This superficial current promotes the retention of sediments along the coast, with several points of convergence/divergence, with maximum intensity offshore the city of Funchal (Reis *et al.,* 2018).

In this study, suspended and bottom sediment dynamics associated with the semi-diurnal tidal cycle is addressed, based on data collected at a fixed station offshore Funchal. Concurrently, some efforts are made to understand LISST 200X (Sequoia Scientific) response to oceanic waters with very low concentration values.

METHODS

On August 7th 2017, a fixed station offshore the city of Funchal (Latitude: 32º37'56.0''N; Longitude: 16º56'10.7''W) was surveyed using NRP "*Auriga*" anchored at the same position (~25,5m depth), during approximately a semi-diurnal tidal cycle (10 hours). A LISST 200Xprobe was hourly lowered into two different levels in the water column (≈10m and ≈23m) in order to determine volumetric SPM concentration and grain size distribution. Water samples (≈5 liters) were collected hourly, at 10m depth, using a pump and filtered onboard to determine SPM concentration and calibrate the LISST200X response. Filters were dried (40ºC) weighted and photographed under a stereomicroscope (115x max. amplification). A superficial bottom sediment sample was also collected using a Smith-McIntyre grab. The sediment was analyzed in the lab for grain size using laser diffraction (Malvern 2000) and sieving (>500µm), after destruction of organic matter (disaggregated particles).

At the same position, for a period of 29 days (26 July -23 august 2017), a structure with an up-looking ADCP working at 614.4 kHz frequency was moored, measuring the current and acoustic backscatter intensity of the water column from 2.11 m above bottom.

LISST data was downloaded from the internal memory and converted to volumetric concentrations (µl/l) using the Matlab algorithms supplied by the manufacturer, assuming randomly shaped particles (Sequoia Scientific, 2008; Sequoia Scientific, 2018). Since LISST concentration limits depend on its optical transmission values and grain size, in a first approach, grain size curve parameters were computed based on the relative frequencies of volumetric concentrations for each size class. LISST 200X data was then validated according to the instructions provided in the instrument's manual (Sequoia Scientific, 2018). All records whose concentration limits were outside the acceptable margins were disregarded (Santos *et al.,* 2018).

Critical depth-averaged velocity for initiation of motion ($U_{cr,motion}$) and suspension ($U_{cr,suspension}$) was computed taking in account the bottom sediment using simple approximation formula (10% accurate according to van Rijn, **www.leovanrijn-sediment.com**):).

$$Ucr, motion = 0.19(d_{50})^{0.1}\log(12h)\,/6d_{50})\; for\; 0.0001 < d_{50} < 0.0005m \; (1)$$

$$Ucr, suspension = 2.8\left[\frac{h}{d_{50}}\right]^{0.1}[(s-1)gd_{50}]^{0.5}\; for\; 0.0001 < d_{50} < 0.002m \; (2)$$

Where: h = water depth (m),

g = acceleration of gravity (m/s^2),

s =ρ_s/ρ_w= sediment density/water density= relative density (-),

d_{50}= median sediment particle size (m)

RESULTS AND DISCUSSION

The fixed station data was collected during spring tide (starting during low tide), under well-established summer conditions with mean air temperatures of 24ºC and strong winds from N-NNE (mean velocity 23-25 km/h; gust speed >40 km/h). The surface wave regime was weakly energetic with wave height ≤ 2m.

At the fixed station site, the collected bottom sediment was classified as fine sand (78% sand, 19% silt and 3% clay). Grain size distributions show a unimodal curve with modal size centered at 105µm (D50= 107µm) and the mean at 86µm. Compositionally, it is dominated by terrigenous particles derived from subaerial alkaline volcanic rock erosion, rich in heavy minerals (clinopyroxene, magnetite, hematite and olivine), rock fragments and plagioclase (Oliveira *et al*., 2018).

The LISST200X temperature sensor registered water temperatures higher than 22.4 ºC. Along the tidal cycle, the surface level (10m) presented higher values due to solar heating (≈23.5 ± 0.35ºC), more stable and well mixed than the bottom level (≈22.5-23.5 ºC). On the other hand, mean current velocity at surface levels was variable with values ranging between 0.05 and 0.58 m/s. Near bottom (23m) the mean current velocities were lower, with maximum values of 0.32 m/s and less variable.

Along the tidal cycle, concentrations obtained by filtering were low, ranging between 0.5 g/m^3 and 8.0 g/m^3. The filters' suspended particles observation show abundance of volcanic terrigenous particles, particularly during flood, but also biogenic remains (phytoplankton and zooplankton) and microplastics (fibers), mostly during ebb. The concentration obtained by LISST200X were also low (< 24,0 g/m^3) with mean values of 7,4 g/m^3 (6.0µl/l) at 23m and 4,5 g/m^3 (3,6µl/l) at 10m, but similar to the ones obtained by direct sampling and filtering (fig.1). The validation routine that was ran through the original LISST dataset, showed that most of the records collected here had to be disregarded due to concentrations below the admitted limit. The remaining samples were flagged as having transmission values in the low signal-to-noise ratio (0.98-0.995) which according to the LISST 200X manual means that the measurements were taken in very clear water but “most likely can still be used” (Sequoia Scientific, 2018). Additionally the reduced particle density of ρ_s=1240 kgm^{-3} suggested by Czuba *et al.,* (2015) to convert LISST volumetric concentrations into mass concentration may prove to be adequate given the very specific nature of Madeira’s natural sediments (volcanogenic heavy minerals and biogenic material).

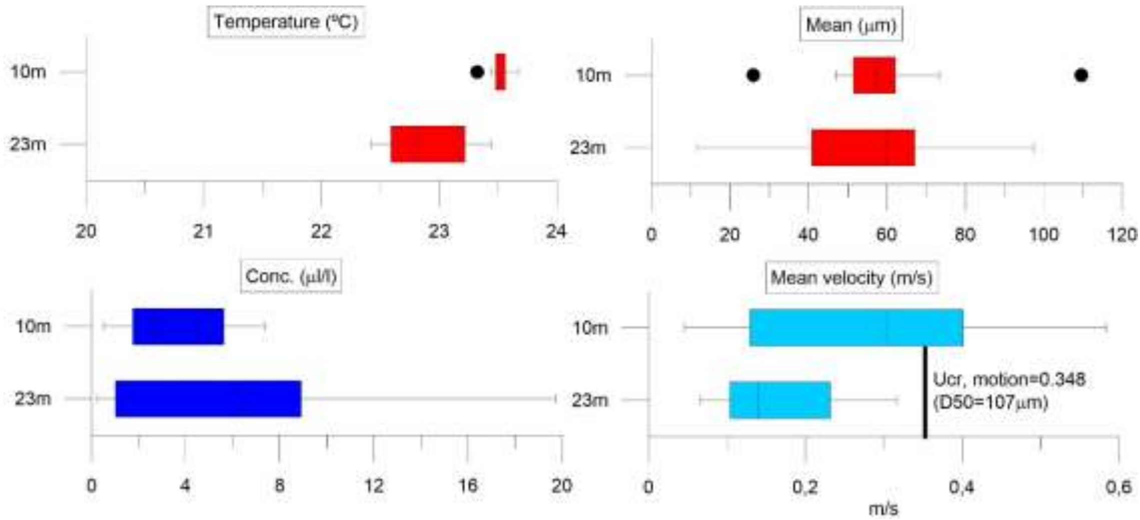

Fig. 1. Fixed station box-whisker plots of temperature (a), suspended particles mean grain-size (b) and concentration (c) obtained with LISST 200X; and mean velocity (m/s) obtained with ADCP 600 (d) at 10m and 23m water depth. In graph d) the bottom sediment velocity of initiation of motion ($U_{cr,motion}$), is represented by a black vertical line, considering a D50 of 107µm. Outliers represented by black dots.

At both levels, LISST 200X grain-size curves (fig.2) show a dominant mode centered at 105µm and a second one at ~250-300µm, normally present at the bottom and also at surface level (10 m) especially significant during ebb. A finer mode is also detected around 6 µm, with higher frequency values also during ebb.

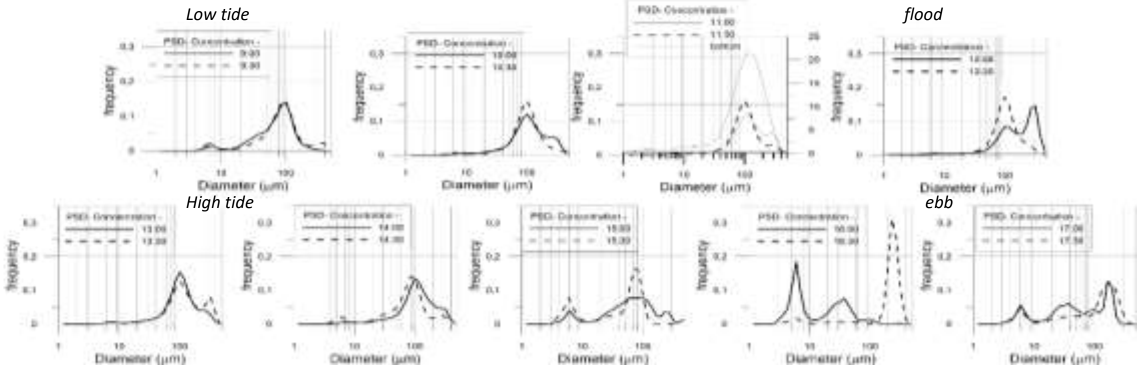

Fig.2. Along tidal cycle, LISST200X grain-size curves (fixed station); at 10m depth (black dashed line) and 23m depth (black solid line); bottom sediments grain-size curve is represented in gray (11:00).

According to this data, the 105µm mode seems to correspond to bottom material transported during flood and deposited in this site during low tide and the coarser mode to microplastics (fibers) and biogenic remains that can easily stay in suspension under very low current velocities due to their higher floatability.

This second modal size may also correspond to living organisms that prefer low current velocities and respond to tidal/light fluctuations; migrating vertically in the water column, for instance, *copepods* (Haney, 1988; Steele, J. & Henderson, W., 1998), and in this case probably juveniles, (~300µm) that tend to dominate a certain size range (García-Comas, *et al.,* 2016).

The ADCP acoustic backscatter data for of the 29 days of deployment (*not shown*), confirmed that during the sampling period (Aug. 7th, 2017) the whole water column presented higher acoustic intensities (> content of suspended particles than the remaining sequence), probably related with higher energy in the environment related with spring tides and SE currents, with possible sediments resuspension and transport from shallower areas. Current velocities during flood were strong enough to maintain in suspension the first modal size of bottom sediment, resuspended elsewhere, since current velocity for suspension is 0.265 m/s and for initiation of motion is 0.348 m/s (fig.1), found at the fixed station site, at surface levels (10m depth).

CONCLUSIONS

During the sampling period bottom sediments seem to be resupended near the coast (possibly by waves) and transported by flood SE currents to be deposited in the fixed station area during ebb (SW currents). Wave data analysis is mandatory to clarify the resuspension periods and transport for deeper areas.

About the validation of LISST200X data in clear waters with volcanic terrigenous and biogenic suspended particles with concentrations below 8 g/m^3 and strong currents. Our data indicate that in respect to grain-size the data seems to agree with bottom sediment signatures, and in respect to concentration the LISST200X yielded values are similar to the collected samples. The particle density values used to convert LISST volumetric concentrations into mass concentration proved to be adequate even with the very specific nature of Madeira's natural sediments (volcanogenic heavy minerals and biogenic material).

REFERENCES

Caldeira, R.M.A. & Sangrà, P. (2012). Complex geophysical wake flows. *Ocean Dynamics*, 62(5): 683-700.

Czuba, J.A., Straub, T.D., Curran, C.A., Landers, M.N., Domanski, M.M. (2015) Comparison of fluvial suspended-sediment concentrations and particle-size distributions measured with in-stream laser diffraction and in physical samples. *Water Resources Research*, 51, 320-340. doi: 10.1002/2014WR015697

García-Comas, C., Lee, Y.C, Chang, CY., Gong, G.C., Hsieh, C.H. (2016). Contribution to the themed section: Advances in plankton modelling and biodiversity evaluation. *Journal of Plankton Research*, 38(4):1006-1020.

Haney, J.F. (1982). Diel pattern of zooplankton behavior. Bull.Mar.Sci, 43:583-603.

Oliveira, A., Santos, A.I., Cunha, S. (2018). Bottom sediment mineralogical and textural variability in the Madeira shelf. *Atas das 5as Jornadas de Engenharia Hidrográfica*, 337-340p.

Reis, J.C., Silva, G., Azevedo, C.C., Caldeira, R.M.A. (2018). Regimes de transporte costeiro na margem sul da ilha da Madeira. *Atas das 5as Jornadas de Engenharia Hidrográfica,* 171-173p.

Rusu, E. and Guedes Soares, C. (2012). Wave energy pattern around the Madeira Islands. *Energy*, 45(1): 771-785.

Rusu, E., Pilar, P., Guedes Soares, C. (2008). Evaluation of the wave conditions in Madeira Archipelago with spectral models. *Ocean Engineering*, 35(13): 1357-1371.

Santos, A. I. (2018). *Acoustic properties of suspended sediments and their implications on using ADCP'S as standalone sediment flux profilers*. Seminário doutoral II - Report prepared under the scope of the PhD in Geology, External Geodynamics, University of Lisbon, Faculty of Sciences, 49pp.

Sequoia Scientific (2008). Processing LISST-100 and LISST-100X data in MATLAB. (Accessed: May 2018).

Sequoia Scientific (2014). Concentration Limits – Advanced. https://www.sequoiasci.com/article/lisst-concentration-limits/ (Accessed: May 2018).

Steele, J. H., & Henderson, E.W. (1998). Vertical migration of copepods. *Journal of Plankton Research*, v.20(4):787-799.

Experimental Investigation of Labyrinth Spillways

Cansu Özyaman, Cahit Yerdelen

Department of Civil Engineering, EU , Izmir, Turkey

cansu.ozyaman@ege.edu.tr; cahit.yerdelen@ege.edu.tr

A labyrinth spillway is a linear spillway that is folded in plan-view. Labyrinth spillway is a good design alternative to control upstream water elevation and increases discharge capacity. However, it can be difficult to make an optimal design due to the many geometric design variables of labyrinth spillways. This study was conducted to improve labyrinth spillway design using different geometric configurations of labyrinth spillway models. In the experiments, triangular, rectangular and linear spillways were used with different number of cycles. Discharge coefficients of the spillways are calculated and compared with the studies in the literature. In addition, 3D velocity measurements were done at the upstream side of the weir at four different cross sections in order to observe the downstream impacts. As a result of the study, it was concluded that labyrinth weirs increase the effective crest length of a spillway significantly, therefore, they increase the flow capacity for a given operating head.

Keywords: Labyrinth spillway, Discharge coefficient, ADV, velocity vector

INTRODUCTION

A labyrinth weir is a linear weir folded in plan view to provide a longer total effective length for a given overall spillway width. Labyrinth weirs can be used to increase outlet capacity for a given spillway crest elevation and length or to increase storage by raising the crest while maintaining spillway capacity (Tullis, J.P 1995).

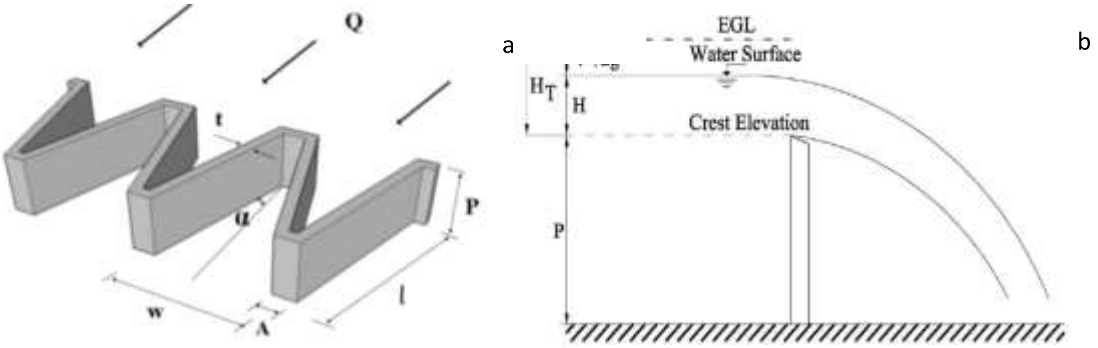

Figure 1. a- Schematic view of the labyrinth trapezoidal weirs (Bilhan, O. 2016) **b-**Weir Parameters on a Sharp Crested Linear Weir (Anderson, 2011)

The capacity of a labyrinth spillway is a function of the total head Ht, the effective crest length L and the discharge coefficient C_d. Discharge coefficient C_d depends on weir height P, total head Ht weir wall thickness t, crest shape, apex configuration, and the angle of the side legs α (Figure 1). Equation (1) is a general equation for linear weirs, and was adopted by Tullis et al. (1995) for labyrinth weirs.

$$Q=\frac{2}{3}*C_d*\sqrt{2g}*L*H_t^{1.5} \quad (1)$$

where Q = labyrinth weir discharge, Cd = dimensionless discharge coefficient, L =crest length, *g* = acceleration constant of gravity, and Ht = total head on the crest.

It is very important to investigate the changes on flow behavior when labyrinth spillway installed in the river channel. Labyrinth spillway applications affect upstream turbulence and therefore sediment deposition or scouring occurs depending on the amount of material that comes from the upstream. Experiments were conducted in order to observe the flow behavior at the upstream side of the weir. 3D velocity measurements were done at the upstream of the weir at four different cross sections. The purpose of this study is to present the effects of labyrinth weir geometries, their number of cycles (N) and angle of side legs on discharge capacity and upstream flow area.

EXPERIMENTS

Experiments were conducted in a 0.7 m wide, 18 m long, 0.5 m deep circulating and slope-adjustable flume, located in Ege University Hydraulic Laboratory (Figure 2). The slope of the flume was fixed at 0.5 %. All the experiments were performed in steady flow conditions.

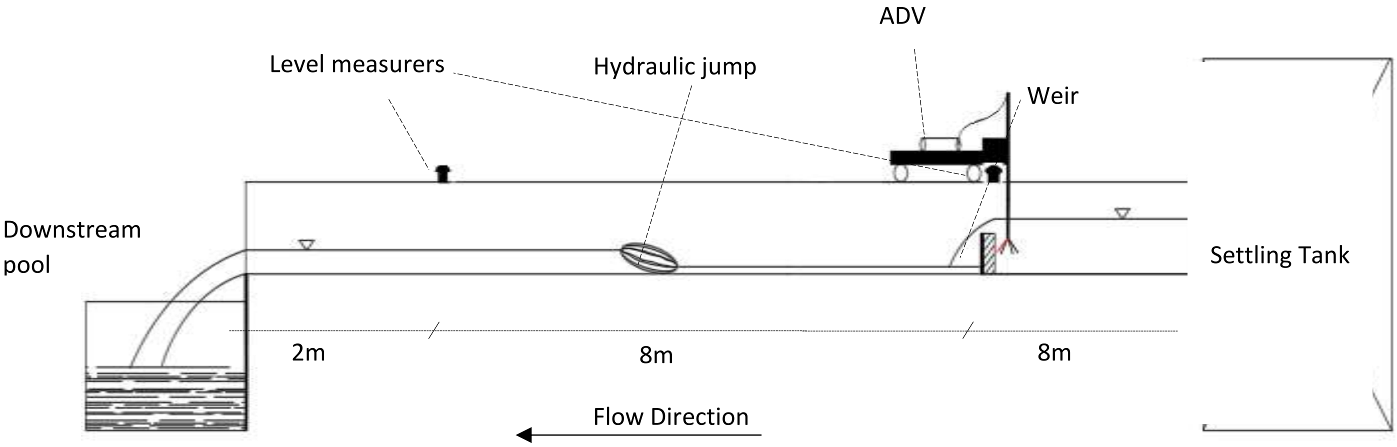

Figure 2. Experiment channel

Experiments were carried out by placing triangular, rectangular and linear spillways having two different number of cycles (N=2, N=3) (Figure 3). Spillways were located 8 meters from the channel entrance. Spillway wall thickness (t) was 2 cm and spillway height was 22 cm and they are same in all experiments. Effective lengths of triangular and rectangular labyrinth spillways were all the same and they were 96 cm. The length of linear weir was 70 cm. Experiments were done at three different discharges (Q=20, 40, 60 l/s). The water level was measured by using ultrasonic level measuring instrument on the crest and after the hydraulic jump (Figure 2).

The three-dimensional velocity components were measured by Nortek Acoustic Doppler Velocimetry (ADV). ADV was installed on movable track above the flume. More than two hundred point measurements were taken with the ADV for each experiment. The duration of 60 second with the sampling rate of 25 Hz were selected. All experimental data were processed using the Velocity Signal Analyzer software written by Mike Jesson. Goring and Nikora’s Phase Space Thresholding method was used to filter the ADV measurements by using this software. The measurements were carried out at 4 cross sections (CS). ADV data taken in vertical direction at an interval of 3 cm. The distance between horizontal measurement points were 5 cm. Measurement sketch is given in Figure 3.

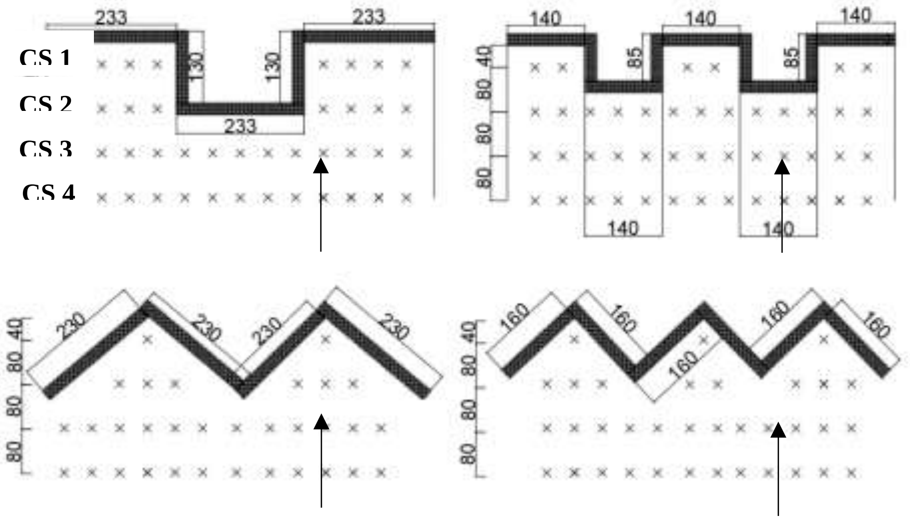

Figure 3. Plan view of the measurement points for triangular and rectangular labyrinth weirs for N=2 and N=3 (unit is mm)

RESULTS AND DISCUSSION

In this study; the discharge coefficients C_d of labyrinth and linear spillways were calculated by implementation of Equation 1. The distribution of velocity vectors in different cross-sections were investigated with velocity data taken with ADV.

Head to weir height ratio H_t/P and discharge coefficients C_D are calculated and given in Table 1. In all experiments, as discharge increases the head on the crest increases. It is apparent from the results that discharge coefficients of the labyrinth weirs are much higher than the conventional linear weirs. The main reason for this is that the crest length of the labyrinth weir is much longer than the conventional linear weir. As shown in Table 1 average discharge coefficient of labyrinth spillways is 0.62 while linear spillway's is 0.84. These results are compatible with the results given in Tullis' study and Bilhan's study. However,

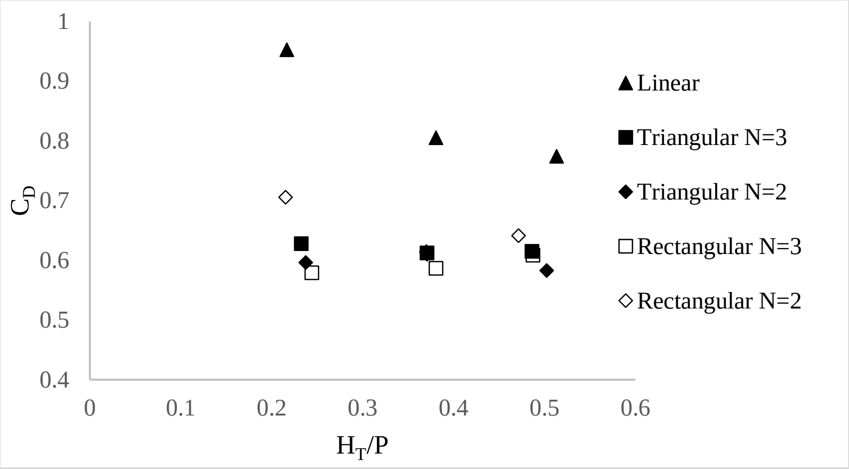

Figure 4 Variation of discharge coefficient (Cd) with head to weir height (Ht/P)

Table 1. Range of parameters

the lack of experiments on various discharges and different crest lengths is an obstacle to provide the tendency of discharge coefficients. It can be said that the close values of C_D is a result of the same effective crest lengths of the labyrinth spillways.

Labyrinth weirs increase flow capacity of spillways due to their longer effective crest lengths. However, increasing turbulence characteristics near the structure significantly affect the sediment motion of the upstream and reduce the sediment deposition. Therefore, the investigation of turbulence movements upstream of the labyrinth spillway is important in terms of determining local sediment behavior.

Classification	**Angle of side legs α**	**Number of cycles N**	**Flowrate Q (l/s)**	**Head on the crest H (cm)**	**H_t/ P**	**C_d**
Rectangular	**0**	**2**	**20.61**	4.7	0.215	0.706
	0	**2**	**40.3**	8	0.371	0.610
	0	**2**	**60.75**	10	0.471	0.641
	0	**3**	**20.45**	5.3	0.244	0.579
	0	**3**	**40.34**	8.2	0.381	0.587
	0	**3**	**60.55**	10.2	0.487	0.608
Triangular	**50**	**2**	**20.17**	5.2	0.237	0.596

	50	**2**	**40.47**	8.1	0.370	0.614
	50	**2**	**60.74**	11	0.502	0.583
	45	**3**	**20.62**	5.1	0.233	0.628
	45	**3**	**40.44**	8	0.371	0.612
	45	**3**	**61.02**	10.5	0.486	0.615
Linear	**90**	**-**	**20.48**	4.7	0.217	0.953
	90	**-**	**40.32**	8.2	0.381	0.805
	90	**-**	**60.74**	11	0.513	0.774

Different velocity patterns were observed among the five experimental designs, particularly distinct between experiments conducted with labyrinth and linear spillways. For all configuration of spillways, it is observed that as the discharge increases, the magnitude of velocity vectors increase. In addition, the components of the velocity vectors are higher for high water depths, especially in the z direction (Figure 5). The magnitude of the velocity vectors increases while approaching the spillway. In triangular spillways, spillway geometry doesn't affect the velocity vector direction at cross section 3 but in rectangular ones it can be said that geometry of spillway affects the velocity vectors of cross section 3.

The velocity vectors at the cross section 3 and cross section 4 were given in Figure 6. Especially the velocity vectors which are closest to the crest are of greatest magnitude. In the cross section 3, the size of the velocity vectors decreased with respect to the cross section 2 (Figure 6).

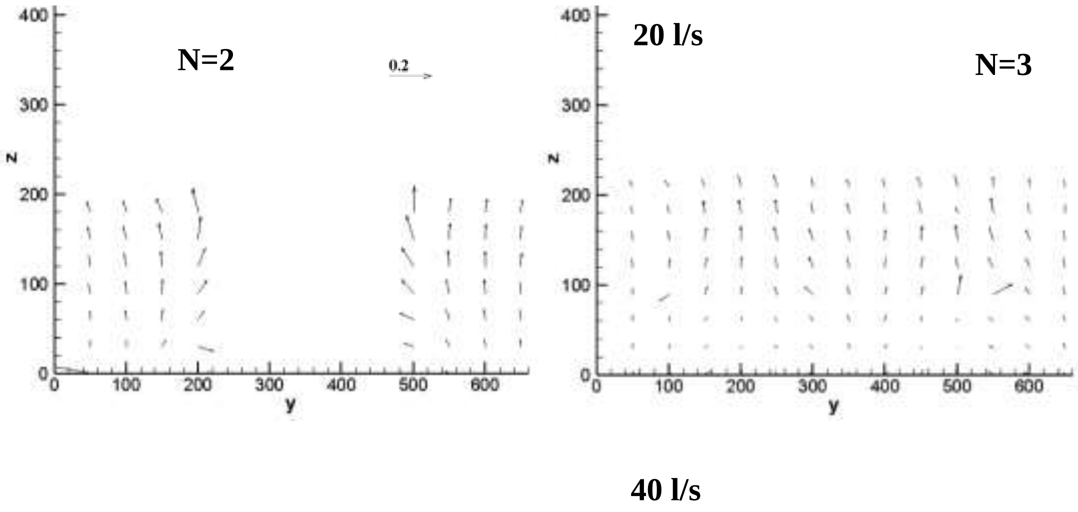

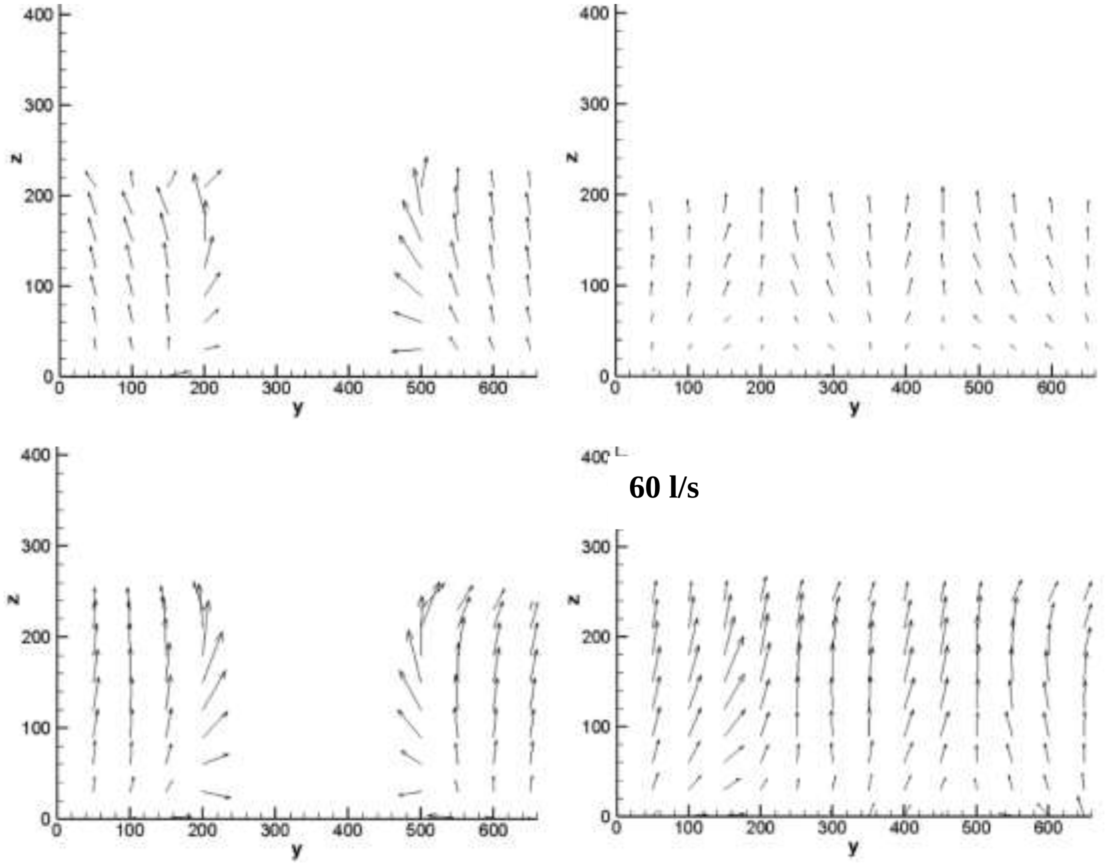

Figure 5. Rectangular spillway CS2 (N=2 on the left, N=3 on the right)

One of the important observations is that when the discharge is increased from 20 l/s to 40 l/s, the average values of the velocity vectors at each cross section are two times bigger, but when the discharge is increased from 40 l/s to 60 l/s, the increment is about 1.2. This variation indicates that discharge is an important design criterion in labyrinth spillways.

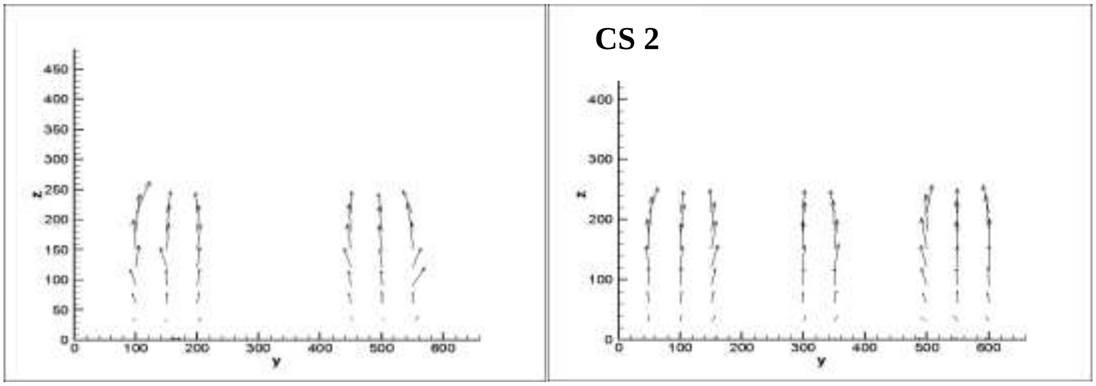

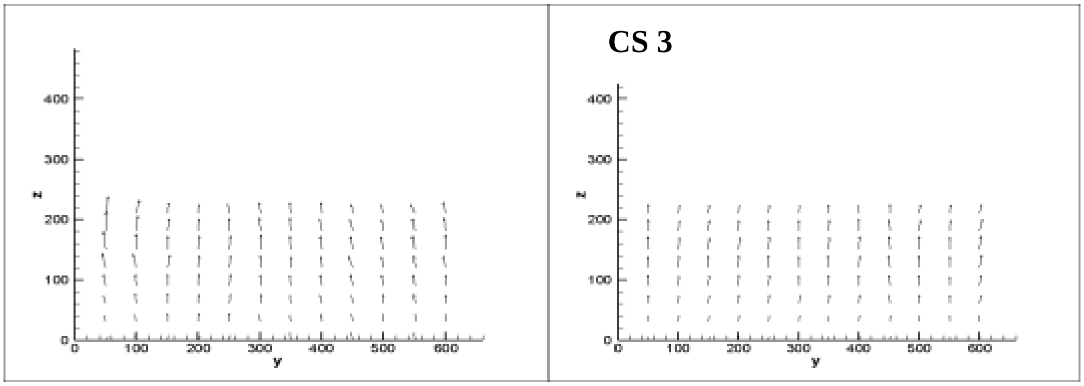

Figure 6. N=2 on the left, N=3 on the right, Triangular spillway, Q=40

The velocity vectors close to the channel bed and spillway corner change their direction and they go downwards in rectangular labyrinth spillways (Figure 5). The direction change of the vectors can initiate the sediment movement and can cause erosion at the upstream of the spillway.

CONCLUSIONS

Because of the zig-zag like geometry of labyrinth spillways, their design depends on many factors. An experimental study is conducted to indicate the effect of labyrinth weir geometries, their number of cycles (N) on discharge capacity and upstream flow area. The crest configuration is one of the significant factors affecting the discharge coefficient for labyrinth spillways. According to the study, it was found that the triangular and rectangular labyrinth spillways are hydraulically more efficient than the linear weirs from the perspective of the discharge capacity.

Velocity vectors were drawn to observe the flow behavior at the upstream side of the spillway. The velocity vector magnitudes show that geometry of the spillway is an important design criterion affecting the particle movement in labyrinth spillways.

Some recommendations for future study; (1) Conducting the experiments at different crest heights and lengths, (2) Using sediment at the upstream side of the spillway.

REFERENCES

Anderson, R. M. 2011: Piano Key Weir Head Discharge Relationships, Utah State University, Msc Thesis.

Bilhan,Ö., Emiroğlu,E., Carol J. Miller. 2016: Experimental Investigation of Discharge Capacity of Labyrinth Weirs with and without Nappe Breakers, World Journal of Mechanics.

Crookston, B.M. 2010: Labyrinth Weirs. Civil and Environmental Engineering, Utah State University, PhD Thesis.

Crookston, B.M., Tullis, B.P. 2013: Hydraulic Design and Analysis of Labyrinth

Weirs. I: Discharge Relationships, ASCE

Falvey, H.T. 2003: Hydraulic design of labyrinth weirs, American Society of Civil Engineers, Virginia

Hinchliff, D. L., and Houston, K. L. 1984: Hydraulic design and application of labyrinth spillways USCOLD Lecture Dam Safety and Rehabilitation, USCOLD, Denver.

Hong S. H., Kim S.J. 2010: Effect of low tail water during drought on scour conditions

downstream of an ogee spillway, River Flow.

Hotchkiss, R.H., D. Faber, D., 2003: Velocity Measurements in Vicinity of a Removable Spillway Weir, World Water & Environmental Resources Congress.

Houston, K. L. 1982: Hydraulic model study of the Ute Dam labyrinth spillway. Rep. No. GR-82-7, Bureau of Reclamation, Denver

Khode, B.V., Tembhurkar A.R. 2010: Evaluation and Analysis of Crest Coefficient for Labyrinth Weir

Mayer, P. G. 1980: Bartletts Ferry project labyrinth weir model studies Georgia Institute of Technology, Atlanta

Sarker, A. 1998: Flow measurement around scoured bridge piers using Acoustic Doppler Velocimeter-ADV, Flow measurement and instrumentations, 9, 217- 227.

Tullis, B.P., Amanian, N. and Waldron, D. 1995: Design of Labyrinth Weir Spillways. Journal of Hydraulic Engineering (ASCE)

Using LISST-100X for measuring pine pollen grains in the waters of the Southern Baltic Sea

Magdalena Maria Pawlik 1*, Dariusz Ficek [1]

1 Institute of Physics, Pomeranian University in Słupsk, Poland

*e-mail: magdalena.pawlik@apsl.edu.pl

The Baltic Sea, by dint of its inland situation and a limited access to oceanic waters constitutes a unique ecosystem. To a large extent, the properties of the waters of the Baltic Sea, basically an inland water body, are determined by allogenic material, supplied mainly by terrestrial runoff and offshore winds. Waters containing both autogenic constituents, i.e. products of the local ecosystem, and allogenic components, are classified as Case 2 (Morel and Prieur 1977). Baltic waters are an exceptional example of Case 2 waters, since they are much richer in both allogenic and autogenic CDOM than other shelf seas (e.g. Kaczmarek and Woźniak 1995, Kowalczuk 1999, Woźniak 2011). One constituent not taken into consideration so far, which could be the source of serious errors in remote measurements, is pine pollen, very large amounts of which reach Baltic waters in spring (Fig. 1).

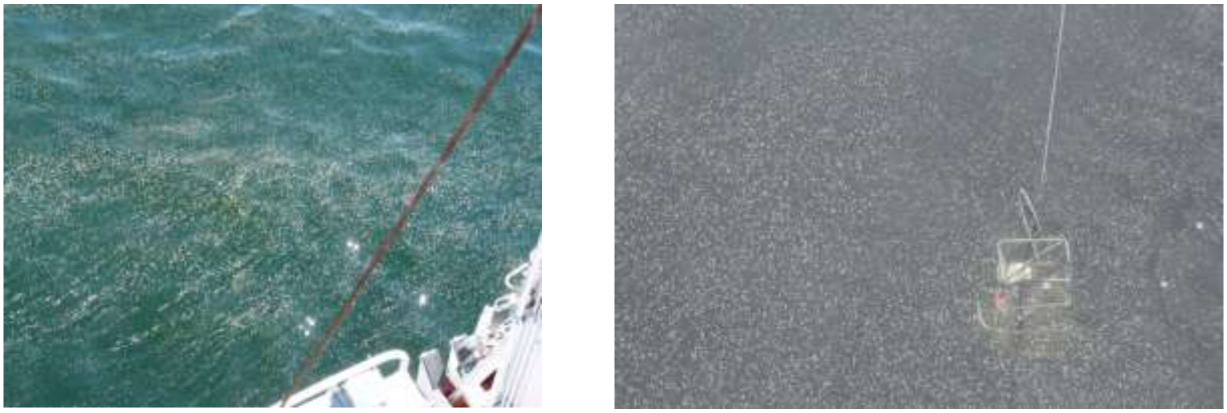

Figure 1. Pine pollen grains in the Southern Baltic.

Measurements were performed during a total of 5 research cruises in the southern Baltic from 2012 to 2018. The study area covers the open waters of the southern Baltic as well as the coastal regions. Cruises took place in the second half of May. During the cruises, the SPM volume concentration was measured continuously in 32 size classes, ranging from 1.25 to 250 µm, using a LISST-100x type B particle size analyzer (Agrawal and Pottsmith, 2000). At the same time, surface water was sampled at selected stations, immediately preserved in Lugol's solution, and sent for microscopic analysis. Sample preservation and microscopic analysis of phytoplankton were carried out in line with the HELCOM recommendations for the Baltic Sea monitoring (HELCOM 2001).

The SPM size distributions measured in Baltic waters in spring (20.05.2014) obtained using the LISST-100X revealed that the dominant particles diameters in the surface water ranged from 29.1 to 109.0 µm with a distinct peak between 47.7 and 56.3 µm (Figure 2).

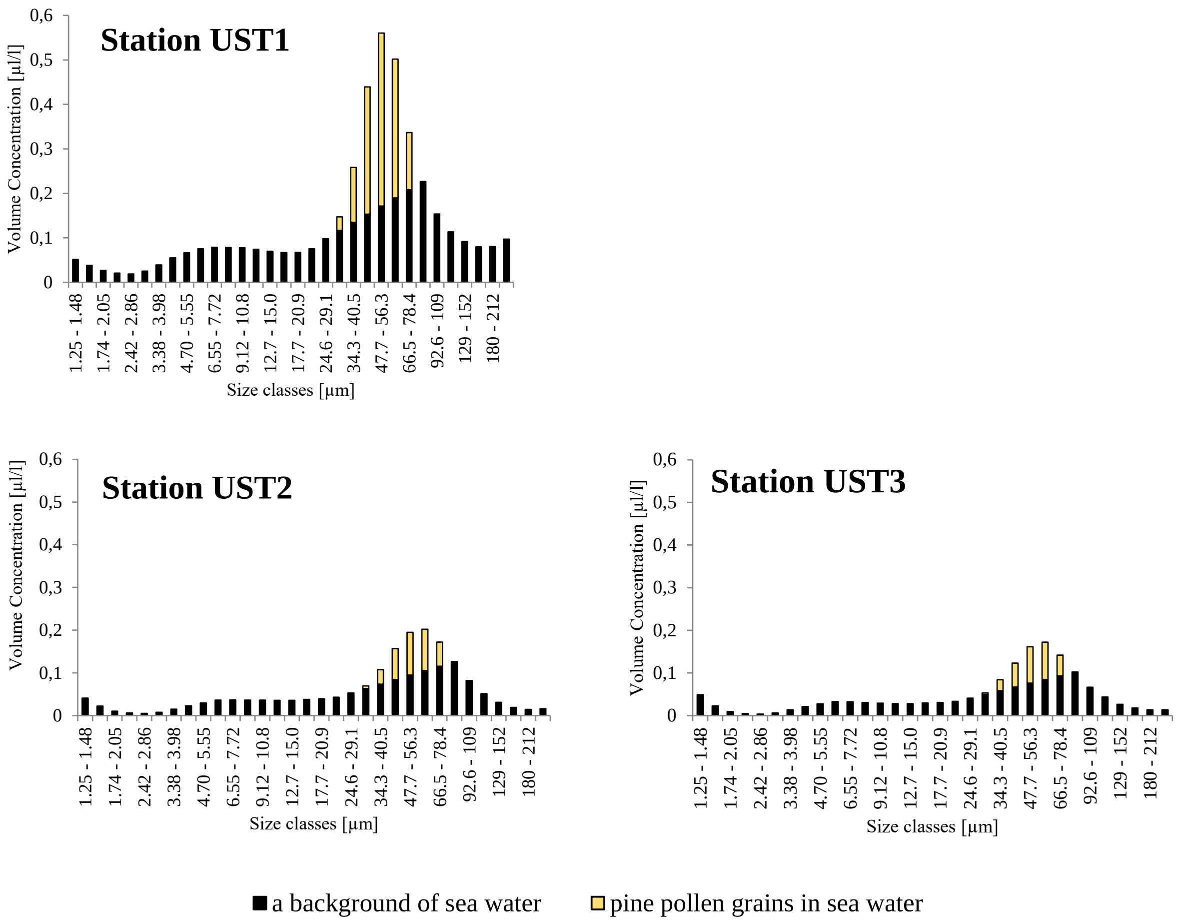

Figure 2. Concentration of suspended particular matter measured 20.05.2014 in surface water at stations UST1, UST2 and UST3 (Pawlik and Ficek, 2016). Concentration of pollen grains in water measured using the method described in this paper are shown in yellow.

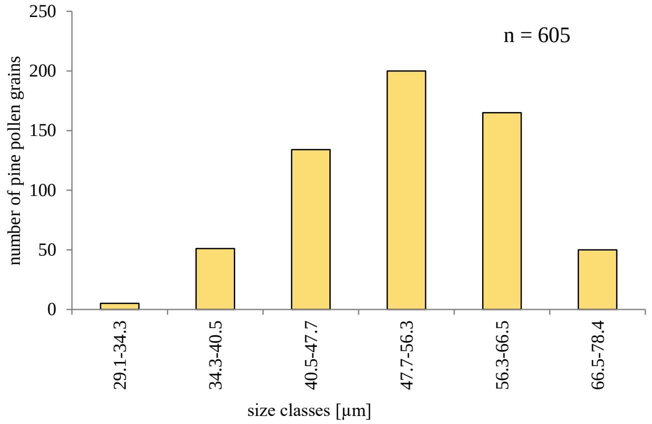

Figure 3. Equivalent spherical diameter (ESD) of pine pollen grains sampled from coastal waters of the Baltic Sea in specific LISST-100x size classes.

Microscopic analysis (see Fig. 3) of those water samples showed that the majority of pine pollen grains within this size classes were from pine trees.

The microscopic measurements of pine pollen grains showed that the equivalent spherical diameter (ESD) of these grains ranged from 29.1 to 78.4 µm, with a maximum between 47.7 and 56.3 µm. Figure 3 lists the diameters of 605 such pollen grains, categorized into the same size classes as used by the LISST-100x instrument for assessing the size distributions of SPM. What's more microscopic measurements demonstrated that, apart from the pollen, the samples analyzed did not contain any large concentrations of phyto- or zooplankton of dimensions within the range of the dominant maximum shown in Fig. 2. Since there are other kind of SPM in the water apart from pine pollen grains, certain simplifications were made when estimating pollen levels. It was assumed that the concentration of SPM with ESD both lower and higher than those measured for pine pollen grains, i.e. < 29.1 µm and > 78.4 µm, constituted a background, and only values above this background could be taken into consideration when estimating pollen grain concentrations. See Pawlik and Ficek (2016) for more information about used method. In accordance with the above scheme the concentration of pollen grains along the entire transect on 20 May 2014 was estimated. Surface water concentrations of pollen in the coastal zone near Ustka showed that up to 3 km from the mouth of the Słupia, more than 20% of the total SPM consisted of pollen grains Moreover, its proportion in the total suspended particulate matter (SPM) might be as high as 30-40% (Fig. 4).

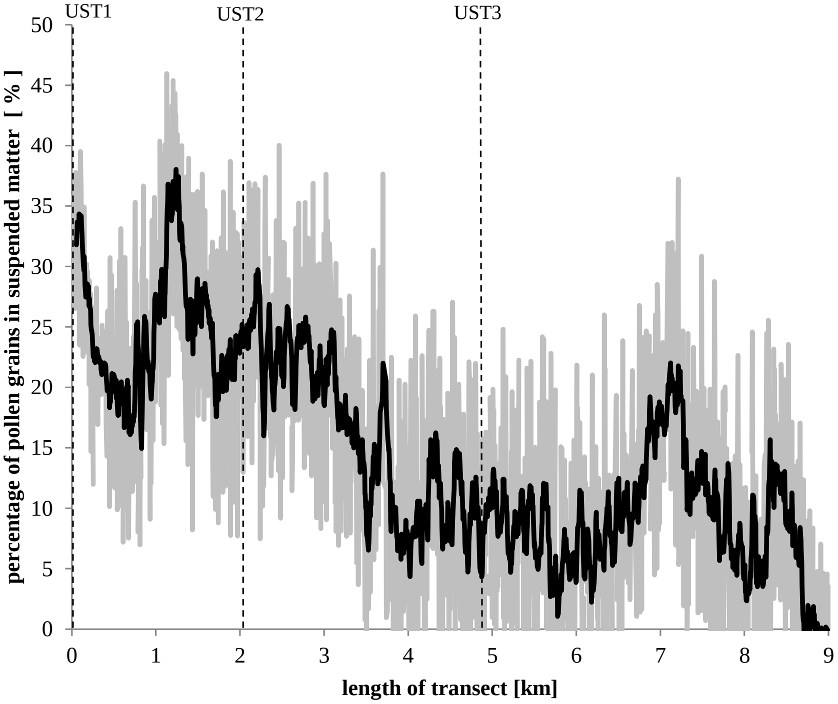

Figure 4. Concentration of pollen grains in surface water measured along the transect on 20.05.2014: relative concentration, i.e. the ratio of the number of pollen grains to the total number of suspended particles. The average value is shown in black (Pawlik and Ficek, 2016).

Such high surface water concentrations of hitherto neglected substances critical to water color formation can give rise to serious errors in remote measurements of water composition and properties in spring.

Acknowledgements

This research was funded by the Project „Satellite Monitoring of the Baltic Sea Environment – SatBałtyk", and by the European Union through the European Regional Development Fund contract No. POIG.01.01.02-22-011/09. This work was also supported by the project awarded to M. M. Pawlik by

National Science Centre, Poland, entitled “Optical Characteristics of Pine Pollen Grains and their affect the quality of remote sensing measurements in the Baltic Sea” (contract No. 2017/25/N/ST10/02578).

References

Agrawal, Y.C., Pottsmith, H.C., (2000). "*Instruments for particle size and settling velocity observations in sediment transport*". Marine Geology 168, 89–114.

HELCOM (2001). *Manual for marine monitoring in the COMBINE programme of HELCOM, Part C. Programme for monitoring of eutrophication and its effects, Annex C-6: Phytoplankton species composition, abundance and biomass.* Balt. Mar. Environ. Prot. Commiss., Helsinki, from http:// www.helcom.fi/groups/monas/CombineManual/AnnexesC/ enGB/ annex6/.

Kaczmarek, S., Woźniak, B. (1995). *The application of the optical classification of waters in the Baltic Sea (Case 2 Waters)*. Oceanologia. 37(2): 285-297.

Kowalczuk, P. (1999). *Seasonal variability of yellow substance absorption in the surface layer of the Baltic Sea*. J. Geophys. Res. 104(C12): 30047–30058, DOI:10.1029/1999JC900198.

Morel, A., Prieur, L. (1977). *Analysis of variations in ocean color*. Limnol. Oceanogr. 22 (4): 709-722.

Pawlik, M.M., Ficek, D. (2016). *Pine pollen grains in coastal waters of the Baltic Sea*. Oceanological and Hydrobiological Studies, 45 (1), 35-41, DOI: 10.1515/ohs-2016-0004.

Woźniak, S.B., Meler, J., Lednicka, B., Zdun, A., Stoń-Egiert, J. (2011). *Inherent optical properties of suspended particulate matter in the southern Baltic Sea*. Oceanologia, 53(3), pp. 691-729.

Mapping of suspended sediment mixing at a confluence zone to improve sediment monitoring of a large river

F. Pomázi, S. Baranya G.T. Török,

MTA-BME Water Management Research Group,

Budapest University of Technology and Economics, 1111 Műegyetem rkp. 3, Budapest, Hungary

pomazi.flora@epito.bme.hu; baranya.sandor@epito.bme.hu; torok.gergely@epito.bme.hu

Introduction

There are several issues related to the movement of sediments in rivers, such as the sedimentation in hydropower plant reservoirs, development of navigational bottlenecks, bed incision due to increased erosional capacity. etc. The need for the quantitative monitoring of sediment transport is therefore crucial, especially in large, international rivers, such as the Danube, that are exposed to multiple uses. Within an ongoing project, called DanubeSediment, implemented in the Danube Transnational Programme, one of the main goals is to work out a recommendation for a state-of-the-art, harmonized sediment monitoring network, which can provide accurate quantitative information on the sediment transport with adequately high temporal resolution. At the moment, there are very different suspended sediment (SS) monitoring methods along the Danube. For instance, in the Hungarian section of the river, the regional water directorates are responsible for collecting SS samples, performing multipoint pump samplings along the monitoring cross-sections, 5 times per year. This method is far not sufficient to gain detailed knowledge on the nature of the sediment movement, and calls for significant improvement.

In order to collect high temporal resolution sediment information for the monitoring stations, the future plan is to mount a fixed acoustic or optical backscatter sensor (ABS or OBS) device at each site. However, these instruments cannot provide representative cross-sectional suspended sediment loads due to the fact that only local measurements are performed, but need cross-sectional calibration. One of the proposed SS monitoring stations in Hungary will be located at Rkm 1790.61, near Gönyű. The location is not optimal for the continuous measurements of sediment transport as a tributary (Mosoni-Duna) inflow 3.5 km upstream of the station strongly affects the local distribution of the suspended sediment concentration, however, due to administrative and physical limitations of the related project, no other location could be chosen. Figure 10 shows a satellite image of the area, where the brownish plume arriving from the tributary can be clearly seen. The tributary, at this water regime, is rich in suspended sediments even though that at mean flow conditions, the Danube River carries 97%, whereas the tributary only 3% of the total flow discharge. Due to the spatio-temporally varying mixing processes, which are likely dependent of the flow discharge and mean SS concentration (SSC) ratios of the joining rivers, it is of great importance to understand how the cross-sectional SSC distribution at the monitoring transect develops at different flow regimes to support the cross-sectional calibration. As a complementary element of the station, the permanent deployment of a horizontal acoustic Doppler current profiler (H-ADCP) is also planned, which could provide the continuous cross-sectional distribution of the SSC, at least in one layer.

As a preliminary step of the monitoring station set up, thorough field measurements are under implementation to reveal the characteristic flow and sediment features at the study site. As of now, two measurement campaigns have been carried out, where a high number of water samples was taken and analysed with different methods, together with fixed and moving boat ADCP measurements.

Figure 10 Satellite map of the Danube near Gönyű monitoring station, indicating plume of the tributary rich in suspended sediment (source: Sentinel-2 satellite)

Field measurement campaigns

First campaign

Two measurement campaigns were carried out in the summer of 2018. During the first one, the goal was to perform a thorough multipoint sampling along the future monitoring cross-section in order to map the distribution of the actual SSC as well as to optimize the number of sampling points for future measurements. To capture the horizontal and vertical variation of the sediment concentration 5 verticals and 10 points per vertical were sampled.

Instead of the pump sampling method, operatively applied by the regional water directorate, an isokinetic sampler was used, to decrease the uncertainty of the sediment data resulted by non-isokinetic sampling. An Acoustic Doppler Velocimeter (ADV; Nortek Vector) and an additional OBS were also mounted on the sampler's frame. A crane was used to move this whole setup (Figure 2), mounted on the measurement pontoon.

The goal of using an ADV was first to gain local, time averaged flow velocity data for the sediment load calculation, second, to investigate if the turbulent kinetic energy (TKE) profiles derived from the high resolution instantaneous velocity time series can be indeed quantified. Besides the ADV, complementary fixed ADCP measurements were also done in each vertical. Due to the typically 0.5-1 Hz sampling frequency of the ADCPs, the quantification of TKE is not feasible with this instrument, but on the other hand, the deployment and the performance of the flow velocity measurements are much easier. Therefore, the goal was to compare the flow velocity profiles from the two measurement methods and to determine if the fixed ADCP can replace reliably the ADV measurements.

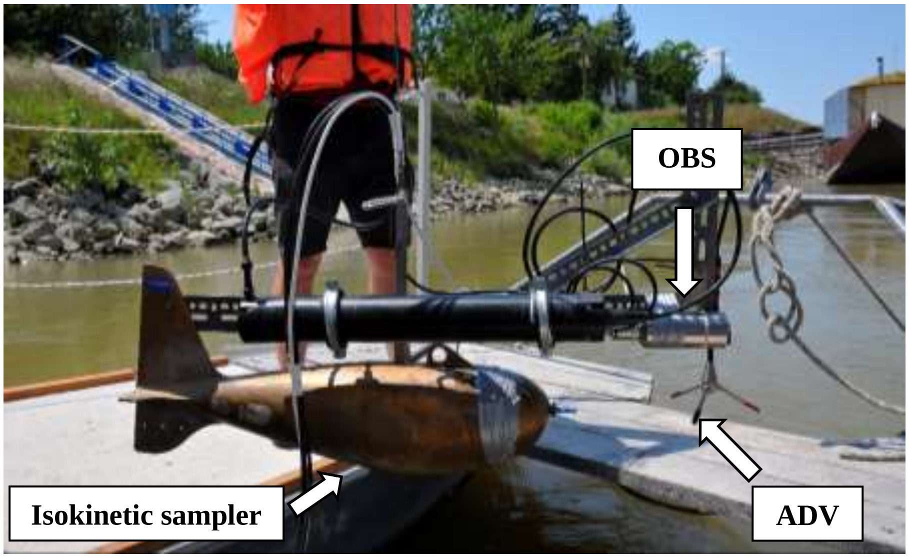

Figure 11 Measurement devices (during the first campaign)

Moving-boat ADCP measurements in the vicinity of the monitoring site were also carried out to reveal the flow conditions as well as to reconstruct the spatially varying SSC distributions from the ADCP backscatter data. The echo based sediment concentration estimation method requires calibration data, which was provided by the physical samples taken with the isokinetic point sampler.

The local suspended sediment concentration values at the sampling points were determined by a laboratory analysis procedure, where the so called filtration method was applied (filtering of the sample with a filter paper of 0.45 μm pore size, drying, weighing) as well as the LISST-Portable|Xr Portable Laser Diffraction Particle Size Analyzer (by Sequoia Scientific, Inc.). The OBS data were also analysed. The OBS and the LISST-P can be used on-site which is a great advantage but the reliability of these data still must be proved.

Second campaign

The second campaign was planned based on the experiences gained from the first one, which were the following:

5 points per vertical is adequate to capture the vertical variation of the SSC;

More vertical, however, might be needed to better reveal the horizontal variation of SSC resulted by the tributary inflow;

Although the application of OBS needs further tests, due to organizational issues this instrument was not used;

The comparison between point ADV and fixed boat ADCP velocity profiles suggested that no ADV measurements are needed but time averaged flow velocity distribution from ADCP can be used instead;

Besides, a larger area was mapped with moving-boat ADCP measurements in order to track the sediment plume arriving from the tributary.

Results

Only the most relevant results will be introduced here, focusing on the cross-sectional variation of the suspended sediment transport. For the first measurement campaign, the cross-sectional suspended sediment load distributions were determined based on the following three methods:

isokinetic point sampling + laboratory analysis using filtration method

isokinetic point sampling + LISST Portable analysis

OBS

Based on the local SSC values, pointwise sediment load values were calculated multiplying the SSC with the local flow velocity, then the vertical distributions were integrated providing local specific suspended sediment load (SSL) along the study cross-section (see Figure 13). In case of the first campaign the results show that the OBS results in permanently higher values comparted to the two other methods. An 50% overestimation is seen, however, the pattern of the cross-sectional variation agrees well. This result suggests that the calibration of the OBS might be biased and a new calibration curve is to be set up for this instrument. The profiles calculated from the filtration method and the LISST-Portable analysis are

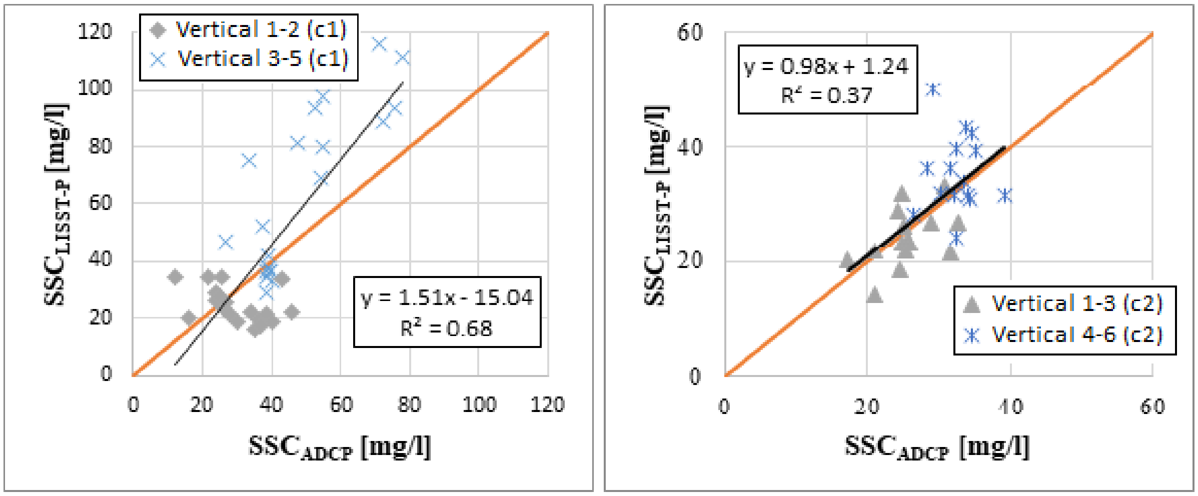

Figure 12 Calibration curves for calculating SSC from ADCP backscatter

based on the same water samples, only the sample analysis differed. Here the agreement is almost perfect for three verticals at the left side of the channel and some discrepancy can be seen for the high SSC zone, where the plume of the tributary is propagating. A likely explanation for the disagreement might be the different composition of the sediment in terms of organic parts, the analysis of which calls for further investigations. The SSL distribution from the second campaign, measured at lower flow discharge (see Table 1) shows a very similar pattern, with lower values.

The total cross-sectional SSL resulted in:

Table 1 Summary of the cross-sectional SSL and flow discharge

Campaign	**Method**	**Discharge [m^3/s]**	**SSL [kg/s]**
1	Filtration	1810	55.19
	LISST-P		66.00
	OBS		90.56
2	LISST-P	1050	26.55

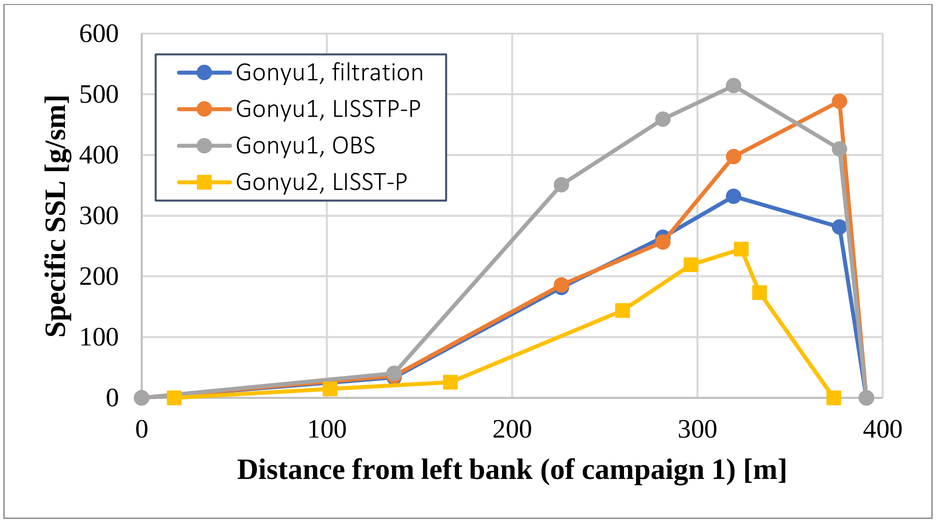

Figure 13 Cross-sectional specific SSL profiles for both the 1st and 2nd field campaigns.

$$SSC = 10^{A+B\cdot(Kc\,(EI-Er\,)+2(10.\log(R)+\alpha.R))}$$

where:	A,B	empirical parameters; derived with least squares fitting [-],
	Kc	conversion factor; estimated [-],
	EI	echo intensity; measured with ADCP [counts],
	Er	reference level; measured with ADCP [counts],
	R	slant distance; measured with ADCP [m],
	α	coefficient describing the absorption of energy by water and attenuation from suspended sediments; estimated [dB/m].

The calibration was performed separately for both measurement campaigns (Figure 14). The verticals in and out of the plume section are distinguished so that to detect the potential effect of the higher concentrations on the calibration. The blue symbols are from the plume section and the gray ones are closer to the left bank. It can be seen that the SSC values covered a smaller range in the second campaign. The values were not so scattered so the linear trend line is on the independent line. However, the coefficient of determination (R^2) is smaller than it was in the first campaign.

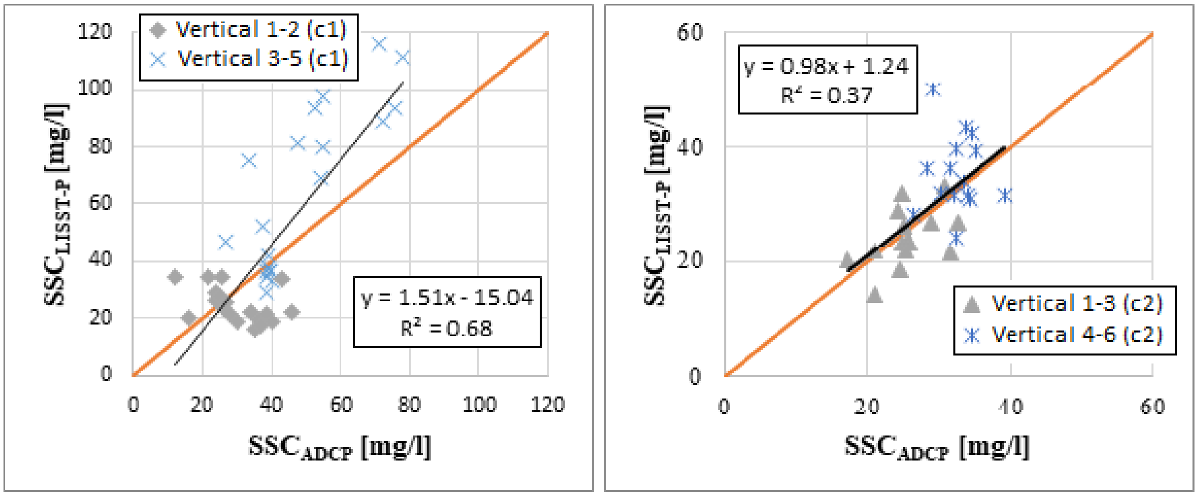

Figure 14 Calibration curves for calculating SSC from ADCP backscatter

Using these calibration curves, the moving boat ADCP backscatter data was also processed in order to get the spatial SSC distribution. Figure 15 depicts the estimated concentration values along the measurement transects for both campaigns. As shown from the previous results, the concentration values are higher at the first campaign, where the flow discharge was also higher. In both cases, a clearly inhomogeneous cross-sectional distribution of the SSC can be seen at the location of the proposed monitoring station, where the higher concentration values characterize the zone at the right bank, i.e. the side of the tributary inflow. However, at the second campaign the spatial variation of the SSC do not suggest that the plume of the tributary is pushed to the right bank all along the distance between the confluence zone and the monitoring transect. Instead, a spatial mixing can be observed as a possible result of the three-dimensional, i.e. swirling character of the flow field. No ADCP data is available from the first campaign, however, the satellite image (Figure 10) clearly show that no transversal mixing takes place at that case. Apparently, the mixing processes differ for the two investigated flow regimes, which on the other hand do not show significant differences at the monitoring site.

Discussion

The first results of a preliminary investigation towards the set up a sediment monitoring station are introduced in this paper to assess the capabilities and limitations of different measurement techniques. At the proposed monitoring station an ABS or OBS instrument would provide pointwise SSC time series at the right bank of the river with high temporal resolution, however, due to the nearby tributary inflow, the cross-sectional pattern of the SSC distribution shows strong inhomogeneity, which has to be considered when the cross-sectional calibration is set up. Therefore, our recommendation is to deploy a H-ADCP, which permanently detects the transversal SSC variation.

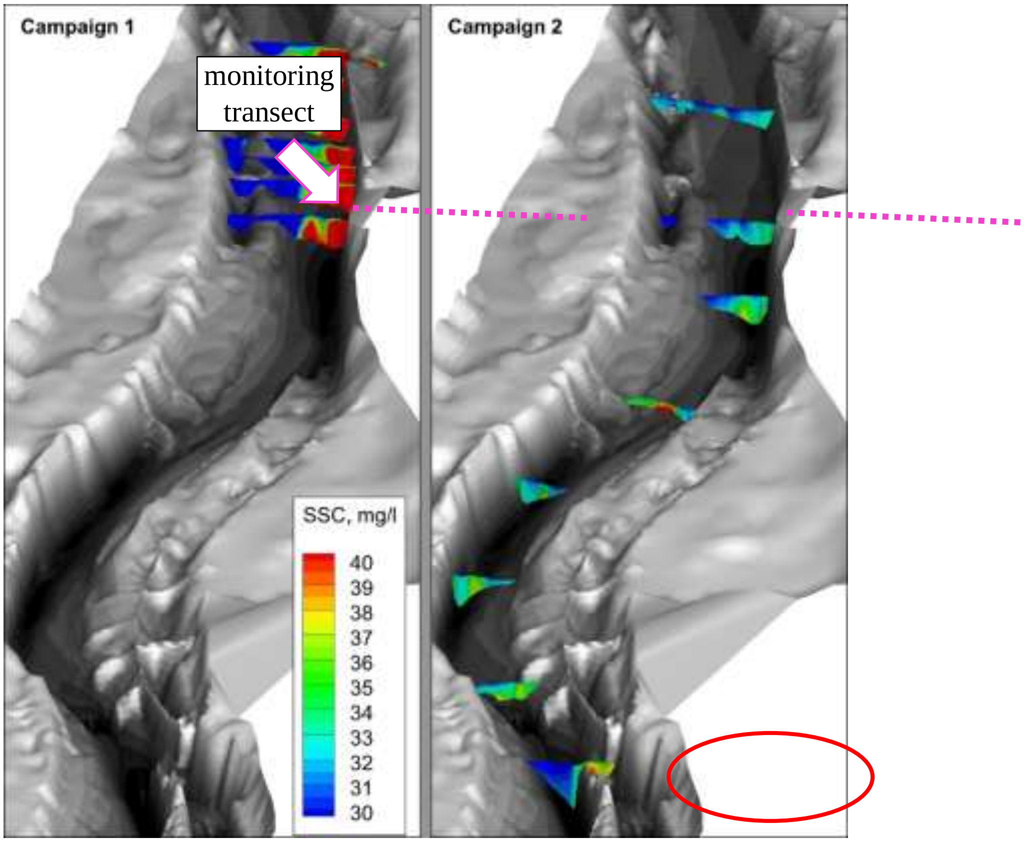

Figure 15 Spatial distribution of estimated cross-sectional SSC (flow direction from bottom to top)

Prior to the establishment of the monitoring system, decisions have to be made on the applied water sample analysis methods as well. According to the experiences gained so far, it is clear that either an ABS or OBS will be mounted for point measurements, the instrument need to be calibrated by local water samples. The advantage of applying an ABS could be its lower sensitivity to the grain size variation compared to the OBS (**www.sequoiasci.com**), however, OBS devices are now conventionally used for long-term sediment measurements and practitioners have much more experiences with this instrument.

As to the water sample analysis, a straightforward method could be the utilization of laser diffraction instruments, which provide information not only on concentration but particle size distribution (PSD) as well. However, according to our experiences the laser based analysis can provide higher concentration compared to the traditional laboratory analysis methods. There are at least two potential explanation of the discrepancy, which should be investigated in more details: i) the filtration laboratory method excludes the particles of a diameter lower than 0.45 μm and ii) the organic content of the water sample can bias the laser based analysis towards higher concentration values.

Once the most adequate water sample analysis methods are found, the cross-sectional calibration of the nearbank measurements have to be performed using multipoint and/or moving boat ADCP measurements. To have an impression about the results from an H-ADCP we extracted the estimated SSC distribution along the cross-section from one horizontal layer from the moving boat data (see Figure 16).

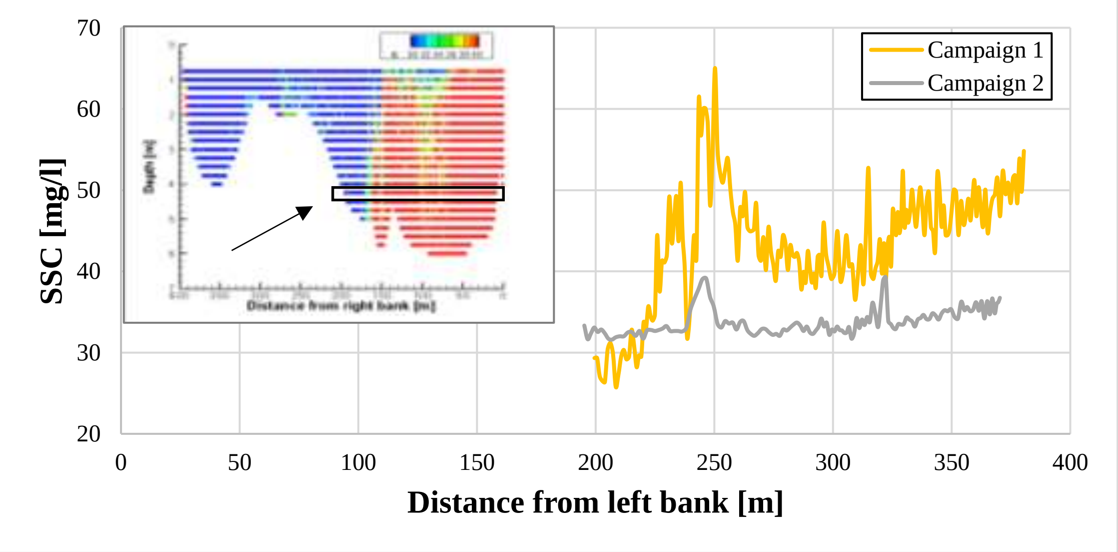

Figure 16 SSC distribution along the cross-section in one layer

The graph clearly shows the inhomogeneity introduced in the above images, but at the same time suggests that there is a strong correlation between the cross-sectional suspended sediment load, the cross-sectional SSC distribution in the given layer and the nearbank, OBS (or ABS) based SSC values. Obviously, a high number of expeditionary measurement campaigns is needed to set up calibration curves, which take into consideration these features, moreover, different water flow regimes have to be investigated, where both the discharge and SSC ratios of the joining rivers cover a large spectrum.

Acknowledgements

The support of the DanubeSediment project, implemented within the Danube Transnational Programme, is acknowledged. Also, we thank the colleagues from the University of Natural Resources and Life Sciences, Vienna (BOKU), Marlene Haimann and Philipp Gmeiner for their valuable support in the measurements and for providing their OBS instrument in the first field campaign.

References

Baranya S., Józsa J. (2013). Estimation of Suspended Sediment Concentrations with ADCP in Danube River. Journal of Hydrology and Hydromechanics, 61(3), 232-240.

https://www.sequoiasci.com/product/lisst-abs/

Information Superiority: from blue to brown water theaters of military operations

Luis Quaresma dos Santos

Centro Meteorológico e Oceanográfico Naval – CEMETOC

Marinha - Instituto Hidrográfico

luis.quaresma@hidrografico.pt

The success of present military operations strongly depends on the understanding of the environment in which they operate, as well as in the use of that knowledge to gain "information superiority" to opposing forces.

Military maritime operations are now changing in location, from deep-open Ocean ("blue-waters") to confined shallow littoral seas ("brown-waters"). A more energetic environment, carrying heavy sediment loads from soil runoff, flooding and bottom suspension, characterizes this new theatre of operations and brings new challenges to this task.

New concepts and environmental variables are now arriving to the military world, increasingly dependent on the knowledge and forecast of oceanographic features, as gravity wave shoaling and breaking, internal wave patterns, nepheloid layer dynamics and sand wave movements.

We know how this complex environment impact military operations but we do not have a complete picture of its behavior and nature, being even more distant from its realistic forecasting. This means that we are still far from the so-called "information superiority" enhancing the success of "brown-water" operations.

The Portuguese Navy, the Portuguese Hydrographic Office (IH) and their partners, are investing in the scientific research and technology development in this field of knowledge, seeking new projects and partners to contribute to a more in-depth knowledge of the dynamics of ocean suspended particles.

Assessing the Suspended Sediment Concentration by means of a Side Looking (Horizontal) ADCP

Nils Ruther [1], Rui Aleixo[2] & Massimo Guerrero [2]

NTNU, Norwegian University of Science and Technology, Norway

Department of Civil, Chemical, Environmental and Materials Engineering, University of Bologna

KEY POINTS

Suspended sediment concentration, Echo profiling ,Attenuation to Backscatter ratio,River monitoring

1 INTRODUCTION

To obtain valuable information about rivers and water courses, scientists and engineers often rely on monitoring stations. These monitoring stations allow to measure several quantities that play a role in hydroenvironmental problems. One of these key variables is the suspended sediment concentration (SSC). In this paper the application of an acoustic based method to determine the SSC in a river is presented. This method is founded on the sonar equation and uses the echo information from an Acoustic Doppler Current Profiler (ADCP) to assess the SSC.

The results from a monitoring station in the river Devoll in Albania are here presented and the method application is discussed. The advantages and disadvantages are highlighted and directions to improve the method are discussed.

2 MODELS AND GOVERNING EQUATIONS

The sonar equation is the basis for the determination of the SSC. The sonar equation in dB can be written as:

$$I_{dB} = C + 10\log(k_s^2 M_s) - 20\log(r_\psi) - 40(\alpha_w + \alpha_s) r\log(e) \quad (1)$$

Where I is the intensity in dB, C accounts for the instrument constants, k_s^2 and M_s are the backscattering coefficient and backscatter strength respectively; $r\psi$ is the geometrical beam spreading and ψ is the near field correction (ψ = 1, in the far-field). αw and αs are the water viscosity and suspended sediment attenuation coefficients, respectively

This equation can be arranged to isolate in the left-hand side the variables related with the SSC features, namely, concentration and particle size distribution (PSD). In the right hand side, the known or measured variables: the received sound intensity, the beam spreading and the sound attenuation in clear water (modeled according to *Medwin & Clay* (1998)) are grouped:

$$10\log(k_s^2 M_s) - 40 r \alpha_s \log(e) = I_{dB} - C + 20\log(r_\psi) + 40\alpha_w r\log(e) \quad (2)$$

Different relationships exist for the backscattering strength, and for the two additive mechanisms producing the attenuation: the scatter attenuation, ζ_{ss}, that spreads energy out of the incident beam and the viscous dissipation, ζ_{sv}, as result of the friction produced by particles to fluid relative motions (*Moore et al*. 2012, *Thorne & Meral,* 2008, *Hanes*, 2012). The suspended sediment attenuation coefficient can be written in terms of the normalized scatter and viscous attenuation coefficients, ζ_{ss} and ζ_{sv} respectively, as $\alpha_s = (\zeta_{ss} + \zeta_{sv}) M_s$.

2.1 The attenuation to backscatter ratio (ABR)

The left hand side of equation (2) includes the terms due to the backscatter ($k_s^2 M_s$) and the attenuation term.

As first pointed out by *Guerrero and Di Federico* (submitted), for a given homogenous sediment concentration, these terms depend on the physical parameters of the sediments, namely the PSD features i.e., mean size, standard deviation, skewness. The measured attenuation to backscatter ratio corresponds to the ratio ABR = ζ_s/k_s^2, which, at a given frequency, in turns is quasi linear correlated to the normalized attenuation (yellow region in Figure 1). The Figure 1 depicts the normalized attenuation as a function of attenuation to backscatter ratio for a variable PSD mean diameter (with standard deviation as a parameter).

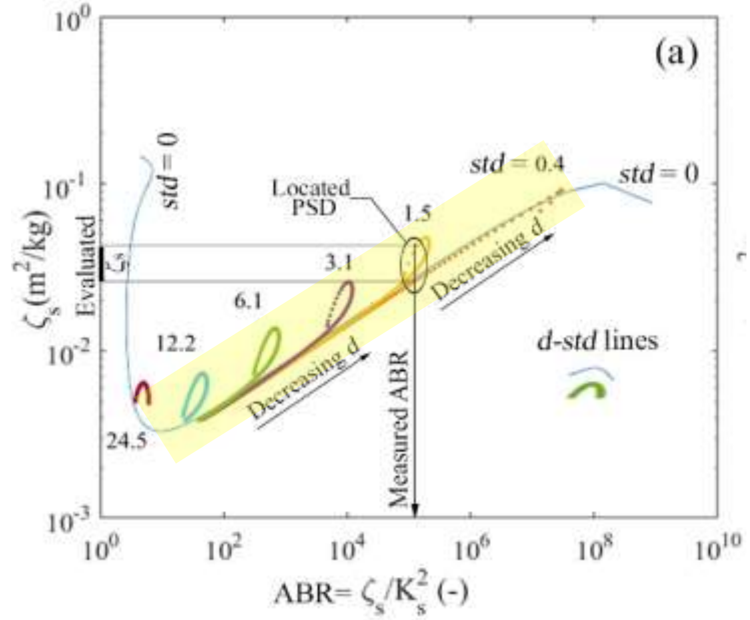

Figure 1. Normalized attenuation function of ABR with changing mean size *d* and standard deviation*std* for a wide set of PSDs.

From Figures 1 it is possible to identify a wide range of ABR (yellow region) with a quasi-linear increasing of the normalized attenuation that depends on the actual PSD of suspended sediment and used frequency.

2.2 Concentration determination

Hanes (2012) discussed the possibility of using single-frequency acoustic beams to measure sand and clay concentrations in uniform suspensions. By deriving eq. (1) along *r*, and assuming that i) the concentration is homogenous and ii) the backscatter change is negligible along *r*, one obtains:

$$\alpha s = (\zeta ss + \zeta sv) Ms = -\alpha w - 2\underline{1}r - 40\log(1\ e)\ \underline{dI}dr\underline{dB} \qquad (3)$$

From equation (3) it is possible to determine the sediment concentration by knowing: the water attenuation, α_w, and the derivative of the echo profile, dI_{dB}/dr, those give the attenuation due to suspended sediment α_s. The normalized attenuation, i.e., the coefficients $\zeta_s = \zeta_{ss} + \zeta_{sv}$, have to be determined for each site by means of specific and periodic calibrations with in-situ sampling collection, which enables the inversion of equation (3) to eventually assess M_s.

Equation (2) can be seen as a fitting problem in the I_{dB}-r plan where the I_{dB} profiling corrected for beam spreading and clear water attenuation (i.e., the right hand side of Equation 2) may be modelled with the correct backscattering strength and sediment attenuation (in the left hand side of Equation 2) which are, respectively, the intercept (*b*) and the slope (*a*) coefficient of a quasi-linear fitting in the form $y = ax + b$. This also provides the attenuation to backscatter ratio ABR = $(\zeta_{ss} + \zeta_{sv})/k_s^2$, that is derived from the slope to intercept coefficients ratio.

A non-trivial relation exists between the PSD features (diameter and standard-deviation) and the ABR

(Figure 1). This relationship allows that a limited region for ζ_s and *d-std* values may be fixed on the basis of a known attenuation to backscatter ratio at a given frequency (as shown in Figure 1). These relationships are fundamental for the determination of the concentration from equation (3) and have to be determined for each river. This is especially relevant for long term monitoring where the actual PSD may largely change along different seasons and the normalized attenuation ζ_s should be not assumed as a calibration constant but rather correlated to backscatter profile shape that is reflected in the measured value of ABR.

3 KOKEL MONITORING STATION ON THE RIVER DEVOLL

The Kokel monitoring station is located in the left bank of the river Devoll, in Albania. This monitoring station is equipped with two side-looking Acoustic Doppler Current Profilemeter working with two frequencies, 0.6 MHz and 1.2 MHz allowing to measure the transversal velocity profile and simultaneously to determine the transversal echo profile. Acquired data is transmitted via wireless to a server in Italy where they can be accessed for post-processing. Besides the ADCP's an ISCO sampler and a water level transducer are also installed. The monitoring station, together with the river section profile are depicted in Figure 2.

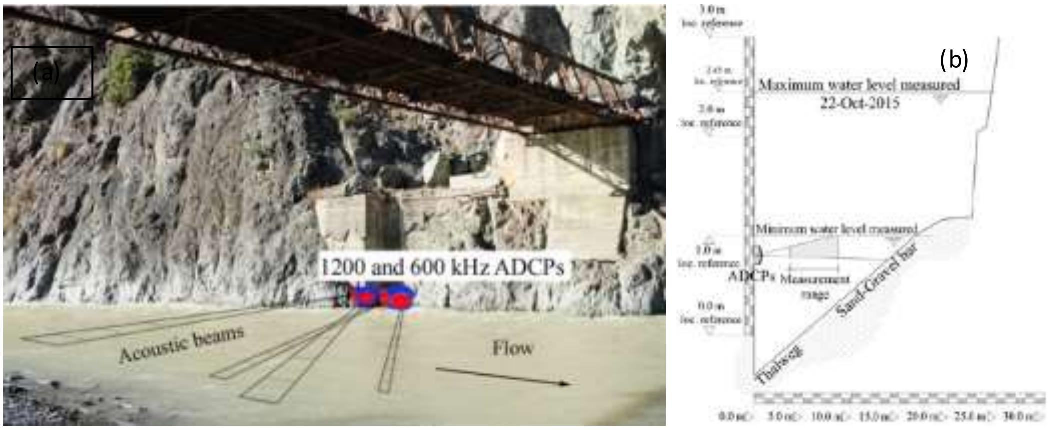

Figure 2. (a) Kokel monitoring station in the left bank of the Devoll river. (b) Devoll river section at the monitoring station location

4 RESULTS AND DISCUSSION

Data from the Devoll river was acquired for almost three years now and processed by means of a software developed to implement the methods described in section 2 in order to extract the suspended sediment concentration from the echo intensity profiles. Figure 3 (a), depicts some echo profiles for different time instants. It is possible to see that depending on the flow conditions the profiles are quite different. The derivative is calculated using a 1st order forward-scheme. Using the data available to determine the derivative of the intensity profiles, the water attenuation, the instrument constant, etc., the attenuation to backscatter ratio is presented in Figure 3 (b).

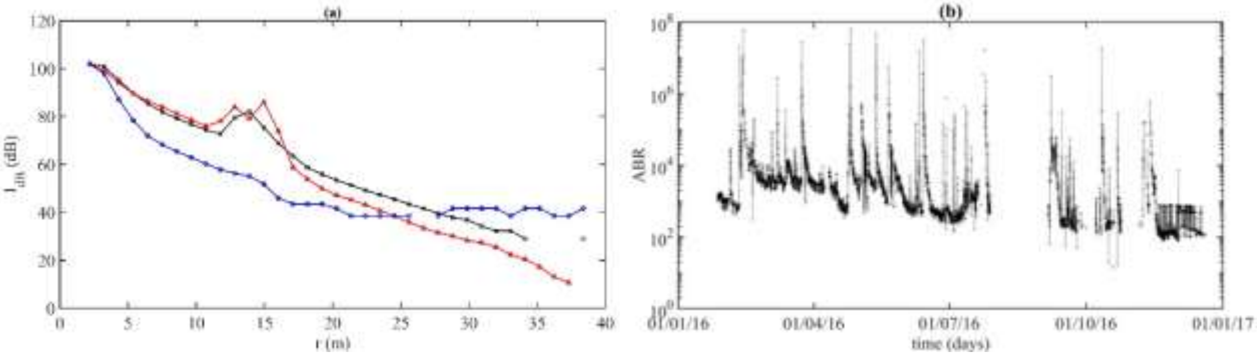

Figure 3. (a) Different profiles obtained at different times. (b) Year long time-series of the attenuation to backscatter ratio (ABR)

A key point of the procedure is the conversion of the ABR values in concentration values. To convert the ABR values in concentration, one needs a calibration function that is a function of the PSD, i.e, diameter and standard-deviation. This function was determined with samples of the suspended sediment transport. The obtained concentration time-series is depicted in Figure 4 together with water level and estimated discharge from water velocity profiles.

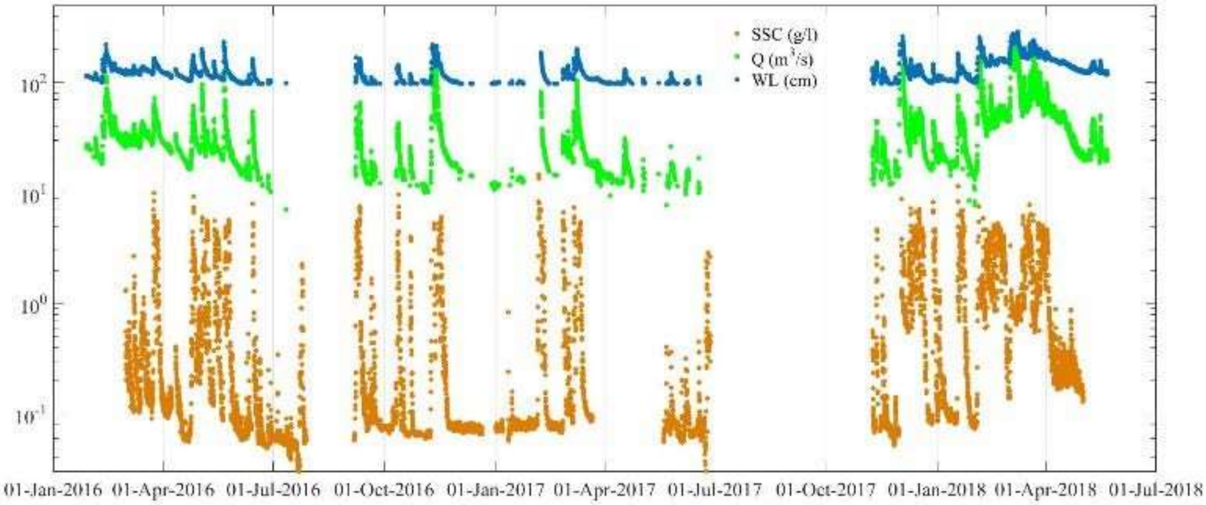

Figure 4. Time series of suspended sediment concentration, SSC, water level, WL, and flow discharge, Q, at Kokel from HADCP monitoring station during the period 1/2016-5/2018 on the Devoll river, Albania.

5 CONCLUSIONS AND FUTURE DEVELOPMENTS

The application of a method to determine the suspended sediment concentration from the echo profiles was used to determine the suspended sediment concentration at the Kokel monitoring station in the

Devoll river. The data was acquired by means of an ADCP working at 0.6 MHz and it was processed by a code developed around the method described in section 2.

To convert the ABR in concentration a calibration function based on semi-empirical relations and suspended sediment samples was used.

This procedure can be used in other rivers provided that an adequate calibration function is available.

REFERENCES

Guerrero, M., DiFederico, V. Suspended sediment assessment by combining sound attenuation and ackscatter measurements – analytical method and experimental validation. Adv. in Water Res. 113 (2018) 167-179.

Guerrero, M., Rüther, N., Szupiany, R., Haun, S., Baranya, S., Latosinski, F. The Acoustic Properties of Suspended Sediment in Large Rivers: Consequences on ADCP Methods Applicability. Water-MDPI. 2016, 8, 13, doi:10.3390/w8010013

Hanes, D.M. On the possibility of single-frequency acoustic measurement of sand and clay concentrations in uniform suspensions. Cont. Shelf Res. 2012, 46, pp. 64–66.

Moore, S.A., Le Coz, J., Hurther, D.& Paquier, A. On the application of horizontal ADCPs to suspended sediment transport surveys in rivers. Cont. Shelf Res. 2012, 46, pp. 50–63.

Thorne, P.D. & Meral, R. Formulations for the scattering properties of suspended sandy sediments for the use in the application of acoustics to sediment transport processes. Cont. Shelf Res. 2008, 28, pp. 309–317.

Impacts of oceanic particles and bubbles on underwater optical wireless communication channel characteristics

Rashmita Sahoo, Palanisamy Shanmugam

Department of Ocean Engineering, Indian Institute of Technology Madras, Chennai – 600036, INDIA

*E-mail: **rashmitasahoo92@gmail.com** ; **pshanmugam@iitm.ac.in**

Abstract

This study describes the effects of different air-sea interface models on the channel characteristics of underwater-to–air optical communication link by Monte Carlo numerical simulation technique. The air-sea interface is considered as a one dimensional slab bounded by the irregular surface and consists of suspended particulates (phytoplankton, suspended sediments, and coloured dissolved organic substances) and wind generated bubbles. The presence of air-sea interface reduces the intensity of light propagating from atmosphere to underwater as well as underwater-to-atmosphere which is estimated from the modelled Bidirectional Transmittance Distribution Function (BTDF). The BTDF is probability distribution function which is a function of wind speed, wavelength and angle of incidence of light at the interface. The results describe the impact of BTDF models varying with wind speed on channel characteristics, mainly normalised power and channel impulse response of a vertically upward communication link which is useful for design and implementation of a physical wireless optical communication system.

1. Introduction

The light propagating from underwater-to-air is influenced by the air-sea interface, suspended particulates and medium inhomogeneity. These effects significantly influence the underwater applications including Wireless Optical Communication between the surface and underwater platforms, underwater target detection, underwater imaging, and search and recovery operations. To date, considerable amount of research has been done on modelling of BTDF and its effects on underwater imaging and remote sensing [1, 2], but its application is limited in the area of underwater optical wireless communication. This work includes the estimation of transmittance and direction of light propagation across air-sea interface from the modelled BTDF.

The air-sea interface is bounded by a random wave and the slope of the random wave is estimated using Cox and Munk model for certain wind speed conditions [3,4]. The thickness of bubble layer and bubble number density at the air-sea interface are the function of wind speed and calculated from the power law equation [1]. Since the water column is inhomogeneous in nature, the medium is stratified into a suitable number of layers having discrete sets of IOPs for vertically upward and downward optical communication. Two different BTDF models for the wind speeds of 12m/s and 14m/s and in-situ measured IOPs are used for the simulation of channel impulse responses. Finally, the simulated impulse responses (CIRs) are compared to describe the temporal channel dispersion [5].

2. Preliminary results

Absorption coefficient, attenuation coefficient, single scattering albedo, volume scattering phase function are the main inherent optical properties used for the simulation of channel impulse response of vertically upward optical communication link. A hyperspectral absorption-attenuation meter (AC-S) was used to measure continuous profiles of beam attenuation ($c_t(\lambda)$) and absorption coefficient ($a_t(\lambda)$) with respect to depth. The measured absorption coefficient is given in Fig.1(a). A Fluorometer-Turbidity Sensor (FLNTU**)** was used to measure chlorophyll concentration with respect to depth, as shown in Fig. 1(a). A multi-angle polarised light scattering meter (LISST-VSF) was used to measure volume scattering phase function values at discrete depths (maximum up to 50 m) with an angular resolution of 0.1-155 degrees. The measured phase function (at 515 nm) at 1m depth is shown in Fig. 1(c).

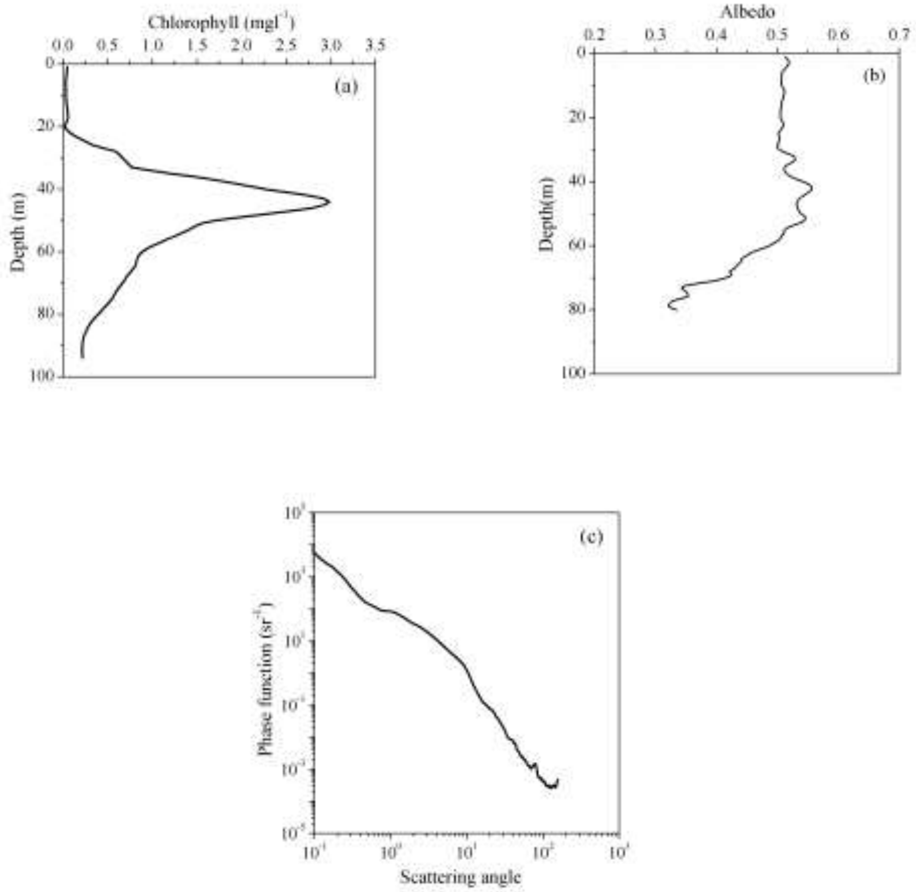

Fig.1. Vertical profiles of the in-situ (a) Chlorophyll concentration, (b) Single scattering albedo, and (c) Scattering phase function from the Bay of Bengal.

BTDF is a bivariate PDF which determines the direction and weight of transmitted photons whenever a photon hits the bubble layer present at sea surface. The BTDF is simulated using Mont Carlo technique for 12m/s and 14 m/s wind speeds, and the results for 550 nm wavelength are shown in Fig. 2. Two different BTDF models are used to simulate channel impulse response at 51m depth for a vertically upward communication link has shown in Fig.3.There is a significant variation between CIRs is observed due to different air-sea interface models.

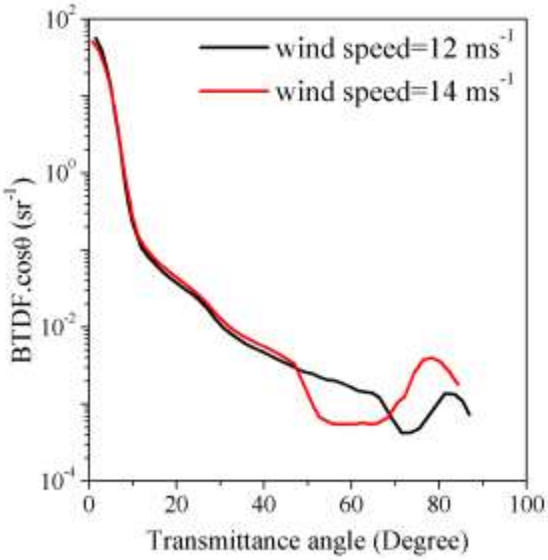

Fig.2. BTDF models for different wind speeds

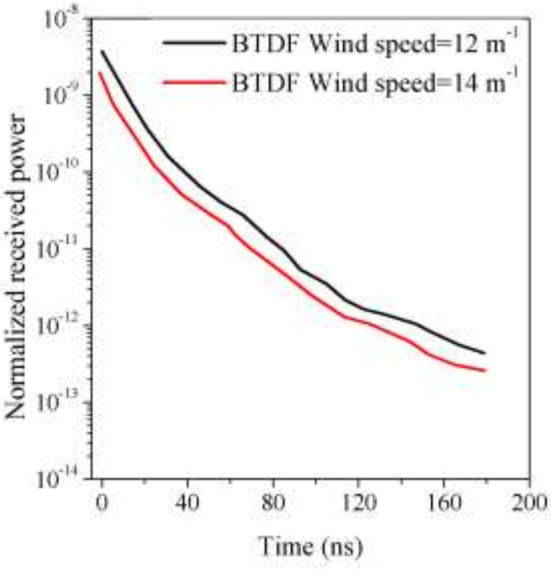

Fig.3. Channel Impulse response at 51m depth for coastal water using aperture= 4" and FOV=180° for different BTDF models.

References

C. Wang, J. Tan, and Q. Lai, “The influence of bubble populations generated under windy conditions on the blue–green light transmission in the upper ocean: An exploratory approach,” Modern Physics Letters B, vol. 30, no. 36, p. 1650420, Dec. 2016.

L. Ma, F. Wang, C. Wang, C. Wang, and J. Tan, “Monte Carlo simulation of spectral reflectance and BRDF of the bubble layer in the upper ocean,” Optics Express, vol. 23, no. 19, p. 24274, Sep. 2015.

W. C. Cox Jr, Simulation, modeling, and design of underwater optical communication systems. North Carolina State University, 2012.

4. M. Hieronymi, “Monte Carlo code for the study of the dynamic light field at the wavy atmosphere-ocean interface”, J. Europ. Opt. Soc. Rap. Public. 8, 13039 (2013).

5. W. C. Cox Jr, Simulation, modelling, and design of underwater optical communication systems. North Carolina State University, 2012.

Measurements of volume scattering function and particle size distribution in natural waters in the Arctic Ocean

H. Sandven[1], A. Kristoffersen[1], Y. C. Chen[1], B. Hamre[1]
E-mail: hakon.sandven@uib.no

[1] Department of Physics and Technology, University of Bergen

ABSTRACT: During the INTAROS 2018 cruise to the Arctic Ocean in July-August 2018, optical instruments including LISST-VSF and LISST-200X were used to investigate the optical properties of ocean particles such as phytoplankton and CDOM in coastal and Arctic waters. Measurements done with LISST-VSF around the ice edge north of Svalbard and in Svalbard coastal waters shows a large variability in the volume scattering function in the upper water column of these environments. The upper turbidity limit of the instrument was reached in highly turbid glacier melt water. Meanwhile, in the very clear water around the ice edge the collected data had a noise level indicating a lower operational limit for the instrument. Some distinct features can be seen in the initial results, for instance a flattening of the VSF curve in the far-forward scattering regime, which is consistent with theory and laboratory measurements of scattering of spheres.

Introduction

High-accuracy quantitative observations of ocean particles such as phytoplankton and CDOM are difficult to obtain in coastal and Arctic waters (Blondeau-Patissier, et al., 2014). Advancement of remote sensing accuracy and the development of new optical in-situ methods requires improved measurements of inherent optical properties (IOPs) of water constituents. These properties include already well-explored quantities like the absorption and scattering coefficients, but also the volume scattering function (VSF). This function represents the ability of particles to scatter light in a certain direction, and is mathematically formulated as

$$VSF(\theta) = \frac{dI(\theta)}{EdV}\,[m^{-1}sr^{-1}],$$

where *E* is the irradiance of an incident unpolarized beam, *dI* is the radiant intensity of the scattered light from the volume element *dV* at an angle θ relative to the incident beam. Here, no azimuthal dependency is assumed, which is the case for media with randomly oriented scatterers. From the VSF, the more widely measured scattering and backscatter coefficients are readily computed (Marken et. al., 2017). In addition, the VSF is an important input in radiative transfer models. The VSF of water constituents has been measured sparingly, especially *in situ*. This is due to the technical difficulty of the measurements, in particular a high demand on the dynamical range of the instrument; the ratio of forward to backward scattered radiance may be larger than 10^7 (M.E. Lee, and M.R. Lewis, 2003). Among the first attempts to measure the VSF we find Tyler (1961) and Petzold (1972), from which the latter has emerged as the most widely cited set of measurements. Modern studies have focused more on laboratory studies, but also includes some in-situ measurements, see Marken et. al. (2017) for an overview.

Methods

The LISST-VSF instrument (Laser In Situ Scattering and Transmissometry; Sequoia Scientific, Inc.) measures the VSF at 515 nm, the large-angle (15˚-155˚) part using eyeball detector, and the forward scattering (0.1˚-15˚) using a ring detector. The particle size distribution has been measured using the LISST-200X (Sequoia Scientific, Inc.). Further optical measurements were done using ac-9 (WetLabs inc.) and Ramses Hyperspectral radiometers (TriOS, Germany). Water samples were collected from three depths at each site, and subsequently filtered and analyzed for determining the IOPs of water constituents and concentration of total suspended matter and chl-a. Temperature and salinity measurements were done using a Castaway-CTD (Xylem, inc.).

The instruments were used during the *INTAROS 2018* research cruise onboard *KV Svalbard* in July-August 2018. Data collection were done on various locations around the ice edge in the Arctic Ocean north of Svalbard. Locations included a variety of different environments encountered in this region; under a large ice floe with approximately one metre thick first-year-ice, in an ice lead (around 1 kilometre long, 250 metres wide), in the marginal ice zone, at the boundary between the marginal ice zone and the open ocean, and in the open ocean. Data were also collected in Arctic fjords in the Svalbard archipelago; Rijpfjorden, Buldrevågen in Hinlopen Strait, and Isfjorden, see figure 1. The former two locations were in small fjords dominated by melt water from glaciers, while the latter location was in a larger fjord further away from glaciers.

In total, nine measurements stations were done. At each station, a small-boat was dispatched from *KV Svalbard* and positioned at least 250 meters from the ship. On the ice floe, and the measurements were done in a similar manner through a hole in the floe. Each of the instruments were lowered into the sea down to depths up to 50 meters using an electric winch, yielding profile measurements of the upper water column. The LISST-VSF, LISST-200X and ac-9 were lowered and raised continuously with approximately 0.5 m/s. Two to three casts were done for each instrument to ensure data validity and provide sufficient sample size.

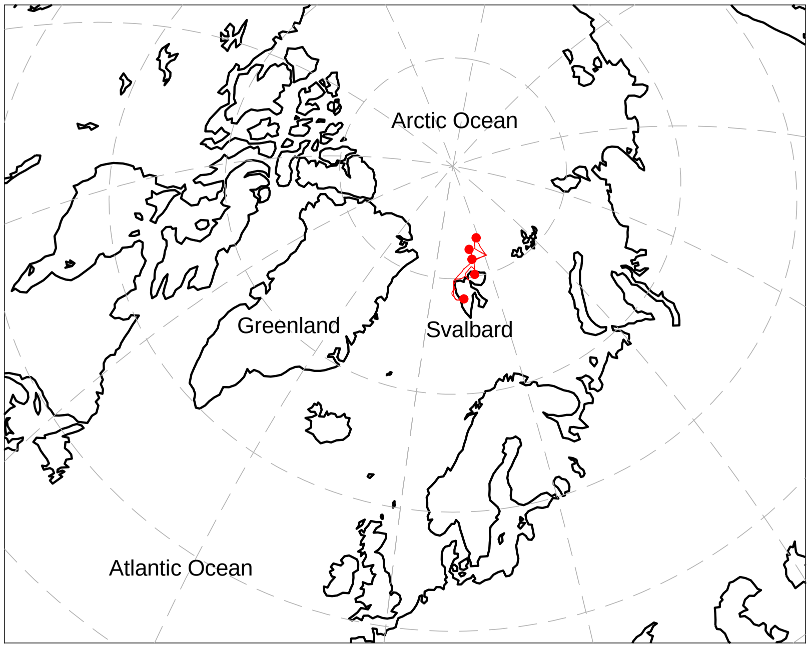

Figure 17: Map showing the GPS track of leg 2 of the INTAROS 2018 cruise, and the general positions of the described measurements stations.

The data processing for the LISST-VSF data consists of removing low-quality data samples and reducing noise using the moving average method. Furthermore, the samples are binned into layers with small depth variations and averaged. Calibration of the instruments was done with milli-Q water. Care was taken to minimize bubbles light contamination from artificial light sources during calibration.

Results and Discussion

The initial results from the LISST-VSF measurements are shown in figure 2. The measurements during the cruise covers a wide range of the VSF occurring in natural waters. The clearest waters studied, under the ice floe and at the ice edge, has minimum values of around 10^{-4} m^{-1} sr^{-1} at angles 110-120 degree, slightly lower than the Petzold clear water measurements. However, for most of the angular domain, the values are higher than the historical data set. For many data samples in the clearest water measurements, the instrument was not able to output values for the eyeball detector measurements, and hence may be close to the lower limit of the eyeball detector. In the most turbid water measured, glacier melt water, the instrument did not record any valid data above 12 metres depth, indicating the upper turbidity limit of the instrument was reached. In the 12-16 meters layer, the mean free path was around 16.7 cm, comparable to the path length of the instrument, and is thus likely influenced by multiple scattering effects.

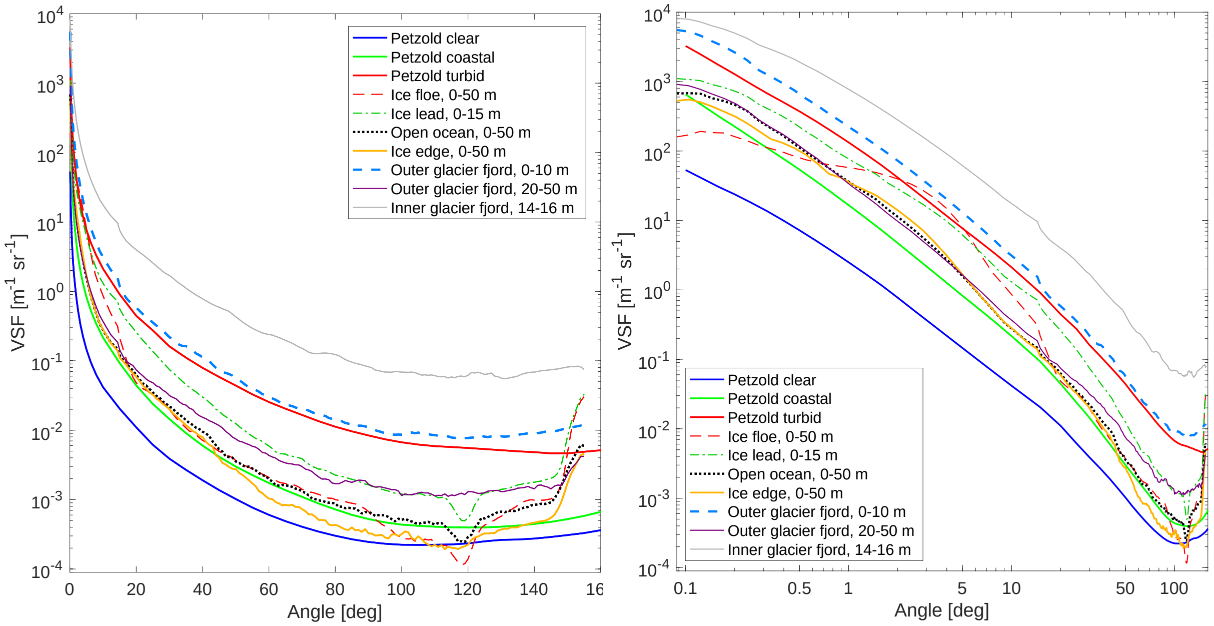

Figure 18: Measured volume scattering functions, plotted with scattering angles 0.1-155 degrees. A selection of results from the INTAROS 2018 cruise is plotted together with the Petzold measurements. Linear x-axis for large-angle emphasis on the left, logarithmic x-axis for small-angle emphasis on the right.

There are some distinct features in the VSF results that are deviating from the Petzold measurements. Increased backscattering close to 160 degrees can be seen in many of the measurements, the exceptions are at the stations with high-turbidity glacier water. At some stations, there is a dip in the VSF around 118 degrees. Whether these features are real or artefacts are a subject of further investigation. There are also visible discontinuities at 15 degrees, where the ring detector and eyeball detector measurements meet, and are thus likely instrumental.

The right plot of figure 2 shows that the forward scattering part of the VSF results diverges from the Petzold measurements when the scattering angle comes close to zero. While the Petzold measurements increases near linearly as the angle approaches zero, the measurements from the LISST-VSF instrument seem to flatten out. In particular, the ice floe results deviate significantly, with high VSF values between 1 and 10 degrees and low values for smaller (and larger) angles, yielding a characteristic flattening. The flattening of the far-forward scattering agrees well with Mie theory, and is supported by laboratory VSF measurements of plastic spheres.

Conclusion

Initial results from the research cruise *INTAROS 2018* show that the VSF, measured with LISST-VSF, vary greatly in the upper water column in different Arctic ocean environments around the Svalbard archipelago, from clear ocean water to high-turbidity glacier melt water. There are some distinct deviations from past VSF measurements in natural waters. In particular, observed flattening in the far-forward scattering, which agrees with theoretical values and laboratory measurements for scattering of spheres. Forward scattering measurements from the LISST-VSF will be highly valuable for future work on scattering of natural and artificial particles, e.g. phytoplankton.

Acknowledgements

We thank the Norwegian Coast Guard, and especially the crew onboard *KV Svalbard* for allocation of ship time and excellent field support during the cruise. We also thank the *INTAROS* project and NERSC for inclusion in the research cruise and support during the cruise.

References

D. Blondeau-Patissier, et al., 2014. “A review of ocean color remote sensing methods and statistical techniques for the detection, mapping and analysis of phytoplankton blooms in coastal and open oceans.” Progress in oceanography 123: 123-144.

M.E. Lee, and M.R. Lewis, 2003. “A New Method for the Measurement of the Optical Volume Scattering Function in the Upper Ocean”. J. Atmos. Oceanic Technol., 20: 563–571.

E. Marken, et al., 2017. Measurement and modeling of volume scattering functions for phytoplankton from Norwegian coastal waters. Journal of Marine Research 75.5: 579-603.

T. J. Petzold, 1972. Volume Scattering Functions for Selected Ocean Waters. Fort Belvoir, VA: Defense Technical Information Center.

J. E. Tyler, 1961. Scattering properties of distilled and natural waters. Limnol. Oceanogr., *6*(4), 451– 456.

Exploratory statistical tools to understand ADCP backscatter response to suspended sediment attribute variations

A.I. Santos (1,2), D. Carinhas (1,3) and A. Oliveira (1)

ana.santos@hidrografico.pt

[1]Instituto Hidrográfico, R. das Trinas, nº 49 – 1249-093 Lisboa, Portugal,

[2]IDL/Faculdade de Ciências da Universidade de Lisboa, Campo Grande, 1749-016 Lisboa, Portugal

[3]IIFA/Universidade de Évora, Palácio do Vimioso Largo Marquês de Marialva, 7002-554 Évora, Portugal

1. INTRODUCTION

The assessment of suspended sediment parameters from the response of acoustic relies on the premise that a relation exists between the acoustic response of an ADCP and the suspended sediment signature present in the measured water column (Thorne & Hanes, 2002, Gartner, 2004, Guerrero et al., 2016, among others). Based on this assumption, is expectable that different suspended sediment signatures (concentration and grain size distributions) will yield different ADCP acoustic responses. In this context, the concept of cluster analysis is to partition sample data into groups or clusters. Clusters are formed such that objects in the same cluster are very similar, and objects in different clusters are very distinct. Considering that different suspended sediment signatures yield different ADCP acoustic responses, in this work, exploratory cluster analysis is applied to ADCP acoustic intensity time series, in order to identify different "populations" of acoustic responses within a time series dataset. Concurrent LISST data will then be used to characterize the identified clusters/populations of ADCP responses in terms of suspended sediment signatures and to determine if the different identified clusters match significantly different suspended sediment populations.

2. METHODS

K-means clustering analysis aims to partition n observations into k clusters in which each observation belongs to the cluster with the nearest mean, serving as a prototype of the cluster. K-means treats each observation in a dataset as an object having a location in space. It finds a partition in which objects within each cluster are as close to each other as possible, and as far from objects in other clusters as possible. Each cluster in the partition is defined by its member objects and by its centroid. The centroid for each cluster is the point to which the sum of distances from all objects in that cluster is minimized. In the case of this work, the concept of distance in the application of the k-means algorithm is substituted by time since the ADCP will respond not to spatial variations of the suspended sediments signatures but to the temporal variation induced by the several forcing agents acting on a single position. K-means cluster analysis was applied to both datasets to the variable pair (time, ADCP I), for k=3 (3 clusters). The Kruskal-Wallis (KW) test is a non-parametric test used to compare three or more populations. In this work, KW test is used to test the null hypothesis (H0) that all populations have equal distribution functions against the alternative hypothesis (H1) that at least two of the populations have different distribution functions. This test was used to test if the resulting 3 populations/clusters identified in the acoustic ADCP response have significantly different suspended sediment signatures (rejection of H0), according to the suspended sediment signatures registered by the LISST (Sigel, 1975; Maroco, 2007).

Two datasets including ADCP with concurrent LISST measurements were collected in 2011 and 2014. Field configurations consisted of one ADCP working at 1228.8 kHz frequency moored looking down together with the LISST probe measuring the current structure in the first meter of the water column with 0.2 m measuring cells (bins), allowing for simultaneous reading of both LISST and ADCP at approximately 80 cm above sea floor. The 2011 dataset was collected at a position offshore S. Pedro de Moel – Z. Piloto at approximately 25 m depth in Sep. 2011 and the second dataset was collected offshore Costa da Caparica at approximately 15 m depth in Oct./Nov. 2014. Further details about these field surveys can be consulted in Santos et al. (2014), and Santos (2016). The results and characterization of the identified populations in these two first datasets was used to apply similar cluster analysis to a third ADCP dataset where no data was available to characterize the sediment populations. This third dataset was collected at the mouth of the Minho estuary in September 2005 using an ADCP working at 614.4 kHz.

3. RESULTS AND DISCUSSION

For the first two datasets, LISST grain size frequency distributions plotted for each identified cluster population showed that cluster analysis yielded in the identification of 3 distinct grain size populations in both datasets in terms of curve shape (not shown). To quantify this distinction, statistical characterization of each cluster via the mean and standard deviation was made for each considered LISST suspended sediment signature and resulting ADCP response, using normalization of the variables. For each dataset, 3 similar populations could be identified (table I, Figure 1):

Population I (“higher” - fine): Characterized by higher than average ADCP I (acoustic intensity) response, higher than average sediment concentrations; lower than average mean grain diameters, sharper than average grain size curves and higher than average fine fraction (<62.5 µm) content ;

Population II (“lower” - coarse): Characterized by lower than average ADCP I response, lower than average sediment concentrations; higher than average mean grain diameters, wider than average grain size curves and lower than average fine fraction (<62.5 µm) content;

Population III (“standard”): Characterized by average ADCP I response, average sediment concentrations; average mean grain diameters, average width grain size curves and average fine fraction (<62.5 µm) content .

Kruskal-Wallis (KW) tests were applied to the three populations identified by cluster analysis in the ADCP acoustic response, to statistically prove that suspended sediment signatures are significantly different. In this test, a Type I (α) error probability of 0.05 was used. Table II shows the results of the KW tests applied to both ADCP I and the suspended sediment variables reported by the LISST data. Both the normalized and real values show the exact statistical position which proves that normalization of the variables had no effect on the results. All tested populations show statistically significant difference in the populations (asymptotic significance=0 => H0 is rejected and the alternative hypothesis H1 is the most probable) for the ADCP I acoustic response in both datasets, proving that the cluster analysis was effective in separating 3 distinct responses. Suspended sediment signature variables’ tests also revealed that the separation of the three different acoustic response populations effectively corresponds to different suspended sediment signatures.

These results applied to the Minho dataset (September 2005) show that 3 similar populations were identified corresponding to the “higher”, “lower” and “standard” (based on ADCP I values) populations characterized in the previous datasets. Although no definitive patterns could be established, the presence of the “higher” (fine) population was associated with ebb and flood current maxima, during spring tides. The “lower” (coarse) population was generally associated with current minima during flood and ebb slacks. If the previously established LISST characterization of the suspended sediment signatures is taken into consideration, it can be established that the Minho outlet was characterized by a fine suspended sediment signature which seems to be in permanent transit in the water column with flood and ebb fluxes. During the tidal slacks, the sediments present in the water column result in a "lower" (coarse) acoustic signature, which might correspond to the transit of coarser flocculated particles rich in organic matter, especially during the beginning of ebb (fig. 3). These coarser particles can be the result of flocculation processes occurring upstream (in the limit of saline oceanic water intrusion), or biogenic coarser particles with higher floatability.

Table I: Statistical characterization of total analyzed datasets and each one of the identified clusters for normalized and real values. Negative normalized Means (μ) imply a lower than average real values (in red) and positive normalized μ (in green) imply higher than average real values. Normalized Means (μ) between -0.5 and 0.5 were considered neutral or close to average (in blue). Population I is shaded in orange; Population II in blue and Population III in green

	Z. Piloto - 2011				**C. da Caparica 2014**			
	Normalized Variable		**Real Value**		**Normalized Variable**		**Real Value**	
	μ	σ	μ	σ	μ	σ	μ	σ
ADCP I (dB)	0.00	1.00	82.78	7.56	0.00	1.00	81.94	4.11
SSC (kgm^{-3})	0.00	1.00	0.30	0.29	0.00	1.00	0.21	0.19
Mean D - VD (μm)	0.00	1.00	129.67	38.54	0.00	1.00	92.08	27.37
StDev - VD (μm)	0.00	1.00	38.66	5.42	0.00	1.00	37.45	4.93
Fine (freq.)	0.00	1.00	0.23	0.12	0.00	1.00	0.45	0.19
					Cluster 1			
ADCP I (dB)	**1.61**	0.45	94.95	3.43	**-0.85**	0.50	78.43	2.05
SSC (kgm^{-3})	**0.57**	0.97	0.46	0.28	**-0.55**	0.31	0.10	0.06
Mean D - VD (μm)	**-0.91**	0.38	94.54	14.55	**0.99**	0.58	119.13	15.78
StDev - VD (μm)	**-0.75**	0.66	34.62	3.59	**0.59**	0.77	40.35	3.81
Fine (freq.)	**1.20**	0.83	0.38	0.10	**-0.99**	0.36	0.26	0.07
					Cluster 2			
ADCP I (dB)	**-0.76**	0.30	77.08	2.28	**1.01**	0.60	79.00	2.45
SSC (kgm^{-3})	**-0.28**	0.88	0.22	0.26	**0.88**	1.07	0.37	0.20
Mean D - VD (μm)	**0.61**	0.90	153.22	34.69	**-0.94**	0.63	121.54	15.07
StDev - VD (μm)	**0.57**	0.87	41.78	4.58	**-0.32**	0.70	40.21	3.43
Fine (freq.)	**-0.66**	0.44	0.15	0.05	**1.05**	0.57	0.25	0.08
					Cluster 3			
ADCP I (dB)	**0.04**	0.32	83.05	2.45	**-0.07**	0.75	81.65	3.07
SSC (kgm^{-3})	**0.03**	1.03	0.30	0.30	**-0.33**	0.76	0.15	0.14
Mean D - VD (μm)	**-0.37**	0.81	116.81	29.80	**-0.20**	0.54	86.48	14.68
StDev - VD (μm)	**-0.40**	0.86	36.48	0.77	**-0.43**	0.91	35.35	0.54
Fine (freq.)	**0.18**	0.85	0.25	0.11	**0.06**	0.56	0.46	0.11

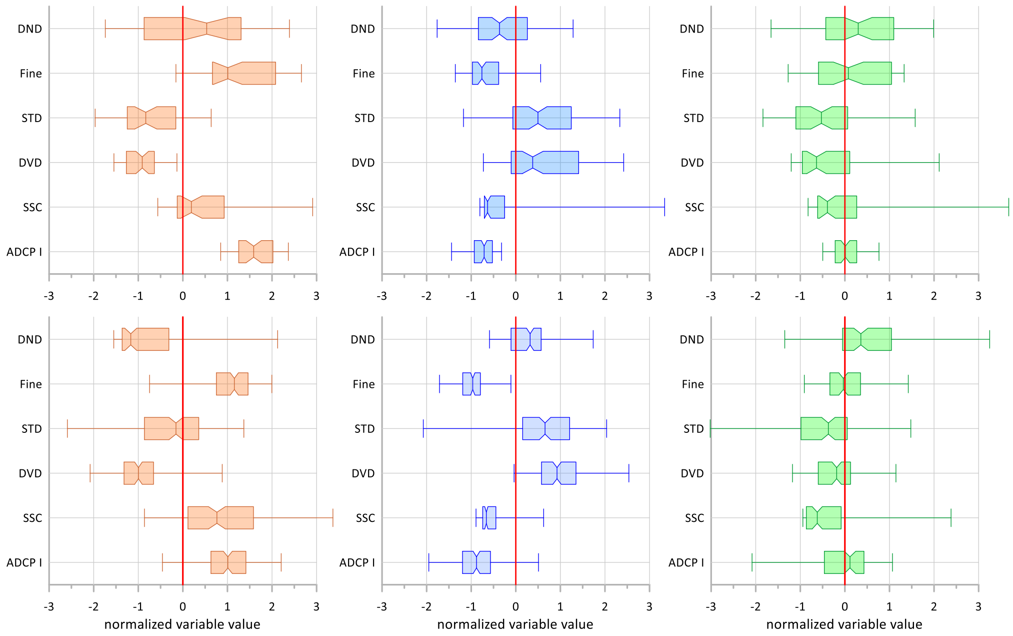

Fig. 2. Box-plot of normalized ADCP I response and LISST grain size signature variables. Population I is shaded in orange; Population II in blue and Population III in green. ADCP I – ADCP acoustic intensity; SSC – Suspended sediment concentration; DVD – Mean diameter for volume distributions; STD – standard deviation (shape of grain size distribution) for the volume distribution grain size curve; Fine – Fine fraction (<62.5 µm) frequency and DND - Mean diameter for particle number distributions.

Table II: Results of Kruskal-Wallis tests applied to both ADCP acoustic response (ADCP I) and the suspended sediment signature variables independently measured by the LISST.

	Z. Piloto - 2011 (n=211)						**C. da Caparica 2014 (n=433)**					
	Normalized Variable			Real Value			Normalized Variable			Real Value		
	X^2_{KW} ($p<0.05$)	df	Asymptotic significance	X^2_{KW} ($p<0.05$)	df	Asymptotic significance	X^2_{KW} ($p<0.05$)	df	Asymptotic significance	X^2_{KW} ($p<0.05$)	df	Asymptotic significance
ADCP I (dB)	172.06	2	0	172.06	2	0	278.52	2	0	278.52	2	0
SSC (kgm^{-3})	50.38	2	0	50.38	2	0	158.57	2	0	158.57	2	0
Mean D - VD (µm)	101.68	2	0	101.68	2	0	309.43	2	0	309.43	2	0
StDev - VD (µm)	72.74	2	0	72.74	2	0	105.91	2	0	105.91	2	0
Fine (freq.)	103.20	2	0	103.20	2	0	330.61	2	0	330.61	2	0

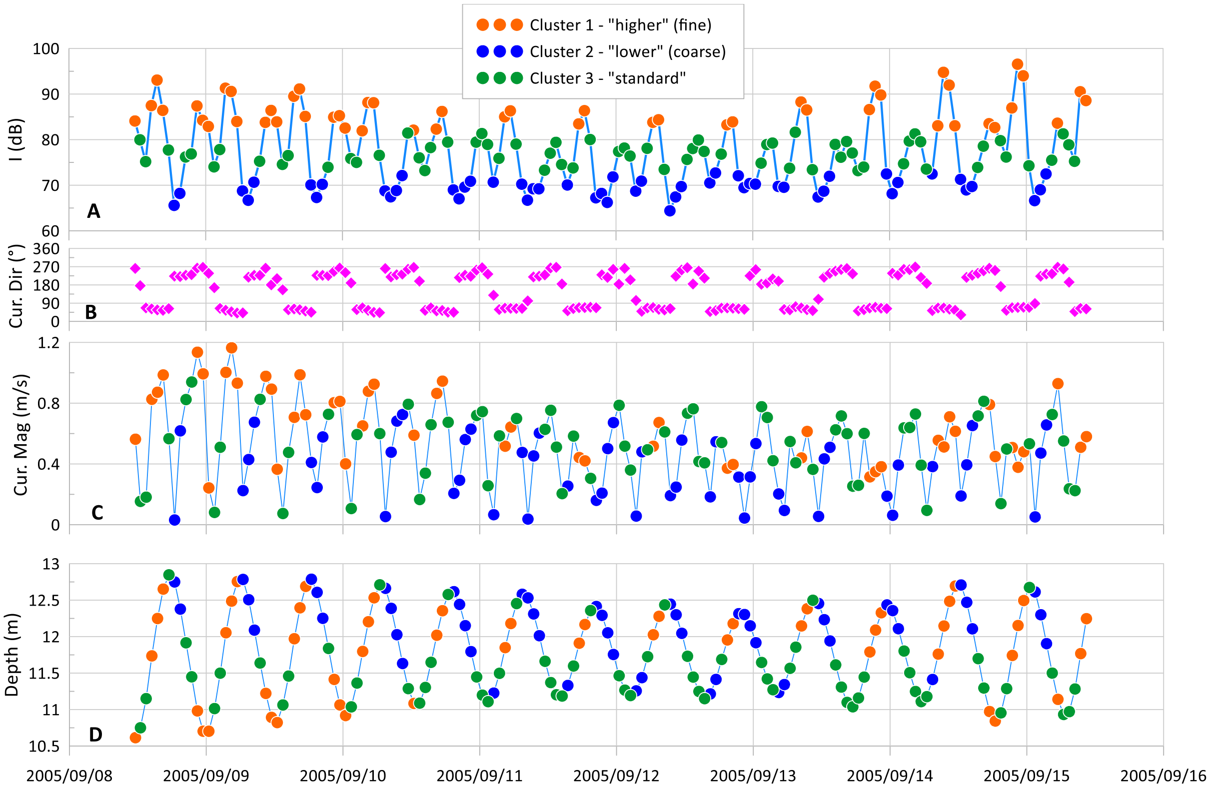

Fig. 3. ADCP (bin 1 – 1.7 above bottom) data time series (1 hour averages) collected at the mouth of the Minho estuary (NW Portugal) in the September 2005 ECOIS survey. A – ADCP acoustic intensity; B – Current direction; C – Current magnitude; D - Depth

4. FINAL REMARKS

Exploratory cluster analysis was applied to two different ADCP acoustic intensity time series in order to identify and separate different populations of acoustic response. These 3 populations were then characterized in terms of suspended sediment signature based on concurrent LISST measurements. Results showed that 3 statistically significantly different populations of suspended sediments could be identified in both datasets based solely on the statistical analysis of ADCP acoustic response.

Based on these results, a similar analysis was applied to a short ADCP time series where no information about suspended sediment signatures was available. Cluster analysis of the acoustic data allowed for a tentative explanation of the sediment transport patterns at the point of deployment, in agreement with the sediment transport patterns that can be observed in any tidal estuary outlet.

5. REFERENCES

Gartner, J. W. (2004). Estimating suspended solids concentrations from backscatter intensity measured by acoustic Doppler current profiler in San Francisco Bay, California. Marine Geology, 211(3), 169-187. doi: 10.1016/j.margeo.2004.07.001

Guerrero, M.; Rüther, N.; Szupiany, R.; Haun, S.; Baranya, S.; Latosinski, F. (2016). The Acoustic Properties of Suspended Sediment in Large Rivers: Consequences on ADCP Methods Applicability. Water, 8, 13. doi: 10.3390/w8010013

Maroco, João (2007) Análise Estatística, 3ª ed, Edições Sílabo, Lisboa

Santos, A. I.; Oliveira, A.; Zacarias, N.; Pinto, J. P.; Ribeiro, M. (2014). Suspended sediment transport patterns on the inner shelf–S. Pedro de Moel (Portugal). Journal of Sea Research, Vol 93, pp.: 47-56.doi : 10.1016/j.seares.2014.04.009

Santos, A. I. (2016). Using ADCP backscatter data as a proxy of suspended sediments in the water column. Seminário de Pós Graduação I - Report done as part of the Advanced Training Course taken under the scope of the PhD in Geology, External Geodynamics, University of Lisbon, Faculty of Sciences

Siegel, Sidney (1975). Estatística não- paramétrica (para as ciências do comportamento), São Paulo: McGraw Hill.

Thorne, P.D. and Hanes, D.M. (2002). A review of acoustic measurement of small-scale sediment processes. Continental Shelf Research, 22, 603-632. doi: 10.1016/S0278-4343(01)00101 7

Testing a biological resuspension footprint model using Lagrangian simulations

Uri Shavit[1], Amit Halamish[1], Shahar Grossbard[1], Shai Asher[1], Merav Gilboa[2], Timor Katz[3], and Gitai Yahel[2]

[1]Civil and Environmental Engineering, Technion, Haifa, Israel

[2]The School of Marine Sciences, Ruppin Academic Center, Michmoret, Israel

[3]Israel Oceanographic & Limnological Research, Tel Shikmona, 31080 Haifa, Israel

Introduction

Resuspension of sediments from the sea floor is crucial for the wellbeing of the ocean ecosystem. It generates mixing between the sediment layers and the water column, it accelerates and controls biological processes and chemical reactions (Vidal 1994, Stahlberg et al. 2006) and affects the distribution of organisms such as bacteria and filter feeders (Cotner 2000, Snelgrove and Butman 1994). As opposed to the so called "physical resuspension" that is generated by strong currents and waves, biological resuspension occurs at the bottom of the sea due to the activity of marine creatures such as fish. It has been suggested that in biologically rich areas such as coral reefs, biological resuspension is dominant over physical resuspension. In deep sea regions, where the currents and waves are negligible, biological activity and gas bubbling are the only known mechanisms that can generate sediment resuspension. And yet, there are surprisingly only a few studies on biological resuspension, and the ones that exist suggest an impact far greater than was previously suspected, often exceeding waves and current driven resuspension (Yahel et al., 2002, Yahel at al., 2008).

The objective of the presented study is to provide the means to estimate the average flux of particles, $\bar{J}_z(kg\, m^{-2} s^{-1})$, that leave the bottom of the sea due to biological resuspension events. This flux is positive upwards and by multiplying it over a given floor area and a given time period, we should be able to provide an estimate of the total mass of particles that is biologically resuspended. Such an estimate is difficult to obtain. A single sensor that measures particle concentration near the bottom cannot provide the desired information about $\bar{J}_z$ without an appropriate model. In fact, the only approach that can provide a direct estimation of $\bar{J}_z$ is a complete mass balance formulation. This can be obtained either by computational fluid dynamics (CFD) solutions or by measuring the velocity and particle concentration around local control volumes together with a solution of the mass balance integral equation. While the former is not computationally feasible at ocean scales, the latter needs to fully cover the control volume faces and inner space by measurements and it is therefore too expensive. To overcome these limitations, we propose a model for $\bar{J}_z$ that is based on point measurements of concentration and velocity. The model is based on some major assumption and the aim of the study is to test their validity. The model was tested against in-situ measurements, experiments in a laboratory flume and lagrangian simulations. In the following we report on the development of the model and an evaluation of its accuracy and assumptions against lagrangian simulations.

Model derivation

We aim at estimating $\bar{J}_z$ by using a stationary sensor that is located downstream from resuspension events and records simultaneously the particle horizontal velocity, u_p, and the particles concentration, $c(kg\, m^{-3})$. Examples of such sensors include an OBS (optical backscatter sensor), LISST (laser-diffraction instrument), ADV (acoustic Doppler velocimeter), the aquatic eddy covariance method and image based techniques. Some sensors measure concentration, some velocity and others measure both.

We limit the model to cases where the vertical particle velocity generated by the resuspension event is significantly larger than the horizontal water velocity, and therefore assume that the advection of the particle cloud begins only after the rise of the particles has ended. Concurrent to the horizontal advection, diffusive mixing and settling take place with time scales that are larger than those of the horizontal advection. We then consider a mass balance approach to use the sensor data in order to estimate the resuspension flux, $\bar{J}_z$. We assume that the number of resuspension events measured during the deployment time is large enough to assume that they represent, on average, the variety of clouds that were generated upstream from the sensor, i.e., the number of events is large enough to use an analogy of a non-point (surface) source to represent, on average, multiple point-source events. We name this assumption as the "deployment long time concept". In order to apply a mass balance, we define a vertical narrow strip of an area $h\Delta y_s$ that is perpendicular to the horizontal flow where Δy_s is the width of the sensor sampling volume and h is an estimate of the average height of the plumes generated by the resuspension events. An integration of the horizontal flux that crosses the vertical strip during time T provides an estimate of the total mass of particles, $M(kg)$, that crossed the strip,

$$M = \Delta y_s \int_{z_0}^{h} \int_{t}^{t+T} c u_p dt\, dz \tag{1}$$

where z_0 is a reference boundary above the bottom. Under the assumption that $c(z)$ and $u_p(z)$ follow some similarity rules, the measurement at a single height can be used to guess the two profiles, however it is obvious that measurements of $c(z)$ and $u_p(z)$ at additional heights will reduce the level of uncertainties. Practically, the integral time and space steps, Δt and Δz_s are determined by the sensor sampling rate and by a product of the vertical cross section area of the sampling volume, $a_s = \Delta z_s \Delta y_s$.

Using the deployment long time concept, we assume that the integral mass balance calculation may use a pseudo steady state condition and therefore M (Eq. 1) is equal to the total mass of particles that were resuspended during time T from a floor surface area of size A. The floor surface area, $A = L\Delta y_s$, is a narrow strip of width Δy_s and a length L that has to be estimated. We propose to use either the particle settling velocity or the diffusive-like mixing, "whoever comes first". The idea behind the settling velocity is that particles that were resuspended far away from the sensor settle before they reach the sensor and therefore,

$$L \cong \frac{u_p h}{2 w_{p_s}} \tag{2}$$

where w_{p_s} is the Stokes settling velocity due to gravity. Alternatively, when diffusive-like mixing is used, L is define as follows,

$$L \cong \frac{u_p}{D} \left(\frac{c_{max}}{c_b} V_s \right)^{2/3} \tag{3}$$

where c_{max} is the highest concentration that is measured among all the resuspension events and D is the mixing diffusivity coefficient. The concentration of the resuspension cloud is defined as the concentration above the background concentration, $c > c_b$. Therefore, if the resuspension cloud was mixed and its concentration became smaller than the background concentration, it cannot be detected and is not considered as a trace of a resuspension event anymore. If the sensor sampling volume, V_s, is approximately a cube ($V_s = \Delta {y_s}^3$), Eq. 3 is rewritten as,

$$L \cong \frac{u_p}{D}\left(\frac{c_{max}}{c_b}\right)^{2/3} \Delta {y_s}^2 \tag{4}$$

The actual length L will be chosen as the smallest value calculated from Eqs. 2 and 3. We derived Eqs. 3 and 4 by assuming that there is at least one resuspension event that took place right at the sensor location such that it measured the concentration c_{max} of the plume. The mass of particles that were measured by the sensor at this event is $m = V_s c_{max}$. While being advected a distance L, the plume was slowly diluted by diffusive-like mixing processes until the concentration reached the background concentration, c_b. The "new" volume that contains the mass m is defined as ℓ^3 such that $m = \ell^3 c_b$. The diffusive length ℓ which is $\ell = (V_s c_{max}/c_b)^{1/3}$ can be estimated as $\ell = \sqrt{Dt}$ where t is the time of mixing ($t = \ell^2/D$) and is equal to the time of advection, $t = L/u_p$ and hence, $L = u_p t = u_p \ell^2/D = u_p (V_s c_{max}/c_b)^{2/3}/D$.

We propose to estimate the average flux of biological resuspension during time T using the calculation of M by Eq. 1 and an estimate of the area A,

$$\overline{J_z} = M/(TL\Delta y_s) \tag{5}$$

When L is estimated using Eq. 2, Eq. 5 becomes,

$$\overline{J_z} = \frac{2w_{p_s}}{Tu_p h}\int_{z_0}^{h}\int_{t}^{t+T} c u_p dt\, dz \tag{6}$$

and when L is estimated using Eq. 4, Eq. 5 becomes,

$$\overline{J_z} = \frac{D}{Tu_p \Delta {y_s}^2}\left(\frac{c_b}{c_{max}}\right)^{2/3}\int_{z_0}^{h}\int_{t}^{t+T} c u_p dt\, dz \tag{7}$$

For either Eq. 6 or 7, the integration over z and the need for multiple sensors and measurements can be simplified if c and/or u_p are either constant or follow some similarity profiles.

Lagrangian particle tracking simulations

Equations 6 and 7 were tested against field and laboratory data, however in both cases a perfect evaluation of the model accuracy is difficult to obtain. Instead, the current paper presents a comparison of Eqs. 6 and 7 against results of tracking simulations of hypothetical particles generated by biological resuspension events. The lagrangian model generates N_{pl} plumes at locations and times that were determined by random sampling of uniform probability density functions (pdf). Each plume was generated by N_p particles that were distributed randomly with a multi-variant normal distribution in the horizontal direction and either uniform or lognormal distributions in the vertical direction. The particles were allowed to move with a uniform horizontal velocity, assuming complete drag, size dependent Stokes settling velocity and homogeneous dispersion, assuming a direct relationship between the diffusivity coefficient D and the dispersion standard deviation $\sigma = \sqrt{2Dt}$. Sensors were simulated at a predetermined position by recording the number of particles found at each time step within the sensor measurement volume. These concentration time series were used to calculate $\overline{J_z}$ by Eqs. 6 or 7 and then compared with the known resuspension imposed by the generation of plumes.

Results and discussion

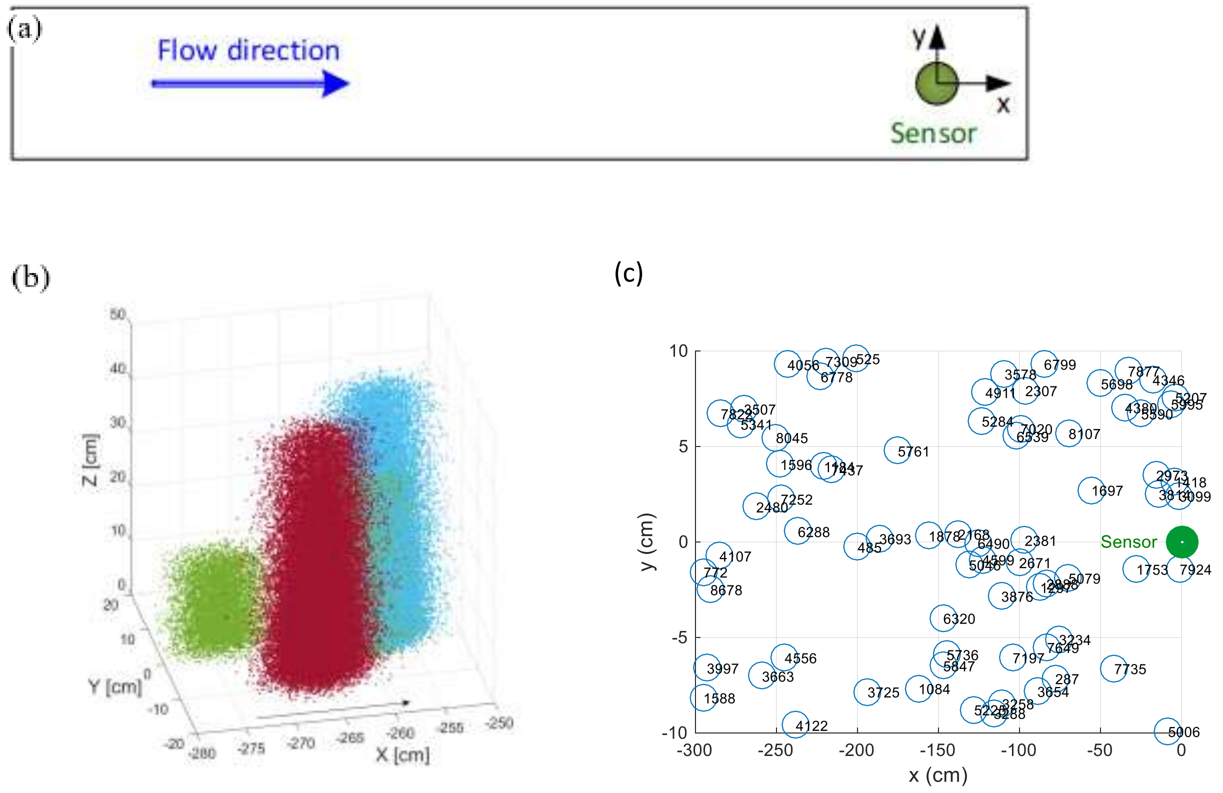

Fig. 1 (a) A top view schematic of the sea floor domain; (b) An illustration of four plumes; (c) Location and time (marked in seconds) of plume generation 3 meter upstream from the sensor (out of 10 m domain length).

Fig. 1a is a top view schematic of the sea floor domain (10 m × 0.2 m) from which plumes of particles were released at random locations and times. Since no variations of the flow direction and intensity were simulated, the width of the domain was set to be twice the width of the plumes. The sensor and the coordinate system are also shown. The model is expected to be valid when the flow direction is not constant. This is explained by the orientation of the domain that is thought to be aligned with the flow direction, with the sensor as the axis of rotation. Fig. 1b shows a close-up 3D scatter image of four plumes. These plumes were generated at different times and locations with a log-normal distribution of the particles location along z. The plumes particles in this specific illustration were advected by the flow, settled by gravity, but experienced no dispersion. The shape of the left plume (green) indicates that it was generated earlier and upstream from the current location. Also shown are some particles that were mixed with the other two larger plumes, indicating that plumes can overlap each other. Fig. 1c illustrates the random location and time of plume generation (sampled from a uniform distribution) 3 m upstream from the sensor. The plume density in this specific case was 0.013 (# $m^{-2}\ s^{-1}$).

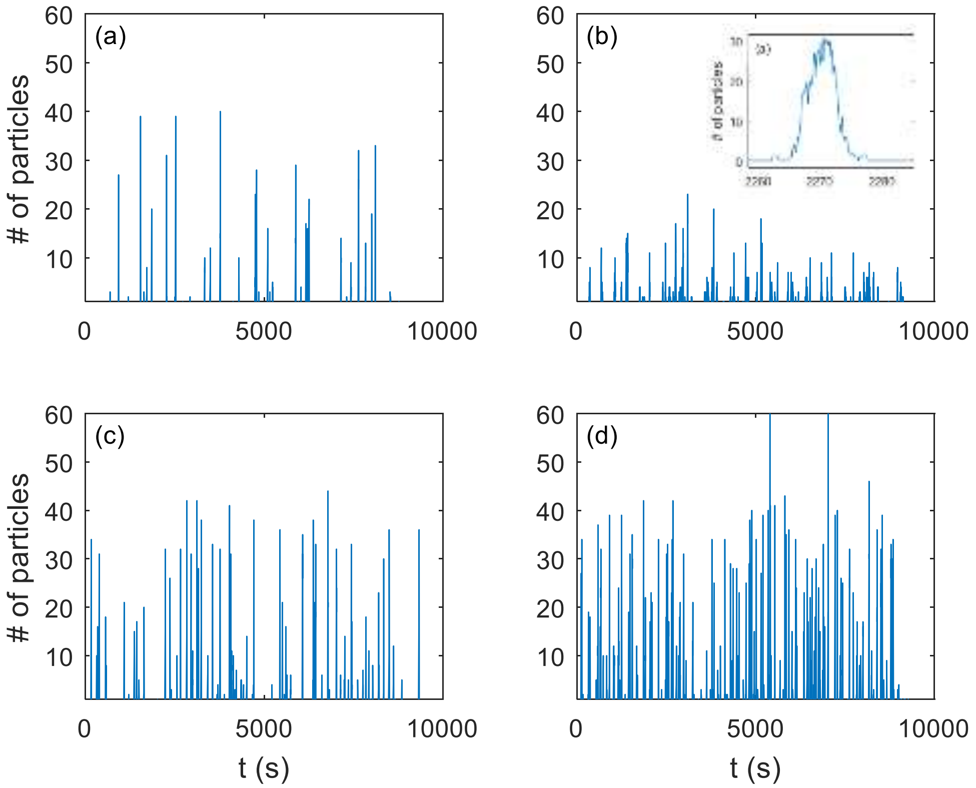

Fig. 2 Examples of concentration signal measured by the sensor. Plumes generation density was $0.005\ \#\ m^{-2}s^{-1}$ in (a) and (b), $0.013\ \#\ m^{-2}s^{-1}$ in (c) and $0.025\ \#\ m^{-2}s^{-1}$ in (d). No dispersion was applied except for the case shown in (b). The insert in (b) is a zoom-in taken from the signal shown in (a).

Fig. 2 shows four time-series measured by the sensor. In these cases the current horizontal velocity was $u_p = 1\ cm\ s^{-1}$ and settling velocity $w_p = -0.05\ cm\ s^{-1}$. It is apparent that as the plumes generation density increases (from $0.005\ \#\ m^{-2}s^{-1}$ to $0.025\ \#\ m^{-2}s^{-1}$, see figure caption for more details) the signal becomes denser. It also shows that concentration decreases when dispersion is applied (Fig. 2d). The insert in (b) shows a zoom-in of the concentration signal generated by one of the plumes in Fig. 2a. An increase of the generation density is likely to improve the prediction of Eq. 6. We postulate, however, that when the density is low the deployment long time concept may still be valid by longer deployments.

An apparent drawback of Eq. 6 is the need to integrate the velocity and concentration along the vertical axis z. It means that one single sensor is not enough and a series of sensors should be mounted one above the other and temporally synchronized. The ability of Eq. 6 to reconstruct the imposed resuspension flux when using a single sensor was tested in Fig. 3. The results are shown for simulations with no dispersion, constant horizontal and settling velocities, uniform particle size and a random distribution of the particle initial vertical location that follows a uniform distribution function. The figure shows the relative difference between the calculated flux by Eq. 6 (j_m) and the imposed flux (j_i). The results are shown for three cases assuming a constant concentration that is measured by a single sensor, positioned at three vertical locations ($z = 0.2h, 0.5h\ \&\ 0.8h$), and for a case with enough sensors to apply an integration along z as indicated by Eq. 6. Fig. 3 shows that the ability of Eq. 6 to provide a good estimate of the resuspension average flux increases with the plumes generation density. This is the case when applying an integration over z or when the sensor is at $0.5h$. However, a lower sensor position results in an overestimation and a higher position results in an underestimation.

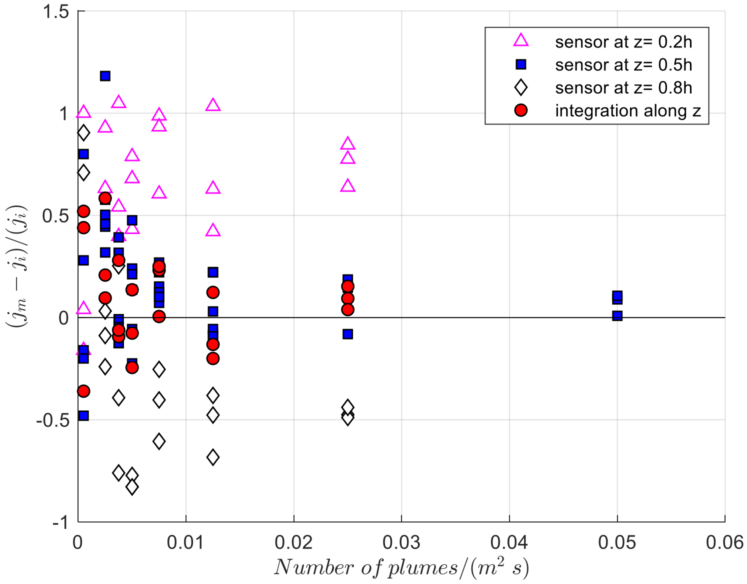

Fig. 3 The relative error in using Eq. 6 (j_i is the imposed flux; j_m is the flux calculated by Eq. 6) as a function of the plumes generation density, assuming a constant concentration, measured at three vertical sensor locations and by integrating the concentration along z.

The ability of Eq. 6 to reconstruct the imposed flux was tested for an initial vertical distribution that follows non-uniform distributions such as log-normal. The results in Fig. 4 show a comparison of three cases: (1) uniform distribution; (2) log-normal distribution ($\mu = 3\ cm$, $\sigma = 1\ cm$); and (3) log-normal distribution ($\mu = 3\ cm$, $\sigma = 2\ cm$). These simulations were obtained for a constant horizontal and settling velocities and zero dispersion. Fig. 4b shows that Eq. 6 provides good flux estimates when the

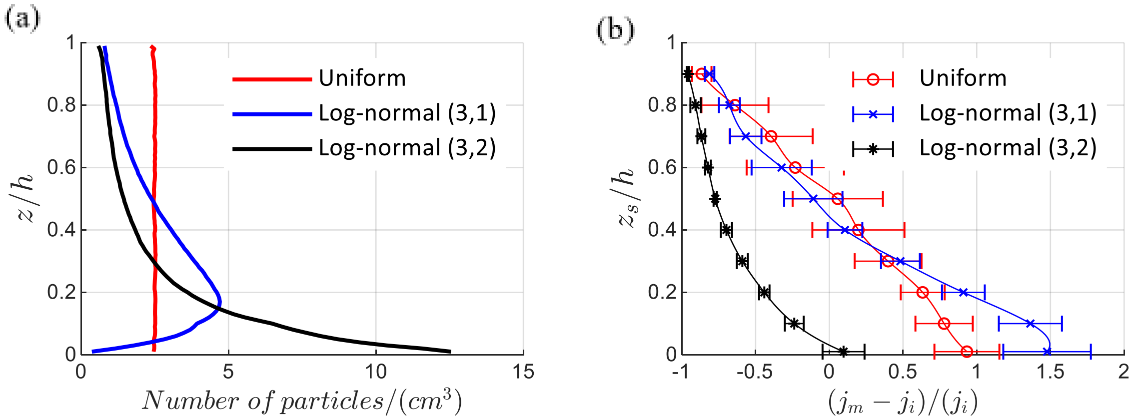

Fig. 4 (a) Vertical profiles of the initial concentration, generated by a uniform and two log-normal distribution functions; (b) The relative error of Eq. 6 as a function of the sensor position z_s.

sensor is positioned at half the plume height for the uniform distribution and the first log-normal distribution ($\mu = 3\ cm$, $\sigma = 1\ cm$), however when the second log-normal distribution was used all the sensor positions provided an underestimation except for the lowest position. The particles of this case sank to the floor before they were sampled by the sensor and as a result Eq. 6 provides an underestimate. It could be claimed however, that the role of heavy particles that were not suspended to significant heights have a limited influence on the water column and are therefore less relevant. Hence, the smaller flux estimated by Eq. 6 could be considered as an appropriate estimate.

Acknowledgment: We wish to acknowledge the generous financial support received from the Israeli Ministry of Science, Technology and Space (Grant 3-12478).

References

Cotner JB (2000) Intense winter heterotrophic production stimulated by benthic resuspension. Limnol Oceanogr 45:1672–1676

Snelgrove PVR, Butman C (1994) Animal-sediment relationships revisited: cause versus effect. Oceanogr Mar Biol an Annu Rev:111–177

Stahlberg C, Bastviken D, Svensson BH, Rahm L (2006) Mineralisation of organic matter in coastal sediments at different frequency and duration of resuspension. Estuar Coast Shelf Sci 70:317–325

Vidal M (1994) Phosphate dynamics tied to sediment disturbances in Alfacs Bay (NW Mediterranean). Mar Ecol Prog Ser 110:211–221

Yahel R, Yahel G, Genin A (2002) Daily cycles of suspended sand at coral reefs: A biological control. Limnol Oceanogr 47:1071–1083

Yahel G, Yahel R, Katz T, Lazar B, Herut B, Tunnicliffe V (2008) Fish activity: a major mechanism for sediment resuspension and organic matter remineralization in coastal marine sediments. Mar Ecol Prog Ser 372:195–209

Measuring light backscattering for lidar applications (where we left off)

Wayne H Slade and Yogesh C Agrawal

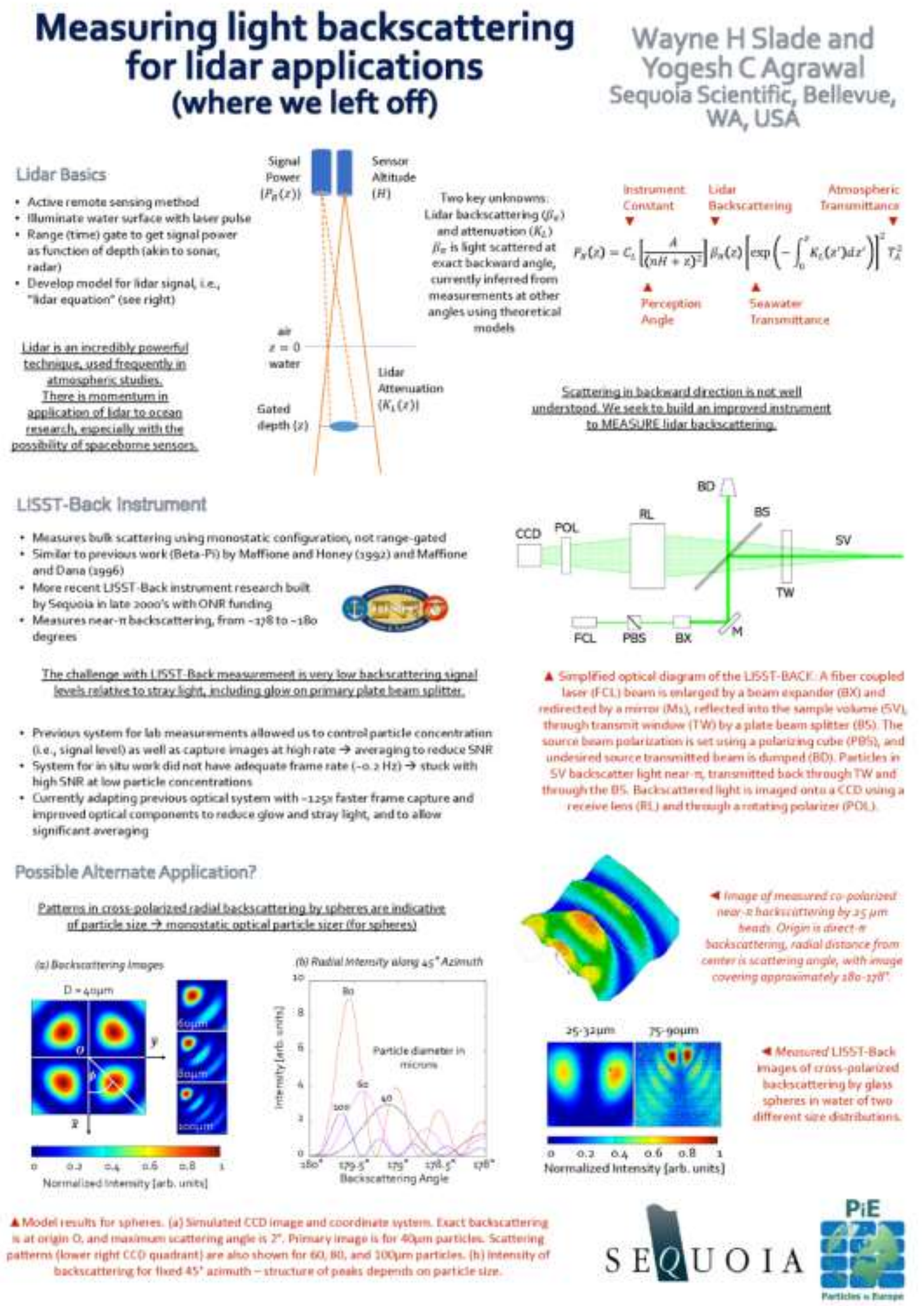

Measuring light backscattering for lidar applications (where we left off)

Wayne H Slade and Yogesh C Agrawal
Sequoia Scientific, Bellevue, WA, USA

Lidar Basics

- Active remote sensing method
- Illuminate water surface with laser pulse
- Range (time) gate to get signal power as function of depth (akin to sonar, radar)
- Develop model for lidar signal, i.e., "lidar equation" (see right)

Lidar is an incredibly powerful technique, used frequently in atmospheric studies. There is momentum in application of lidar to ocean research, especially with the possibility of spaceborne sensors.

Two key unknowns: Lidar backscattering (β_π) and attenuation (K_L) β_π is light scattered at exact backward angle, currently inferred from measurements at other angles using theoretical models

Instrument Constant ▼ Lidar Backscattering ▼ Atmospheric Transmittance ▼

$$P_R(z) = C_L \left[\frac{A}{(nH+z)^2}\right] \beta_\pi(z) \left[\exp\left(-\int_0^z K_L(z')dz'\right)\right]^2 T_A^2$$

▲ Perception Angle ▲ Seawater Transmittance

Scattering in backward direction is not well understood. We seek to build an improved instrument to MEASURE lidar backscattering.

LISST-Back Instrument

- Measures bulk scattering using monostatic configuration, not range-gated
- Similar to previous work (Beta-Pi) by Maffione and Honey (1992) and Maffione and Dana (1996)
- More recent LISST-Back instrument research built by Sequoia in late 2000's with ONR funding
- Measures near-π backscattering, from ~178 to ~180 degrees

The challenge with LISST-Back measurement is very low backscattering signal levels relative to stray light, including glow on primary plate beam splitter.

- Previous system for lab measurements allowed us to control particle concentration (i.e., signal level) as well as capture images at high rate → averaging to reduce SNR
- System for in situ work did not have adequate frame rate (~0.2 Hz) → stuck with high SNR at low particle concentrations
- Currently adapting previous optical system with ~125x faster frame capture and improved optical components to reduce glow and stray light, and to allow significant averaging

▲ Simplified optical diagram of the LISST-BACK. A fiber coupled laser (FCL) beam is enlarged by a beam expander (BX) and redirected by a mirror (M1), reflected into the sample volume (SV), through transmit window (TW) by a plate beam splitter (BS). The source beam polarization is set using a polarizing cube (PBS), and undesired source transmitted beam is dumped (BD). Particles in SV backscatter light near-π, transmitted back through TW and through the BS. Backscattered light is imaged onto a CCD using a receive lens (RL) and through a rotating polarizer (POL).

Possible Alternate Application?

Patterns in cross-polarized radial backscattering by spheres are indicative of particle size → monostatic optical particle sizer (for spheres)

(a) Backscattering Images

(b) Radial Intensity along 45° Azimuth

▲ Model results for spheres. (a) Simulated CCD image and coordinate system. Exact backscattering is at origin O, and maximum scattering angle is 2°. Primary image is for 40µm particles. Scattering patterns (lower right CCD quadrant) are also shown for 60, 80, and 100µm particles. (b) Intensity of backscattering for fixed 45° azimuth – structure of peaks depends on particle size.

◄ *Image of measured co-polarized near-π backscattering by 25 µm beads. Origin is direct-π backscattering, radial distance from center is scattering angle, with image covering approximately 180-178°.*

◄ *Measured* LISST-Back images of cross-polarized backscattering by glass spheres in water of two different size distributions.

SEQUOIA

PiE
Particles in Europe

Spatial patterns in suspended particles and physical water column structure in the central North Sea under late spring stratified conditions.

Karline Soetaert, Kirstin Schulz, Theo Gerkema

Royal Netherlands Institute for Sea Research - **NIOZ-Yerseke**, and Utrecht University

Abstract

We report water column properties including particle distribution in a 700 km long transect, from 53.8 to 59.4 dg N, in the central part of the North sea in May-June 2018.

The particle size spectra showed a consistent spatial trend and were strongly influenced by water column stability. The surface waters over the entire transect had similar multimodal particle spectra, with two clear peaks, one in the nano- and in the micro range. Near the pycnocline, larger particles, probably aggregates appeared as a third prominent peak. The waters below the pycnocline showed a particle size spectrum that was more uniformly distributed over the size classes, but that were subtly different in the deep waters south of the Doggersbank, on the Doggersbank, and in the Fladen Grounds. \

The interchangeability of sensors and comparison between direct – indirect measurement techniques : A 1 year calibration strategy report

S. Thant[1], Y. Plancke[2], S. Claeys[2]

[1]Antea Group, Antwerp, Belgium

[2]Flanders Hydraulics Research, Antwerp, Belgium

Keywords : LISST-100X, flocs, interchangeable sensors, turbidity, sediment, YSI, Aanderaa, Scheldt river

Introduction

Measuring sediment transport and understanding sediment behavior is still one of the most challenging aspects in river engineering. Flanders Hydraulics Research performs each year field measurement campaigns in the Scheldt-estuary to obtain multiple datasets which allow (1) the evaluation of the system, (2) an increase of our system understanding and (3) validation of numerical models. To gather and obtain these valuable datasets, a thorough understanding of the working and properties of the different measuring instruments and -techniques is crucial. Thereby, differences between measuring techniques (both direct and indirect) and the interchangeability of instruments play a major role.

This paper discusses 4 seasonal field campaigns (consisting each out of measurements at 5 different locations) that were organized in 2017 to calibrate the longterm deployed monitoring instruments (YSI and Aanderaa). Therefor multiple water and sediment samples have been collected using pump samplers and also extra Aanderaa/YSI instruments and a LISST-100X sensor have been deployed.

Study area

The Schelde-estuary has a length of 160 km and is located in Flanders and the Netherlands (figure 1). The estuary is characterized by a macro-tidal regime, ebb and flood currents, a longitudinal salinity gradient and important sediment transports (both sand and silt), which lead to important morphological changes.

In 2001 Flanders and the Netherlands signed a memorandum of understanding in which a “Long Term Vision” (LTV) strategy and its objectives for the Scheldt-estuary was defined. The LTV focusses on the three main functions of the estuary: (1) safety against flooding, (2) port accessibility and (3) nature. In 2010 an integrated monitoring program (called “MONEOS”) was agreed to evaluate the effects of the different projects on the physical and ecological system (Plancke et al., 2012).

At 5 measuring locations along the Schelde-estuary, continuous measurements of different physical parameters are being executed (figure 1):

Lillo (KM 53 from the mouth, mesohaline), 2 Aanderaa-Seaguard instruments

Oosterweel (75 KM from the mouth, mesohaline), 1 Aanderaa-Seaguard instrument

Kruibeke (91 KM from the mouth, oligohaline), 1 YSI instrument

Schellebelle (141 KM from the mouth, fresh water), 1 YSI instrument

Melle (150 KM from the mouth, fresh water), 1 YSI instrument

Figure 19 : Overview of the 5 measuring locations along the river Scheldt.

Materials and Methods

Specific field campaigns were organized to calibrate the long term installed Aanderaa (acoustic and optical) and multiparameter YSI instruments, carried out by the additional deployment of Aanderaa and YSI instruments, a LISST-100X and the collecting of multiple water and sediment samples using pump samplers. The goal is to evaluate the indirect method (acoustical and optical sensors) with the ground truth through sampling (direct method).

The following parameters were measured during the field campaigns:

Aanderaa instruments (Seaguard 500/2500): measurement of turbidity (OBS), pressure, conductivity, temperature and flow magnitude and –direction

YSI instruments (6920 V2) : measurement of turbidity (OBS), pressure, conductivity, temperature, oxygen level

LISST-100X : measurement of grain size distribution and sediment concentration.

Centrifugal pump : water sampling; afterwards sediment concentration (filtration) and grainsize distribution (laser diffraction) were determined at the lab

LISST-100X

The LISST-100X is an optic measurement instrument using light diffraction by sediment particles. The defracted light is detected by the 32 detector rings (forward scattering) giving a measure of volume concentrations of sediment. The device also provides information on the granulometry of the in situ sediment. A Path Reduction Module of 80% was used.

Centrifugal pump

The opening of the hose of the centrifugal pump is fixed at the frame, most ideally at the same height of the acoustic and optic instruments. One liter samples were taken at regular intervals.

At the two most down-estuarine locations, Lillo and Oosterweel, calibration campaigns were performed from an anchored vessel. During the calibration campaigns the long-term instruments are collected from their fixed position and mounted on a frame together with additional Aanderaa instruments, a LISST-100X sensor and the inlet of the pump sampler, positioned ± 30 cm above the bed. Measuring frequencies are 10'' for the Aanderaa instruments and LISST-100X while pump samples are collected based on real-time registered turbidity (through a pigtail connection), in order to cover full concentration range.

At the other three locations measurements were performed from a jetty (floating pontoon). The longterm YSI hosting locations were equipped with an extra YSI instrument, A LISST-100X sensor and an automatic pump sampler. All of the extra sensors and samplers were positioned at the same height of the OBS sensor of the permanent YSI instrument, ± 1 m below the water surface. Sampling frequency is 5', 10", 10" and 5' for the permanent YSI, extra YSI, LISST-100X and automatic pump sampler respectively.

An overview of the planned calibration campaigns and the planned provided equipment is given in appendix.

Results & Discussion

Problems and difficulties encountered when performing the measurement campaigns

Despite careful planning, and executing the campaigns according a best practice approach, ambient in situ conditions influenced the measurement results (Appendix). The execution of complex monitoring campaigns contains calculated (but partly inevitable) risks and error sources. Except of system failures (equipment breakdown, damages, replacement with backup) the most difficult part is a real-time anticipation of the set-up (programming, sampling rate, adapting the equipment with filters or path-reductions, changing the monitoring position) to capture the target phenomena of the water body.

Therefor a good preliminary preparation based on system knowledge was crucial, but evenly important a direct anticipation of the researcher based upon real-time captured information.

The data of the different campaigns was then analyzed for sediment concentration and grain size distribution for the different measurement techniques. Regression models were made. Below the results are summarized by measurement location.

Turbidity versus SSC values

For almost all measuring campaigns a good agreement between the different measurement techniques can be found. Patterns in sediment concentration during the campaigns are the same for the different techniques used at most of the monitoring locations. The additional YSI and Aanderaa instruments confirm the patterns observed in the data of the long-term installed equipment. An exception is Melle,

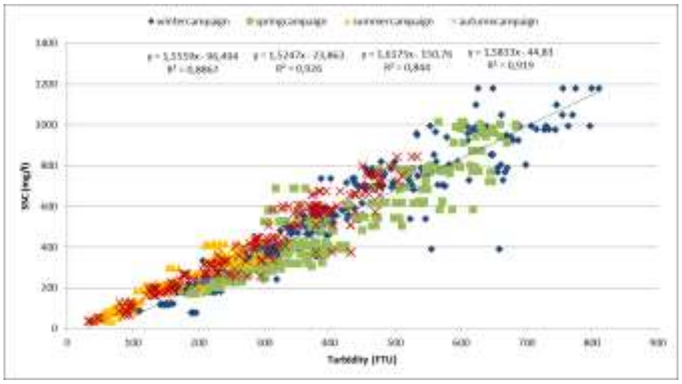

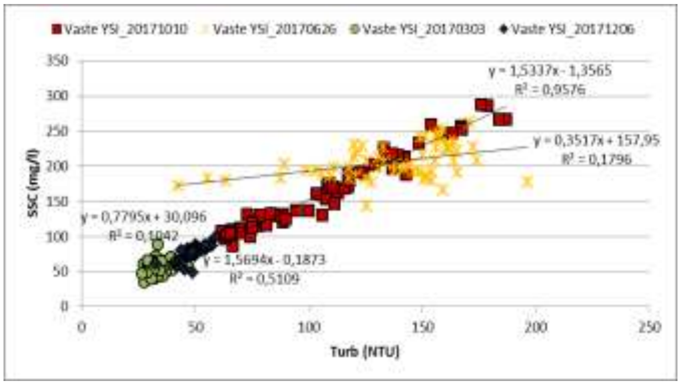

Figure 20 : Overview of regressions for the seasonal measuring campaigns at Lillo (left) and Schellebelle (right).

where the patterns strongly deviate between instruments and techniques. The reason for this deviance is yet unclear. For each measuring campaign a linear regression was set for sediment concentration and turbidity. Except for the case of Schellebelle, no seasonal differences in relations were found (Figure 2). The linear regression obtained for the summer campaign of Schellebelle diverges from the other campaigns that year indicating a possible seasonal trend at this location, plausibly caused by changing biological conditions (Figure 2).

Grain size

Huge discrepancies in median grainsizes and –distributions were observed between the LISST-100X (50 – 160 µm) and the results obtained from the Matersizer analyses of the automatic water samples (9 – 13 µm). It is clear that the LISST-100X in situ “sees” different grains-sizes than what is obtained out of the analysed water samples. A plausible explanation is that the LISST-100X is detecting flocs (both organic/inorganic matter) in the water. These flocs can have a significant surface area which is detected by the LISST-100X, the latter translating it to a significantly high grainsize. However, the general processing of the pump sample (preparation/conservation) may result in the destruction or breakdown of these flocs into single grains. Therefore the grainsizes obtained in the lab will be significantly smaller than those detected by the LISST-100X. Density calculation of flocs, deduced from the mass concentration (water samples) and volume concentrations (LISST-100X) also give an indication of differences in grain-size.

Floc density was calculated as follows: $\rho floc = \mathrm{\rho s} - \left(1 - \frac{\alpha}{\mathrm{\rho s}}\right)(\rho s - \rho w)$

With $\alpha = \frac{\mathrm{m}}{\mathrm{V}}$ and $n = 1 - \frac{\alpha}{\mathrm{\rho s}}$ And : ρs = density sediment, ρw = density water, m = mass concentration, V = volume concentration

Calculated floc densities during the measuring campaign of March 10th 2017, as shown in figure 3, indicates the presence of very watery flocs. By using floc density, changes in sediment type during the campaign can be identified. As discussed by Mikkelsen et al. (2006) the interaction between volume concentration and floc size, the latter inversely related to density, can give an idea of the ongoing sediment processes. The principles of Mikkelsen et al. (2006) however don’t agree to the data of the measuring campaign shown in figure 3 and further research is necessary. Aside from density calculations, a mobile camera, filming the in situ situation, as performed by Mikkelson et al. (2006), could give a conclusive answer to whether flocs do or do not cause the discrepancy in median grainsize.

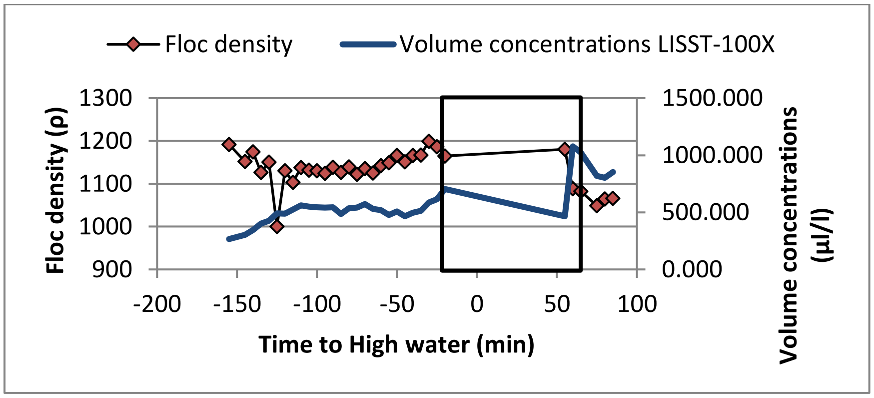

Figure 21 : Calculated floc density and volume concentrations during measuring campaign of March 10th 2017. Black box indicating a possible change in sediment type.

Inter instrument differences (Aanderaa – YSI)

4 Aanderaa Seaguard instruments, deployed together for a measuring campaign at Lillo or Oosterweel, all show the same pattern in terms of turbidity. The absolute measured values however, tend to differentiate between instruments. Figure 4 shows clearly the differentiation between instruments 72/64 and 315/318, especially from 3 hours till 5 hours after high water. The discrepancy is particular since instruments with calibration numbers 64, 72 and 315 were calibrated together by the Aanderaa Company, which states that all instruments measure exactly the same after calibration.

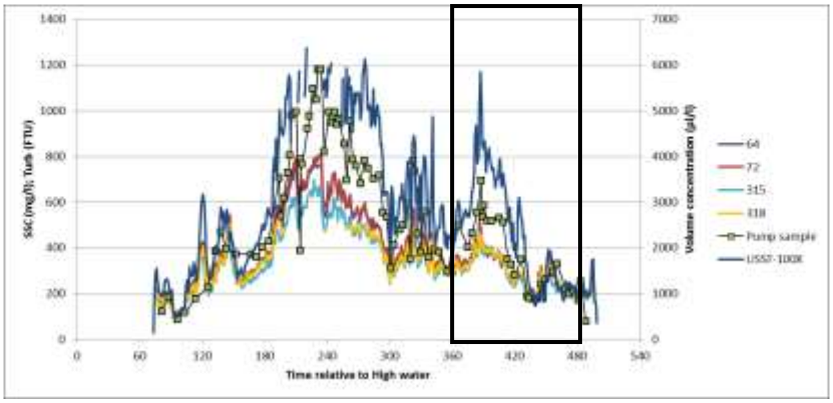

Figure 22 : Winter calibration campaign at Lillo, using 4 Aanderaa instruments. Black box indicating the period of the discrepancy.

Conclusions

2017 : 4 seasonal calibration campaigns, 5 locations (Lillo, Oosterweel, Kruibeke, Schellebelle and Melle)

Calibration of long-term installed YSI and Aanderaa instruments

Patterns in sediment concentrations in good agreement between all instruments and techniques (exception Melle)

Small deviations between absolute values of different Aanderaa instruments (different reaction or susceptibility for changes in sediment grainsize?)

Huge discrepancies in median grainsize pump samples (9 – 13 µm) and LISST-100X (50 – 160 µm) → presence of flocs

References

Agrawal, Y.C.; Whitmire, A.; Mikkelsen, Ole A.; Pottsmith, H.C. (2008). Light scattering by random shaped particles and consequences on measuring suspended sediments by laser diffraction. Journal of Geophysical Research. 113, CO4023.

Mikkelsen, O., Hill, P., Milligan, T. (2005). Single-grain, microfloc and macrofloc volume variations observed with a LISST-100 and a digital floc camera. Journal of Sea Research. 55, 87 – 102.

Plancke, Y., Vanlierde, E., Taverniers, E., Mostaert, F. (2012). Monitoring of physical parameters within the scope of the Dutch-Flemish integrated monitoring program, in: Hydraulic Measurements and Experimental Methods 2012 Conference (HMEM 2012), Snowbird, Utah, August 12-15, 2012. 1-6.

Thant, S.; Plancke, Y.; Claeys, S.; Verwaest, T.; Mostaert, F. (2018a). Kalibratiemetingen voorjaar 2017: Meetlocaties Lillo, Oosterweel, Kruibeke, Schellebelle en Melle. Versie 1.0. WL Rapporten, 15_024_1. Waterbouwkundig Laboratorium: Antwerpen.

Thant, S.; Plancke, Y.; Claeys, S.; Peeters, D.; Mostaert, F. (2018b). Kalibratiemetingen zomer 2017: Meetlocaties Lillo, Oosterweel, Kruibeke, Schellebelle en Melle. Versie 1.0. WL Rapporten, 15_024_2. Waterbouwkundig Laboratorium: Antwerpen.

Thant, S., Plancke, Y., Claeys, S., Peeters, D.; Mostaert, F. (2018c). Kalibratiecampagnes najaar 2017: Meetlocaties Lillo, Oosterweel, Kruibeke, Schellebelle en Melle. Versie 1.0. WL Rapporten, 15_024_3. Waterbouwkundig Laboratorium: Antwerpen.

Thant, S., Plancke, Y., Claeys, S., Peeters, D.; Mostaert, F. (2018d). Kalibratiemetingen winter 2017: Metingen te Lillo, Oosterweel, Kruibeke, Schellebelle en Melle. Versie 1.0. WL Rapporten, 15_024_4. Waterbouwkundig Laboratorium: Antwerpen.

Van Damme, S., Ysebaert, T., Meire, P., Van den Bergh, E. (1999). Habitatstructuren, waterkwaliteit en leefgemeenschappen in het Schelde-estuarium. Rapport Instituut voor Natuurbehoud 99/24, Brussel.

Van zoet naar zout water – Galgeschoor en Groot Buitenschoor, [website], **https://scheldeschorren.be/wp/land-en-water/water/van-zoet-naar-zout-water/**, (accessed 24 july 2018)

APPENDIX (next page)

Table 2 : Overview of provided and deployed instruments + cause for deviations/data loss

		Long term YSI	Extra YSI	Long term Aanderaa's	Extra Aanderaa's	LISST-100X	Pump samples	Cause deviation
Lillo	28/02/2017	▨	▨	2;2	2;2	v;x	v;v	Saturation LISST-100X (no PRM used)
	9/06/2017	▨	▨	2;2	3;3	v;x	v;v	Cable for datatransfer LISST-100X damaged day before
	7/09/2017	▨	▨	2;2	2;2	v;x	v;v	LISST-100X did not log
	19/01/2018	▨	▨	2;2	2;2	v;v	v;v	
Oosterweel	1/03/2017	▨	▨	1;1	3;3	v;x/v	v;v	Some periods no data because of saturation despite the use of PRM 80%
	8/06/2017	▨	▨	1;1	4;4	v;x	v;v	Problems with data cable
	6/09/2017	▨	▨	1;1	2;2	v;x	v;v	LISST-100X did not log
	20/01/2018	▨	▨	cancelled	cancelled	cancelled	cancelled	Storm conditions
Kruibeke	10/03/2017	1;1	1;1	▨	▨	v;x/v	v;v	Some periods no data because of saturation (no PRM used)
	29/06/2017	1;0	1;1	▨	▨	v;x/v	v;x/v	No longterm YSI because of maintainance works, LISST-100X no data for certain periods, pump samples --> miscommunication lab = no grainsize distributions
	18/10/2017	1;1	1;0	▨	▨	v;x/v	v;v	Additional YSI defect by consequende no usefull data, LISST-100X only data for certain periods due to saturation of sensor (no PRM used)
	1/12/2017	1;1	1;0	▨	▨	v;x/v	v;v	Additional YSI defect by consequende no usefull data, LISST-100X only data for certain periods due to saturation of sensor (no PRM used)
Schellebelle	3/03/2018	1;1	1;0	▨	▨	v;v	v;v	No additional YSI, attempt to increase frequency of longterm YSI (failed)
	26/06/2017	1;1	1;1	▨	▨	v;v	v;v	
	10/10/2017	1;1	1;0	▨	▨	v;x/v	v;v	No additional YSI, LISST-100X only data for certain periods due to saturation of sensor (no PRM used)
	6/12/2017	1;1	1;1	▨	▨	v;v	v;v	
Melle	31/03/2017	1;1	1;1	▨	▨	v;v	v;v	
	25/08/2017	1;1	1;0	▨	▨	v;v	v;v	No additional YSI provided
	11/10/2017	1;1	1;0	▨	▨	v;v	v;v	No additional YSI provided
	8/12/2017	1;1	1;0	▨	▨	v;v	v;v	Mobiele YSI defect bijgevolg onbruikbare data

1st Calibration campaign (spring)	2nd Calibration campaign (summer)
3rd Calibration campaign (autumn)	4th Calibration campaign (winter)

1;1	1 instrument provided, 1 instrument used during campaign
1;0	1 instrument provided, no instrument used during campaign
v;v	Instrument used during campaign, correct measurements
v;x	Instrument used during campaign, no measurements
v;x/v	Instrument used during campaign, only measurements for certain periods
▨	Not applicable for this measuring location

Effects of oyster aquaculture on water clarity and suspended particle dynamics in Chesapeake Bay, Virginia, U.S.A.

Turner, Jessica S., Massey, Grace M., Kellogg, M. Lisa, and Friedrichs, Carl T.

Virginia Institute of Marine Science, Gloucester Point, Virginia 23062, U.S.A.

Oyster aquaculture in Virginia is a rapidly growing industry, contributing substantially to the state's economy. As the oyster aquaculture industry grows in Virginia, with it grow concerns about possible negative impacts on water quality as well as hopes that oysters' high water filtration rates could improve water quality. In terms of possible negative impacts, shellfish aquaculture can enrich surrounding waters and sediments with organic matter in the form of biodeposits, contributing to localized hypoxic conditions (Cranford et al., 2009; Forrest et al., 2009; Mallet et al., 2006; Mckindsey et al., 2011; Newell, 2004). In terms of positive impacts, oysters are efficient filter feeders, removing phytoplankton and detritus from the water column (Bayne and Newell, 1983; Haven and Morales-Alamo, 1970, 1966; Holyoke, 2008). One market-sized oyster is able to filter up to 163 liters per day in summer (Riisgard, 1988). Furthermore, oyster aquaculture has recently been proposed as an alternate "best management practice" (BMP) to meet total maximum daily load (TMDL) allocations for nutrient trading in Virginia (Cerco and Noel, 2007; Kellogg et al., 2014; Newell, 2004; Newell and Mann, 2012). As the industry grows and becomes incorporated into management practices, it is imperative that we understand what impacts, if any, these aquaculture operations have on their local environments. This study investigated water clarity dynamics at four aquaculture sites in southwestern Chesapeake Bay.

The goal of this study was to measure how observed conditions varied (i) among aquaculture sites as well as (ii) within vs. outside waters directly in contact with cages at individual aquaculture sites, referred to as the farm footprint. Observed conditions include current velocity, suspended particle properties, water clarity (via Secchi disk and radiometer), Chlorophyll-*a* concentrations (Chl), and colored dissolved organic matter (CDOM).

Observed conditions were measured at four oyster farms during summer and fall 2017 and spring 2018 (Table 1). Water clarity parameters were measured via: a) profiler cruises with designated stations and b) dataflow cruises with flow-through sampling on a moving vessel. On all cruises, sampling was conducted bracketing maximum tidal current through the site, either flood or ebb. On profiler cruises, in situ particle size distributions and settling rates were captured by the Particle Imaging Camera System (PICS) and the Laser in situ Scattering and Transmissometry (LISST), alongside measurements of total suspended solids (TSS) and their organic content, CDOM, and Chl (Figure 1a). On dataflow cruises, current velocity and water clarity were measured concurrently while the vessel was underway using an acoustic Doppler current profiler (ADCP) and a YSI CTD with multiple sensors, including Chl and turbidity (Figure 1b).

Site	Gear	Wave exposure	Seasons sampled
White Stone-Windmill Point	Floating	Very high	Summer & Fall 2017
White Stone-North Point	Floating	Very high	Spring 2018
Chapel Creek	Near-bottom	Moderate	Summer 2017
Big Island	Floating	Very low	Summer 2017
Lynnhaven	Near-bottom	Low	Summer & Fall 2017

Table 1: Basic characteristics of the four commercially operating aquaculture sites visited in this study, including gear type, wave exposure, and seasons visited.

Figure 1. (a) Profiler cruise instrumentation deployed on a stationary frame, and (b) Dataflow cruise instrumentation mounted to the vessel while underway.

At the scale of all four sampling sites, water clarity varied widely among sites (Figure 2). For all variables, the two northern and more wave-exposed sites, White Stone and Chapel Creek, were significantly clearer than the two southern and more enclosed sites, Big Island and Lynnhaven. At the two northern sites, light penetrated more deeply in terms of both Secchi depth and light attenuation, turbidity and TSS concentrations were lower, and a larger fraction of TSS was composed of organic matter. At the two southern sites, light was attenuated at shallower depths, turbidity and TSS concentrations were higher, and a smaller fraction of TSS was composed of organic matter.

At the scale of the farms themselves, one observation that differentiated waters within the footprint of oyster farms from waters outside or upstream was a difference in particle size. At the two largest oyster farms, particle size in terms of median diameter by volume (d50v) was larger within and downstream of

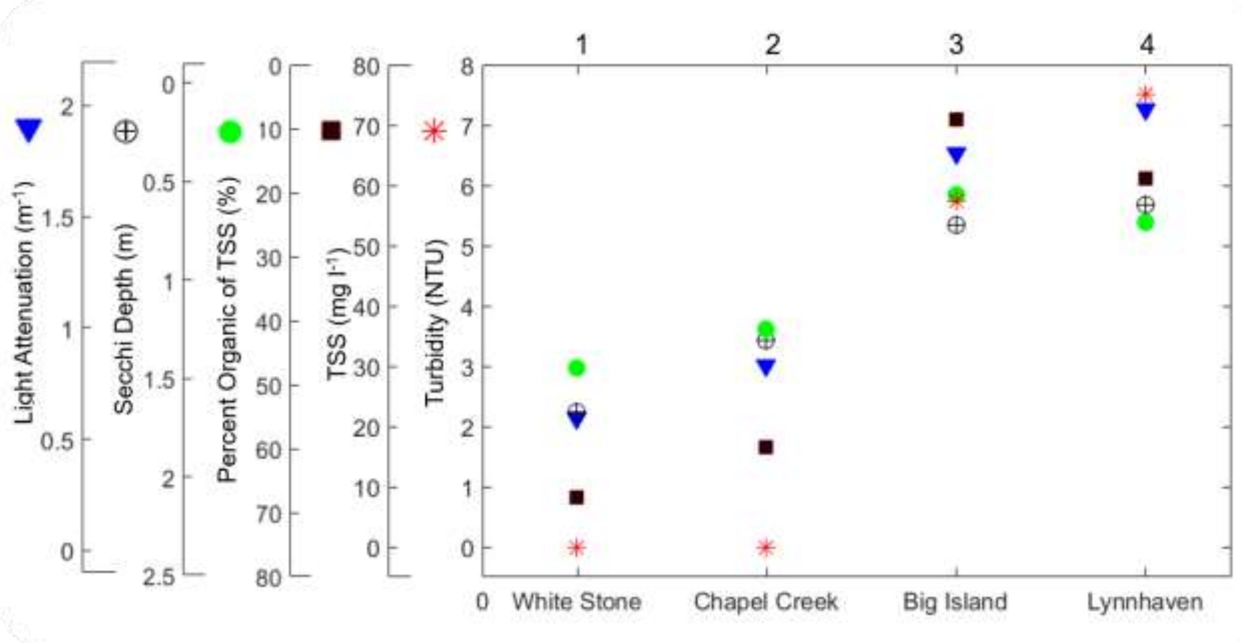

Figure 2. Mean summer water clarity differences among sites in light attenuation (m^{-1}), Secchi depth (m), percent organic content of TSS, TSS ($mg\ l^{-1}$), and turbidity (NTU). For all variables, White Stone and Chapel Creek values were significantly different from Big Island and Lynnhaven values.

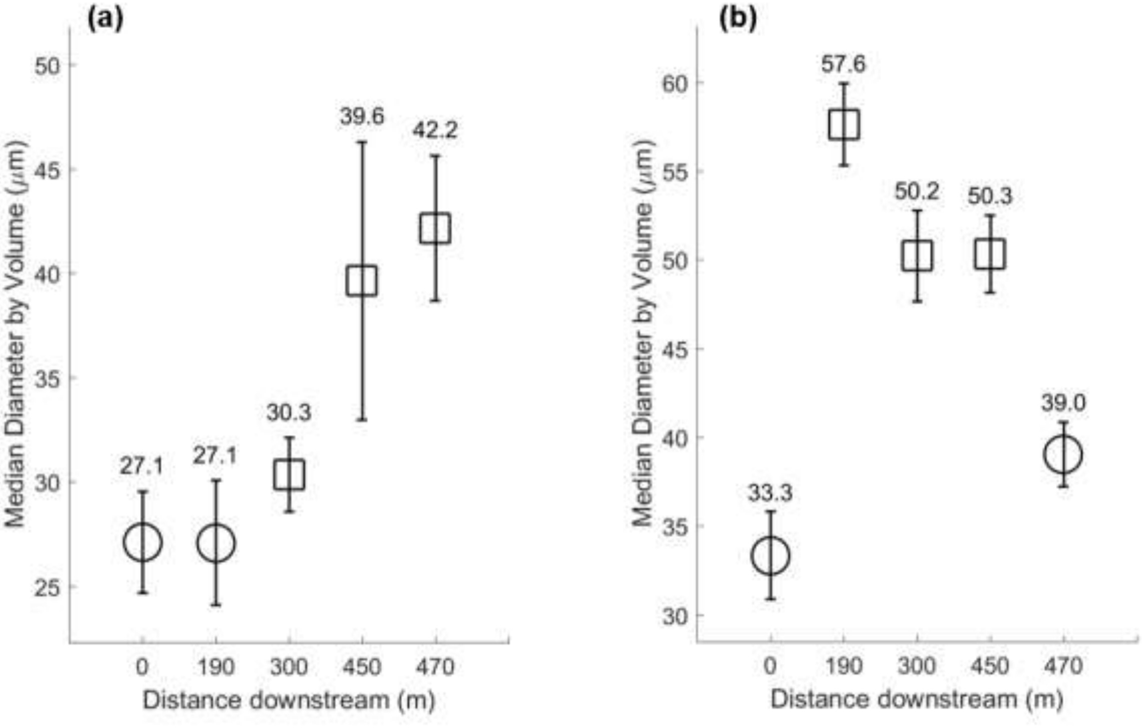

Figure 3. Particle size differences in d50v (um) at (a) White Stone and (b) Lynnhaven, the two largest oyster farms sampled during summer 2017 using the LISST-100x deployed for two-minute bursts. Squares indicate measurements in waters inside or downstream of the oyster farm footprints. Circles indicate measurements in waters upstream or outside of the oyster farms. Error bars indicate +/- 1 standard error.

the oyster farms (Figure 3). Particle size differences within vs. outside cages may indicate repackaging of fine suspended materials into oyster biodeposits. Interestingly, while particle size differed, particle concentrations in terms of LISST total volume concentration (µl l^{-1}) and bottle-sample TSS (mg l^{-1}) were not significantly different within versus outside of the two largest farms. This difference in size alone could be beneficial by allowing more light to reach the bottom due to decreased light scattering.

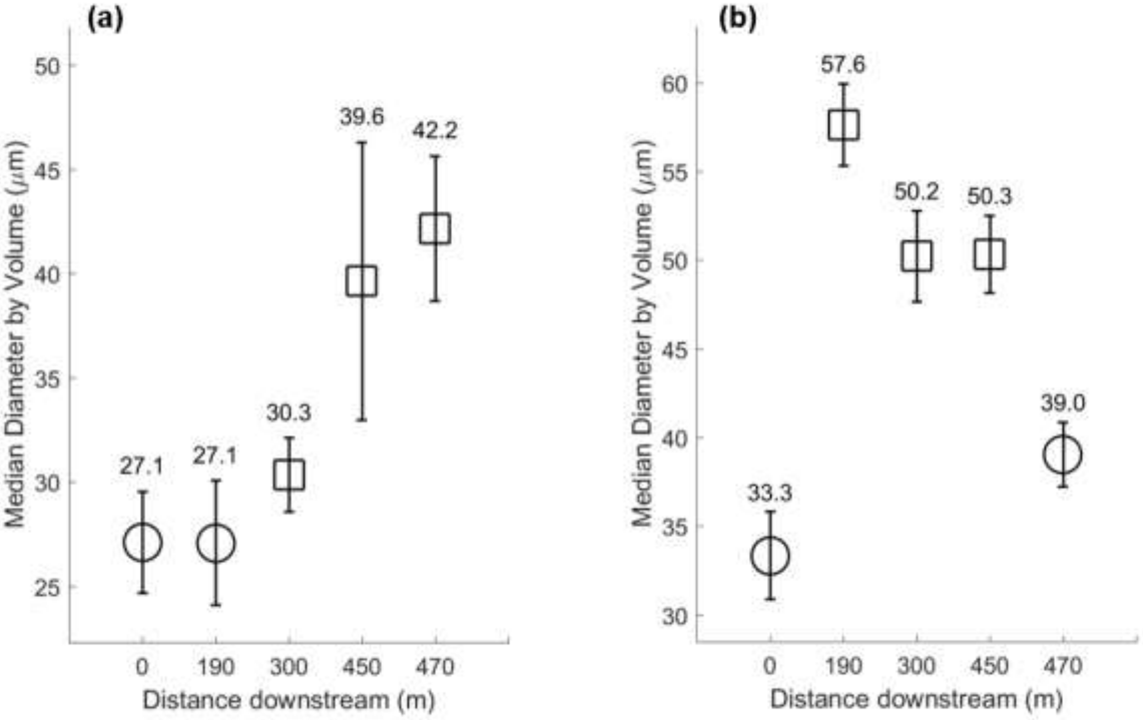

Figure 3. Particle size differences in d50v (um) at (a) White Stone and (b) Lynnhaven, the two largest oyster farms sampled during summer 2017 using the LISST-100x deployed for two-minute bursts. Squares indicate measurements in waters inside or downstream of the oyster farm footprints. Circles indicate measurements in waters upstream or outside of the oyster farms. Error bars indicate +/- 1 standard error.

However, overall the particle size effect is a minor one, and no other effects of either oyster filtration or organic enrichment were measured. Mixing of water between the aquaculture site and surrounding waters likely hid any obvious reduction in suspended particle concentration within the aquaculture site associated with oyster filtration. In other aquaculture settings, oyster biodeposits have been found to be redistributed over large areas by currents, making it unlikely that concentrated organic deposits remain on-site long enough to have negative effects (Cornwell et al., 2014; Crawford et al., 2003; Newell, 2016; Rice, 2016; Testa et al., 2015). Homogeneity of waters within and outside of oyster farms may be indicative of this kind of dispersal.

Results of this study suggest that the modification of overall water clarity by oyster farms is difficult to detect in situ, particularly at sites with high current velocities and widely spaced cages. The lack of organic enrichment has positive implications for commercial oyster growers. Aquaculture farms with relatively low cage/oyster density located in well-flushed areas are unlikely to have negative impacts on local water clarity.

References

Bayne, B.L., Newell, R., 1983. Physiological Energetics of Marine Molluscs, in: Saleuddin, A., Wilbur, K. (Eds.), The Mollusca, Vol. 4. Physiology, Part 1. Academic press, Academic Press, New York, NY.

Cerco, C.F., Noel, M.R., 2007. Can Oyster Restoration Reverse Cultural Eutrophication in Chesapeake Bay? Estuaries and Coasts 30, 331–343. doi:10.1007/BF02700175

Cornwell, J., Owens, M., Kellogg, L., 2014. Oyster Restoration, Aquaculture and Nitrogen Removal - A Biogeochemist's Perspective, in: The Chesapeake Bay Program Website. Univeristy of Maryland & Virginia Institue of Marine Science.

Cranford, P.J., Hargrave, B.T., Doucette, L.I., 2009. Benthic organic enrichment from suspended mussel (Mytilus edulis) culture in Prince Edward Island, Canada. Aquaculture 292, 189–196. doi:10.1016/j.aquaculture.2009.04.039

Crawford, C.M., Macleod, C.K.A., Mitchell, I.M., 2003. Effects of shellfish farming on the benthic environment. Aquaculture 224, 117–140. doi:10.1016/S0044-8486(03)00210-2

Forrest, B.M., Keeley, N.B., Hopkins, G.A., Webb, S.C., Clement, D.M., 2009. Bivalve aquaculture in estuaries: Review and synthesis of oyster cultivation effects. Aquaculture 298, 1–15. doi:10.1016/j.aquaculture.2009.09.032

Haven, D.S., Morales-Alamo, R., 1970. Filtration of particles from suspension by the American Oyster Crassotrea virginica. Biol. Bull. 139, 248–264.

Haven, D.S., Morales-Alamo, R., 1966. Aspects of biodeposition by oysters and other invertebrate filter feeders. Limnol. Oceanogr. 11, 487–498. doi:10.4319/lo.1966.11.4.0487

Holyoke, R.R., 2008. Biodeposition and Biogeochemical Processes in Shallow, Mesohaline Sediments of Chesapeake Bay. University of Maryland.

Kellogg, M.L., Smyth, A.R., Luckenbach, M.W., Carmichael, R.H., Brown, B.L., Cornwell, J.C., Piehler, M.F., Owens, M.S., Dalrymple, D.J., Higgins, C.B., 2014. Use of oysters to mitigate eutrophication in coastal waters. Estuar. Coast. Shelf Sci. 151, 156–168. doi:10.1016/j.ecss.2014.09.025

Mallet, A.L., Carver, C.E., Landry, T., 2006. Impact of suspended and off-bottom Eastern oyster culture on the benthic environment in eastern Canada. Aquaculture 255, 362–373. doi:10.1016/j.aquaculture.2005.11.054

Mckindsey, C.W., Archambault, P., Callier, M.D., Olivier, F., 2011. Influence of suspended and off-bottom mussel culture on the sea bottom and benthic habitats: a review. Can. J. Zool. 89, 622–646. doi:http://dx.doi.org/10.1139/z11-037

Newell, C., 2016. Oyster Environmental Interactions, in: Miscellaneous Publications. The University of Maine Digital Commons, p. 9.

Newell, R., 2004. Ecosystem influence of natural cultivated populations of suspendesion-feeding bivalve molluscs: a review. J. Shellfish Res.

Newell, R.I.E., Mann, R., 2012. Shellfish Aquaculture: Ecosystem Effects , Benthic-Pelagic Coupling and Potential for Nutrient Trading. A Report Prepared for the Secretary of Natural Resources, Commonwealth of Virginia.

Rice, M.A., 2016. Environmental Impacts of Shellfish Aquaculture : Filter Feeding to Control Eutrophication, in: Tlusty, M., Bengston, D., Halvorson, H., Oktay, S., Pearce, J., Rheualt, R. (Eds.), Marine Aquaculture and the Marine Environment: A Meeting for the Stakeholders in the Northeast. University of Massachusetts Boston. Falmouth, MA.

Riisgard, H.U., 1988. Efficiency of particle retention and filtration rate in 6 species of Northeast American bivalves. Mar. Ecol. Prog. Ser. 45, 217–223. doi:10.3354/meps045217

Testa, J.M., Brady, D.C., Cornwell, J.C., Owens, M.S., Sanford, L.P., Newell, C.R., Suttles, S.E., Newell, R.I.E., 2015. Modeling the impact of floating oyster (*Crassostrea virginica*) aquaculture on sediment-water nutrient and oxygen fluxes. Aquac. Environ. Interact. 7, 205–222. doi:10.3354/aei00151

Hydropower development impacts on river connectivity: Lessons learned from sediment management in reservoir and run-of-river hydropower projects

Maria Ubierna, Cristina Diez and Sabrina Upadhyay

International Hydropower Association (IHA)

mu@hydropower.org ; **cds@hydropower.org; su@hydropower.org**

Hydropower has a prominent role in the transition to clean energy systems and in mitigating the impacts of climate change. In order to continue to supply the increasing demand of water and energy, thousands of reservoir and run-of-river hydropower projects are in the pipeline worldwide.

However, reservoir and run-of-river hydropower projects disrupt river flow, which impacts geomorphological processes such as river meandering, sediment deposition, and floodplain formation. Thus, basin and regional-scale planning in hydropower development is extremely important. Site selection and design (either reservoir or run-of-river) is critical for sustainable hydropower development. Besides minimizing connectivity impacts, basin-scale planning contributes to minimizing cumulative environmental effects and planning mitigation measures more effectively.

These cumulative impacts have a direct effect on the lateral connectivity (i.e. between river and floodplain), longitudinal continuity (upstream to downstream), as well as the vertical connectivity (between the channel and contiguous groundwater) of sediment transportation. The recognition to assess these impacts at the basin, country, or regional level is emerging to minimize hydropower development impacts on river connectivity.

Dams trap bed sediment load and a fraction of the suspended sediment load. Over time, sedimentation and sediment-related issues undermine the capacity of hydropower projects to deliver water and energy services in addition to the upstream negative effects of delta formation and downstream scour or “hungry water” effect.

Sediment management contributes to maintaining the storage capacity, reducing the operating risks, and minimising river connectivity impacts. Managing sediment is essential to extend the life of a project, to ensure a reliable and sustainable source of water and energy, and to maintain the river connectivity.

There is a general conception that a reservoir hydropower project disrupts the river flow more than a run-of-river project. However, there is no consensus when considering the cumulative effects of multiple projects. Under the current energy transition and the exacerbation of climate change, there is an increasing need to understand the cumulative effects, the river basin planning, and the sediment management options.

Fig. 1 Jirau run-of-river hydropower project. Sluice gates on the right side.

To address this issue, the IHA sediment management programme gathered more than 20 case studies to promote strategies and case studies for effective sediment management that, while slowing the rate of storage loss, will bring sediment inflow and discharge into balance for the benefit of river connectivity.

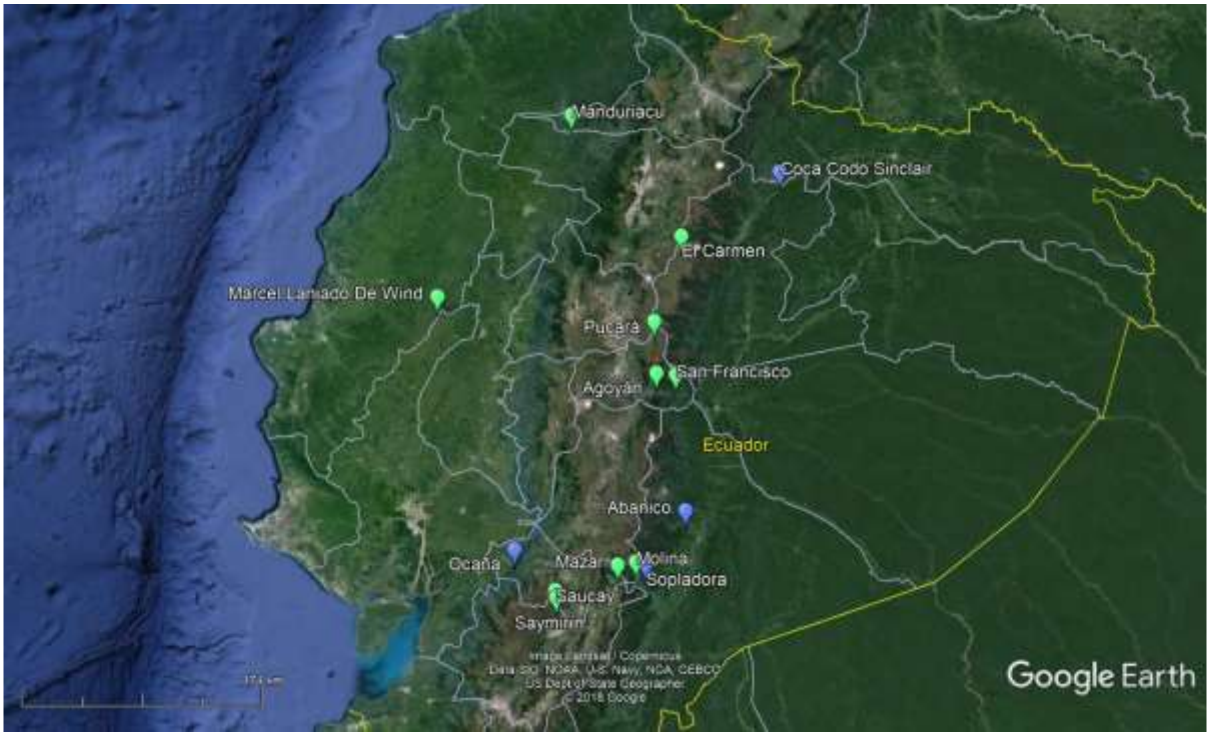

Fig 2. Distribution of reservoir (green) and run-of-river (blue) hydropower projects in Ecuador.

Lessons learned show that sediment management planning in the initial stages of concept and design is fundamental to minimise sedimentation effects in the river as well as to maximise the hydroplant's benefits. Sediment monitoring is essential to plan effective sediment management strategies.

Our ongoing research study analyses the classification of reservoir and run-of-river projects in the Andean region and its implications on sediment transportation at the basin level. The study is based on the characterisation of hydropower assets, in terms of the official classification (reservoir or run-of river), size, sediment management infrastructures, and geographical distribution.

The International Hydropower Association (IHA) will present key findings, from the sediment management programme, to achieve sediment balance in hydropower projects. IHA will also share additional findings on reservoir and run-of-river hydropower projects regarding the cumulative effects at the river basin scale in Ecuador.

Underwater Wide-Field Tomography of Sediment Resuspension

Adi Vainiger [1], Yoav Y. Schechner [1], Tali Treibitz [2], Aviad Avni [2] , David S. Timor[3]

[1] Viterbi Faculty of Electrical Engineering, Technion - Israel Institute of Technology, Haifa, Israel.

[2] Leon H. Charney School of Marine Sciences - University of Haifa, Israel. [3] Ha-Aliya Street 38, Nesher , Israel

adi.vainiger@gmail.com; yoav@ee.technion.ac.il ; ttreibitz@univ.haifa.ac.il; aavni@univ.haifa.ac.il;

Sediment resuspension affects physical, chemical and biological processes in the sea [1-3]. Biological sediment resuspension, caused by activity of benthic fish is common [4]. These events are temporally abrupt and spatially discrete. Understanding resuspension requires a wide set of methods [5-9]. Existing in-situ methods quantify sediment resuspension in cm-scale [10-16]. We seek multi-meter-scale measurements of these events using far-field cameras. We develop an imaging technology designed to (a) observe the seafloor and the water medium above it from a distance, (b) sense sediment resuspension events, and (c) algorithmically quantify the resuspension.

Our technology quantifies the amount of material lifted, and its spatio-temporal distribution. The spatial distribution of the particles is three-dimensional (3D). Hence, we develop an imaging system to reconstruct sediment resuspension in 3D. To achieve this, the evolving sediment plume is imaged against a diffuse backlight. Imaging is done simultaneously from multiple directions (Fig. 1[Left]). The resuspended particles affect light that reaches the cameras. Analysis uses a computed tomography (CT) principle [17-20]. Medical CT, as a means for volumetric sensing, motivates this. Underwater imaging is challenging [21-24]. Refractions and reflections complicate imaging even in controlled lab settings. Moreover, a large

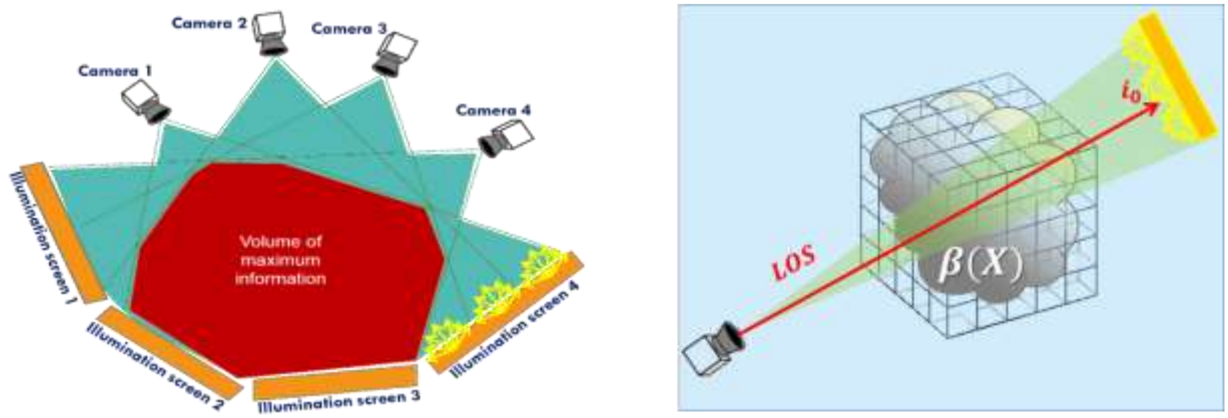

Figure 1: [Left] Illustration of tomographic system. [Right] LOS of a pixel.

submerged system affects flow and consequently may bias measurements. Therefore, we develop optical and algorithmic techniques, aiming to reduce as much as possible these obstacles.

Let a screen have radiance i_0. Pixel p in a camera senses the radiance along a line of sight (LOS), as shown Fig. 1[Right]. Particles in the medium have extinction cross section σ. The extinction coefficient is $\beta = \sigma\rho$, where ρ is the particles' density. The optical depth on the LOS is

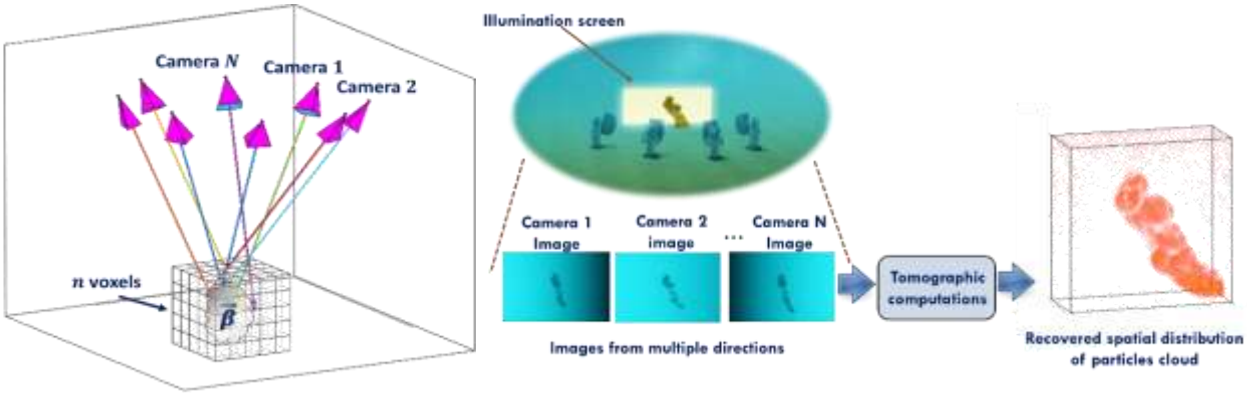

Figure 2: [Left] Projections from n voxels to m pixels. [Right] Flow of simulations environment.

$$\tau = \int_{\mathrm{LOS}} \beta(r)dr. \tag{1}$$

The transmitted radiance is

$$i = i_0 e^{-\tau}. \tag{2}$$

Let β^{Water}, $\beta(r)^{\mathrm{Sediment}}$ be the extinction coefficients of water and sediment particles, respectively. The radiance reaching pixel p through sediment-free water is $i_p^{\mathrm{W}} \triangleq i_0 e^{-\int_{\mathrm{LOS}} \beta^{\mathrm{Water}} dr}$. Then, the radiance through the resuspension is

$$i_p = i_p^{\mathrm{W}} e^{-\int_{\mathrm{LOS}} \beta(r)^{\mathrm{Sediment}} dr}. \tag{3}$$

Hence, the optical depth is

$$\tau_p = -\ln\left(\frac{i_p}{i_p^{\mathrm{W}}}\right) = \int_{\mathrm{LOS}} \beta(r)^{\mathrm{Sediment}} dr. \tag{4}$$

Tomographic setups have multidirectional LOSs through the scene (Fig. 2[left]). From Eq. (4),

$$\tau_{\mathrm{p}} \approx \sum_v a_{p,v} \beta_v^{\mathrm{Sediment}} \triangleq \vec{a}_p \vec{\beta}^{\mathrm{Sediment}}, \tag{5}$$

where $a_{p,v}$ is the length of the ray segment in the LOS of pixel p, in voxel v. Here $\beta_v^{\mathrm{Sediment}}$ is the sediment extinction coefficient of voxel v. Let $\vec{\beta}^{\mathrm{Sediment}} \in \mathbb{R}^{n\times 1}$ represent the volumetric extinction coefficients in all voxels $v \in 1..n$. The overall sampled data is $\vec{\tau} \in \mathbb{R}^{m\times 1}$ representing sampled optical depths in each pixel $p \in 1..m$. Then,

$$\vec{\tau} \approx A\vec{\beta}^{\mathrm{Sediment}}. \tag{6}$$

Here $A \in \mathbb{R}^{m\times n}$ is a projection matrix. The volumetric extinction coefficient is estimated by

$$\hat{\beta} = argmin\|A\vec{\beta} - \vec{\tau}\|_2^2. \tag{7}$$

We tested this concept using both simulations and experiments. Physics based rendering [25-27] synthetically simulates underwater imaging. The simulation analyzes the rendered images and performs 3D tomographic reconstruction. This enables optimization of the system. Simulations (Fig. 2[Right]) show successful reconstruction of synthetic clouds. We performed experiments in a research seawater pool. The optical system contained eight sealed cameras, directed to the volume of interest above a lighting screen (Fig. 3). We externally controlled the cameras to simultaneously image the scene from several perspectives. We used openCV [28], a calibration board, markers on the screen and Agisoft [29], to calibrate the system geometry. This led us to the projection matrix A used in Eqs. (6,7). Before each resuspension event, we imaged the lighting screen. Inspired by the *communicating vessels principle*, we built an injection system. A bucket contained MP SILICA $12-26[um]$ particles suspended in water at density of 22.5 $[gr/l]$. Two liters were drained within ~ 63 sec, to shoot a resuspended cloud from the middle of the lighting screen. Resuspension was imaged at 10 fps.

Fig. 4[Left] shows two viewpoints: without sediment (I^{W}), then a resuspension event and finally the sediment optical depth. We used AIRtool [30] for Simultaneous Algebraic Reconstruction Technique

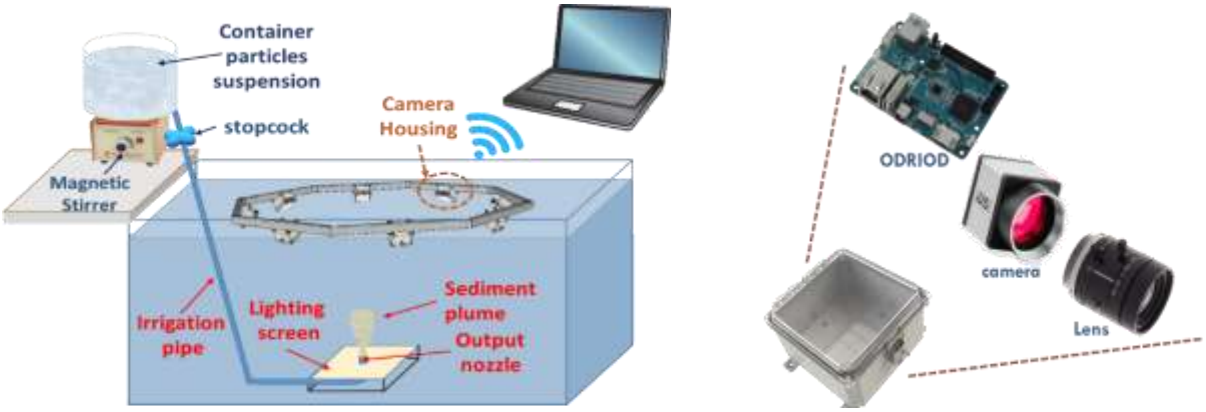

Figure 3: [Left] Camera housings are mounted on an octagonal frame. The frame resides ~2.5[m] above the lighting screen. From middle of lighting screen, emerges an output nozzle. [Right]Each housing contains an ODRIOD XU-4, an IDS UI-3260 camera, and a Tamron M112FM12 lens Figure

(SART) [31] in the tomography analysis. Fig. 4[Right] shows a meter-scale recovery of the sediment cloud (green channel), in $2[cm]$ voxel resolution.

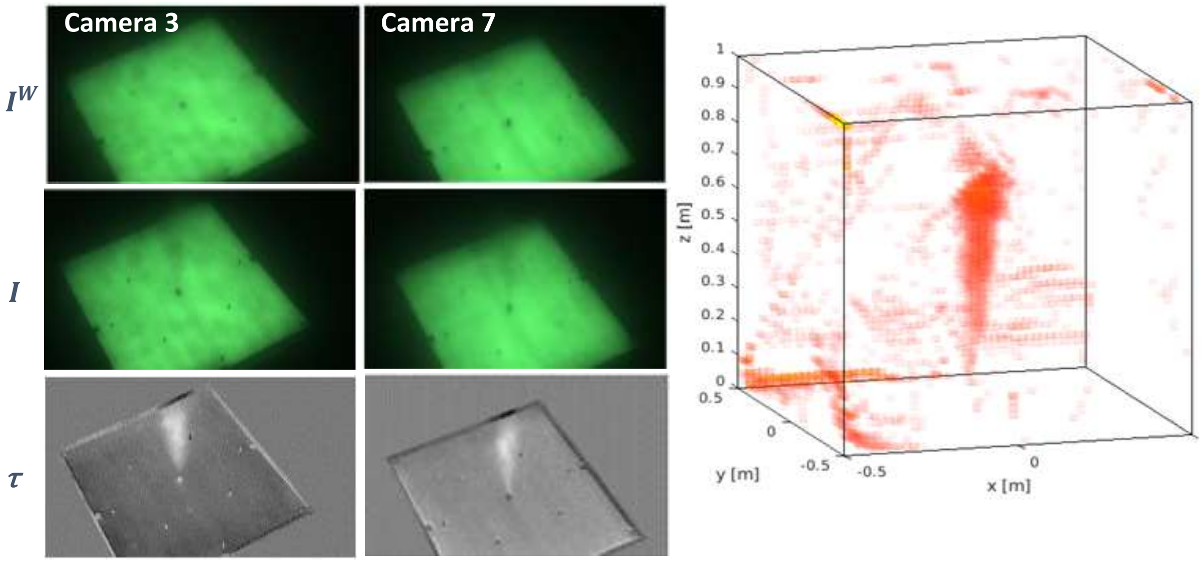

Figure 4: [Left] top - Background images (I^{W}), middle - Sediment cloud images (I), bottom - Optical depth images(τ) .[Right] Sediment cloud 3D recovery.

We envision future developments to obviate active lighting in tomographic setups. Such a system may enable research of marine animals which create resuspension events. The system can advance other underwater imaging applications.

We thank M. Fisher, Y. Goldfracht, L. Dehter, B. Herzberg, A. Levy , J. Fischer, S. Cohen, M. Groper, S. Farber for assisting in system construction and experiments. We thank V. Holodovsky, A. Levis, A. Aides, T. Katz, U. Shavit, G. Yahel, S. Grossbard for fruitful discussions, and I. Talmon J. Erez for technical support. YYS is a Landau Fellow - supported by the Taub Foundation and Israeli Ministry of Science, Technology and Space (Grant 3-12478). His work is conducted in the Ollendorff Minerva Center. Minerva is funded through the BMBF. TT is supported by The Leona M. and Harry B. Helmsley Charitable Trust and The Maurice Hatter Foundation.

References

Valeur JR, Jensen A, Pejrup M. Turbidity, particle fluxes and mineralisation of carbon and nitrogen in a shallow coastal area. Marine and freshwater research. 1995;46(1):409-18.

Tengberg A, Almroth E, Hall P. Resuspension and its effects on organic carbon recycling and nutrient exchange in coastal sediments: in situ measurements using new experimental technology. Journal of Experimental Marine Biology and Ecology. 2003;285:119-42.

Wainright SC. Stimulation of heterotrophic micro plankton production by resuspended marine sediments. Science. 1987;238(4834):1710-2.

Katz T, Yahel G, Reidenbach M, Tunnicliffe V, Herut B, Crusius J, Whitney F, Snelgrove PV, Lazar B, Resuspension by fish facilitates the transport and redistribution of coastal sediments. Limnology and Oceanography. 1;57(4):945-58.

Yahel G, Yahel R, Katz T, Lazar B, Herut B, Tunnicliffe V, Fish activity: a major mechanism for sediment resuspension and organic matter remineralization in coastal marine sediments. Marine Ecology Progress Series. 2008;372:195-209.

Shavit U, Halamish A, Grossbard S, Asher S, Gilboa M, Katz T, Yahel G, Testing a biological resuspension footprint model using Lagrangian simulations. PiE 2018.

Grossbard S, Gilboa M., Katz T, Yahel G., Shavit U, Developing a laboratory simulator for the study of resuspension events. PiE 2018.

Gilboa M, Katz T, Shavit U, Grosbard S , Torfstien Adi, Yahel G, Novel approach to measure the rate of sediment resuspension at the ocean and to estimate the contribution of fish activity to this process. PiE 2018.

Yahel G, Gilboa M, Grossbard S, Vainiger A, Treibitz T, Schechner Y, Shavit U, Katz T, Biological activity: an overlooked, mechanism for sediment resuspension, transport, and modification in the ocean. PiE 2018.

Raffel M, Willert CE, Scarano F, Kähler CJ, Wereley ST, Kompenhans J., *Particle image velocimetry: a practical guide*. Springer; 2018.

Elsinga GE, Scarano F, Wieneke B, van Oudheusden BW., Tomographic particle image velocimetry. Experiments in fluids. 2006;41(6):933-47.

Klinner J, Willert C. Tomographic shadowgraphy for three-dimensional reconstruction of instantaneous spray distributions. Experiments in fluids. 2012;53(2):531-43.

Shahi S, Kuru E., An experimental investigation of settling velocity of natural sands in water using Particle Image Shadowgraph. Powder Technology. 2015 ;281:184-92.

Thompson CE, Couceiro F, Fones GR, Helsby R, Amos CL, Black K, Parker ER, Greenwood N, Statham PJ, Kelly-Gerreyn BA., In situ flume measurements of resuspension in the North Sea. Estuarine, Coastal and Shelf Science. 2011;94(1):77-88.

Fugate DC, Friedrichs CT. Determining concentration and fall velocity of estuarine particle populations using ADV, OBS and LISST. Continental Shelf Res.2002;22(11-13):1867-86.

Ochiai S, Kashiwaya K., Measurement of suspended sediment for model experiments using general-purpose optical sensors. Catena. 2010;83(1):1-6.

Aides A, Schechner YY, Holodovsky V, Garay MJ, Davis AB. Multi sky-view 3D aerosol distribution recovery. Optics Express. 2013 ;21(22):25820-33.

Alterman M, Schechner YY, Vo M, Narasimhan SG. Passive tomography of turbulence strength. In European Conference on Computer Vision 2014 pp. 47-60. Springer.

Holodovsky V, Schechner YY, Levin A, Levis A, Aides A, In-situ multi-view multi-scattering stochastic tomography. Proc. IEEE Int. Conf. Computational Photography 2016.

Levis A, Schechner YY, Talmon R. Statistical tomography of microscopic life. Proc. IEEE Computer Vision and Pattern Recognition 2018 pp. 6411-6420.

Treibitz T, Schechner YY. Turbid scene enhancement using multi-directional illumination fusion. IEEE Transactions on Image Processing. 2012;21(11):4662-7.

Treibitz T, Schechner Y, Kunz C, Singh H., Flat refractive geometry. IEEE transactions on pattern analysis and machine intelligence. 2012;34(1):51-65.

Schechner YY, Karpel N., Attenuating natural flicker patterns. Proc. MTS/IEEE OCEAN 2004, Vol. 3, pp. 1262-1268.

Sheinin M, Schechner YY., The next best underwater view. Proc. IEEE Computer Vision and Pattern Recognition 2016 pp. 3764-3773.

Pharr M, Jakob W, Humphreys G., *Physically based rendering: From theory to implementation.* Morgan Kaufmann; 2016.

Narasimhan SG, Gupta M, Donner C, Ramamoorthi R, Nayar SK, Jensen HW., Acquiring scattering properties of participating media by dilution. In ACM TOG 2006 Vol. 25, No. 3, pp. 1003-1012.

Mobley CD. *Light and water: radiative transfer in natural waters.* Academic press; 1994.

https://pypi.org/project/opencv-python/

http://www.agisoft.com/pdf/photoscan-pro_1_4_en.pdf

http://www2.compute.dtu.dk/~pcha/AIRtoolsII/AIRtoolsManual.pdf

Andersen AH, Kak AC., Simultaneous algebraic reconstruction technique (SART): a superior implementation of the ART algorithm. Ultrasonic Imaging. 1984;6(1):81-94.

Quantification of SPM floc sizes in coastal seas: intercomparison of LISST100X, LISST HOLO2 and PCAM measurements

Verney, Romaric[1] ; Becker, Marius[2] ; Jacquet, Matthias[1] ; Le Berre, David[1] ; Herbst, Gabriel[2] and Winter, Christian[2]

[1]IFREMER, DYNECO/DHYSED laboratory, CS10070, 29280 Plouzané, France (romaric.verney@ifremer.fr)

[2]Institute of Geosciences, Kiel University, Germany

Introduction

In estuaries and coastal seas, suspended particulate matters (SPM) are mainly aggregated in flocs, of variable shape, size, density and hence settling velocity. The latter is crucial as it controls the SPM fluxes in coastal ecosystems, from turbidity maximum formation to turbid plume or mudflat dynamics (Many et al., 2016 ; Fettweis et al., 2006, Dyer and Manning 1999 among others). Hence quantifying floc sizes in situ has become a true challenge over the last decades, and various instruments were designed to measure these floc characteristics. Mainly in situ devices fall in two categories:

Camera systems, providing direct 2D floc silhouettes (Mikkelsen et al., 2006; Smith and Friedrichs, 2011…) and for some of these devices also measuring floc settling velocities;

Laser diffraction systems, providing floc size distribution after inversion of the diffracted light using kernels built from the Mie theory (Agrawal and Pottsmisth, 1994)

Recently, a hybrid system was built using digital in line holography, which combines laser diffraction and 2D visualisation of flocs after hologram reconstruction (Graham and Nimmo-Smith, 2010). This system is then an alternative of the usual camera system, as 2D views of flocs can be reconstructed at different virtual focal planes, hence providing "always in focus" flocs silhouettes.

This study aims at investigating the performances and complementarity of each of these devices for measuring floc size distribution in coastal seas, based on LISST100X, LISST HOLO2 and PCAM measurements.

Study site and methods

Measurements were conducted at the mouth of the macrotidal Seine Estuary (France), at the interface between the estuary and the adjacent Seine Bay (La Carosse station, 49°28.830N, 0°1.828W - Figure 1) on April 1st, 2018, during spring tide. Exceptionally this year the river discharge was very high during winter and early spring, and still above 1000m^3/s during the field campaign (mean annual river discharge is around 470m^3/s)

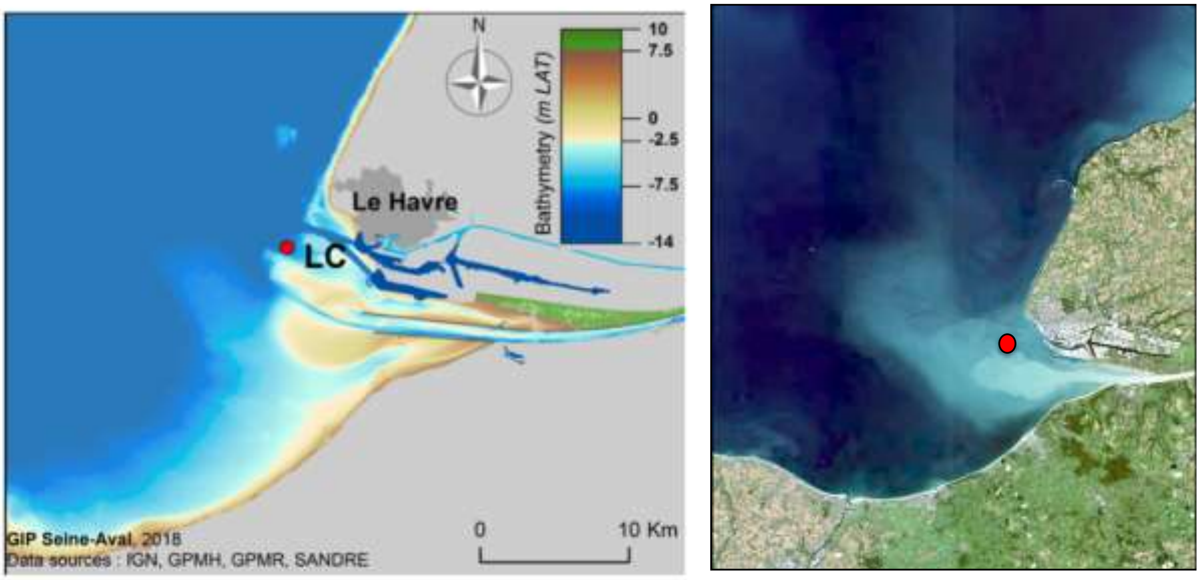

Figure 1: location of the field survey in the Seine Estuary mouth (France): bathymetry (left) and Landsat 8 satellite image of the turbid plume (right)

For the experiment, different instruments are deployed from a profiling frame (Figure 2) over a full tidal cycle. A Seabird 19plus CTD combined with an OBS3+ and a FLNTU Wetlabs are used to monitor the salinity and turbidity gradients. Particle size distribution are observed from:

A LISST 100X type C, measuring floc size distribution at 1Hz over 32 logarithmically spaced classes from 2 microns to 356 microns (random shape model),

A LISST HOLO2 digital holographic camera, taking images at 1Hz. Data are processed with the HOLOBatch software provided with the instrument.

A PCAM device, combining a Canon EOS60D camera (5184x3456 pixels, 4.7x4.7 microns pixel size) and a green laser sheet in the focal plane, that permits to take images of floc silhouettes and limit the presence of out of focus particles. PCAM takes 1 image every 3s. Floc pictures are next processed with Matlab routines using the image processing toolbox.

The frame equipped with all instruments was deployed every 30min over the tidal cycle, collecting data all along a vertical profile from the surface to the bottom. After each profile, 1min data collection was performed at fixed depths (1m below the surface, mid depth and 1m above the bed – Figure 2 right). Every hour, surface and bottom SPM samples were collected from a horizontal Niskin bottle equipped with a FLNTU Wetlabs.

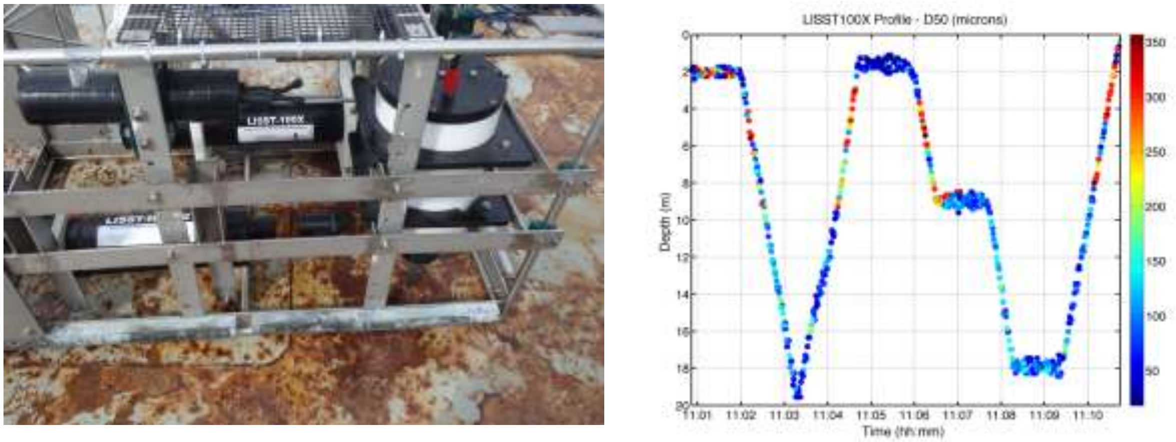

Figure 2: Illustration of the profiling frame equipped with the LISST100X, LISST HOLO2 and PCAM (left), typical profile showing the measurement strategy

Results

SPM dynamics at the tidal scale

The SPM dynamics observed during the tidal cycle on spring tide is typical of coastal sites under the influence of an estuary: during flood, tidal currents are the strongest and induce sediment resuspension with characteristic sizes below100microns and concentration around 100mg/l close to the bed. During high water slack, low current velocities favour aggregation and floc settling, and suspended solid concentration decreases down to 10mg/l (Figure 3). At late ebb and during low water slack, the turbid brackish surface plume reaches the study site, characterized by salinity below 25PSU and SSC larger than 20mg/l. Based on LISST100X measurements, median floc sizes range from 100microns and 200microns in the first 10m above the bed, except during the maximum flood current period. During flood at the surface,

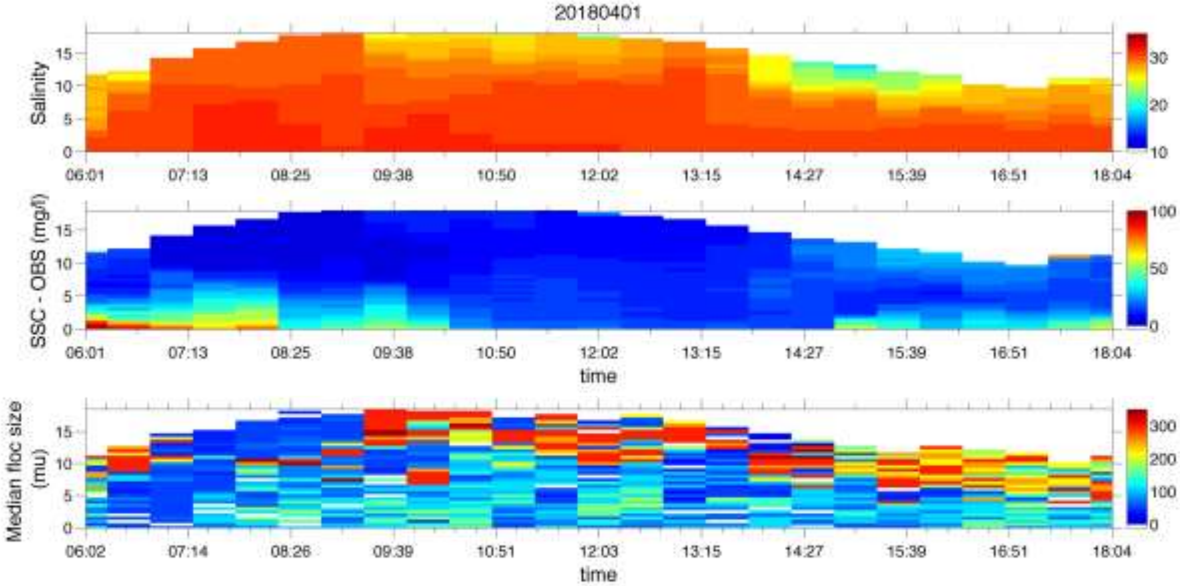

Figure 3: Salinity, suspended solid concentration and LISST100X median floc size dynamics at the tidal scale on spring tide (April 1st, 2018).

marine waters are featured by small flocs (D50 around 50microns). The salinity gradient, through the Schlieren effect, clearly interferes with the LISST100X measurements. It is then difficult to evaluate the SPM dynamics at the water surface.

Multi-instrument floc size observation

A preliminary investigation of the comparison of the floc sizes obtained from the different instruments is illustrated in Figure 4 et 5. A visual comparison of the floc images obtained from the PCAM and the LISST HOLO2 is proposed in Figure 4. These pictures were collected on April 1st 2018 at 11h06, at mid depth (concentration around 10mg/l. At this depth, the LISST100X floc size distribution is characterized by a D50 around 100microns and a mode at 200microns (Figure 5). Results from the LISSTHOLO2, for this

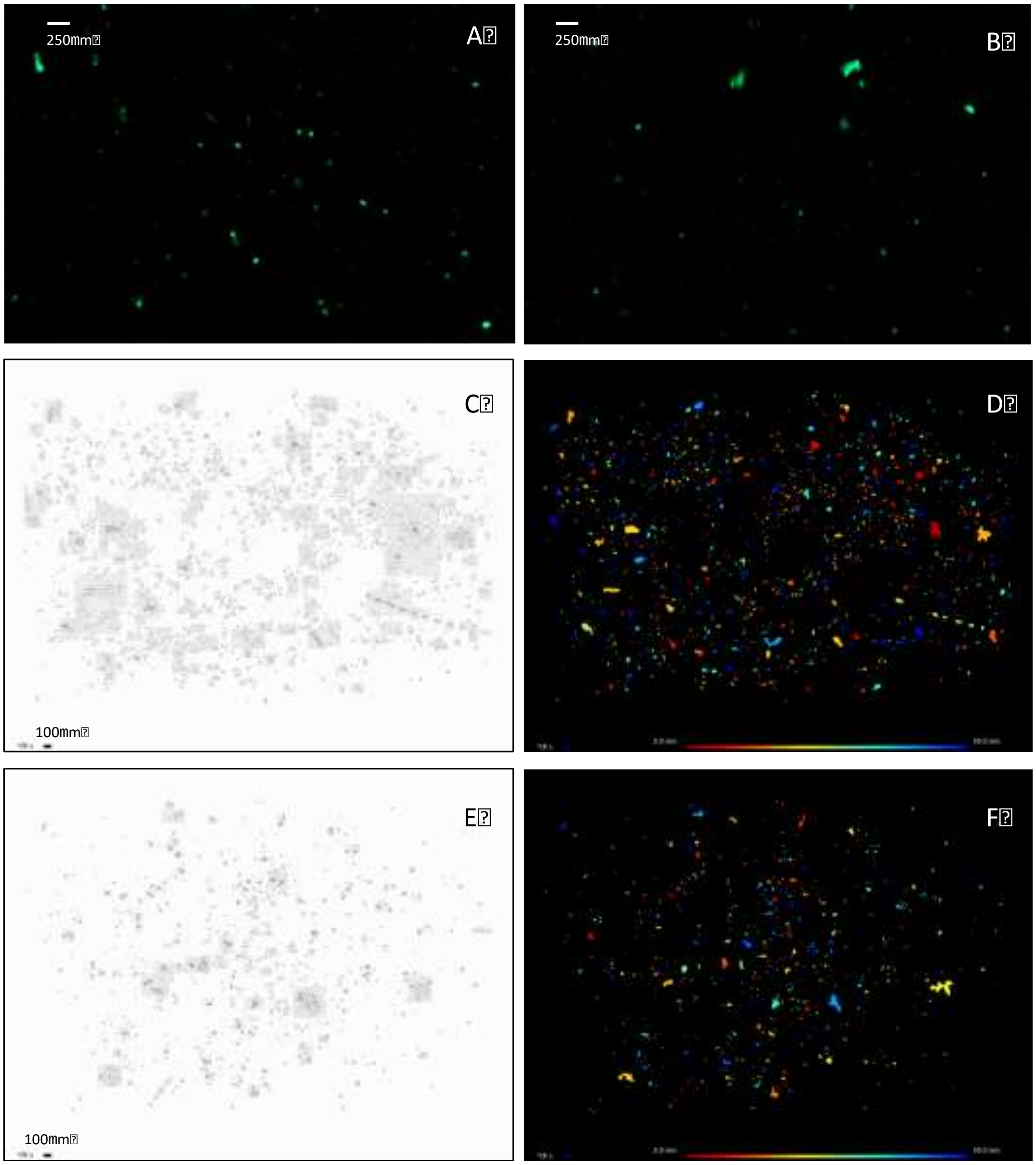

Figure 4: Examples of PCAM (A,B) and reconstructed LISST HOLO2 (C,D,E,F) floc images collected at 11h06 at mid depth. Note that the picture scale is different for the two instruments.

example, show a smaller floc size range. If this result is expected for the lower diameters (LISST HOLO lowest resolution is around 20microns), the PSD obtained from images (C,D) does not show particles larger than 150microns, contrary to the LISST100X. However, at these sizes, only few particles can be observed per image. More images must now be analysed to get a statistically representative distribution before comparison.

A complete analysis of the PCAM images is under progress, but few comparisons can be made from the raw pictures: PCAM largest flocs are in the range of 100-200microns, similar to the LISST HOLO2, and the LISSTHOLO2 “reconstruct” far more small particles (smaller than 50microns) than the PCAM observe. These observations will be further investigated with more details, exploring more images from both instruments, and different conditions (in terms of SSC).

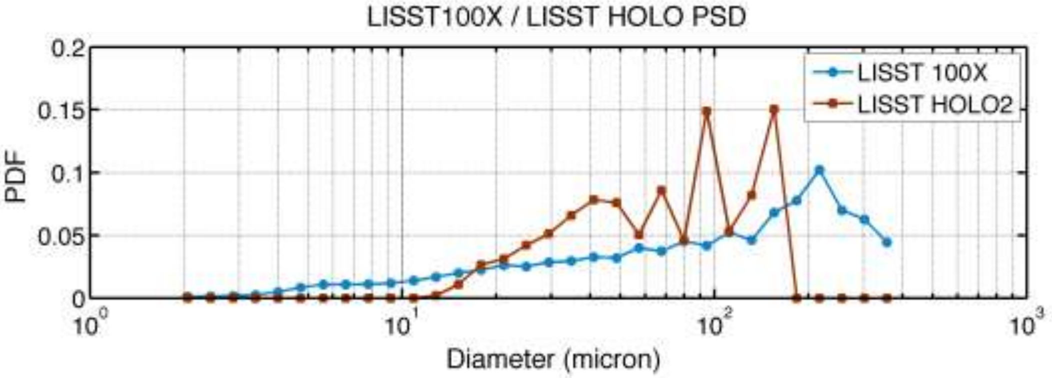

Figure 5: Floc size distribution obtained from the LISST100X and the LISSTHOLO2 (normalized volume distribution – single picture)

References

Agrawal, Y. C. and Pottsmith, H. C. (1994). "Laser diffraction particle sizing in STRESS." Continental Shelf Research 14(10-11): 1101-1109.

Dyer, K. R. and Manning, A. J. (1999). "Observation of the size, settling velocity and effective density of flocs, and their fractal dimension." Journal of Sea Research 41: 87-95.

Fettweis, M., Francken, F., Pison, V. and Van den Eynde, D. (2006). "Suspended particulate matter dynamics and aggregate sizes in a high turbidity area." Marine Geology 235(1-4): 63-74.

Graham G.W. and W. A. M. Nimmo Smith (2010) “The application of holography to the analysis of size and settling velocity of suspended cohesive sediments”. Limnology and Oceanography. Methods 8, 1–15 (2010).

Many, G., Bourrin, F., Durrieu de Madron, X., Pairaud, I., Gangloff, A., Doxaran, D., Ody, A., Verney, R., Menniti, C., Le Berre, D. and Jacquet, M. (2016). "Particle assemblage characterization in the Rhone River ROFI." Journal of Marine Systems 157: 39-51.

Mikkelsen, O. A., Hill, P. S. and Milligan, T. G. (2006). "Single grain, microfloc and macrofloc volume variations observed with a LISST-100 and digital floc camera." Journal of Sea Research 55: 87-102.

Smith, S. J., and C. T. Friedrichs. (2011). Size and settling velocities of cohesive flocs and suspended sediment aggregates in a trailing suction hopper dredge plume. Continental Shelf Research. 10: S50–.

Biological activity: an overlooked, mechanism for sediment resuspension, transport, and modification in the ocean

Gitai Yahel[1], Merav Gilboa[1,2], Shahar Grossbard[3], Adi Vainiger[4], Tali Treibitz[5], Yoav Schechner[4], Uri Shavit[3], and Timor Katz[6]

The School of Marine Sciences, Ruppin Academic Center, Michmoret, Israel

Institute of Earth Sciences, the Hebrew University of Jerusalem, Jerusalem, Israel

Civil and Environmental Engineering, Technion, Haifa, Israel

Electrical Engineering, Technion, Haifa, Israel

Department for Marine Technologies, University of Haifa, Haifa, Israel

Israel Oceanographic & Limnological Research, Tel Shikmona, Haifa, Israel

In high-energy habitats; waves and currents dominate sediment resuspension dynamics and, therefore, also mass transfer processes from the sediment to the overlying water (Ståhlberg et al., 2006) and ultimately, sediment geochemistry and composition (Sarmiento & Gruber 2006). However, even in relatively shallow coastal seas, physical resuspension is a rare event and bottom areas deeper than 50 m are rarely affected by physical forcing (Danielsson et al., 2007; Capet et al., 2016). In the deep sea and abyssal plains as well as in calm coastal habitats, organic matter accumulates and other processes such as molecular diffusion and bioturbation by invertebrates living in the sediment (Meysman et al., 2006) were believed to control sediment transformation and mass flux across the sediment–water interface (Aller and Aller, 1998; Berner, 1980). Systematic observation and anecdotal evidence have been mounting in the last two decades suggesting that large mobile animals such as fish, marine mammals, and crustaceans resuspend large amount of sediment as they search for food or find shelter in the seafloor (Fig 1, (Katz et al., 2012, 2009; Robert and Juniper, 2012; Yahel et al., 2008, 2002). In some low energy environment, this biologically induced resuspension was shown to be a major controller of the near-bottom suspended sediment concentration and composition (Villéger et al., 2017). Observations of biologically induce resuspension range from tropical coral reefs to boreal fjords and from shallow water all the way to the abyss and submarine tranches, where other resuspension process are largely absent. Nevertheless, to date, biologically induced resuspension is not accounted for in geochemical models of the ocean (Capet et al., 2016) or in assessing sediment transport.

The prominence of fish activity was shown at coral reefs (<20 m) in the sheltered Gulf of Aqaba, Red Sea, where, despite the shallowness of these systems, the effect of wind, waves and currents on sediment resuspension was minor. Resuspension activities by fish numbered >1.5 resuspension events m^{-2} h^{--1} and were confined to daytime. Correspondingly, the concentration of suspended sand near the bottom was twice as high during the day than at night (Fig.2) and vertical profiles showed a sharp increase of SSC (2-6 folds) toward the bottom during the daytime, but not at night. An in situ experiment in which fish were excluded from a large section (250 m^2) of the reef resulted in elimination of the day - night differences and a significant decrease in daytime SSC over the treated reef section in comparison to open control sites (Yahel et al., 2002).

Figure 1. Groundfish and marine mammals activity resulting in sediment resuspension. In all photos but B animals are searching for food at the bottom. A. Atlantic cod (*Gadus morhua,* depth of 450 m) in the North sea (see Katz et al. 2009 for more details). B. Slender sole (*Lyopsetta exilis*; 10 cm length) in Saanich Inlet (~90 m depth) borrowing for shelter in the bottom (see Katz et al. 2009 for more details). C. A Bluespotted ribbontail ray (*Taeniura lymma*) and Red Sea goatfish (*Parupeneus forsskali*) at the Gulf of Aqaba (Photo. Hagai Nativ). D. Spotted eagle ray (*Aetobatus narinari*, Photo: Lance Sagar). E. Grey whale (*Eschrichtius robustus,* Photo: Flip Nicklin), and F. Walrus (*Odobenus rosmarus, Photo: Goran Ehlme*)

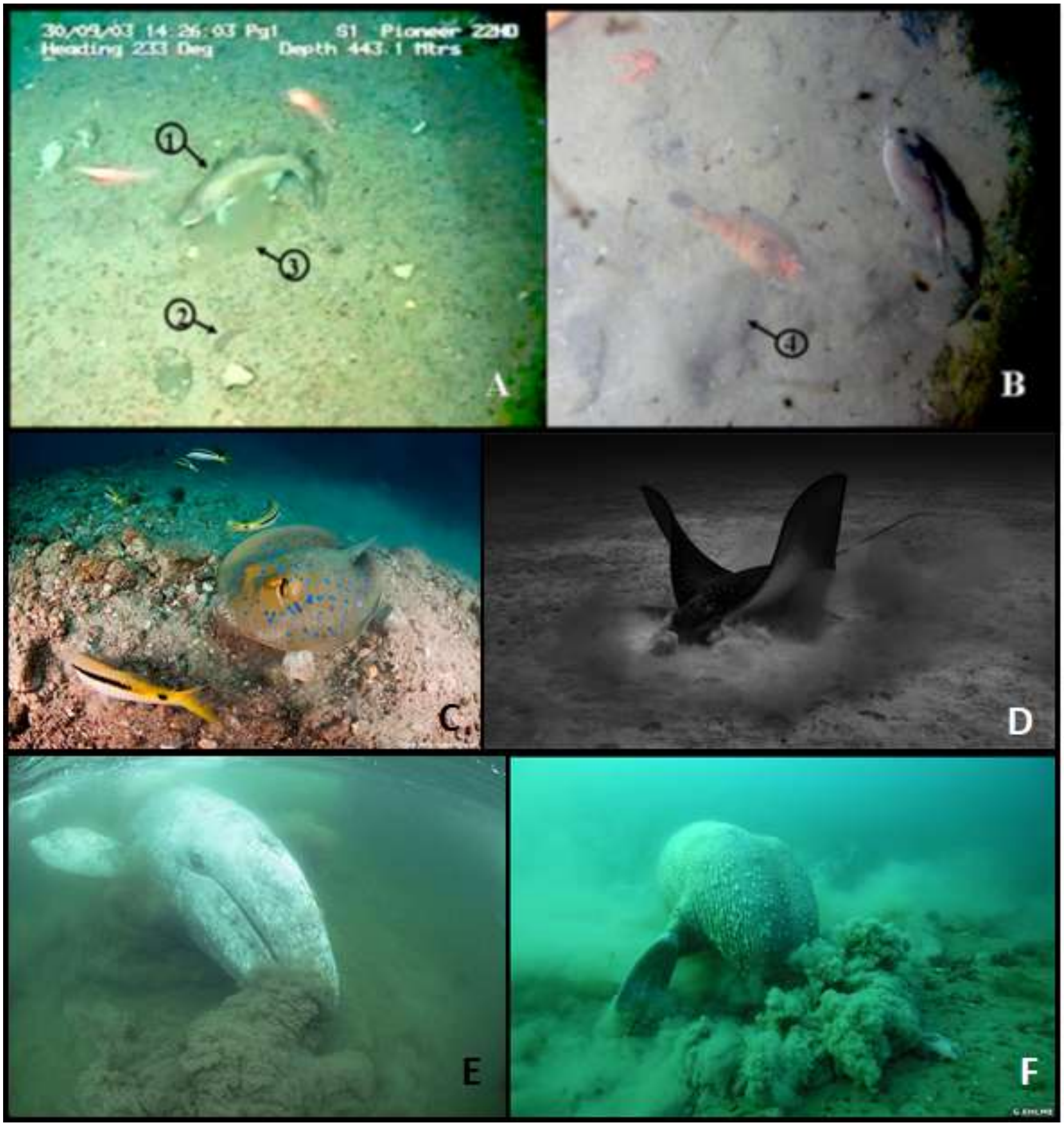

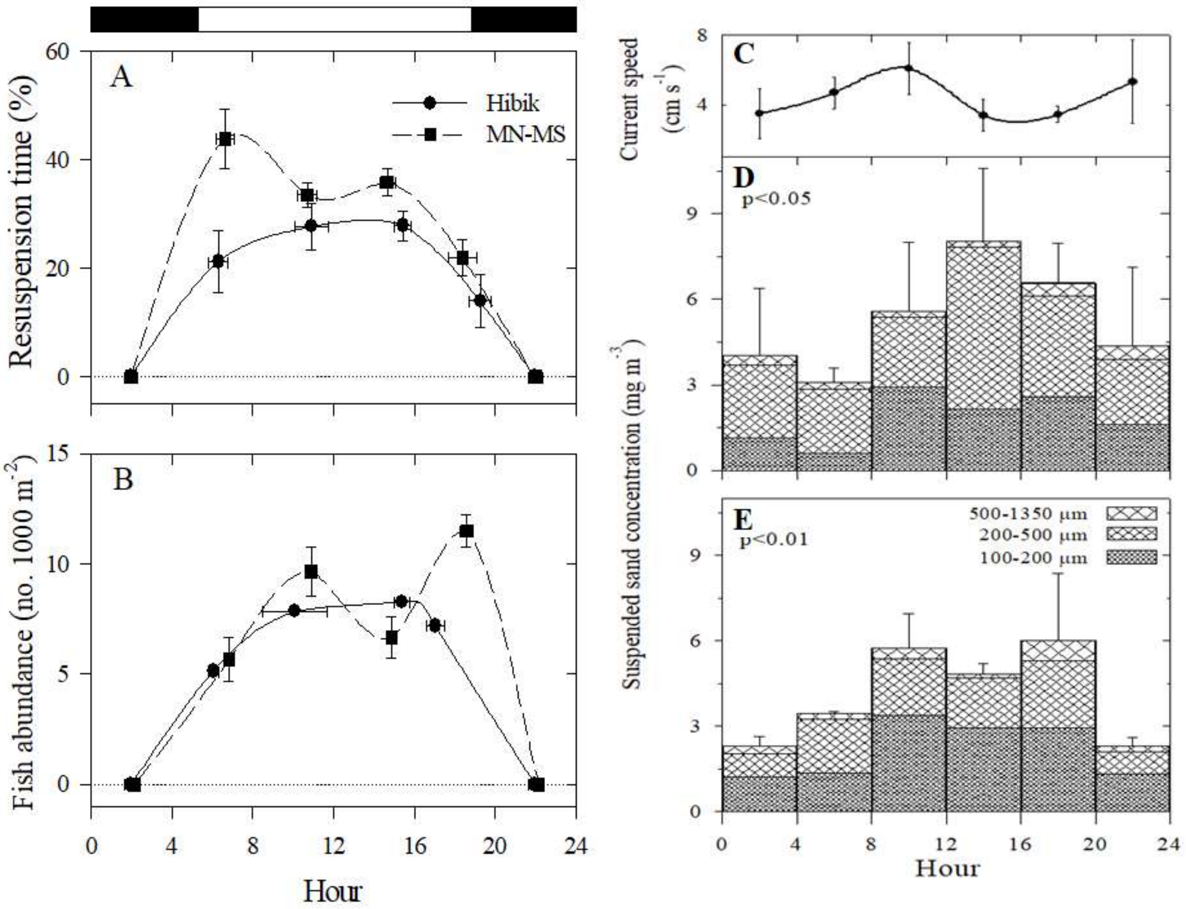

Figure 2. Daily cycles of fish activity (left) and the levels of suspended sediment (sand) in two coral reefs in the gulf of Aqaba. A. Sediment disturbance time, B. Abundance of the Goatfish *Parupeneus forsskali* at the coral reefs of Hibik and Eilat. C. Near-bottom current speed during the time of the sampling. D. and E. Daily cycle of suspended sand concentration in Eilat (D) and Hibik (E). Vertical error bars = SE; Horizontal bars and column width = time span of surveys or sampling. See Yahel et al. (2002) for more details.

Some 20000 km from the Gulf of Aqaba, in partly anoxic Northeast pacific fjords, a dense population of slender sole fish were shown to cause about 4 resuspension events m^{-2} h^{-1} and were also by far the dominant cause for sediment resuspension (Yahel et al. 2008). Rough estimates suggest that the activity of these fish, as they borrow for shelter in the sediment, resuspended about a kg of sediment m^{-2} d^{-1} causing a distinct benthic nepheloid layer over the oxygenated margins (Katz et al. 2012). The benthic nepheloid layer disappear few tens of meters deeper in the anoxic and azoic basin below. This intense fish activity, evident by distinct “spikes” of turbidity, was shown to decrease carbon sequestration (Yahel et al. 2008), enhance silica dissolution (Katz et al. 2009) and nutrient mineralization, and transport large amount of sediment from the oxygenated margins where the fish dwelt, to the deep, anoxic, and azoic basin of the fjord (Katz et al. 2012).

Fish induced resuspension is very different from the resuspension induced by bottom currents or waves. Physical agents are relatively rare events (e.g., storms) that acts over large swaths of the bottom, affect mostly the upper few mm, and last prolong periods (hours-days). In contrast, biological resuspension, is punctuated, acting over a small patches of sediments, penetrates deep (up to tens of cm) and is chronic in nature, as fish (and other animals) are commonly present in most habitats throughout the year. In the deep sea and the abyssal plains, where physical forcing are absent, the persistent biological activity may be the sole force that disturb and resuspended sediment (Robert and Juniper, 2012).

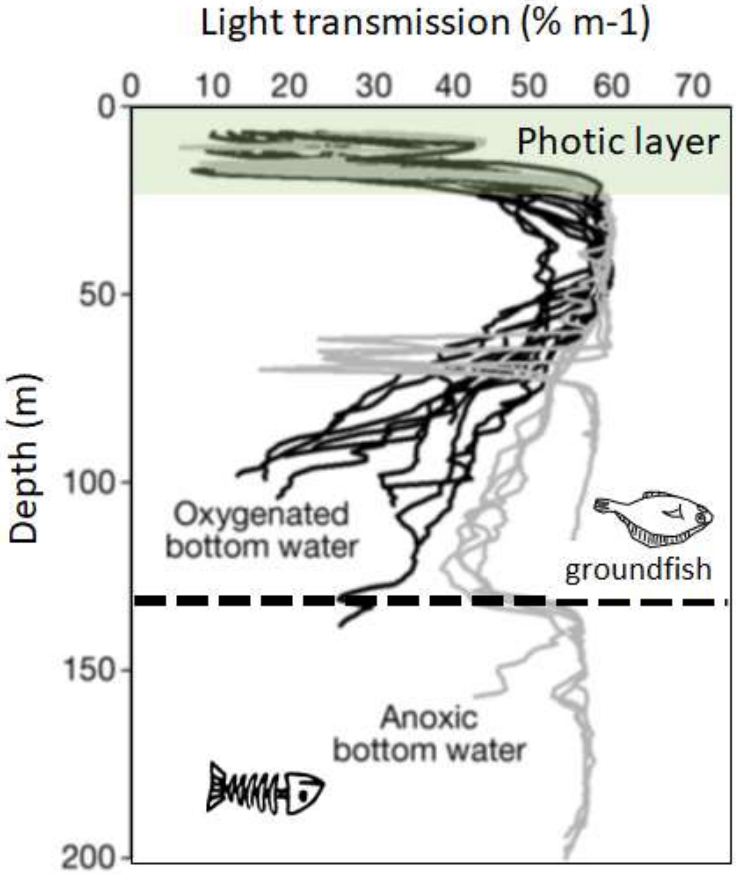

Figure 3: Vertical profiles of light transmission (a proxy for suspended particles concentration) along a transect beginning at the inner anoxic basin of Effingham Inlet, (West coast Vancouver Island, Dallimore et al. 2005). Black lines are profiles taken in locations of oxygenated bottom water where fish would be active, grey lines are profiles taken in the same day in regions having anoxic bottom water with no fish. A well-developed nepheloid layer was always present over oxygenated bottom water but absent in 7 of the 8 profiles taken over anoxic bottom water. (see Yahel et al. 2008 for more details)

To date, our knowledge regarding the rate and extent of sediment resuspension in the ocean is scarce, partly due to the lack of accepted and applicable methods designed for its quantification. Specifically, there is a lack in methods to quantify resuspension flux continuously and to estimate the contribution of biological resuspension to this flux. The sporadic and intens nature of fish (and other animals) induced resuspension pose a special challenge when trying to approach this problem. Simulation and visualization of sediment “clouds” initiated by fish may help to better understand particle dynamics. Such efforts presented by Grosbard et al. and Vainiger et al. (this meeting) whereas Gilboa et al. and Shavit et al. (this meeting) suggest novel methodology, aimed quantify overall and biologically induced resuspension flux in the ocean, respectively.

This research was funded by the Israeli Ministry of Science, Technology and Space (3-12478).

References

Aller, R.C., Aller, J.Y., 1998. The effect of biogenic irrigation intensity and solute exchange on diagenetic reaction rates in marine sediments. J. Mar. Res. 56, 905–936. https://doi.org/10.1357/002224098321667413

Berner, R.A., 1980. Early Diagenesis: A Theoretical Approach. Princeton University Press.

Capet, A., Meysman, F.J.R., Akoumianaki, I., Soetaert, K., Grégoire, M., 2016. Integrating sediment biogeochemistry into 3D oceanic models: A study of benthic-pelagic coupling in the Black Sea. Ocean Model. 101, 83–100. https://doi.org/10.1016/j.ocemod.2016.03.006

Danielsson, Å., Jönsson, A., Rahm, L., 2007. Resuspension patterns in the Baltic proper. J. Sea Res. 57, 257–269. https://doi.org/10.1016/j.seares.2006.07.005

Katz, T., Yahel, G., Reidenbach, M., Tunnicliffe, V., Herut, B., Crusius, J., Whitney, F., Snelgrove, P.V.R., Lazar, B., 2012. Resuspension by fish facilitates the transport and redistribution of coastal sediments. Limnol. Oceanogr. 57. https://doi.org/10.4319/lo.2012.57.4.0945

Katz, T., Yahel, G., Yahel, R., Tunnicliffe, V., Herut, B., Snelgrove, P., Crusius, J., Lazar, B., 2009. Groundfîsh overfishing, diatom decline, and the marine silica cycle: Lessons from Saanich Inlet, Canada, and the Baltic Sea cod crash. Global Biogeochem. Cycles 23. https://doi.org/10.1029/2008GB003416

Meysman, F.J.R., Middelburg, J.J., Heip, C.H.R., 2006. Bioturbation: a fresh look at Darwin's last idea. Trends Ecol. Evol. 21, 688–695. https://doi.org/10.1016/j.tree.2006.08.002

Robert, K., Juniper, S.K., 2012. Surface-sediment bioturbation quantified with cameras on the NEPTUNE Canada cabled observatory. Mar. Ecol. Prog. Ser. 453, 137–149. https://doi.org/10.3354/meps09623

Ståhlberg, C., Bastviken, D., Svensson, B.H., Rahm, L., 2006. Mineralisation of organic matter in coastal sediments at different frequency and duration of resuspension. Estuar. Coast. Shelf Sci. 70, 317–325. https://doi.org/10.1016/j.ecss.2006.06.022

Villéger, S., Brosse, S., Mouchet, M., Mouillot, D., Vanni, M.J., 2017. Functional ecology of fish: current approaches and future challenges. Aquat. Sci. 79, 783–801. https://doi.org/10.1007/s00027-017-0546-z

Yahel, G., Yahel, R., Katz, T., Lazar, B., Herut, B., Tunnicliffe, V., 2008. Fish activity: A major mechanism for sediment resuspension and organic matter remineralization in coastal marine sediments. Mar. Ecol. Prog. Ser. 372. https://doi.org/10.3354/meps07688

Yahel, R., Yahel, G., Genin, A., 2002. Daily cycles of suspended sand at coral reefs: A biological control. Limnol. Oceanogr. 47.-563.